Characterization of PM2.5 Episodes in the San Joaquin Valley Based on Data Collected During the NASA DISCOVER-AQ Study in the Winter of 2013

REPORT TO THE

California Air Resources Board Research Division

Project # 14-307

Prepared by:
Dr. Christopher D. Cappa[1]
Dr. Qi Zhang[2]

[1]Department of Civil and Environmental Engineering
[2] Department of Environmental Toxicology
University of California, Davis
One Shields Avenue, Davis, CA, 95616

April 12, 2018

DISCLAIMER

The statements and conclusions in this report are those of the contractor and not necessarily those of the California Air Resources Board. The mention of commercial products, their source, or their use in connection with material reported herein is not to be construed as actual or implied endorsement of such products.

ACKNOWLEDGEMENTS

In addition to the major funding provided by CARB Project # 14-307, portions of this study were supported by NASA. This manuscript has not been reviewed by the funding agencies and no endorsement should be inferred.

The analysis described in this report was partially conducted by postdoctoral researchers with guidance from their faculty mentors. These postdocs are the lead authors of some of the individual chapters that have been or will be published in peer-reviewed journals. The postdoc team consisted of the following individuals:

- Gouri Prabhakar – postdoctoral scholar, CEE Dept, UC Davis
- Dominique Young – postdoctoral scholar, Environmental Toxicology Dept, UC Davis

The authors thank the many people involved in the collection and analysis of the DISCOVER-AQ data, especially Dr. Caroline Parworth, Dr. Xiaolu Zhang, Dr. Hwajin Kim and Dr. Sonia Collier.

The authors would like to thank William Vance (CARB) for grant management support.

TABLE OF CONTENTS

LIST OF FIGURES

LIST OF TABLES

ABSTRACT

The San Joaquin Valley (SJV) in California experiences persistent air quality problems associated with elevated particulate matter (PM) concentrations due to anthropogenic emissions, topography, and meteorological conditions. Thus, it is important to unravel the various sources and processes that affect the physico-chemical properties of PM in order to better inform pollution abatement strategies and improve parameterizations in air quality models. Ground and aircraft data from the DISCOVER-AQ field study have been analyzed to develop insights into the factors that govern wintertime particulate pollution in the San Joaquin Valley (SJV) air basin, with a particular focus on particulate ammonium nitrate (AN). The results provide an explicit case-study illustration of how nighttime chemistry can influence daytime surface-level AN concentrations, complementing previous studies in the SJV. The observations exemplify the critical role that nocturnal chemical production of AN aloft in the residual layer (RL) can play in determining daytime surface-level AN concentrations. Further, they indicate that nocturnal production of AN in the RL, along with daytime photochemical production, can contribute substantially to the build-up and sustaining of severe pollution episodes. The exceptionally shallow nocturnal boundary layer heights characteristic of wintertime pollution events in the SJV intensifies the importance of nocturnal production aloft in the residual layer to daytime surface concentrations. The observations also demonstrate that dynamics within the RL can influence the early-morning vertical distribution of AN, despite low wintertime wind speeds. This overnight reshaping of the vertical distribution above the city plays an important role in determining the net impact of nocturnal chemical production on local and regional surface-level AN concentrations. Entrainment of clean free tropospheric air into the boundary layer in the afternoon is identified as an important process that reduces surface-level AN and limits build-up during pollution episodes. The influence of dry deposition of HNO_3 gas to the surface on daytime particulate nitrate concentrations is important but limited by an excess of ammonia in the region, which leads to only a small fraction of nitrate existing in the gas-phase even during the warmer daytime. However, in late afternoon, when diminishing solar heating leads to a rapid fall in the mixed boundary layer height, the impact of surface deposition is temporarily enhanced and can lead to a substantial decline in surface-level particulate nitrate concentrations; this enhanced deposition is quickly arrested by a decrease in surface temperature, which drops the gas-phase fraction to near zero. The overall importance of enhanced late afternoon gas-phase loss to the multiday build-up of pollution events is limited by the very shallow nocturnal boundary layer. The case study here demonstrates that mixing down of AN from the RL can contribute a majority of the surface-level AN in the morning (here, ~80%), and a strong influence can persist into the afternoon even when photochemical production is maximum. The particular day-to-day contribution of aloft nocturnal AN production to surface concentrations will depend on prevailing chemical and meteorological conditions.

The other major particulate constituent besides AN observed during DISCOVER-AQ was organic aerosol (OA). Approximately, half of this OA was from primary sources (cooking, vehicles and wood combustion) and half from secondary sources. The concentration of primary OA was largest

in the early evening and at nighttime, a result of the particularly shallow nocturnal boundary layer and enhanced local emissions during this time. The concentration of secondary OA varied to a lesser extent with time of day, reflecting a more regional source, although there was a secondary OA component that behaved similarly to AN, suggesting nocturnal production. Although specific to the SJV, the observations and conceptual framework further developed here provide general insights into the evolution of pollution episodes in wintertime environments.

To summarize, our observations and box-modeling lead to the following overall conceptual model of ammonium nitrate dynamics over population centers within the SJV, and in the SJV as a whole.

- Nocturnal formation of AN within the residual layer is a key production mechanism. The extent of formation in the RL depends largely on the NO_2 and O_3 concentrations that exist just prior to sunset, as these feed the RL.
- When wind speeds are low, nocturnal AN production in the RL can be substantial over pollution centers. Entrainment of RL air to the surface can drive lead to very large concentrations of AN at the surface in the mid-to-late morning, after sunrise. The AN concentrations in the morning after sunrise are controlled almost entirely by processes that occurred overnight in the RL, given the very shallow nocturnal boundary layer.
- When wind speeds are higher, export of NO_2 from pollution centers via horizontal advection limits local AN formation but contributes to a regional background of AN. There will be less contrast between AN concentration within the nocturnal boundary layer and the RL over cities, and thus much smaller changes in the surface AN concentration in the morning.
- Altitudinal variability in nocturnal advection has a strong influence on the early morning AN vertical profile shape, and consequently on the timing and peak surface concentration of AN in the mid-to-late morning as RL air is entrained to the surface mixed layer.
- Nocturnal AN formation at the surface is limited within pollution centers by titration of O_3 by NO as a consequence of the very shallow nocturnal boundary layer.
- Daytime formation of AN via NO_2 photooxidation is an important production mechanism within pollution centers where daytime NO_2 is somewhat elevated.
- Entrainment of typically cleaner free tropospheric air maximizes during the daytime and is a substantial sink for AN and other pollutants. The entrainment rate of free troposphere (and associated dilution) is similar to the photochemical production rate and with similar timing, such that these can be largely offsetting. Entrainment of free troposphere air is the key AN sink during pollution episodes.
- Dry deposition of HNO_3 as a sink for AN is strongly limited by excess NH_3 and low nighttime temperatures. The total ammonia/nitrate ratio is sufficiently large that ammonia control is unlikely to have a substantial impact on AN concentrations.
- Strong AN-driven pollution episodes occur when production of AN exceeds loss day after day. This is largely controlled by processes that occur in the nocturnal residual layer, but modulated through feedbacks that occur through advection of NO_2 from cities to surroundings and through daytime production and loss.

1 EXECUTIVE SUMMARY

1.1 Background:

Despite years of efforts, particulate matter (PM) air pollution in the San Joaquin Valley (SJV) of California remains the worst in the state, often exceeding the US Environmental Protection Agency (EPA) 24-hour standard for PM with aerodynamic diameters less than 2.5 micrometers ($PM_{2.5}$) of 35 $\mu g\ m^{-3}$. Most often, these exceedance periods are during the winter. To address this problem, it is necessary that the sources and atmospheric processes that contribute to high PM levels are understood in detail. The winter PM issues are confounded by there being low wind speeds and a very shallow and stable boundary layer, which together limit dispersion of pollutants. This issue is exacerbated by the unique SJV topography, which leads to trapping of pollutants and the occurrence of multi-day build-ups of pollution.

1.2 Objectives and Methods:

This project used aircraft and ground measurements made in January and February, 2013 within the SJV during the NASA DISCOVER-AQ study to refine and update the conceptual model of $PM_{2.5}$ in the SJV during winter. This project has served to: (i) elucidate the sources that contributed to the observed $PM_{2.5}$ episodes; (ii) improve understanding of the atmospheric processes, including emissions, that led to the build-up/dissipation of the episodes; and (iii) update the conceptual model for $PM_{2.5}$ formation in the SJV in winter months

The specific tasks to achieve these goals included:

Task 1: Analysis of spatial and temporal distributions of $PM_{2.5}$
Task 2: Numerical modeling of $PM_{2.5}$ during DISCOVER-AQ in support of conceptual model development.
Task 3: Updating of the conceptual model of $PM_{2.5}$ formation in the SJV.

These tasks proved highly interrelated and, ultimately, are difficult to separate into distinct discussions; detailed analysis and discussion of the outcomes from these tasks are combined in the Chapters that follow. Chapter 2 focuses on understanding the diurnal variability in particulate ammonium nitrate (AN) concentrations and assessing the key source pathways and sinks. Chapter 3 provides a broader discussion of the overall particulate matter composition and temporal variability, as well as places the results from DISCOVER-AQ (in 2013) in a broader context.

1.3 Results

The measurements made during DISCOVER-AQ are ideally suited for assessment and updating of the conceptual model of $PM_{2.5}$ formation in the SJV during winter as they provide vertical, temporal and spatial coverage. During DISCOVER-AQ (in 2013) two distinct pollution events were observed. Analysis of the observations confirms that wintertime submicron PM in the SJV is primarily composed of organic aerosol (OA) and ammonium nitrate (AN), with small contributions from ammonium sulfate, ammonium chloride and metal salts. The OA and AN exhibit distinctly different diurnal profiles. The ground-level OA concentrations are typically largest at night, with approximately half from primary (biomass burning, vehicles, cooking) and half from secondary

sources (nighttime and daytime chemical production, both at the surface and above the ground). These are strongly modulated by the dynamics of the boundary layer.

Considering AN, during DISCOVER-AQ (in 2013) the surface AN concentration increased rapidly starting at daybreak, and persisted through the late morning, peaking around 10-11 am, before declining through the afternoon, differing substantially from the OA behavior. The behavior in 2013 also differed from similar measurements in 2010, which showed a flat diurnal profile and lower concentrations. This difference between years is most related to differences in (i) meteorological conditions (wind speed, temperature, humidity and solar irradiance), and (ii) O_3 concentrations. Combining the surface measurements of AN with vertical profiles of AN and other gas-phase species and meteorological variables allowed for assessment of formation and loss pathways. The observations, coupled with a box model, demonstrate that nighttime formation of AN in layers above the surface have a controlling influence on daytime surface concentrations, and this is strongly linked to O_3 and NO_2 concentrations just prior to sunset. Horizontal advection in above-surface layers overnight serves to reduce peak concentrations within pollution centers (i.e. cities), but does not actually remove pollution from the SJV as a whole, only spreads it out regionally. Daytime AN production is found to be slow in the wintertime, but nonetheless an important production mechanism. The dominant AN loss process is found to be daytime entrainment and dilution. Once the daytime mixed layer is fully grown, air is exchanged with the (typically) much cleaner free troposphere. This daytime entrainment offsets or even overwhelms much of the daytime photochemical production. Entrainment of cleaner free tropospheric air serves as a net pollution sink for the entire SJV, both within and outside of pollution centers. This physical process provides an important limitation on pollution build-up during pollution events. Dry deposition of HNO_3 gas, with subsequent loss of AN via evaporation, plays a limited role in reducing AN concentrations. This is because the SJV has a large excess of ammonia; most nitrate is in the form of AN, which strongly limits loss via this pathway. The extent of ammonia reduction to strongly impact AN concentrations is too large to be a feasible control strategy; instead, control efforts should focus on NO_x.

1.4 Conclusions

Overall, our analysis lead to the following conceptual model of particulate pollution dynamics over population centers within the SJV, and in the SJV as a whole. (i) Both OA and AN contribute importantly to the 24-h average $PM_{2.5}$ concentrations during pollution events, but with very different temporal dependencies. OA is most important at night and AN most important during the day. Greater understanding of the chemically-resolved diurnal variability across years will help in developing effective control strategies. (ii) AN concentrations are controlled by both nocturnal processes, primarily occurring above the surface, and daytime processes. Reductions in NO_x are likely to have a strong impact on future AN concentrations, with the largest impact on the nighttime formation.

2 THE OBSERVATIONAL ASSESSMENT OF THE ROLE OF NOCTURNAL RESIDUAL-LAYER CHEMISTRY IN DETERMINING DAYTIME SURFACE PARTICULATE NITRATE CONCENTRATIONS

2.1 Introduction

Nocturnal processing of nitrogen oxides, NO_x (= NO + NO_2) can strongly influence daytime air quality (Dentener and Crutzen, 1993;Brown et al., 2006d). At night, once photochemical reactions shutdown, NO_x reacts with ozone (O_3) to form nitrate radical (NO_3) and dinitrogen pentoxide (N_2O_5) (Reactions 1 through 3a). N_2O_5 can react heterogeneously with airborne particles to form either nitric acid (HNO_3) (Reaction 4a) or, in the presence of particulate chloride, nitryl chloride ($ClNO_2$) (Reaction 4b, where Y_{ClNO2} represents the molar yield of $ClNO_2$ with respect to the N_2O_5 reacted). In the presence of basic species like ammonia (NH_3), HNO_3 can be neutralized to form particulate nitrate ($NO_3^-{}_{(p)}$). NO_3 radicals can alternatively react with volatile organic compounds (VOCs), which suppresses HNO_3 formation (Reaction 3b). Much research has focused on the influence of nocturnal NO_x processing on the regional budgets of NO_x and O_3 and on the oxidative capacity of the atmosphere during subsequent mornings (e.g. Thornton et al., 2010;Brown et al., 2006c;Wild et al., 2016). The corresponding impact of nighttime production of $NO_3^-{}_{(g+p)}$, a key nocturnal sink for NO_x, on local and regional air quality can be considerable (Lowe et al., 2015;Pusede et al., 2016) but is less often considered in detail.

$NO + O_3 \rightarrow NO_2 + O_2$ (R1)

$NO_2 + O_3 \rightarrow NO_3 + O_2$ (R2)

$NO_2 + NO_3 \leftrightarrow N_2O_5$ (R3a)

$NO_3 + VOC \rightarrow products$ (R3b)

$N_2O_5 + H_2O(het) \rightarrow 2HNO_3$ (R4a)

$N_2O_5 + Cl^-(het) \rightarrow Y_{ClNO2} + (2 - Y_{ClNO2})NO_3^-$ (R4b)

The importance of nocturnal NO_x chemistry to $NO_3^-{}_{(p)}$ production can be especially important in the winter. Relative to summer, nights in winter are longer, colder and more humid, and biogenic VOC emissions tend to be smaller. This allows for a larger fraction of NO_2 to be oxidized to HNO_3 via the N_2O_5 hydrolysis pathway (Cabañas et al., 2001;Wagner et al., 2013) and colder temperatures favor partitioning of nitrate to the particle-phase (Stelson and Seinfeld, 1982). In winter, night time HNO_3 production can more efficiently compete with daytime photochemically driven production due to the low photolysis rates and hydroxyl radical concentrations (Wagner et al., 2013;Pusede et al., 2016). Multiday pollution events (i.e. periods with elevated particulate matter concentrations) can occur when meteorological conditions inhibit dispersion, as is the case

with persistent cold air pool formation often found in valley regions (Whiteman et al., 2014;Baasandorj et al., 2017). During the daytime, sunlight driven convection leads to an evolution of the near-surface temperature profile and causes the atmosphere to be reasonably well mixed up to some height (typically less than 1 km; c.f. **Figure 2-1**). Radiative cooling in the late afternoon leads this mixed layer (ML) to decouple and separate into a shallow, near surface-level nocturnal boundary layer (NBL) and a residual layer (RL) aloft, the behavior of which can be further modified by valley flows.

Nocturnal conversion of NO_x to $NO_3^-(p)$ can occur either in the NBL or the RL. Surface NO emissions can substantially limit direct production of $NO_3^-(p)$ in the NBL by titrating O_3, depending on the initial conditions. Nocturnal surface NO emissions do not directly influence the decoupled RL, with chemical production of $NO_3^-(p)$ dependent on the NO_x, O_3 and particulate matter in the mixed layer at the time of decoupling. Box and 3D models have been previously used to assess the contribution of nocturnal processes in the RL to the daytime surface concentrations of particulate matter (PM), especially $NO_3^-(p)$ (Riemer et al., 2003;Curci et al., 2015). Yet, computational models often have difficulty in accurately predicting surface $NO_3^-(p)$ in many regions, particularly in the winter season, despite good estimations of NO_x emissions (Walker et al., 2012;Terrenoire et al., 2015), although this is not always the case (e.g. Schiferl et al., 2014). Here, airborne and ground measurements made over Fresno, CA in the San Joaquin Valley (SJV) during the wintertime 2013 DISCOVER-AQ (Deriving Information on Surface Conditions from COlumn and VERtically resolved observations relevant to Air Quality; Appendix A) (Crawford and Pickering, 2014) study are used to further develop our understanding of the role that different factors play in determining surface-level $NO_3^-(p)$ concentrations.

Winters in Fresno are characterized by frequent multiday pollution episodes (Chow et al., 1999;Watson and Chow, 2002c), when $PM_{2.5}$ (PM with aerodynamic diameter < 2.5 μm) mass concentrations exceed the 24-hour National Ambient Air Quality Standard (NAAQS) of 35 μg m^{-3} (**Figure 2-2**). Fresno is one of the largest cities in the San Joaquin Valley (SJV), which is largely an agricultural area and suffers from some of the worst air pollution in the United States (American Lung Association, 2014). Shallow daytime mixed layer heights and low wind speeds in winter lead to the accumulation of pollutants across the valley (San Joaquin Valley Air Pollution Control District, 2003). Previous observations in the SJV region have found a build-up of NH_4NO_3 during pollution episodes (e.g. Chow et al., 2008a). Approximately 30 – 80% of the wintertime $PM_{2.5}$ mass in this region is ammonium nitrate (NH_4NO_3), with a strong diurnal variability, and most other $PM_{2.5}$ being organic matter (Chow et al., 2006b;Ge, 2012;Young et al., 2016;Parworth et al., 2017). During DISCOVER-AQ specifically, $NO_3^-(p)$ was found to represent 28% of non-refractory $PM_{1.0}$ (PM with aerodynamic diameter < 1 μm) mass on average (Young et al., 2016).

An important role for nocturnal $NO_3^-(p)$ production in this region has been previously identified based on observations of long-term trends, the spatial and diurnal variability in $NO_3^-(p)$, and the chemical environment in and around Fresno. For example, Watson and Chow (2002c) reported a

sharp, early morning (~9 am) increase in surface $NO_3^-(p)$ concentrations on many days of a severe pollution episode in 2000 and suggested that this behavior was consistent with mixing down of nitrate-rich air from the RL aloft. Young et al. (2016) and Parworth et al. (2017) observed similar behavior more than a decade later during DISCOVER-AQ in 2013. Pusede et al. (2016) characterized the relationship between long-term (multi-year) surface measurements of wintertime $NO_3^-(p)$ and NO_2 in Fresno and Bakersfield and showed that the decline in $NO_3^-(p)$ in SJV over time (2001-2012) was predominately driven by reduced nocturnal $NO_3^-(p)$ production in the residual layer. The balance between production, especially night time production, and daytime losses was identified by them as critical to understanding the multiday build-up during pollution events. Further, they concluded from DISCOVER-AQ aircraft measurements that much of the $NO_3^-(p)$ production was localized over the cities given the sharp urban-rural gradients in $NO_3^-(p)$; the spatial gradients in 2013 (from (Pusede et al., 2016)) seem to be sharper than gradients in 2000 (from (Chow et al., 2006b)), likely reflecting the increasing localization of the $NO_3^-(p)$ pollution to the urban centers as overall $NO_3^-(p)$ concentrations in the region have decreased. Brown et al. (2006a) observed that the number concentration of accumulation mode particles (0.32-1.07 μm) often increased above the surface at 90 m AGL compared to surface (7 m AGL) measurements during night, and suggested that this was due to growth of smaller particles into the accumulation mode via $NO_3^-(p)$ formation. They also observed that the concentration of $NO_3^-(p)$ at 90 m AGL often increased at night, suggestive of *in situ* production.

The present study builds on this literature by examining the role that aloft nocturnal nitrate production, in concert with other processes, has in determining surface $NO_3^-(p)$ concentrations during the DISCOVER-AQ campaign that took place in January and February 2013 in the SJV. Our study combines aircraft and surface observations from DISCOVER-AQ (**Figure 2-3**). During DISCOVER-AQ, two pollution episodes were observed during which $PM_{2.5}$ concentrations were elevated (Young et al., 2016). The analysis here focuses on quantitative assessment of $NO_3^-(p)$ concentrations during this first episode (14 – 22 January) in terms of the processes that govern the $NO_3^-(p)$ diurnal behavior; the observed behavior during this first episode is qualitatively compared with that during the second episode (30 January – 6 February) to examine the factors that contribute to episode-to-episode variability. On flight days, *in situ* measurements of the vertical profiles of particulate and gas concentrations above Fresno (and other SJV cities) were made three times: in the mid-morning (~9:30 am), around noon and in the mid-afternoon (~2 pm). These measurements allow for assessment of the daytime evolution of the vertical distribution of PM and gases as well as characterization of the time-varying boundary layer height. They also allow for determination of the overnight evolution of the PM vertical distribution, which can be used to characterize the factors that control $NO_3^-(p)$ concentrations in the RL. The influence of processes occurring aloft on the temporal evolution of $NO_3^-(p)$ surface concentrations is quantitatively evaluated for this case-study using an observationally constrained 1D box model. The box model accounts for both vertical mixing (entrainment) of air to the surface and for photochemical $NO_3^-(p)$ production, as well as $NO_3^-(p)$ loss processes. Ultimately, the observations and analysis further illustrate how daytime surface-level $NO_3^-(p)$ concentrations depend on a combination of both nocturnal and

daytime production of $NO_3^-(p)$, vertical mixing, altitude-dependent advection in the RL overnight, daytime entrainment of clean air from the free troposphere (FT) and evaporation-driven dry deposition. The model and observations are used to examine the relative importance of these different pathways during the case-study episode considered. This work adds to the existing literature by providing an observationally based, case-study demonstration of how nocturnal processes occurring aloft—in concert with other processes—exert a major control over the evolution of pollution episodes within the SJV specifically, and likely in other regions as well.

2.2 Materials and Method

Airborne *in-situ* measurements (such as particle scattering, gas-phase concentrations, RH and temperature) during the DISCOVER-AQ campaign were made by a suite of instruments on board the P3-B NASA aircraft. The flight path flown during each of the three legs for each flight day is shown in **Figure 2-3**. The aircraft measurements were complemented by a network of ground measurement sites, of which Fresno was one. At Fresno, continuous, *in situ* measurements of the chemical composition and physical properties of particulate matter were performed along with measurement of NAAQS regulated pollutants (Zhang et al., 2016b;Young et al., 2016;Parworth et al., 2017). Local conditions during DISCOVER-AQ were relatively cool (T_{avg} = 7.9 °C) and dry (RH_{avg} = 69%) with frequent sunshine and no visible fog. All data are archived at the DISCOVER-AQ website (NASA Atmospheric Science Data Center). Details of all measurements made are provided in Appendix A and summarized in **Table 2-1**.

2.3 Results and Discussion

2.3.1 Vertical distribution of particulate nitrate

The concentration and vertical distribution of $NO_3^-(p)$ in the RL ($[NO_3^-(p)]_{RL}$) in the morning serves as the initial condition constraint on what is mixed down to the surface as the day advances and the ML rises. Thus, knowledge of the vertical distribution of $NO_3^-(p)$ in the RL near sunrise is needed to predict the temporal evolution of surface-level $NO_3^-(p)$ during the daytime, as will be done below. Night time flights were not made during DISCOVER-AQ to allow for characterization of the overnight evolution of the RL. However, the early morning (~09:30 local time) vertical profiles over Fresno allow for characterization of the vertical structure of most of the RL near sunrise (~07:10 local time), as the surface boundary layer height at this point is still quite shallow (~50 m; see Appendix B for a description of the mixed boundary layer height determination method, **Figure 2-4** and **Figure 2-5**). Fast measurements of total NO_3^- (gas + particle, $NO_3^-(g+p)$) were only available for a subset of flights (Pusede et al., 2016), and particulate-only NO_3^- measurements were not made with sufficient time resolution, less than about a minute, to allow for robust characterization of the $NO_3^-(p)$ vertical profile. Therefore, $NO_3^-(p)$ vertical profiles for each flight during Episode 1 are estimated from *in situ* measurements of dry particle scattering and the influence of water uptake on scattering, i.e. from the particle hygroscopicity,

and calibrated against the slower PILS measurements (Appendix A, **Figure 2-6**). The derived, observationally constrained $NO_3^-_{(p)}$ profiles based on the estimated $NO_3^-_{(p)}$ exhibit generally good correspondence with the sparser direct measurements of $NO_3^-_{(g+p)}$, although on one of the two days available for comparison the total NO_3^- somewhat exceeds the estimated $NO_3^-_{(p)}$ below ~75 m (**Figure 2-7**). This indicates that the estimation method is reasonable, especially since most nitrate is expected to be in the particle-phase (Parworth et al., 2017) given the high relative total ammonium ($NH_3 + NH_4^+$) concentrations (**Figure 2-8**). Only four out of five flight days during Episode 1 have been included in this analysis due to insufficient data on 16 January.

Over Fresno, the observed afternoon (~2:30 pm) $NO_3^-_{(p)}$ concentrations are nearly constant with altitude up to ~400 m (the daytime boundary layer height) (**Figure 2-7**B) whereas the early-morning $NO_3^-_{(p)}$ concentrations decrease steeply with altitude up to ~350 m (**Figure 2-7**A). Corresponding vertical profiles for NO, NO_2, O_3, relative humidity, temperature and total particle scattering are shown in **Figure 2-9** (early morning) and **Figure 2-10** (afternoon). Like $NO_3^-_{(p)}$, all indicate substantial differences between the early morning and afternoon profile shapes. This provides a strong indication that altitude-specific processes occur overnight that lead to a reshaping of the $NO_3^-_{(p)}$ vertical profile. At some altitudes the $NO_3^-_{(p)}$ in the early-morning RL is greater than the $NO_3^-_{(p)}$ measured in the previous afternoon, indicating net production, while at other altitudes the early-morning RL $NO_3^-_{(p)}$ is less than the previous afternoon, indicating net loss (**Figure 2-7**). As noted by Pusede et al. (2016), there tend to be sharp concentration gradients in $NO_3^-_{(p)}$ and NO_x between the city and surrounding areas, with lower concentrations outside the city. Thus, whether $NO_3^-_{(p)}$ at a given altitude increases or decreases overnight results from the competing effects of chemical production versus horizontal advection bringing in this (typically) cleaner air from outside the city. (In the absence of a strong jet aloft and no convective mixing, night time entrainment of cleaner FT air into the RL is expected to be considerably slower than horizontal advection.) Like $NO_3^-_{(p)}$, the boundary layer is reasonably well mixed with respect to NO_x, O_3 and particles at the time when decoupling of the RL occurs, around 3 pm the previous day (**Figure 2-9**). Box model calculations indicate that the expected local nocturnal chemical production of nitrate in the RL should exhibit relatively minor vertical variation due to variations in temperature and RH alone (**Figure 2-10**). In other words, without advective loss or dilution processes of either $NO_3^-_{(p)}$ or the precursor gases it is expected that the $NO_3^-_{(p)}$ concentration would increase to a similar extent at all RL altitudes.

The substantial changes observed in the shape of the vertical profile overnight indicate that night time differential advection in the RL is a major factor in determining the shape of the morning $NO_3^-_{(p)}$ vertical profile during this pollution episode. Differential horizontal advection serves to directly export $NO_3^-_{(p)}$ from the urban area and import cleaner air from surrounding areas. Secondarily, as NO_x concentrations are also lower outside of the Fresno urban area (Pusede et al., 2014), this differential advection will also influence the over-city concentrations of precursors gases (NO_x and O_3; **Figure 2-9** and **Figure 2-11**) and consequently the altitude-specific nitrate production, with decreases likely. This is supported by surface-level measurements of NO_x and O_3

made in Fresno and in the nearby and much more rural cities of Parlier (located 35 km SE of Fresno) and Madera (located 40 km NW of Fresno). The NO_x and NO_2 concentrations are higher and the O_3 lower in Fresno compared to the surrounding cities throughout the day, and the instantaneous nitrate production rate ($[NO_2][O_3]$) is substantially higher in Fresno in the late afternoon, when decoupling occurs (**Figure 2-12**). The important implication is that overnight advection both directly and indirectly alters the vertical $NO_3^-{}_{(p)}$ profile and decreases the over-city $NO_3^-{}_{(p)}$ concentrations in the morning, which will consequently serve to limit the extent of localized pollution build-up during events. The impact of overnight differential advection on reshaping the vertical distribution of $NO_3^-{}_{(p)}$ has likely increased over the last 15 years as the sharpness of the urban-rural concentration gradients has increased (Chow et al., 2006b;Pusede et al., 2016). Nonetheless, the $NO_3^-{}_{(p)}$ advected from urban areas in the RL will contribute to the regional SJV background and serve to sustain $NO_3^-{}_{(p)}$ levels across the valley during pollution episodes.

In the summer, transport and dispersion of pollutants has been attributed to low-level winds (less than 500 m AGL) in the SJV (Bao et al., 2008). We suggest that a similar, but weaker, circulation may exist even in the winter, just at much slower wind speeds, and that this advection overnight is what leads to differential wash out and the establishment of the particular vertical $NO_3^-{}_{(p)}$ concentration profiles in the RL. The concentration of $NO_3^-{}_{(p)}$ will likely be lowest in the early-morning RL at altitudes where horizontal advection has the greatest impact. Wind profiler measurements made in nearby Visalia, CA (65 km SE of Fresno) indicate that during the night (19:00 – 07:00) there was local maximum in the mean wind speed at ~250 m, which is around the altitude at which the early-morning $NO_3^-{}_{(p)}$ concentration is minimum (**Figure 2-13a**). Below 250 m there was a monotonic increase in the night time mean wind speed with altitude, with very slow speeds observed at the surface. Above 250 m the mean wind speed was relatively constant to ~450 m, above which it increased with altitude. Explicit comparison between the vertical profiles of night time mean wind speed and the estimated early-morning $NO_3^-{}_{(p)}$ concentration indicates an inverse relationship (r = -0.98) between the two (**Figure 2-14**). This is consistent with the idea that differential advection as a function of altitude overnight serves to shape the early-morning concentration profiles. The wind direction at lower altitudes (~150 m) was generally more variable than those at higher altitudes (285 m or 450 m), and with a general shift from more westerly at lower altitudes (but above the surface) to more northerly near the top of the RL (**Figure 2-13b**). (Note: vector average wind speeds for each individual night were calculated and then a scalar average of these night-specific vector averages was calculated to give the episode-average mean wind speeds. This averaging process emphasizes directional consistency of the winds on a given night, but not between nights.) The increase in $NO_3^-{}_{(p)}$ concentration at ~400 m AGL in the early-morning profile, especially noticeable on Jan 21 (**Figure 2-15**), could result from a slowing of the winds near the top of the RL or from enhanced recirculation of pollutants at higher altitudes. Regardless of reason, this work indicates that the gradient between the local (above city) and regional $NO_3^-{}_{(p)}$ and precursor gases, evident in Pusede et al. (2016), is an important factor in determining the night time evolution of the RL vertical profile. Explicit characterization of the

temporal evolution of the vertical structure of $NO_3^-{}_{(p)}$ within the night time RL would provide further insights into the altitude-specific processes that control the shape of the early-morning profile (and thus the concentration of $NO_3^-{}_{(p)}$ aloft that can be mixed to the surface in daytime).

The difference between the concentration of $NO_3^-{}_{(p)}$ at each altitude of the early morning vertical profile and that at 3 pm on the preceding afternoon ($\Delta[NO_3^-{}_{(p)}]_{RL}$) yields the net overnight NO_3^- production or loss in the RL. If it is assumed that the layer with the highest $NO_3^-{}_{(p)}$ is not influenced by advection, then the $\Delta[NO_3^-{}_{(p)}]_{RL}$ in this layer provides an estimate of the maximum chemical production (PNO_3^-). This estimate of PNO_3^- is certainly a lower bound on actual nitrate formation given the assumption of no influence of horizontal advection, and this also does not account for produced nitrate that remains in the gas-phase (although this is likely to be small). On average, the observations indicate that chemical production overnight in the RL leads to an approximate doubling over the initial $NO_3^-{}_{(p)}$ concentration, or 10-25 $\mu g\ m^{-3}$ of $NO_3^-{}_{(p)}$ produced over the course of the night for this episode (**Table 2-2**). Observed day-to-day variability in PNO_3^- likely results from day-to-day variations in precursor (NO_x and O_3) concentrations and N_2O_5 reactivity, as well as limitations of the assumption of no advection in this layer. To assess the reasonableness of this estimate of PNO_3 as a maximum production rate, values of the night-specific average rate coefficients for N_2O_5 heterogeneous hydrolysis (k_{N2O5}) and associated uptake coefficients (γ_{N2O5}) needed to reproduce the observed PNO_3^- are back-calculated based on the initial NO_x, O_3, and wet particle surface area and assuming $ClNO_2$ formation is negligible (see Appendix C and **Table 2-2**). The derived k_{N2O5} values range from 1.3 – 5.1 x 10^{-5} s^{-1} with corresponding γ_{N2O5} from 2.5 x 10^{-4} to 4.8 x 10^{-4}. These are smaller than values observed under water-limited conditions in other field studies (Brown et al., 2006d;Bertram et al., 2009) and lower than expected based on lab experiments (Bertram et al., 2009). γ_{N2O5} values separately calculated from the particle composition measurements, following Bertram et al. (2009), are larger than the above back-calculated values, with $\gamma_{N2O5} \sim 10^{-3}$, and more consistent with the literature. This suggests that the PNO_3^- is, in fact, a lower estimate and that the $NO_3^-{}_{(p)}$ concentration in even the lower layers of the RL is influenced by advection. Box model calculations using the (too low) back-calculated k_{N2O5} and γ_{N2O5} yield ~15-42% NO_x conversion to HNO_3 overnight during this episode. If instead $\gamma_{N2O5} = 10^{-3}$ is used, the calculated overnight conversion is somewhat larger, ~52%. Also, if k_{N2O5} and γ_{N2O5} were assumed sufficiently large such that they are not rate limiting the overnight conversion increases further to ~63%. It should be noted that during this episode the surface O_3 overnight is essentially completely titrated away by 6 pm (**Figure 2-16**). The reaction between NO_2 and O_3 (R1) is thus very slow and night time chemical production of $NO_3^-{}_{(p)}$ at the surface in the NBL is comparably small.

2.3.2 Vertical mixing, photochemical production and sinks of particulate nitrate

The observed episode average surface-level $NO_3^-{}_{(p)}$ concentration exhibits a distinct, rapid increase starting at ~ 8 am, then peaks around 10 – 11 am local time (LT) and decreases fairly continuously

after the peak, especially between 1 – 4 pm (**Figure 2-17A**). For reference, time series of $NO_3^-(p)$ during the pollution episode, along with CO, NO, NO_2, O_3, temperature, surface radiation, and PM_1 are shown in **Figure 2-18**. Both Young et al. (2016) and Pusede et al. (2016) noted this increase, arguing it is a signature of nocturnal nitrate production. Here, we provide a more detailed examination of the specific influence of vertical mixing and nocturnal $NO_3^-(p)$ production in the RL on the observed daytime variability in surface-level $NO_3^-(p)$ using an observationally constrained one dimensional box model (see Appendix D for details). In brief, the model accounts for time-dependent mixing between air in the mixed boundary layer and the RL, daytime photochemical production of nitrate, gas-particle partitioning of nitrate, entrainment of clean air from the free troposphere into the ML and loss of nitrate via dry deposition to calculate the time-dependent evolution of the surface-level $NO_3^-(p)$ concentration. The observed vertical profiles of $NO_3^-(p)$ concentrations in the RL (referred to as $[NO_3^-(p)]_{RL}$ and taken as the observed early-morning and noon profiles) provide a unique constraint for understanding and quantifying the influence of vertical mixing specifically, allowing us to expand on previous studies. The model is additionally constrained by the surface-level concentrations of NO_2 and O_3, and temporally varying ML height. The evolution of the daytime ML height and rate of entrainment are determined using the Chemistry Land-surface Atmosphere Soil Slab (CLASS) model (https://classmodel.github.io/; Ouwersloot and Vilà-Guerau de Arellano, 2013). The CLASS model is constrained by observations of the time-dependent vertical profile measurements of temperature, RH and other gas-phase species over Fresno and by T and RH profiles and surface sensible heat flux measurements at nearby Huron, CA (~83 km SSW of Fresno) (Appendix B). Starting at around 8 am, the ML begins to grow vertically by entraining air from the RL. It is assumed that air within the ML is instantaneously mixed throughout the volume. Within the (shrinking) RL the $NO_3^-(p)$ is assumed to retain the initial profile shape until it reaches the maximum ML height observed in the afternoon (~12:30 pm). After this point entrainment of free tropospheric air (FT) begins. The concentration of $NO_3^-(p)$ in FT air is determined from the vertical profile observed around noon. While entrainment of FT air also alters the NO_2 and O_3 concentrations in the mixed layer, since these are constrained by the surface observations (within the mixed layer) this is accounted for. Photochemical production of HNO_3 is calculated based on the oxidation of NO_2 by hydroxyl radicals, with wintertime concentrations estimated to peak around [OH] = 10^6 molecules cm^{-3} at noon in the region, with contributions from $O(^1D) + H_2O$ (from O_3 photolysis), HONO photolysis and CH_2O photolysis (Pusede et al., 2016). The OH concentration is assumed to scale linearly with the observed solar radiation (**Figure 2-19**).

The average calculated daytime temporal evolution of surface $NO_3^-(p)$ from the observationally constrained box model agrees reasonably well with the average of the surface observations from the four Episode 1 flight days considered (**Figure 2-20A**). (The observed diurnal average in **Figure 2-18** uses all of the days from Episode 1 whereas in **Figure 2-20** only four flight days are included. This is because the initial early-morning $NO_3^-(p)$ vertical profile is required as input to the model.) The model predictions for the individual flight days also exhibit generally good agreement with the $NO_3^-(p)$ observations except in the late evening, discussed further below (**Figure 2-15**).

Specifically, the observationally constrained model also shows a rapid increase in $NO_3^-(p)$ beginning at 8 am, a peak around 10-11 am and a gradual, time-varying decrease through the afternoon.

Consideration of the individual processes occurring in the model demonstrates that vertical mixing down of $[NO_3^-(p)]_{RL}$ and the shape of the $[NO_3^-(p)]_{RL}$ vertical profile predominately control the morning-time evolution of the surface $NO_3^-(p)$ during this episode (**Figure 2-20** and **Figure 2-21**). The particularly steep rise in the surface-level $NO_3^-(p)$ in the morning results from the combination of the NBL height being exceptionally shallow (only ~20 m) and the $NO_3^-(p)$ in the low-altitude region of the RL being greater than the $NO_3^-(p)$ in the early-morning NBL. The peak and turnover in surface-level $NO_3^-(p)$ occurs when even higher RL layers, where $[NO_3^-(p)]_{RL} < [NO_3^-(p)]_{ML}$, are entrained. In other words, the temporal evolution of the surface-level $NO_3^-(p)$ is linked to the shape of the early-morning vertical NO_3^- profile. Further, it should be noted that the exact model behavior is dependent on the timing of the CLASS-predicted boundary layer height increase, with the initial increase and timing of the surface-level $NO_3^-(p)$ peak being particularly sensitive to the shape of the rise between 8 and 10 am. Nonetheless, because the NBL is so shallow here, only ~3-12% of the daytime ML height, the surface concentration is strongly impacted by the concentrations in the RL and the initial (pre-8 am) surface-level nitrate has control over daytime concentrations. Thus, the model results demonstrate that the observation of the large 10 am peak in $NO_3^-(p)$ is a clear indication of the strong influence of nocturnal processes occurring aloft—both chemical production and advection-driven local loss—on daytime surface concentrations.

As an extreme counter-example, if there were no $NO_3^-(p)$ in the RL, mixing would have led to an initial decline in the early morning surface $NO_3^-(p)$ (**Figure 2-21A**). Alternatively, if the aloft $NO_3^-(p)$ concentration were assumed to be equal to that from the previous day at 3 pm (and with no vertical variability), there would not have been a sharp increase in the morning surface $NO_3^-(p)$ (**Figure 2-21B**). Instead, there would have been a more gradual increase from the morning into the afternoon due largely to the increasing influence of photochemical production. This is representative of a case in which there was neither aloft production of $NO_3^-(p)$ nor losses from advection, such that the early-morning RL concentration was determined entirely by carry-over from the prior day; in this case the difference between the early-morning surface concentration and that in the RL is small compared to the observations. If, instead, the RL $NO_3^-(p)$ concentration at all altitudes had been equal to the maximum $NO_3^-(p)$ observed in the RL (no vertical gradient in the RL), then the morning peak in surface-level $NO_3^-(p)$ would have occurred later and the $NO_3^-(p)$ concentration would be substantially higher throughout a greater fraction of the day (**Figure 2-21C**). This is representative of a case in which nocturnal production in the RL occurred, but where advection did not serve to reshape the $NO_3^-(p)$ vertical profile in the RL. Clearly, export of pollution from the relatively compact Fresno urban area to the broader region (and import of cleaner air) plays an important role in determining the daytime surface-level concentration of $NO_3^-(p)$, multi-day build up and the population exposure in this urban area. While it has previously been suggested that the morning increase in surface-level $NO_3^-(p)$ is indicative of mixing down of

$NO_3^-(p)$ in the RL (Watson and Chow, 2002c;Pusede et al., 2016;Young et al., 2016), the current study provides an explicit, observationally constrained demonstration of this effect and highlights the dual roles of chemical production and advective loss in the RL.

The time-evolving relative contributions of surface-level $NO_3^-(p)$ from the NBL, the RL and photochemical production are individually quantifiable from the model for this episode (**Figure 2-20**B). As the ML rises, the relative contribution of $NO_3^-(p)$ from the RL rapidly increases reaching ~80% at the 10-11 am peak. After this point, the relative contribution of $NO_3^-(p)$ from photochemical production increases continuously. By the time that decoupling of the NBL occurs (~3 pm), photochemically produced $NO_3^-(p)$ comprises 58% of surface-level $NO_3^-(p)$ while $NO_3^-(p)$ from the previous nights' RL still comprises 40%; the contribution of $NO_3^-(p)$ that was in the NBL is negligible (<2%). Pusede et al. (2016) showed that future decreases in NO_x emissions are more likely to decrease night time than daytime $NO_3^-(p)$ production. The results here therefore suggest that decreases in $NO_3^-(p)$ may be more apparent, on average, in the morning than the afternoon since the fractional contributions of night time-produced versus daytime-produced $NO_3^-(p)$ shift throughout the day. However, care must be taken when interpreting observations from individual days since the meteorological conditions that favor observation of an early morning increase will not always occur (discussed further below). Since it is assumed here that OH scales with solar radiation, the potential for enhanced production of OH (and subsequently $NO_3^-(p)$) in the early morning via e.g. HONO photolysis is not accounted for in the model (Pusede et al., 2016). If this process were included, the increase in morning surface-level $NO_3^-(p)$ would be even greater than is already calculated from mixing down of $NO_3^-(p)$ in the RL. Since the observationally constrained model already predicts a somewhat larger peak at 10 am for surface-level $NO_3^-(p)$ concentrations compared to the observations, early-morning photochemical production appears to have had a relatively limited influence on the morning surface-level $NO_3^-(p)$ compared to mixing down of nocturnal $NO_3^-(p)$ during this episode.

While vertical mixing and the shape of the $NO_3^-(p)$ vertical profile are what predominately drive the morning temporal evolution in the surface-level $NO_3^-(p)$ (especially the peak) for this episode, the afternoon behavior, especially between ~1 pm and 4 pm, is shaped by the balance between photochemical production and loss via (i) dilution by entrainment of FT air and (ii) evaporation of $NO_3^-(p)$ and subsequent dry deposition of HNO_3 gas, i.e. a gas-phase pump for $NO_3^-(p)$ loss. Here, the relative importance of these loss pathways is considered. The latter process (gas-phase pump) has been previously considered by Pusede et al. (2016) while the former (FT entrainment) was not. Loss through dry deposition of $NO_3^-(p)$ is negligible since deposition velocities for HNO_3 (v_d = 1 – 10 cm s^{-1}) are much larger than for particles (v_d = 0.001 – 0.1 cm s^{-1}) (Meyers et al., 1989;Horii et al., 2005;Farmer et al., 2013;Pusede et al., 2016). These loss mechanisms ultimately limit the extent of the pollution episode build up. Once the daytime model ML reaches maximum height entrainment into the ML of typically cleaner air from just above the ML (i.e. from the FT) occurs. The time-evolving entrainment rates are estimated from the CLASS model (Appendix C).

Considering the gas-phase pump, the warm (typically 290 K) and dry (RH = 40% or less during the campaign) afternoon conditions enhance evaporation of $NO_3^-{}_{(p)}$ relative to night time and early morning conditions, thereby increasing loss through dry deposition of HNO_3 gas in the afternoon (Pusede et al., 2016). However, total ammonia is in substantial excess (3.8 – 8.9 times $NO_3^-{}_{(g+p)}$ on a molar basis), with thermodynamic calculations indicating that the gas-phase fraction of NO_3^- is <0.15 during the daytime and near zero at night when it is colder and RH is higher (**Figure 2-8**). These estimates of the gas-phase fraction of NO_3^- are similar to the observational measurements of Parworth et al. (2017), who determined the daytime and night time averages during the first episode were 0.08 ± 0.03 (1σ) and 0.04 ± 0.05 (1σ), respectively. Importantly, the gas-phase fraction here is substantially smaller than that estimated in Pusede et al. (2016) who found a daytime gas-phase fraction of 0.4 (median) and a 24-h average of 0.15. Consequently, loss of nitrate via the gas-phase pump is less than in their analysis and suggests that the role of this pathway was likely overestimated. The general influence of the gas-phase fraction on loss via dry deposition is shown in **Figure 2-22**. In general, the results indicate that the gas-phase fraction has a strong influence on the loss of $NO_3^-{}_{(p)}$ due to HNO_3 deposition.

Including both FT entrainment and dry deposition, the box model reasonably reproduces the observed afternoon decrease in surface-level $NO_3^-{}_{(p)}$. This allows assessment of the relative importance of these two loss processes by turning them off one at a time (**Figure 2-20C**). The calculations indicate that entrainment of clean FT air plays an important role in the afternoon surface concentration decline. Without entrainment, the model predicts that the afternoon $NO_3^-{}_{(p)}$ would be ~18% higher, leading to a double-humped daytime profile. Despite the relatively low gas-phase fraction, the gas-phase pump also contributes to the afternoon decline. The model results indicate that these two loss processes contribute approximately equally to the afternoon decline. There are, however, a few hours when the gas-phase pump is potentially of extreme importance. When the RL decouples and the surface mixed layer becomes quite shallow the rate of loss due to dry deposition is enhanced. This leads to a rapid decrease in surface-level $NO_3^-{}_{(p)}$. Yet, the concurrent decrease in the NBL temperature and increase in RH and NH_3 enhances partitioning of nitrate to the particle-phase, thereby limiting the impact of this rapid decline over time. (In the model here, the decoupling is assumed to occur very rapidly while the temperature and RH changes are from observations and occur more gradually. If the decoupling was actually slower the influence of the gas-phase pump at this point in time would be reduced and the modelled decrease in $NO_3^-{}_{(p)}$ that occurs around 3-5 pm would be less than shown.)

The model predicts that after decoupling and cooling occur the surface-level $NO_3^-{}_{(p)}$ will continue to decrease at ~2% h^{-1} overnight via the gas-phase pump, which is similar to the loss rate observed between midnight and 7 am (**Figure 2-20A**). If the gas-phase pump is turned off completely (i.e. the nitric acid deposition velocity is set to zero) there is an increase in the modelled $NO_3^-{}_{(p)}$ that begins at ~3 pm (when decoupling occurs) and continues until 6 pm (**Figure 2-20C**). This is a result of the continual decrease in temperature and increase in RH enhancing partitioning to the particle-phase. Although not a focus of this study, on some days, there is a sharp increase in

surface-level $NO_3^-(p)$ observed in the evening, starting around 8 pm (LT). While this could theoretically result from enhanced partitioning to the particle-phase at night, the timing does not match the observed temperature and RH variations. Surface-level chemical production of nitrate via N_2O_5 hydrolysis could alternatively be the source of this increase, but given the near-zero surface-level O_3 concentration due to titration by NO the production via this pathway would be insufficient. This evening increase is observed on many days, although with somewhat variable timing and magnitude (**Figure 2-21**). Thus, it may be that the evening increase results from advection to the measurement site of air from a not-to-distant location (given low wind speeds) that has higher surface concentrations. Regardless, while the reason for this night time increase in surface $NO_3^-(p)$ remains unclear, the occurrence does not impact the analysis of the early-morning and daytime $NO_3^-(p)$ behavior.

The cumulative impact of the nocturnal production in the RL, daytime photochemical production and afternoon loss processes is that the $NO_3^-(p)$ concentration at ~3 pm, the point when decoupling of the RL occurs, is slightly higher than that at 8 am during the episode. Therefore, there is a gradual net increase (average of 1.32 $\mu g\ m^{-3}\ day^{-1}$) in surface-level $NO_3^-(p)$ as the episode progresses, albeit with day-to-day variability (**Figure 2-17B**). For comparison, the 24-h average surface-level $NO_3^-(p)$ increases by 0.66 $\mu g\ m^{-3}\ day^{-1}$. While decreasing NO_x emissions and $NO_3^-(p)$ production, especially nocturnal production (Pusede et al., 2016), is the most direct and reliable route towards decreasing surface $NO_3^-(p)$ concentrations (Kleeman et al., 2005), decreases in NH_3 could theoretically also have some influence on $NO_3^-(p)$ by increasing the efficiency of the gas-phase pump. However, this will only be the case if NH_3 decreases exceed decreases in NO_x by at least a factor of five such that the ratio between the two is changed substantially and the gas-phase fraction is increased (**Figure 2-8**). Such preferential targeting of NH_3 sources is therefore highly unlikely to be an efficient control strategy, at least for the SJV where the total ammonia-to-nitrate ratio is large. In regions where the $NH_4^+(g+p)$:$NO_3^-(g+p)$ molar ratio is closer to unity, the nitrate partitioning is more sensitive to changes in this ratio and thus ammonia control could potentially prove effective.

2.3.3 Comparison between episodes

The above analysis focuses on observations made during one pollution episode, but there was a second pollution episode observed during DISCOVER-AQ (Jan. 30-Feb. 5, 2013). The episode-averaged diurnal behavior of the surface $NO_3^-(p)$ concentration for this second episode showed evidence of an early morning increase, but the increase is not as sharp as the first episode (**Figure 2-23**). Additionally, the day-to-day variability in the surface $NO_3^-(p)$ was much greater during the second episode; on some days, there was minimal evidence of an early-morning increase but on others there was a substantial increase. The shapes of the early morning vertical $NO_3^-(p)$ profiles (around 9:30 am) were notably different during Episode 2 on two of the flight days as well, as was the evolution of the profiles from morning to afternoon (**Figure 2-24**). The afternoon mixed layer heights were much higher during Episode 2 than Episode 1, ranging from 600-700 m AGL

compared to 300-400 m AGL, respectively. The early-morning mixed layer heights were also higher during Episode 2 (~170 m) compared to Episode 1 (around 70 m). During Episode 1, the surface-level winds exhibit a consistent shift in direction from easterly in the early morning (5-8 am) to southerly in the later morning (9 am-12 pm), and the mean surface-level wind speed increased over this same period, from 0.31 m s^{-1} to 0.82 m s^{-1} (**Figure 2-23**). In contrast, during Episode 2 there was a lack of day-to-day consistency in the surface wind direction, especially during the early morning (5-8 am), and there was a more substantial change in the mean surface-level wind speed from early morning to later morning, from 0.32 m s^{-1} to 1.12 m s^{-1} (**Figure 2-23**). The Episode 2 mean night time aloft wind speeds were also overall lower and more constant with altitude, with little variability from 150 m to 400 m, although still with a substantial increase from the surface (**Figure 2-25**). The aloft nocturnal winds during Episode 2 were somewhat more variable than Episode 1 winds in terms of the wind direction (**Figure 2-13** vs. **Figure 2-25**).

Overall, this increased day-to-day variability in both the surface $NO_3^-{}_{(p)}$ and wind behavior, and a difference in the evolution of the $NO_3^-{}_{(p)}$ vertical profiles from early morning to late morning/early afternoon in Episode 2 compared to Episode 1, suggests that the meteorological conditions during the second episode were generally less conducive to simple interpretation using the mixing model discussed above. Instead, it seems that advection and export from the urban area were of increased importance during Episode 2, both overnight and especially in the early-to-mid morning. The contrasting behavior between the two episodes suggests that while the observation of a sharp, early-morning rise and peak in surface-level $NO_3^-{}_{(p)}$ (such as during the first episode) might be generally considered a strong indicator of the production of $NO_3^-{}_{(p)}$ in the RL, the absence of such a feature does not preclude an important role for nocturnal production aloft.

2.3.4 Linking to other regions

Production of $NO_3^-{}_{(p)}$ in the RL can vary widely based on initial concentrations of its precursor gases, as well as the rate of heterogeneous uptake of N_2O_5 by particles. It may be that production of $NO_3^-{}_{(p)}$ via the N_2O_5 hydrolysis pathway may be significant in the aloft RL in other regions with similar geographical and meteorological conditions, such as Salt Lake Valley, Utah (Kuprov et al., 2014;Baasandorj et al., 2017). However, in valley regions with lower NO_x or O_3 the nocturnal PNO_3^- may be lower, thus limiting the importance of this pathway (Akira et al., 2005;Bigi et al., 2012). Among other factors, the extent to which nocturnal $NO_3^-{}_{(p)}$ formation occurs more-so in the surface layer versus in layers aloft will depend importantly on the extent of NO_x emissions at the surface (which titrate O_3, suppressing particulate nitrate formation), the absolute and relative height of the nocturnal boundary layer (which affects the rate HNO_3 deposition and the air volumes in which nitrate production occurs), and gradients in RH, T and NH_3 (Kim et al., 2014).

For example, Baasandorj et al. (2017) observe at their valley wall and valley floor sites in wintertime Utah that O_3 concentrations near the surface remain well-above zero even during pollution episodes, thus allowing for surface-level $NO_3^-{}_{(p)}$ formation overnight, substantiated by

direct measurements of N_2O_5, in addition to formation aloft. Nitrate-specific diurnal profiles were not reported. In Shanghai, China, Wang et al. (2009) observed in fall 2007 that both O_3 and NO_2 remain elevated at night at the surface, with a concomitant increase in surface $NO_3^-(p)$. And in wintertime Seoul, Korea, Kim et al. (2017) observed relatively limited diurnal variability in O_3 and NO_2 concentrations measured at 60 m, with both remaining elevated throughout the night. However, they did not observe any notable build up in $NO_3^-(p)$ overnight, but did observe $NO_3^-(p)$ to increase and peak in the morning, as here. In contrast, in Fresno here the night time surface O_3 levels during Episode 1 were nearly zero, suppressing surface $NO_3^-(p)$ formation. This near-zero nocturnal O_3 is similar to observations by Kuprov et al. (2014) made a few years before Baasandorj et al. (2017) at one of the same valley floor sites in Utah, reflecting year-to-year differences. Such differences can influence the extent to which a notable increase in $NO_3^-(p)$ is observed to occur in the early morning as air is entrained from the residual layer to the surface. This is because if surface production and production in the residual layer are similar in magnitude the contrast between the two will be reduced and entrainment will appear to have a less apparent impact on the diurnal profile. However, because the effective volume of the residual layer is typically much larger than the nocturnal boundary layer (as is the case here), even without an observed increase in $NO_3^-(p)$ at the surface in the morning the $NO_3^-(p)$ produced in the residual layer can still dominate the overall $NO_3^-(p)$ burden during the day.

Additionally, comparison between the Baasandorj et al. (2017) observations of late afternoon surface NO_2 and O_3 (which reflect the initial conditions within the residual layer) with the Fresno observations indicates differences can exist in how nocturnal production in layers aloft influences the build-up and sustaining of $PM_{2.5}$ in pollution episodes. They observed during a strong $PM_{2.5}$ episode a slow build-up of $PM_{2.5}$ followed by a plateau lasting multiple days. During this period, late-afternoon O_3 concentrations decreased over time while late-afternoon NO_2 was approximately constant (in the daily average). Consequently, the nitrate radical production rate in the residual layer, and thus the N_2O_5 and $NO_3^-(p)$ production rates, decreased over time in their study. In contrast, for Episode 1 here, the late-afternoon nitrate radical production rate increased over time across the episode (by 0.25 $\mu g\ m^{-3}\ day^{-1}$), with only a moderate decrease in the daytime O_3 over time (**Figure 2-18**). These differences reflect the different photochemical conditions between the regions, and illustrate the coupling between the daytime photochemical conditions (i.e. O_3 production) and night time $NO_3^-(p)$ formation above the surface.

2.4 Conclusions

This work combines surface and aircraft observations made during a pollution episode in 2013 to demonstrate that in the San Joaquin Valley (specifically Fresno, CA) production of $NO_3^-(g+p)$ in the nocturnal residual layer can play a crucial role in determining daytime surface concentrations of particulate NO_3^- in winter, when photochemical production is relatively slow and morning boundary layers are extremely shallow. The influence of processes occurring in the aloft RL on $NO_3^-(p)$ surface concentrations is evident in the $NO_3^-(p)$ diurnal variability, specifically the

occurrence of a mid-morning peak in surface-level $NO_3^-(p)$. While the mid-morning peak has been previously suggested as a signature of nocturnal nitrate production aloft (Watson and Chow, 2002c;Brown et al., 2006a;Pusede et al., 2016;Young et al., 2016;Lurmann et al., 2006), the current study makes novel use of vertical profiles of $NO_3^-(p)$ concentrations measured multiple times on individual days to quantitatively illustrate the importance of nocturnal processes on surface concentrations. The analysis shows that the $NO_3^-(p)$ concentration in the morning-time mixed boundary layer can be dominated by nocturnally produced $NO_3^-(p)$; vertical mixing in the early morning, which entrains air from the residual layer into the surface mixed layer, has a particularly large impact on the surface concentrations here due to the nocturnal boundary layer being exceptionally shallow. In the afternoon, photochemically produced nitrate contributes the majority of the total $NO_3^-(p)$ burden for the episode examined, but still with a substantial contribution from nocturnal production. The case-study here illustrates that nocturnal $NO_3^-(p)$ production can play a critically important role in the build-up and sustaining of pollution episodes in the SJV, supporting previous suggestions made, in part, on the basis of calculated chemical production values and an assessment of multi-year trends in the relationship between $NO_3^-(p)$ and NO_2 (Pusede et al., 2016).

The current work also demonstrates that a difference exists between the shape of the typical vertical profiles of $NO_3^-(p)$ in afternoon and early-morning over Fresno. This difference is shown to very likely result from altitude-specific horizontal advection in the nocturnal RL leading to differential wash-out of $NO_3^-(p)$ and precursor gases, rather than from differences in chemical production rates. Consequently, there is a steep vertical gradient in $NO_3^-(p)$ in the early-morning RL that, in turn, influences the temporal evolution of surface-level $NO_3^-(p)$ during the day, especially in early morning. Ultimately, differential advection is shown to have an important role in limiting the maximum surface-level concentration of $NO_3^-(p)$ observed within the urban area during the day, a result of the urban-rural gradients being particularly steep (Pusede et al., 2016). Absent this overnight export of pollution from the city, nitrate pollution would build up during pollution events to a much greater extent. However, advection likely contributes to the build-up of $NO_3^-(p)$ throughout the valley, outside of the cities. Daytime loss processes are also shown to help limit the multi-day build-up of surface-level $NO_3^-(p)$. Afternoon entrainment of air from the cleaner free troposphere into the ML (and export of mixed-layer air to the FT) is shown to be an important loss process for particulate nitrate. Janssen et al. (2012;2013) have similarly identified afternoon loss via FT entrainment as an important process shaping the diurnal variability of surface-level organic aerosol concentrations in forested areas that are dominated by organic aerosol. Loss of $NO_3^-(p)$ via dry deposition of HNO_3 and subsequent evaporation of NH_4NO_3 is found to contribute to afternoon particulate nitrate loss, but the effect is limited by the (relatively) high afternoon boundary layer and the small gas-phase fraction of nitrate (<0.15). However, this gas-phase pump may have a substantial influence on the surface concentrations in the few hours just after decoupling of the RL occurs, when the boundary layer height is low and it is still sufficiently warm. Consistent with previous suggestions (Kleeman et al., 2005;Pusede et al., 2016), we conclude that control strategies for the region should focus on reduction of concentrations of NO_x and O_3 (the latter of which might require VOC controls) in the mid-afternoon, specifically around the time that

the RL decouples from the surface layer, as this largely determines the production rate of nitrate in the aloft RL.

2.5 Appendix A: Measurements

2.5.1 A1 Airborne Measurements

Airborne measurements used in this paper were made from the P3-B NASA aircraft during the DISCOVER-AQ field campaign in January-February, 2013 in San Joaquin Valley (SJV), California. All data are available from the publicly accessible DISCOVER-AQ website (NASA Atmospheric Science Data Center).

The P3-B was equipped with an array of instruments to measure both gas and particle-phase properties. A TSI-3563 nephelometer provided total scattering from dry particles at 450, 550 and 700 nm and scattering at 550 nm by particles at 80% RH (Beyersdorf et al., 2016). Gas-phase NH_3 was measured using a cavity ringdown spectroscopy with a Picarro G2103 (von Bobrutzki et al., 2010), using the NOAA aircraft NH_3 inlet and calibration scheme as in Nowak et al. (2010). Measurements of NO, NO_2, NO_x, and O_3 were obtained through a 4-channel chemiluminiscence instrument (Brent et al., 2015). CO and CH_4 were measured with a differential absorption CO measurement spectrometer (Sachse et al., 1987). Total gas (HNO_3) + particle (NH_4NO_3) nitrate were measured using thermal dissociation – laser induced fluorescence (TD-LIF), where HNO_3 and volatilizable particulate nitrate are converted into NO_2 for detection (Day et al., 2002). While the TD-LIF instrument is not optimized for particle sampling, most of the particulate mass was in the submicron size range and thus inertial losses will likely only lead to a small (if any) negative bias in the measured particulate nitrate (Pusede et al., 2016). Aerosol size distributions for 0.06 – 1.0 μm diameter particles were measured with an ultra-high sensitivity aerosol spectrometer (UHSAS). The UHSAS uses an optical sizing method, but is calibrated relative to mobility diameter. The P3-B flew throughout the SJV on 10 days and performed vertical spirals over six sites across the valley, including Fresno. The location of these sites and the flight path are shown in **Figure 2-3**. This same flight path was repeated three times every day between approximately 8:30 am and 3:00 pm, with vertical profiles over Fresno at approximately 9:30-10:00 am, 12-12:30 pm and 2:30-3:00 pm. This enables assessment of the evolution of the species-specific vertical profile during the day across the valley. Out of the ten research flights during the campaign, only eight of them have been used here due to gaps in the dataset. Four of these days are during the first pollution episode (Jan. 18, 20, 21 and 22) and four are during the second pollution episode (Jan. 30 and 31, and Feb. 1 and 4).

Observations of the light scattering coefficient at 550 nm (σ_{sca}) for dry and humidified particles (no size cut-off) made from the P3-B (Beyersdorf et al., 2016) have been used to estimate the vertical distribution of PM mass and $NO_3^-{}_{(p)}$ concentrations. Scattering is linearly related to the total mass concentration of PM. The observed hygroscopicity is dependent on particle

composition, with higher hygroscopicity indicative of a higher particulate inorganic fraction and lower hygroscopicity indicative of a higher particulate organic fraction; the relationship between hygroscopicity and the inorganic fraction (or the organic fraction) is reasonably linear when the inorganic species are primarily ammonium sulfate and ammonium nitrate (Zhang et al., 2014), as these have similar hygroscopicities (Petters and Kreidenweis, 2007). The particulate nitrate concentration is much larger than the particulate sulfate concentration, as determined from both the surface and aircraft measurements (< 600 m AGL), with nitrate-to-sulfate mass ratios of 8 and 16, respectively (both determined from PILS measurements). Thus, the observed hygroscopicity is primarily reflective of the particulate nitrate fraction (Parworth et al., 2017). More specifically, a linear relationship was observed between surface-level measurements of dry σ_{scat} and $PM_{1.0}$ (= black carbon (BC) + non-refractory $PM_{1.0}$, (NR-PM_1)) mass concentrations in Fresno (slope = 2.83 $m^2\ g^{-1}$ with intercept forced through zero; **Figure 2-6A**). Only data points between 8 am and 4 pm were included in determining this relationship to reflect the time period during which the airborne measurements were obtained. The observed relationship for dry, surface-level σ_{sca} and NR-PM_1 is used to estimate the NR-PM_1 concentration during the vertical profiles from the aircraft dry σ_{scat} measurements. The hygroscopicity (water uptake) of a particle depends on its chemical composition. Inorganic components, predominantly NO_3^- and ammonium in the wintertime SJV region (Young et al., 2016), are highly hygroscopic while organic components of PM_1 tend to have much lower hygroscopicity (Petters and Kreidenweis, 2007). Thus, measurements of the particle hygroscopicity can be used to estimate the ratio of inorganic to organic mass in the sampled PM (Massoli et al., 2009;Parworth et al., 2017). The average particle hygroscopicity was characterized by the optical hygroscopicity parameter, γ defined by Equation A1.

$$\gamma = \frac{\ln\left[\frac{\sigma_{sca,wet}}{\sigma_{sca,dry}}\right]}{\ln\left[\frac{100-RH_{dry}}{100-RH_{wet}}\right]} \quad \text{(A1)}$$

where $\sigma_{scat,wet}$ and $\sigma_{scat,dry}$ are the scattering coefficients (in Mm^{-1}) measured under wet (RH_{wet} = 80%) and dry (RH_{dry} = 20%) conditions respectively. The parameter γ varies reasonably linearly with the particle inorganic mass fraction (Massoli et al., 2009). Therefore, an initial estimate of $NO_3^-{}_{(p)}$ concentrations at high time resolution, and thus as a function of altitude, is obtained from the equation $[NO_3^-{}_{(p)}] = \gamma \cdot \sigma_{sca,dry}/2.83$. The factor of 2.83 has units of $m^2\ g^{-1}$ and comes from the σ_{scat} versus NR-PM_1 relationship determined above. However, previous studies show some variability in the linear relationship between γ and inorganic mass fraction and, importantly, typically have slopes somewhat less than unity and non-zero intercepts, as is assumed in the above conversion (e.g. Massoli et al., 2009). Therefore, the low-time-resolution aircraft PILS $NO_3^-{}_{(p)}$ measurements (which are not appropriate for vertical profiles) were used to calibrate the above high-time-resolution $NO_3^-{}_{(p)}$ estimates. There was a strong, linear correlation between the $NO_3^-{}_{(p)}$ observed by the PILS and the initially estimated $NO_3^-{}_{(p)}$ (**Figure 2-6B**). This demonstrates the general validity of the estimation approach. However, the PILS $NO_3^-{}_{(p)}$ concentrations were, on average, 22% lower than the initially estimated $NO_3^-{}_{(p)}$. Therefore, the initially estimated $NO_3^-{}_{(p)}$

concentrations were adjusted downwards by 22%, and the final expression relating $\sigma_{sca,dry}$ (in Mm^{-1}) and γ to $NO_3^-{}_{(p)}$ concentrations (in $\mu g\ m^{-3}$) is:

$$[NO_3^-{}_{(p)}] = \frac{\cdot\sigma_{sca,dry}}{3.63} \quad \text{(A2)}$$

The uncertainty in the estimated $[NO_3^-{}_{(p)}]$ is approximately 20%, based on the scatter around the best-fit line in **Figure 2-6**.

2.5.2 A2 Ground Measurements

Fresno (36.745 °N, 119.77 °W) was a "supersite" where comprehensive, continuous measurements of the chemical and physical properties of particulate matter were made. Chemical composition of non-refractory $PM_{1.0}$ was measured by a High Resolution Time-of-Flight-Aerosol Mass Spectrometer (HR-ToF-AMS) (Young et al., 2016). The soluble fraction of $PM_{3.0}$ was characterized using a Particle-Into-Liquid Sampler (PILS) coupled to an ion chromatograph (Parworth et al., 2017). Gas-phase water-soluble species were collected at 5 - 7 hr time resolution using an automatic-switching annular denuder system placed in front of the PILS and were analyzed offline with ion chromatography after extraction (Parworth et al., 2017). The combination of the denuder measurements and the particle measurements allowed for determination of the gas-phase fraction of nitrate. Light extinction and light absorption coefficients were measured using the UC Davis cavity ringdown-photoacoustic spectrometer, and scattering coefficients were determined by difference (Cappa et al., 2012;Lack et al., 2012). Refractory black carbon concentrations were measured using a single particle soot photometer (Schwarz et al., 2006b). *In situ* gas-phase measurements of NO, NO_2 and O_3, along with environmental factors (T and RH) were made by the California Air Resources Board. Particle size distributions were measured using a Scanning Mobility Particle Sizer (SMPS; size range: 10 – 800 nm), and an Aerodynamic Particle Sizer (APS; 700 nm – 6 μm). Measurements included in the current study are listed in **Table 2-1**.

Additionally, a radiosonde was used to obtain vertical profiles of pressure, temperature and humidity over nearby Huron (36.203 °N, 120.103 °W) twice a day, once in the morning around 8 AM and again in the evening 4 PM. Diurnal measurements of the surface heat flux and friction velocity were determined from measurements made with a sonic anemometer at Huron. Measurements of wind speed and wind direction as a function of altitude at nearby Visalia, CA are from the National Oceanic and Atmospheric Administration (NOAA) Profiler Network (https://www.esrl.noaa.gov/psd/data/obs/instruments/WindProfilerDescription.html).

2.6 Appendix B: Determining Mixed Boundary Layer Height

The mixed layer (ML) heights have been determined from each of the vertical profiles of potential temperature (θ), relative humidity (RH), CO and CH_4 measured from the P3-B aircraft. Example profiles for each of the three flight legs on 18 January 2013 are shown in **Figure 2-24**. The altitude

at which there is a strong change in the slope, from approximately altitude-independent to having a steep gradient, is determined to be the top of the ML. The vertical profile measurements allow for determination of the ML height over Fresno around 10:00 am, 12:30 pm and 2:30 pm. The ML height at 8 am is separately determined from the radiosonde measurements at nearby Huron (located 83 km SSW), as the flight data do not allow for characterization of ML height this early. It is assumed that the 8 am ML measurements at Huron are representative of the ML heights in Fresno. The observed ML height increases with time from 8 am until approximately noon or 1 pm, after which it is approximately constant. The rise in ML height with time is modelled using the Chemistry Land-surface Atmosphere Soil Slab (CLASS) model (Vilà-Guerau De Arellano, 2015). The CLASS model allows for estimation of ML heights with finer time resolution than the observations (i.e. in between flights; shown as black dots in **Figure 2-5**) and of the corresponding time-dependent entrainment velocities. The model input parameters are constrained by observations from nearby Huron of the nocturnal boundary layer height, the morning inversion strength (~ 8 am), the sensible surface heat flux, the friction velocity, and the lapse rate through the residual layer, as well as by an estimate of the subsidence rate based on Trousdell et al. (2016). The model inputs are adjusted to ensure that the modelled ML growth agrees reasonably well with the observations from the P3-B over Fresno (**Figure 2-5**). The resulting average entrainment velocities in the afternoon (1 – 4 pm) from the CLASS model agree well with independently determined entrainment rates based on afternoon decline in $SO_4^{2-}{}_{(p)}$ for the Episode 1 days. Since $SO_4^{2-}{}_{(p)}$ is effectively non-volatile and since photochemical production via oxidation of SO_2 is relatively slow, the decline in $SO_4^{-}{}_{(p)}$ in the afternoon can be attributed solely to dilution from entrainment of "clean" FT air since the influence of the gas-phase pump is small. After 3 pm the boundary layer is assumed to linearly drop over a 1-hour period to the NBL height observed at 8 am the same day. A relatively rapid (~1 h) decline in the mixed layer height is consistent with wintertime observations of diurnal BLH profiles (Bianco et al., 2011).

The sensitivity of the box model to the boundary layer growth predicted by the (observationally constrained) CLASS model has been examined. An alternative boundary layer growth profile was estimated by fitting the observed P3-B ML heights using a sigmoidal function (**Figure 2-26**). The general shapes of the CLASS and sigmoidal profiles are similar, although the sigmoidal profile exhibits a somewhat faster rise. Entrainment of FT air in the afternoon for the sigmoidal growth profile was accounted for using the average entrainment rates estimated from the observed $SO_4^{2-}{}_{(p)}$ loss rates and assuming that entrainment begins at noon, when the BL height was near the maximum. The same linear decrease in the BL height starting at 3 pm was assumed. The use of this alternative model yields a diurnal $NO_3^{-}{}_{(p)}$ profile for Episode 1 that is very similar to that obtained using the CLASS model (**Figure 2-26**). This indicates that the general behavior of the diurnal surface $NO_3^{-}{}_{(p)}$ profile is not particularly sensitive to the treatment of the BL rise and that the results obtained here are robust.

2.7 Appendix C: Nocturnal Reactions in the RL

2.7.1 C1: N_2O_5 production and heterogeneous reactivity

The gas-phase and heterogeneous chemistry occurring in the RL was assumed to follow the reaction scheme indicated by Reactions 1-4. Focusing first on the heterogeneous hydrolysis of N_2O_5, one estimate of the night-specific average rate coefficients for N_2O_5 heterogeneous hydrolysis (k_{N2O5}) is obtained through consideration of the initial concentrations of precursor gases and the observed maximum overnight increase in the RL $NO_3^-{}_{(p)}$, PNO_3^-. More specifically, a 1D box model including nocturnal gas-phase chemistry and heterogeneous reaction of N_2O_5 with particles was run iteratively to determine an average k_{N2O5} for the night (19:00-08:00; 13 hours) such that it reproduced the observed PNO_3^-. The observed chloride at Fresno was small (1% of $PM_{1.0}$) during the episode, and thus formation of nitryl chloride ($ClNO_2$) can be reasonably neglected (Young et al., 2016). Since, the boundary layer is fairly well-mixed in the afternoon, surface-level observations of NO_x, O_3, $NO_3^-{}_{(p)}$, particle wet surface area and temperature at 3 pm on the preceding day were used as initial conditions. Based on back-calculated k_{N2O5} values, night-specific values of heterogeneous N_2O_5 uptake coefficient (γ_{N2O5}) were determined from:

$$k_{N2O5} = \frac{\omega \cdot S_a \cdot \gamma_{N2O5}}{4} \qquad \text{(C1)}$$

where ω is the mean molecular speed of N_2O_5 (256 m s^{-1}), S_a is wet particle surface area, and γ is the N_2O_5 heterogeneous uptake coefficient (Brown et al., 2006d). The wet particle surface area was calculated from the observed dry particle size distributions, particle hygroscopicity and RH. The resulting back-calculated k_{N2O5} values from Eqn. C1 were in the range 1.3 – 5.1 x 10^{-5} s^{-1}. The corresponding back-calculated γ_{N2O5} were in the range 2.5 x 10^{-4} to 4.8 x 10^{-4} (**Table 2-2**), which as noted in the main text are somewhat smaller than values observed under water-limited conditions in other field studies and lower than expected based on lab experiments (Bertram et al., 2009).

A second estimate of the γ_{N2O5} values is calculated from the particle composition following Bertram et al. (2009). The calculated γ_{N2O5} depend on the particle water content (specifically, the $[H_2O]/[NO_3^-{}_{(p)}]$ and thus RH) and the chloride fraction. The composition-calculated γ_{N2O5} (~ 10^{-3}) are larger than the above back-calculated values and more consistent with the literature although on the lower side of previous measurements (Brown et al., 2006d;Bertram et al., 2009). That the back-calculated γ_{N2O5} are smaller than the γ_{N2O5} calculated from the composition is likely a consequence of the PNO_3^- being an under-estimate relative to the true overnight production in the RL. This is because the observed PNO_3^- is taken as the difference between the previous afternoon and early morning $NO_3^-{}_{(p)}$ concentration in the aloft RL layer having the maximum morning concentration. This does not account for the influence of advection, which is most likely going to reduce the morning $NO_3^-{}_{(p)}$ relative to if there were no advection.

2.7.2 C2: Reactions with VOCs

Not considered in the above is the reaction of the NO_3 radical with VOCs. NO_3 radicals react rapidly with alkenes and more slowly with alkanes and other species. NO_3 reaction with VOCs can lead to hydrogen abstraction and direct formation of HNO_3, especially for reactions with alkanes. For alkenes and aromatics, NO_3 reaction typically proceeds via NO_3 addition and formation of organic nitrates. The latter would suppress formation of particulate inorganic nitrate but can serve as an important source of particulate organic nitrate (Kiendler-Scharr et al., 2016). Organic nitrate formation has been observed as an important source of summertime organic aerosol in Bakersfield, CA (also in the SJV) (Rollins et al., 2012). VOC concentrations and reactivity are likely much lower during the colder winter compared to the warmer summer (Pusede et al., 2014), and thus reaction of VOCs with NO_3 radicals is likely much suppressed.

Concentrations of a broad suite of VOCs were measured via whole air canister sampling during DISCOVER-AQ. These measurements can be used to assess the potential influence of NO_3 reaction with VOCs on HNO_3 and $NO_3^-{}_{(p)}$ formation. The nitrate reactivity towards each VOC is calculated as $k_{VOC+NO3}$·[VOC], where the $k_{VOC+NO3}$ is the VOC-specific rate coefficient and [VOC] is the VOC concentration (Ng et al., 2017). Average afternoon VOC concentrations are used, which should be representative of the initial concentrations in the RL. The VOCs are ranked according to their reactivity with NO_3. The top 20 VOCs are considered explicitly, and all other VOCs are lumped into a common VOC species with the average concentration and k_{rxn} of these species (**Table 2-3**). Reactions between NO_3 and alkenes and aromatics are assumed to form (unreactive) organic nitrates while reactions between NO_3 and all other species are assumed to form HNO_3 and an organic product species. The influence of NO_3 reaction with VOCs on $NO_3^-{}_{(p)}$ is assessed by calculating the overnight production of HNO_3 both with and without VOCs using typical afternoon NO (3 ppb), NO_2 (20 ppb) and O_3 (27 ppb) concentrations and for k_{N2O5} ranging from 1 x 10^{-5} s^{-1} to 3 x 10^{-4} s^{-1}. HNO_3 produced from N_2O_5 hydrolysis is tracked separately from HNO_3 produced from NO_3 reaction with VOCs. The HNO_3 production via N_2O_5 hydrolysis decreases marginally when VOC reactions are included. The HNO_3 suppression ranges from ~12% for k_{N2O5} = 10^{-5} s^{-1} to 5% for k_{N2O5} = 10^{-4} s^{-1} (**Figure 2-27**). However, the calculations indicate that much of this HNO_3 suppression is potentially offset by HNO_3 production from reaction of NO_3 with non-alkene or aromatic compounds. For larger k_{N2O5} the net suppression is only 5%, with the suppression decreasing as k_{N2O5} decreases. At the lowest k_{N2O5} (10^{-5} s^{-1}) the calculations indicate that the inclusion of the NO_3 + VOC reaction actually leads to an increase in the net HNO_3 production (**Figure 2-27**). Overall, these calculations suggest that reaction of NO_3 with VOCs has a relatively minor influence on the overnight local production of HNO_3 in the RL.

2.8 Appendix D: Box Model Details

The box model for calculating the time-varying surface concentrations of $NO_3^-{}_{(p)}$ accounts for: (i) mixing of air in the aloft RL with the surface air, including the time-dependent rise and fall of the

boundary layer; (ii) daytime photochemical production of HNO_3 from the OH + NO_2 reaction; (iii) T- and RH-dependent gas-particle partitioning of ammonium nitrate; (iv) afternoon entrainment of air from the free troposphere; (iv) competition between condensation of HNO_3 onto existing suspended particles versus loss via dry deposition; (v) dry deposition of particulate $NO_3^-{}_{(p)}$. The kinetic equations were solved in the data analysis program Igor (Wavemetrics) and set up using the kinsim Igor package, developed by Harold Stark (http://www.igorexchange.com/node/1333). The model was initialized with the observed $NO_3^-{}_{(p)}$ measured by the AMS at surface-level at 12 am and run in 10 minute steps. For each time step, the photochemical production equations used the instantaneous observed NO_2 and temperature, and estimated OH concentration and ML height. The fraction of NO_3^- in gas-phase, *f*, for each time step was determined based on the instantaneous conditions using the chemical thermodynamic model, ISORROPIA II in the forward mode, with the phase state set as metastable (Fountoukis and Nenes, 2007). ISORROPIA was initialized with the observed particulate composition, specifically NO_3^- and SO_4^{2-} (AMS), and Na^+, K^+ and Cl^- (PILS). (The PILS and AMS sampled particles of somewhat different size, with the PILS sampling PM_3 and the AMS PM_1. The AMS observations are available at higher time-resolution, and thus preferable to use here. However, there are challenges in quantitative characterization of Na^+, K^+ and Cl^- using the AMS, and thus the PILS was used instead for these species. Comparison of the AMS and PILS NO_3^- and SO_4^{2-} indicates that the AMS-measured concentrations are ~10% lower than for the PILS, attributable to mass between 1 and 3 μm (Parworth et al., 2017). The Na^+, K^+ and Cl^- ions are minor components of the total PM_3, and thus the AMS-PILS difference has minor influence on the calculations here.) Since the PILS was not functioning on 18th January, 2013, the ionic compositions of K^+ and Cl^- were estimated from the linear relationship between PILS and AMS composition (Equations C1-C2). Since Na^+ measured by PILS was generally constant during the episode it was assumed to be the same on 18th. The diurnally varying concentrations of total $NH_{3(g+p)}$ for ISORROPIA were calculated as the sum of $NH_4^+{}_{(p)}$ measured by AMS and $NH_{3(g)}$ measured by the denuder at the surface in Fresno; since the denuder measurements were averages over 6-7 hours, the $NH_{3(g)}$ concentration was linearly interpolated between the individual measurements to allow for estimation with higher time resolution. The 6-7 hour average denuder-based $NH_{3(g)}$ measurements compare reasonably with the point $NH_{3(g)}$ measurements made on board the P3-b at the lowest altitude over Fresno. The fraction of NO_3^- predicted to be in the gas-phase was also found to be in generally good agreement with the observations (**Figure 2-28**); (Parworth et al., 2017).

$$[Cl^-] = 1.24 * [Cl^-]_{AMS} \quad \text{(D1)}$$

$$[K^+] = -0.036 * [Org]_{AMS} \quad \text{(D2)}$$

As the boundary layer rises, starting around 8 am, and air from the RL is mixed into the surface air, the instantaneous $NO_3^-{}_{(p)}$ concentration at the surface ($[NO_3^-{}_{(p)}]_{surf}$) is calculated as:

$$\left[NO_3^-{}_{(p)}\right]_{surf,t} = \left[NO_3^-{}_{(p)}\right]_{surf,t-1} + \left\{\left[NO_3^-{}_{(p)}\right]_{surf,t-1} - \left[NO_3^-{}_{(p)}\right]_{RL,t}\right\} \times \left\{1 - \frac{w_e \cdot \Delta t}{BLH}\right\} \quad \text{(D3)}$$

where t and t-1 represent the current and previous time steps respectively, *BLH* is the boundary layer height (m AGL), w_e is the entrainment velocity and $[NO_3^-{}_{(p)}]_{RL,t}$ is the concentration of $NO_3^-{}_{(p)}$ in the layer of air that is entrained. Between 8 am and (approximately) noon, the vertical $NO_3^-{}_{(p)}$ profile within the remaining RL (above the instantaneous BLH) is assumed to remain unchanged from the early-morning observed profile. The vertical $NO_3^-{}_{(p)}$ profile is updated to that observed during the second flight once the BLH (from the CLASS model) reaches the ML height observed around noon.

The daytime photochemical production of HNO_3 was calculated from Reaction DR1 (Burkholder et al., 2015, http://jpldataeval.jpl.nasa.gov).

$$NO_2 + OH \rightarrow HNO_3;\ k_{OH} = 2.8 \times 10^{-11}\ cm^{-3}\ molecule^{-1}\ s^{-1} \quad \text{(DR1)}$$

The OH concentration at a given time step was assumed to scale with the solar radiation flux (*SR*) as:

$$[OH]_t = \left(\frac{SR_t}{SR_{max}}\right)[OH]_{max} \quad \text{(D4)}$$

where the maximum daytime OH concentration is assumed to be $[OH]_{max} = 1 \times 10^6$ molecules cm^{-3}, after (Pusede et al., 2016). The rate coefficient for condensation of $HNO_{3(g)}$ onto suspended particulates, k_{cond}, was calculated based on collision theory (Seinfeld and Pandis, 2006b) as:

$$k_{cond} = \sum_i \beta_i * 2 * D_{p,i} * D * 10^{-4} * dN_i \quad \text{(D5)}$$

where the summation is over particle size, $D_{p,i}$ is the mean particle diameter in the size bin i (m), and dN_i is the number concentration in the size bin i (m^{-3}). The term β_i is the size-dependent Fuchs correction in the continuum regime, given by:

$$\beta_i = 0.75 * \frac{1+Kn}{Kn^2+1.283*Kn+0.75} \quad \text{(D6)}$$

where $Kn = \lambda/D_{p,i}$, and λ is the gas mean free path (65 nm). The parameter D is the diffusion coefficient of HNO_3 gas in air ($cm^2\ s^{-1}$) given by (De Andrade et al., 1992):

$$D = 10^{-4.7773} * T^{1.366} \quad \text{(D7)}$$

where T is ambient temperature (K). The corresponding evaporation rate coefficient (k_{evap}) is determined as:

$$k_{evap} = \frac{K_{eqm}}{k_{cond}} \quad \text{(C8)}$$

where K_{eqm} is the instantaneous (temperature and RH-dependent) equilibrium partitioning coefficient for ammonium nitrate. The rate coefficient for loss of gas-phase HNO_3 or $NO_3^{-}{}_{(p)}$ from dry deposition, k_{dep} (s^{-1}) is:

$$k_{dep} = \frac{v_d}{BLH} \quad \text{(C9)}$$

where v_d is the deposition velocity ($cm\ s^{-1}$) and BLH is the time-dependent boundary layer height. The $HNO_{3(g)}$ deposition velocity has been shown to vary linearly with wind speed (Ma and Daggupaty, 2000). Here, it was assumed that:

$$v_d = 1 + 9 * (\frac{ws - ws_{min}}{ws_{max} - ws_{min}}) \quad \text{(C10)}$$

where ws is the observed wind speed, and ws_{min} and ws_{max} are the minimum and maximum values observed. The bounds of Eqn. C10 (lower limit v_d = 1 cm s^{-1} and upper limit 10 cm s^{-1}) were chosen to span previously observed ranges. While the accuracy of the empirical Eqn. C10 is not known, we note that use of a constant v_d of 0.07 cm s^{-1} does not change the box model output substantially (**Figure 2-28**). Of course, if the actual v_d is lower than estimated here the influence of dry

deposition on $NO_3^{-}{}_{(p)}$ concentrations would be decreased. The $NO_3^{-}{}_{(p)}$ deposition velocity was assumed to be 0.01 cm s^{-1}, consistent with much slower deposition of particles than soluble gases such as HNO_3. Dry deposition occurred both during the daytime and nighttime.

2.9 Figures

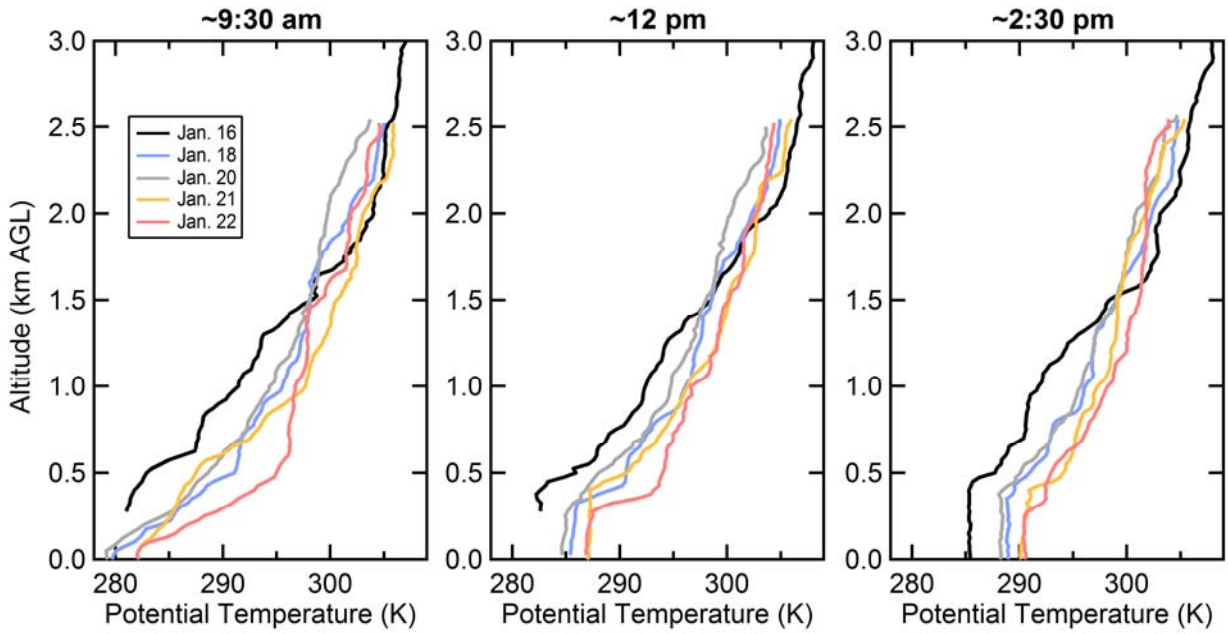

Figure 2-1: Vertical profiles of potential temperature over Fresno measured by the P-3B for pollution Episode 1 flight days for (left) the morning profile, (middle) the late morning/early afternoon profile and (right) the afternoon profile.

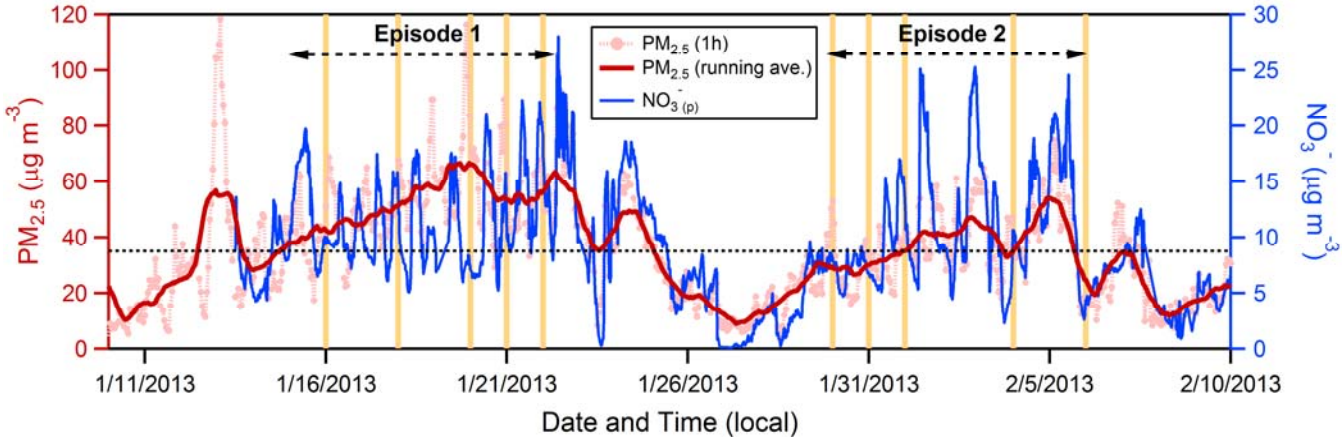

Figure 2-2: Time series of surface $PM_{2.5}$ concentration (µg m^{-3}) measured in Fresno during the DISCOVER-AQ campaign for 1 h averages (light red dotted line) and for a running average (red line; smoothed over 24 h), along with the 1 h average $NO_3^-{}_{(p)}$ concentration (blue line). The vertical orange lines indicate the days on which airborne measurements were made. The horizontal dashed black line indicates the NAAQS 24 h standard of 35 µg m^{-3} for $PM_{2.5}$.

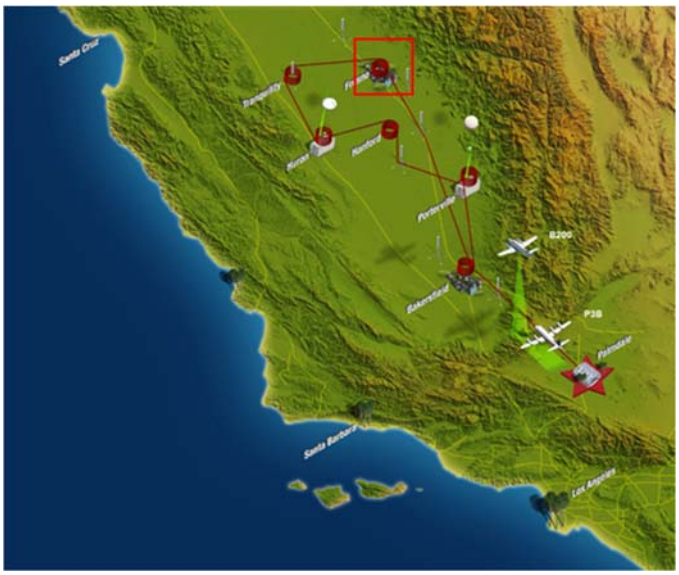

Figure 2-3: Map of San Joaquin Valley, California showing the flight paths of the P3-B and B200 aircrafts and the location of the six sites over which vertical spirals were done. Image from: http://discover-aq.larc.nasa.gov/multimedia.html. The Fresno site is indicated with a red box.

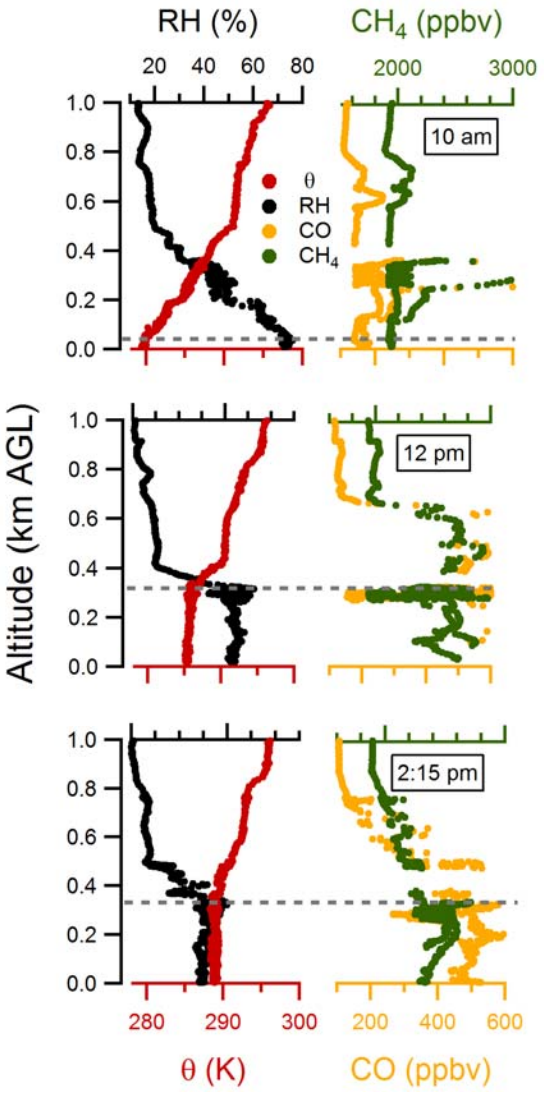

Figure 2-4: Vertical profiles of potential temperature, θ (K), relative humidity, RH (%), mixing ratios of carbon monoxide, CO (ppbv), and methane, CH_4 (ppbv) measured from the P3-B aircraft over Fresno on 18th January, 2013. The horizontal dashed grey line indicates the mixed boundary layer heights.

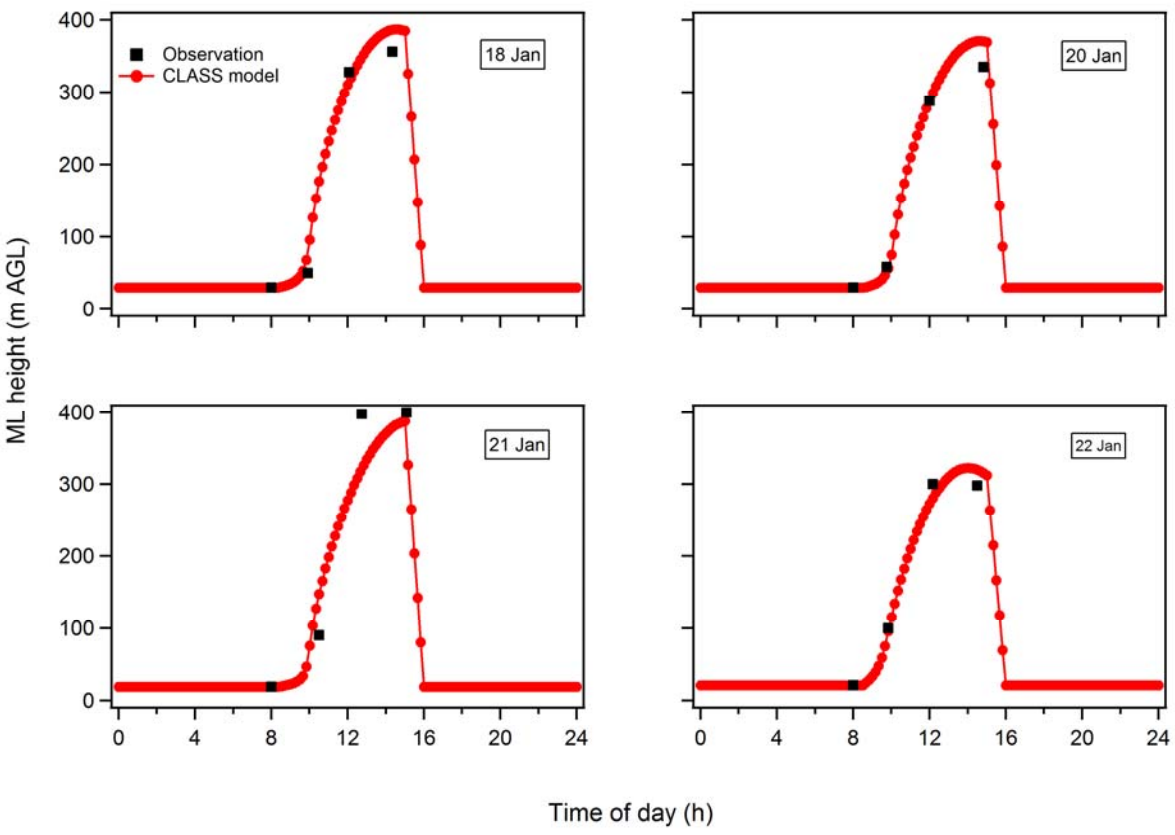

Figure 2-5: Evolution of the ML height with time (starting at 8 am) on the four flight days in Episode 1. The observational constraints are shown as black circles, where the first point comes from nearby balloon sonde measurements and the last three from the P3-B vertical profiles.

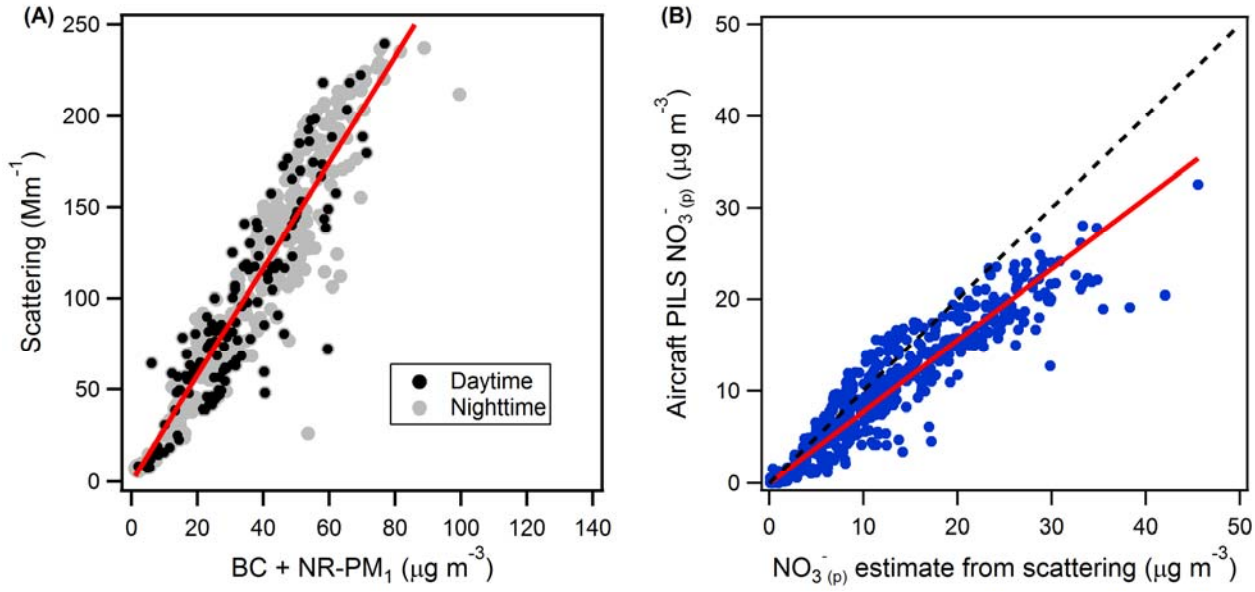

Figure 2-6: (A) Total particle scattering at 550 nm (Mm^{-1}) versus $PM_{1.0}$ mass (submicron black carbon, BC + non-refractory $PM_{1.0}$, NR-PM_1) concentration (µg m^{-3}) observed at ground-level in Fresno. The solid red line is the orthogonal distance regression fit including data only during the daytime (black circles) between 8 am and 4 pm; slope = 2.83 $Mm^2µg^{-1}$. (B) $NO_{3\,(p)}^-$ concentration measured by PILS on P3-B aircraft versus that estimated from scattering using the relation $NO_{3\,(p)}^- = \gamma \cdot \sigma_{sca,dry}/2.83$. The solid red line is the linear fit to the data, with slope = 0.78. The dashed black line is the 1:1 line.

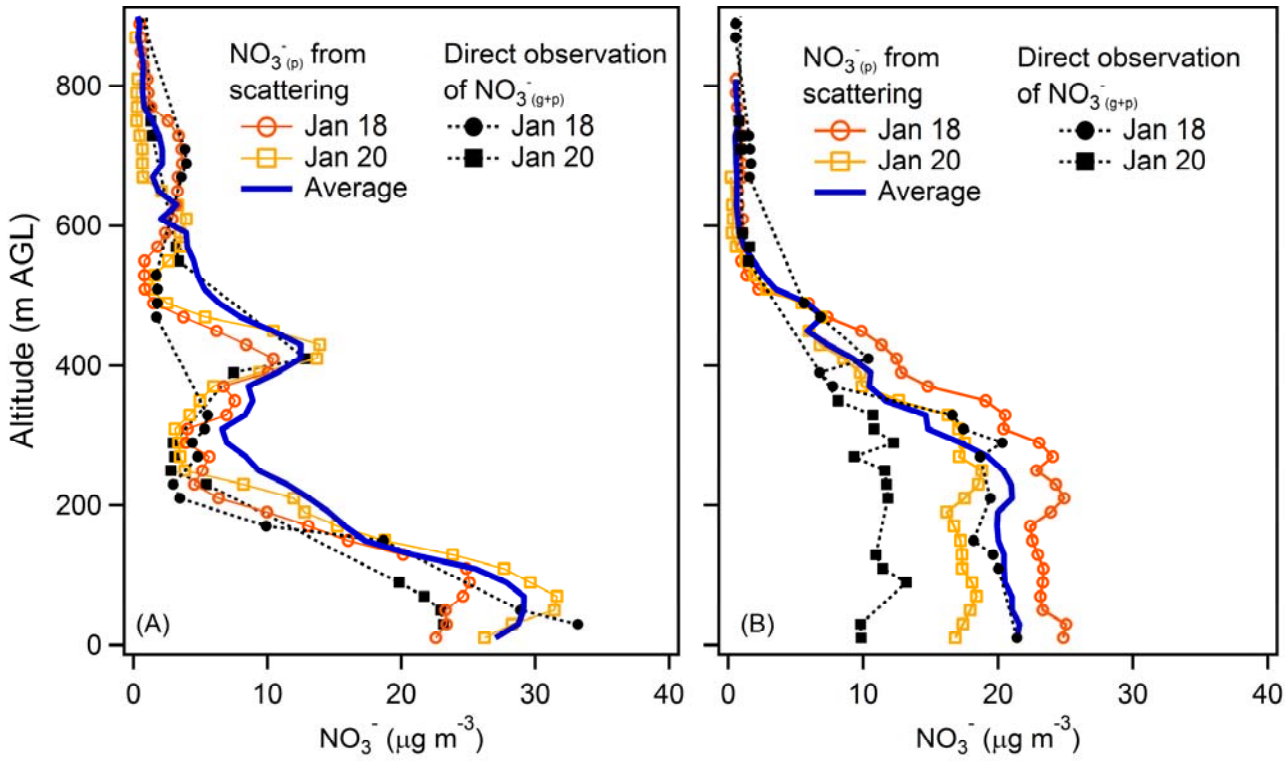

Figure 2-7: Vertical profiles for two individual flight days of particulate nitrate concentrations estimated from *in situ* total particle scattering measurements (open markers) and total nitrate (gas + particle) concentrations measured by the TD-LIF (solid black markers) for (A) the morning (~9:30 am) and (B) the afternoon ~2:30 pm. The solid blue lines indicate the average $NO_3^-{}_{(p)}$ vertical profiles for all four flight days of Episode 1 (Jan 18, 20, 21 and 22).

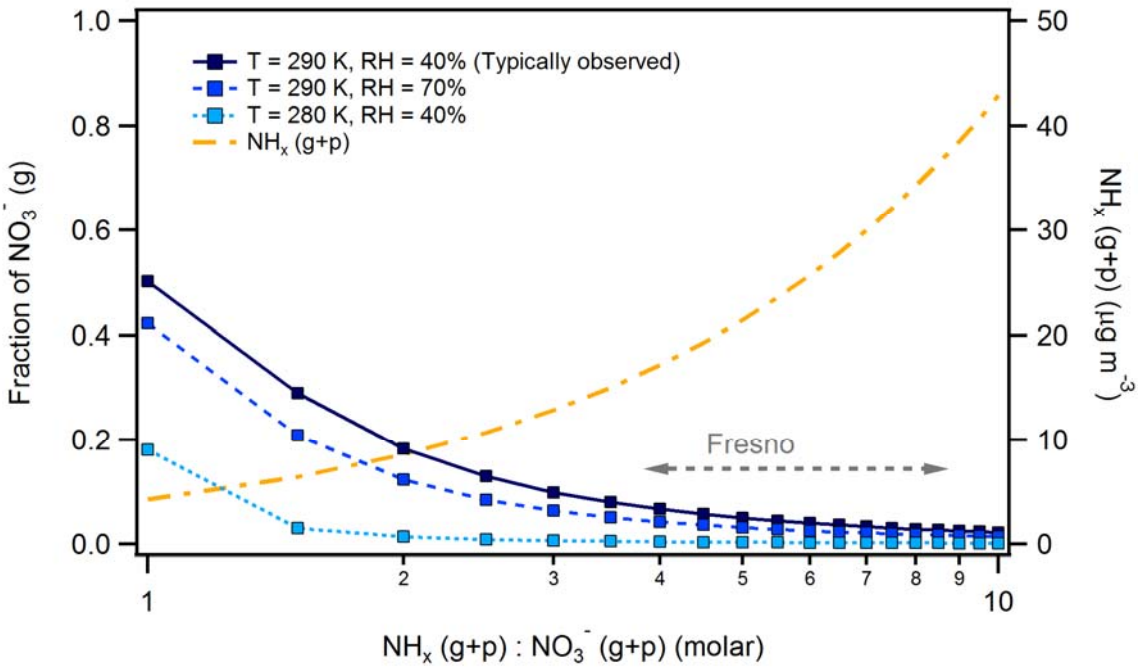

Figure 2-8: The gaseous fraction of total nitrate versus the molar ratio of total ammonia to total nitrate (ppb) under different environmental conditions (blue lines). The total ammonia is the sum of $NH_{3(g)}$ measured on P3-B close to ground (< 20 m AGL) and $NH_4^+{}_{(p)}$ at ground-level measured by PILS at approximately same time. The total nitrate is the $NO_3^-{}_{(g+p)}$ measured by TD-LIF close to ground (< 20 m AGL). The grey dashed arrow indicates the observed range of molar ratio values during the campaign period. The total (gas + particle) ammonia is shown for reference (orange line).

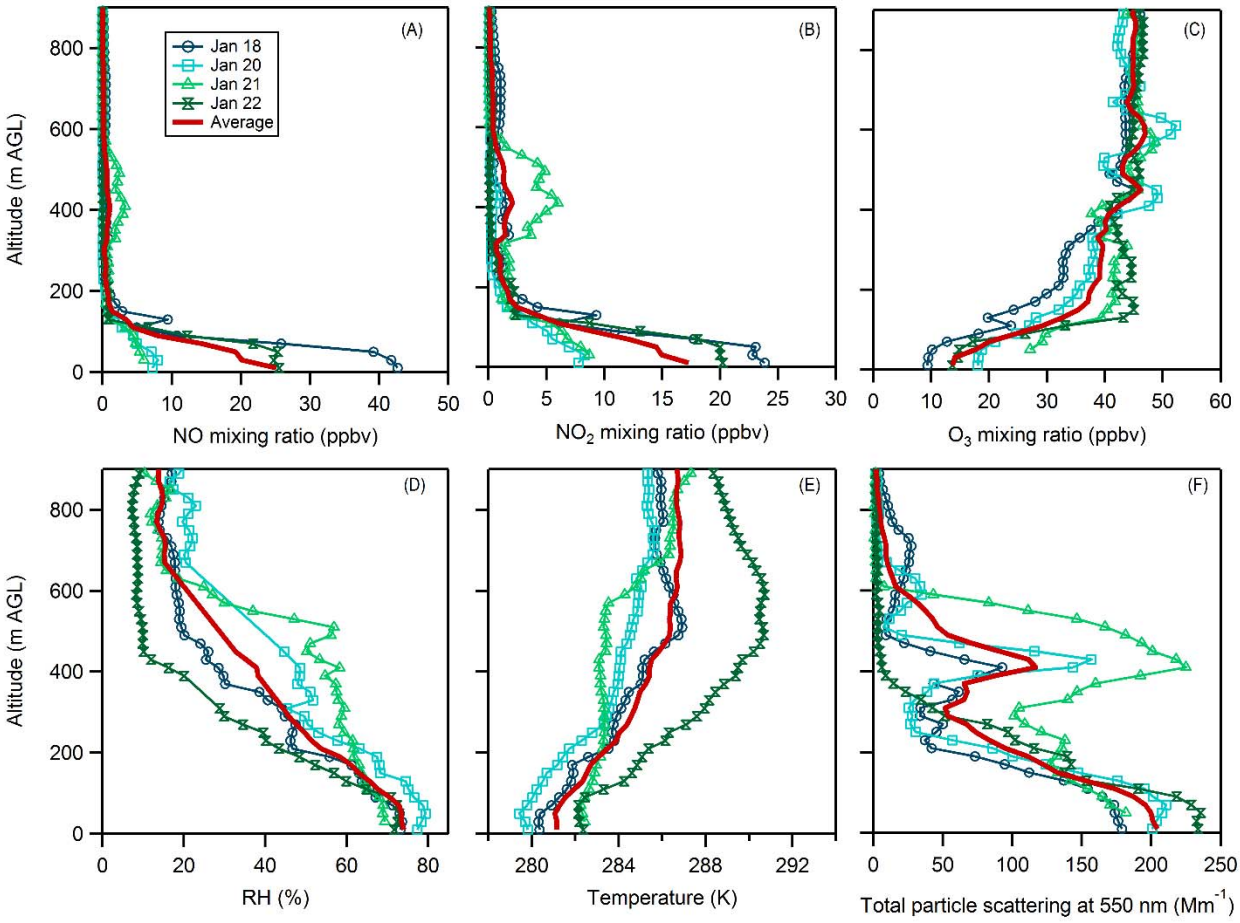

Figure 2-9: Vertical profiles on individual flight days of (A) NO mixing ratio (ppbv), (B) NO_2 mixing ratio (ppbv), (C) O_3 mixing ratio (ppbv), (D) RH (%), (E) ambient temperature, in K, and (F) total particle scattering at 550 nm in the morning (~9:30 am) over Fresno. Individual days are shown as green and blue and the average as the solid red line.

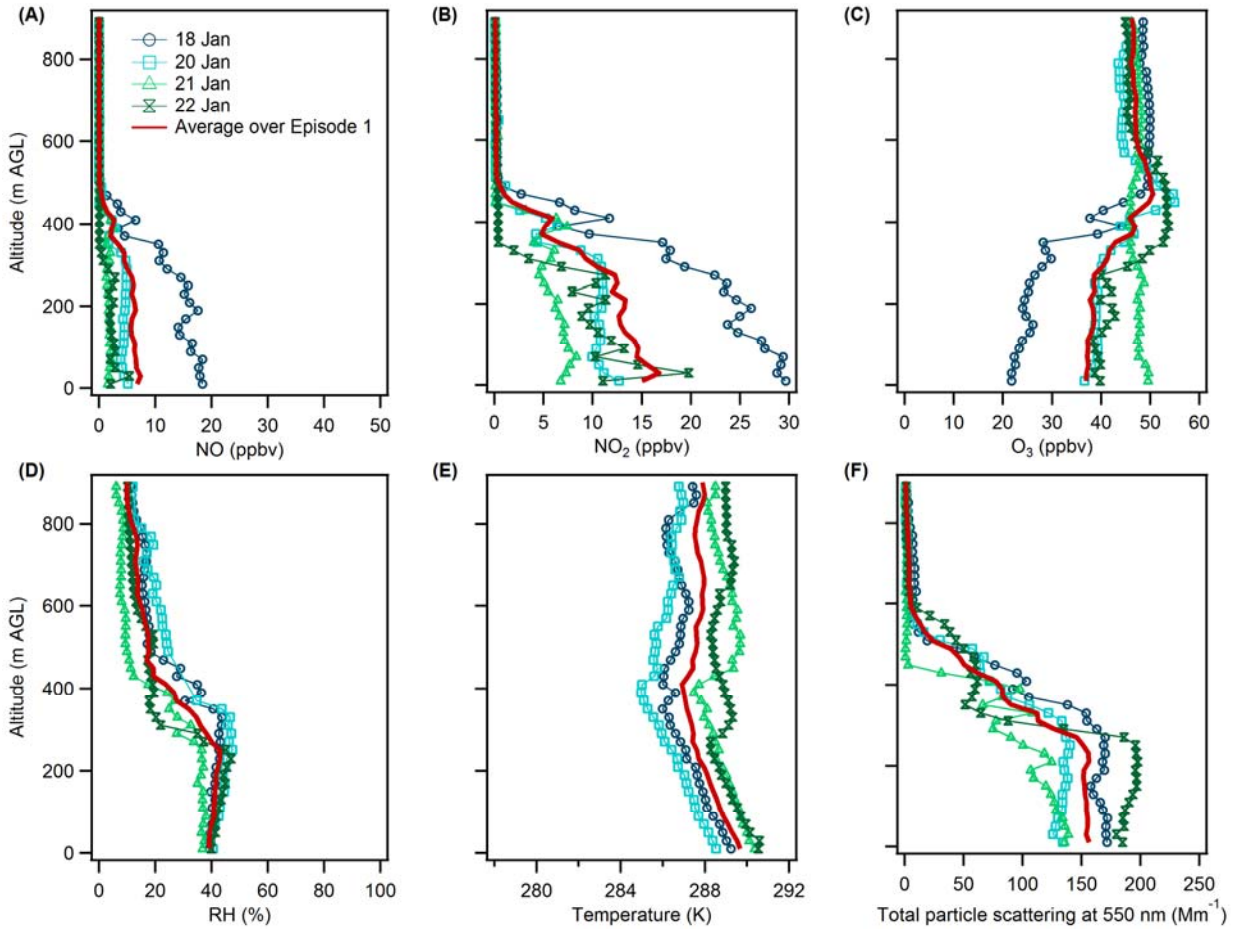

Figure 2-10: The observed afternoon (2:30 pm) vertical profiles over Fresno on individual flight days during the first episode of: (A) the NO mixing ratio (ppbv); (B) the NO_2 mixing ratio (ppbv); (C) the O_3 mixing ratio (ppbv); (D) relative humidity (%); (E) ambient temperature (K); and (F) the total particle scattering at 550 nm. Individual profiles are shown with symbols and the average profile is shown as a solid red line.

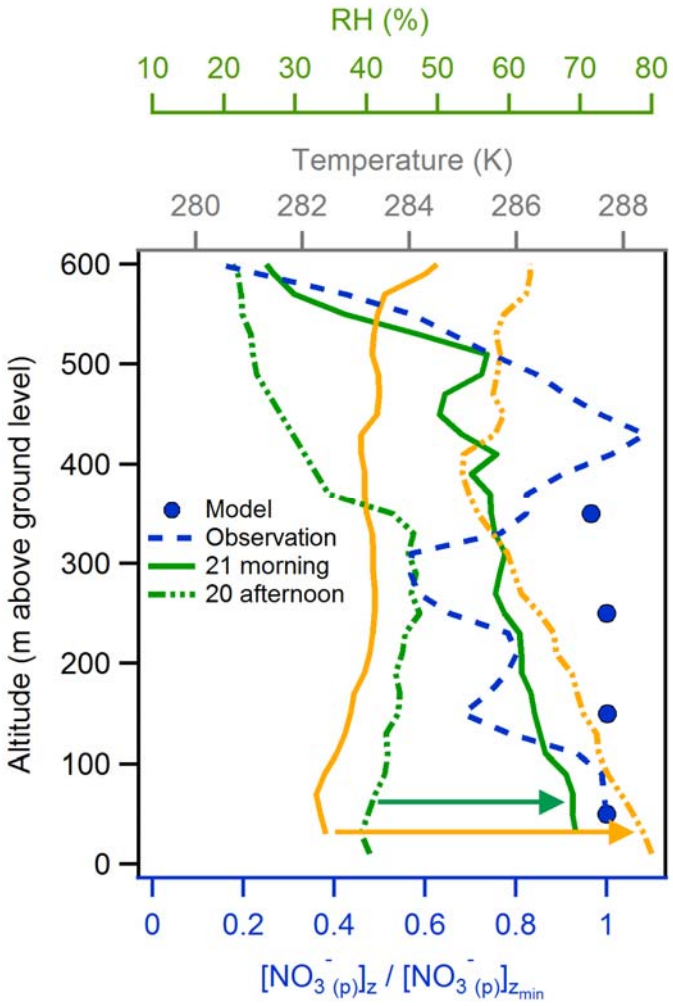

Figure 2-11: The vertical distribution of the observed normalized $NO_3^-{}_{(p)}$ (dashed blue line) for the first flight leg (early morning) on 21 Jan early morning along with box model prediction of the same (blue dots). (The normalized $NO_3^-{}_{(p)} = [NO_3^-{}_{(p)}]_z/[NO_3^-{}_{(p)}]_{z\min}$, where z is altitude and $z_{\min}$ is lowest altitude.) Also shown are vertical profiles of temperature (yellow) and relative humidity (green) observed during the third flight leg (afternoon) on 20 Jan (dashed lines) and during the first flight leg (early morning) on 21 Jan morning (solid lines). The horizontal arrows indicate the overnight evolution of temperature and RH.

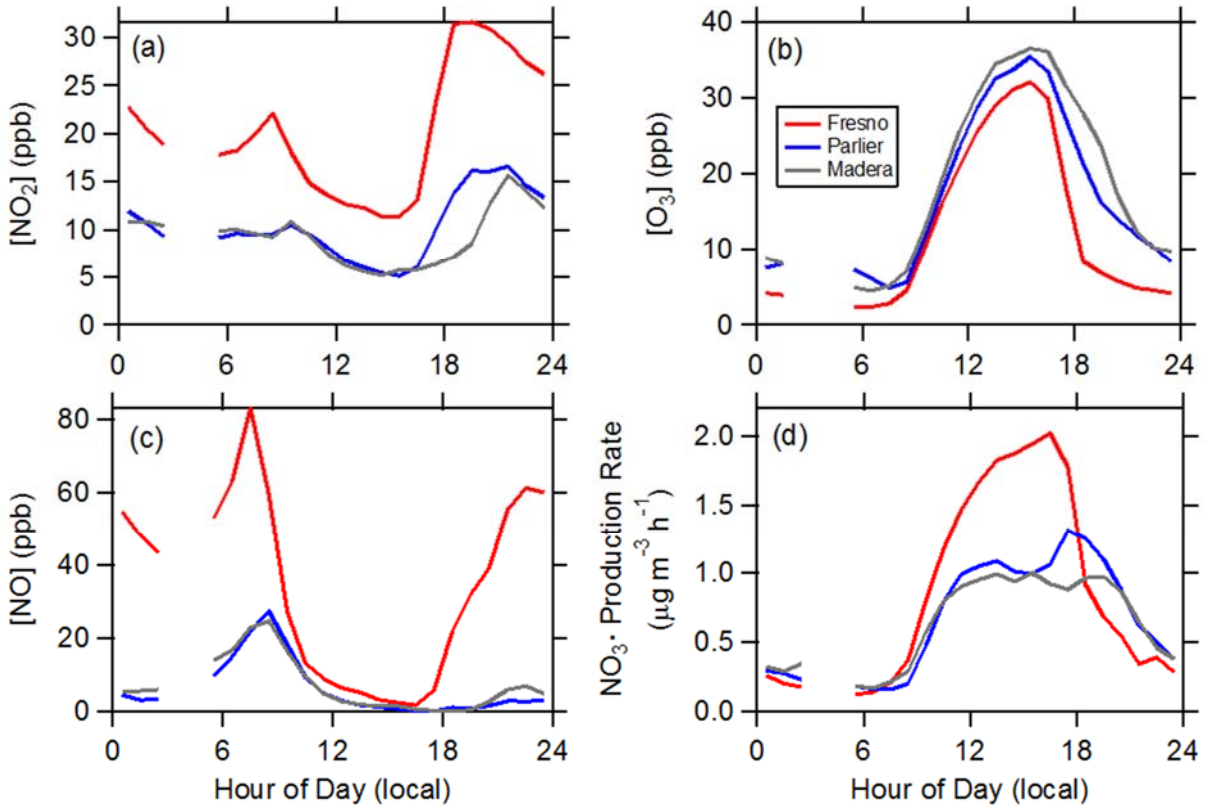

Figure 2-12: Diurnal profiles of (a) NO_2, (b) O_3, (c) NO and (d) the instantaneous NO_3· production rate for (red) Fresno, (blue) Parlier and (gray) Madera.

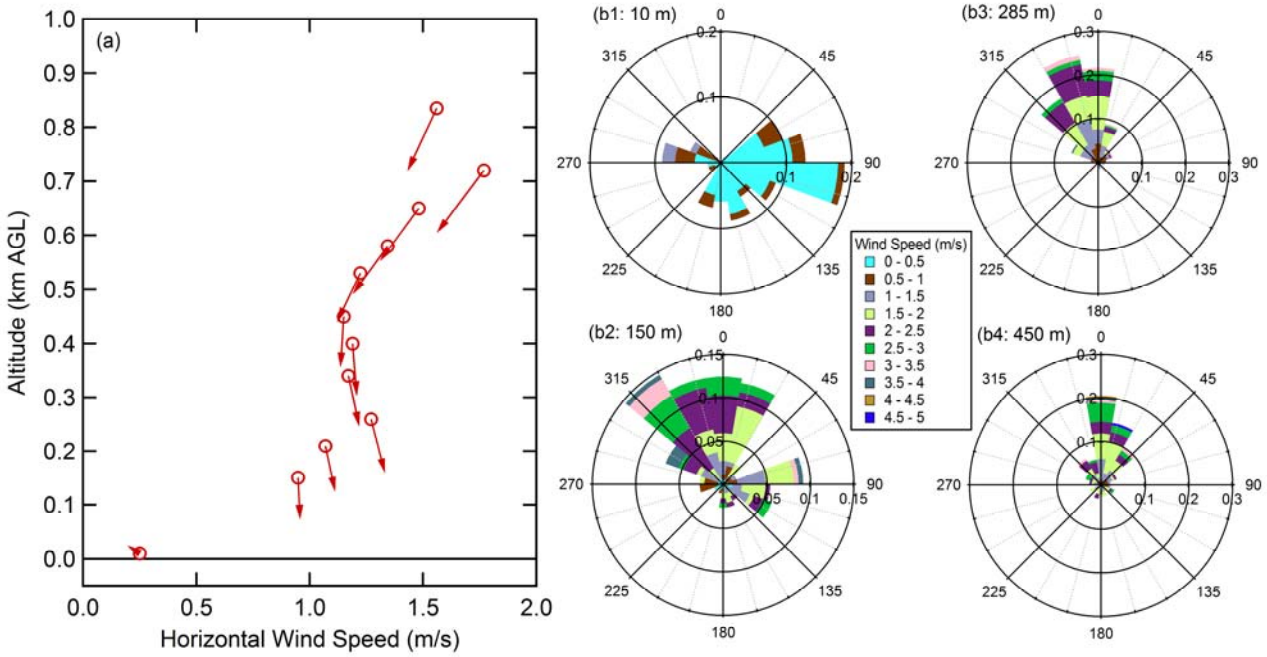

Figure 2-13: (a) Vertical profile of the average night time (19:00-07:00) horizontal winds over Visalia, CA (65 km SE of Fresno) and the surface (10 m) wind in Fresno for flight days during Episode 1 (Jan. 18, 20, 21, and 22). The length of the arrows corresponds to the wind speed and the direction to the average wind direction, with the measurement height indicated by the circle on the tail of the arrow. (b) Corresponding wind roses for (b1) the surface, (b2) 125-175 m, (b3) 225-345 m, and (b4) 400-500 m. The length of each arc corresponds to the normalized probability and the colors indicate the wind speed (m/s; see legend). Data are from the National Oceanic and Atmospheric Administration, Earth System Research Laboratory, Physical Sciences Division Data and Image Archive (https://www.esrl.noaa.gov/psd/data/obs/datadisplay/, accessed 3 June 2017).

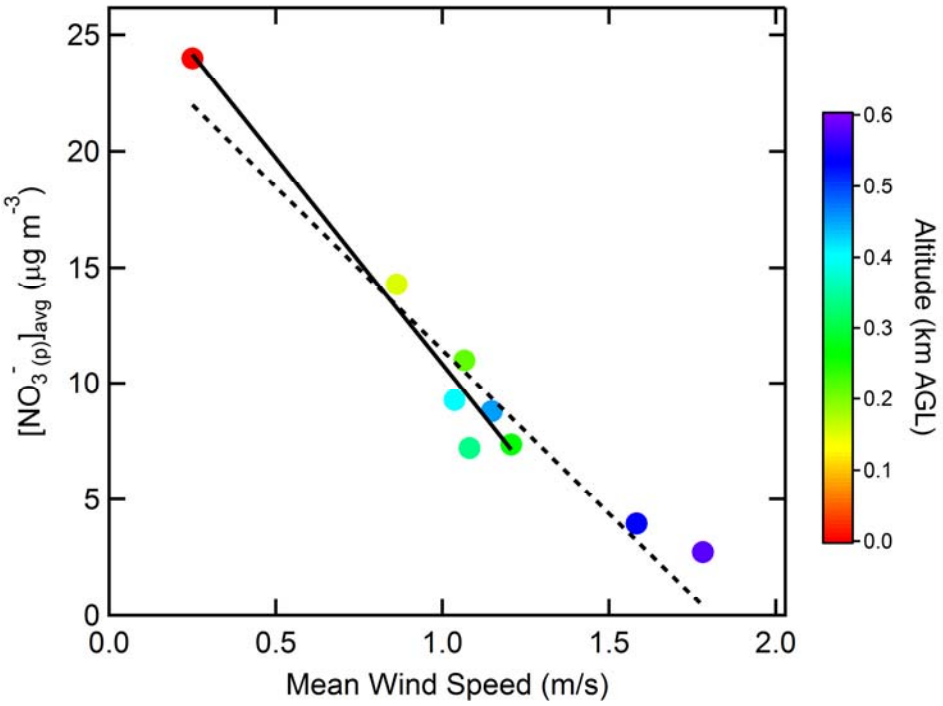

Figure 2-14: Relationship between the Episode 1 average vertical profiles of estimated $NO_3^{-}{}_{(p)}$ concentrations and the night time mean wind speed. The mean wind speed is for only the nights preceding flight days. Points are colored according to altitude above ground level. The solid black line is a linear fit for altitudes < 0.45 km, with slope = -17.8 µg.s m^{-4} and intercept 28.6 µg m^{-3} and r = -0.98. The dashed black line is a fit to all points below 1 km (r = -0.96).

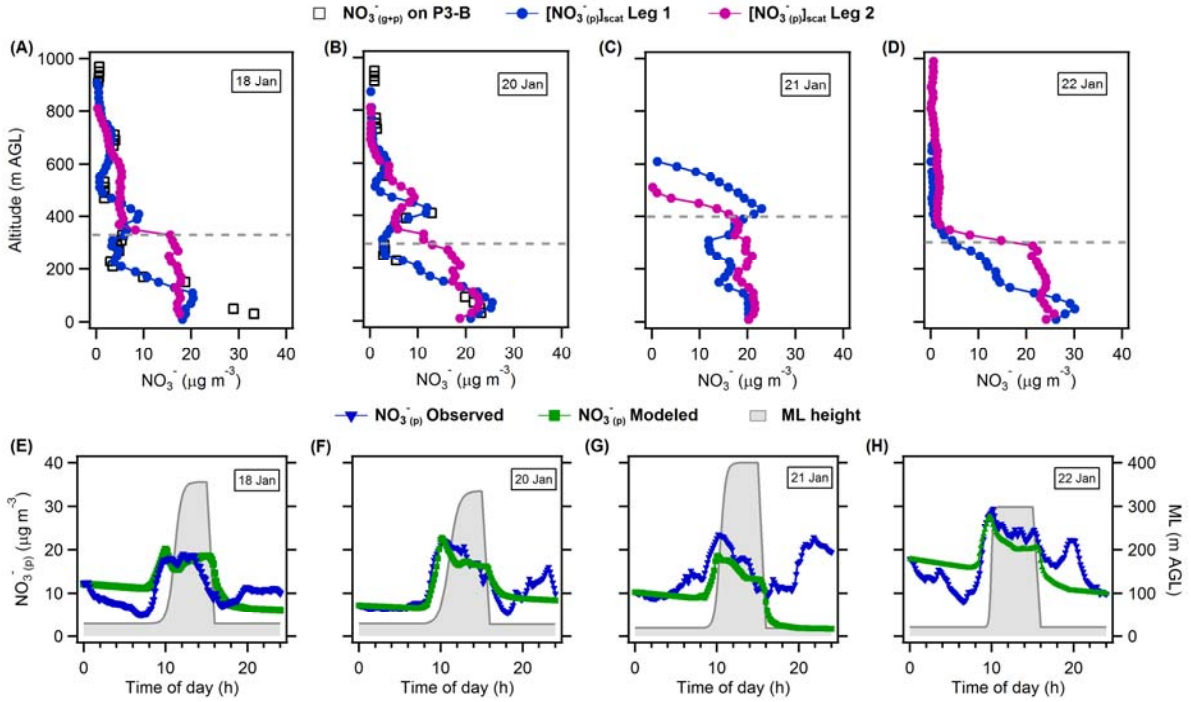

Figure 2-15: (A-D) The observed vertical profiles of $NO_3^-{}_{(g+p)}$ (black squares) from the TD-LIF and $NO_3^-{}_{(p)}$ (blue circles) for the first flight leg, along with the $NO_3^-{}_{(p)}$ for the second flight leg (purple circles). The horizontal dashed grey lines indicate the ML height at the time of the Fresno profile during flight leg 2. (E-H) The diurnal variation in the observed (blue) and modeled (green) surface-level $NO_3^-{}_{(p)}$ for each flight day in Episode 1. The temporal variation in the BLH (grey shaded area) is shown for reference.

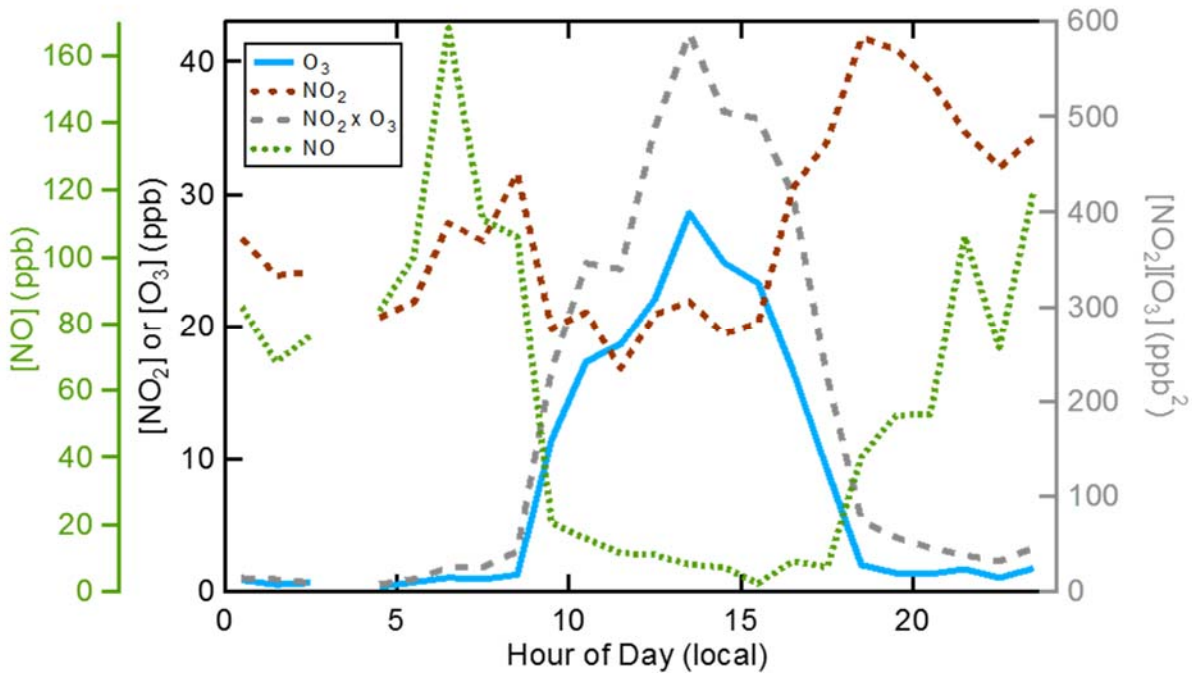

Figure 2-16: Diurnal profiles for ozone (blue), NO_2 (brown), NO (green) and the product of O_3 and NO_2 (gray) for the first pollution episode.

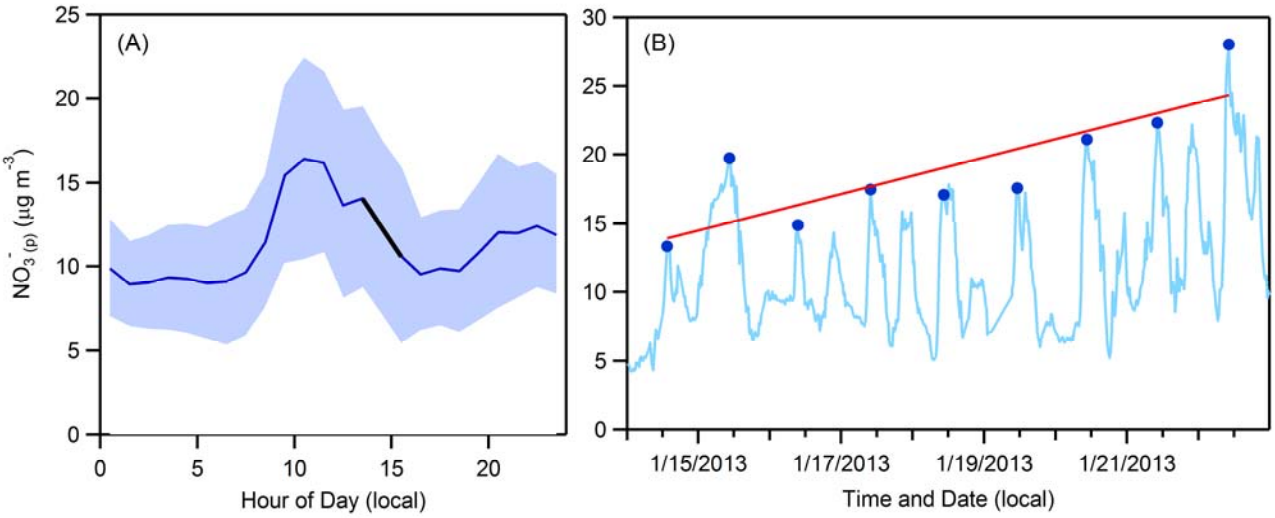

Figure 2-17: (A) Average diurnal profile (solid line) of surface $NO_{3\,(p)}^{-}$ for all days of Episode 1. The shaded area indicates the 1σ standard deviation. The solid black line is a linear fit ($r^2 = 0.99$) to the data between 1:30 pm and 3:30 pm. (B) Time series (solid blue line) of surface-level $NO_{3\,(p)}^{-}$ during Episode 1. The circles indicate the daytime peak values. The linear fit (red line) to the daytime $NO_{3\,(p)}^{-}$ peaks suggest an increase of 1.32 µg m^{-3} day^{-1}.

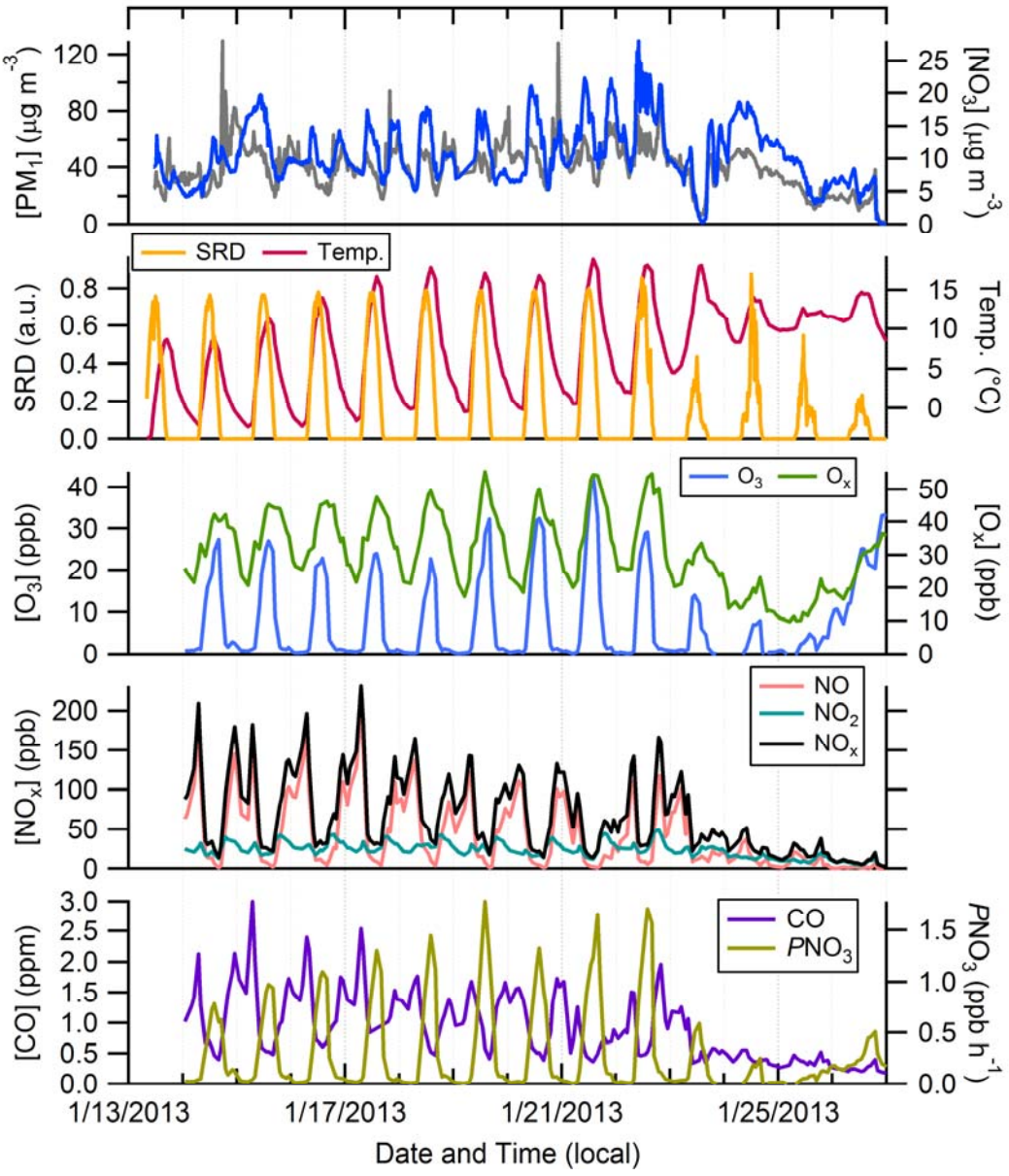

Figure 2-18: Time-series of observed (top-to-bottom) PM_1 and particulate NO_3^- concentrations, solar radiation (SRD) and temperature, O_3 and O_x concentrations, NO, NO_2 and NO_x concentrations, and CO concentrations with the instantaneous nitrate radical production rate, calculated as $PNO_3 = k_{NO3}[NO_2][O_3]$.

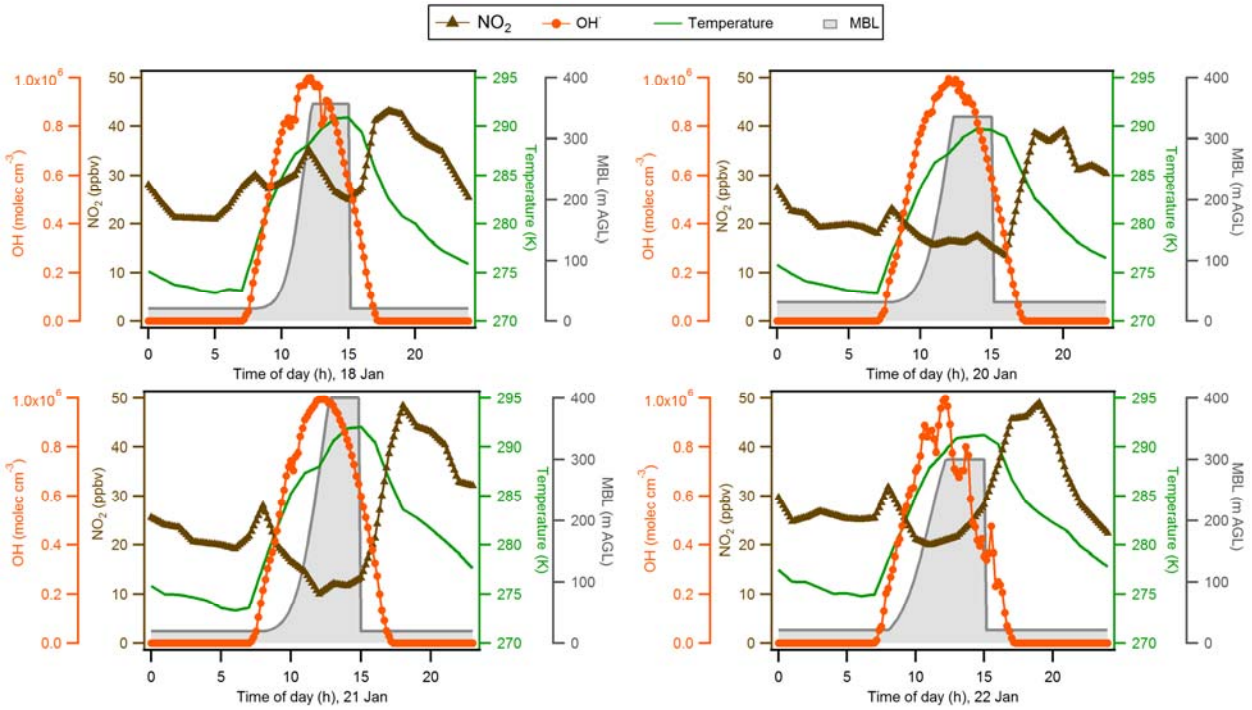

Figure 2-19: Ground observations of NO_2 (brown triangles) and temperature (green line) and the estimated OH (orange circles) and boundary layer height (gray) that are used to as inputs to the mixing model for each of the four flight days in Episode 1.

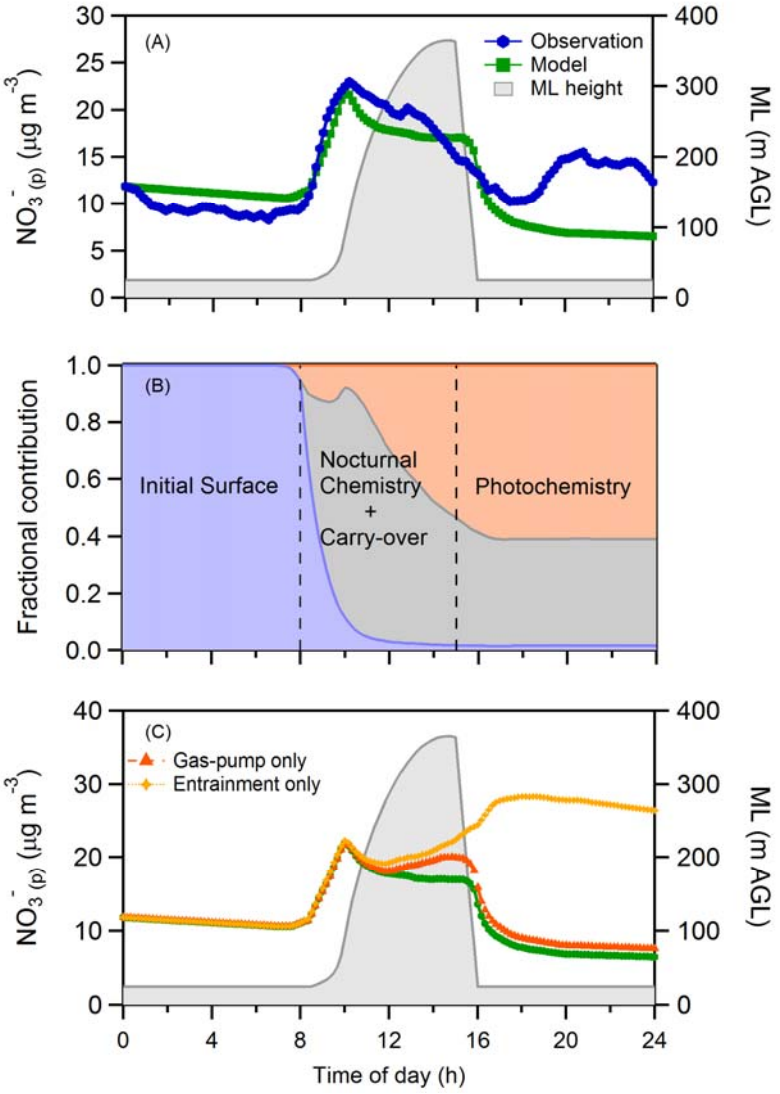

Figure 2-20: (A) Comparison between the observed (blue circles) and observationally constrained model predicted (green squares) diurnal profile of the surface $NO_{3\,(p)}^{-}$ concentration (µg m^{-3}) for the four flight days (18th, 20th, 21st and 22nd January, 2013) during Episode 1. Also shown is the diurnal variation in the boundary layer height (gray), as constrained by daytime measurements. (B) The diurnal variation in the simulated fraction of the total surface-level $NO_{3\,(p)}^{-}$ contributed by the initial surface-level $NO_{3\,(p)}^{-}$ (i.e. that at surface-level at 12:00 am), the $NO_{3\,(p)}^{-}$ mixed down from the RL, and $NO_{3\,(p)}^{-}$ produced from daytime photochemical reactions. (C) Comparison between the simulated diurnal profile when all processes are included (green squares, same as Panel A) and when only one $NO_{3\,(p)}^{-}$ sink at a time is considered. The individual sinks considered are only entrainment of free troposphere air (yellow crosses) or only dry deposition of HNO_3 via the gas-phase pump (orange triangles).

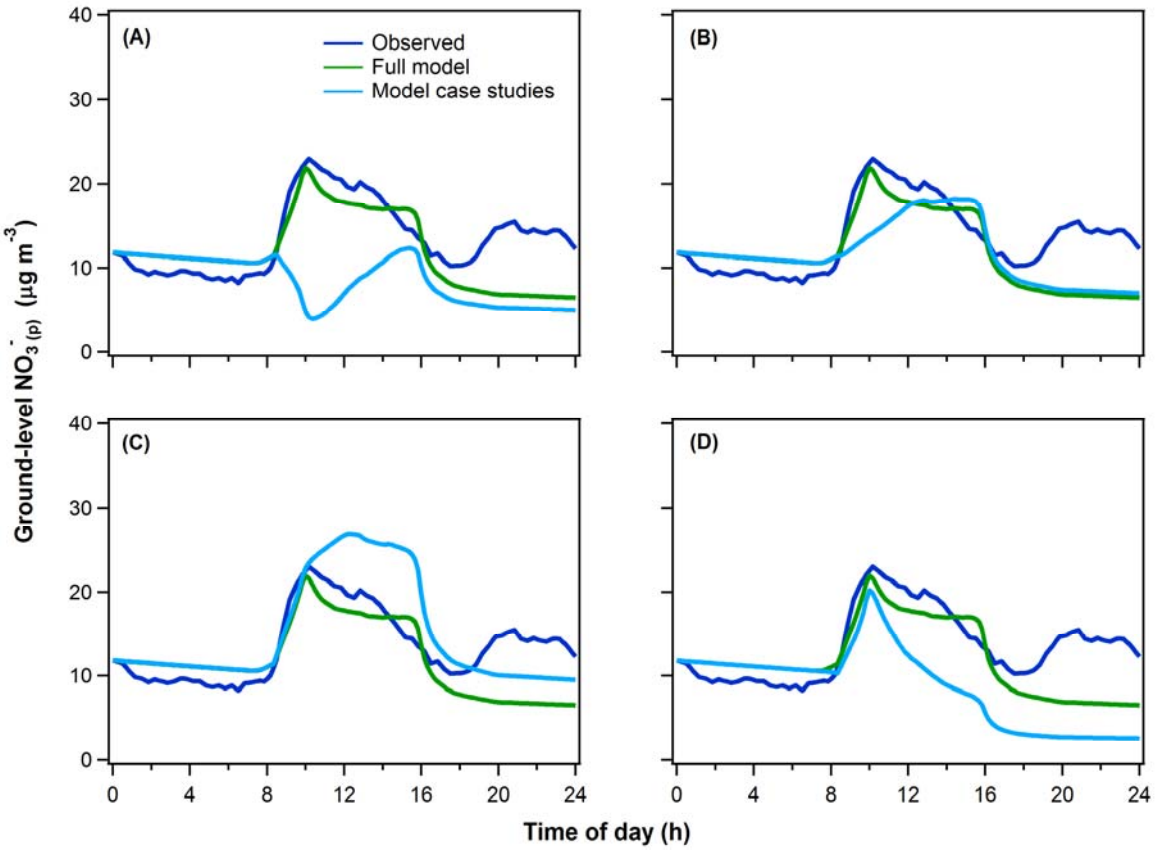

Figure 2-21: Model predictions of the diurnal variation in surface-level $NO_3^-{}_{(p)}$ under (A-C) different assumptions regarding the $NO_3^-{}_{(p)}$ concentration and vertical variability in the early-morning RL, or (D) without daytime photochemical production of $NO_3^-{}_{(p)}$. In all panels the blue curve shows the observations and the green curve shows the full observationally constrained model results (identical to Figure 6) for the average of the four flight days in Episode 1. For (A-C), the assumptions were: (A) The $[NO_3^-{}_{(p)}]_{RL}$ is equal to zero; (B) The $[NO_3^-{}_{(p)}]_{RL}$ is constant with altitude and equal to the $NO_3^-{}_{(g+p)}$ at 3 pm previous afternoon, corresponding to a case of zero net production or loss; (C) the $[NO_3^-{}_{(p)}]_{RL}$ is constant with altitude and equal to the maximum observed $[NO_3^-{}_{(p)}]$ in the early-morning RL profile.

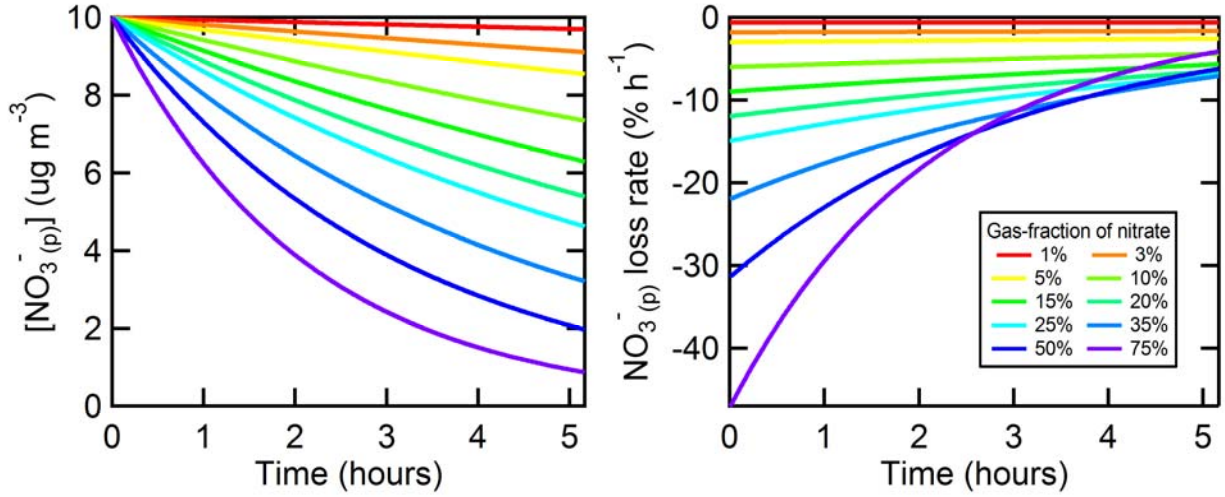

Figure 2-22: (left) Example model results of the influence of gas-phase HNO_3 deposition on $NO_3^-(p)$ concentrations for different assumed gas-phase nitrate fractions (indicated by color). Here, a constant v_d = 7 cm s^{-1} and mixed-layer height of 400 m are used, and the gas and particles are assumed to remain in equilibrium at all times. The initial $NO_3^-(p)$ concentration is 10 μg m^{-3}. For Fresno, the observed daytime gas-phase nitrate fractions are <10%. (right) The corresponding instantaneous $NO_3^-(p)$ loss rate, in percent. The loss rate is independent of the assumed initial $NO_3^-(p)$ concentration.

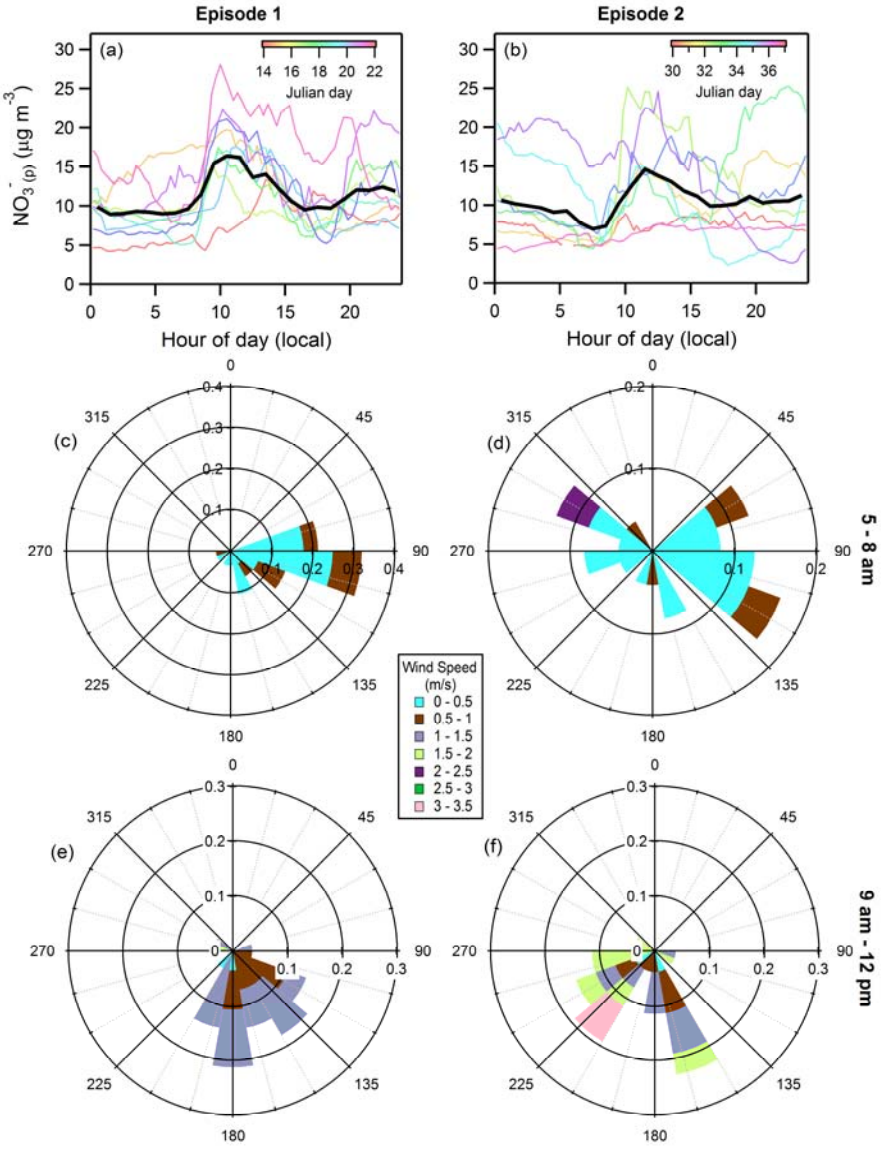

Figure 2-23: (Top panels) Diurnal variation in the surface-level particulate nitrate concentration during (a) the first episode and (b) the second episode. The solid black lines are the average profile over the episode and the colored lines are for individual days. (Middle/Bottom panels) Wind roses for surface-level (10 m) winds in Fresno for the early morning (5 – 8 am) during (c) episode 1 and (d) episode 2, and for the late morning (9 am – 12 pm) during (e) episode 1 and (f) episode 2.

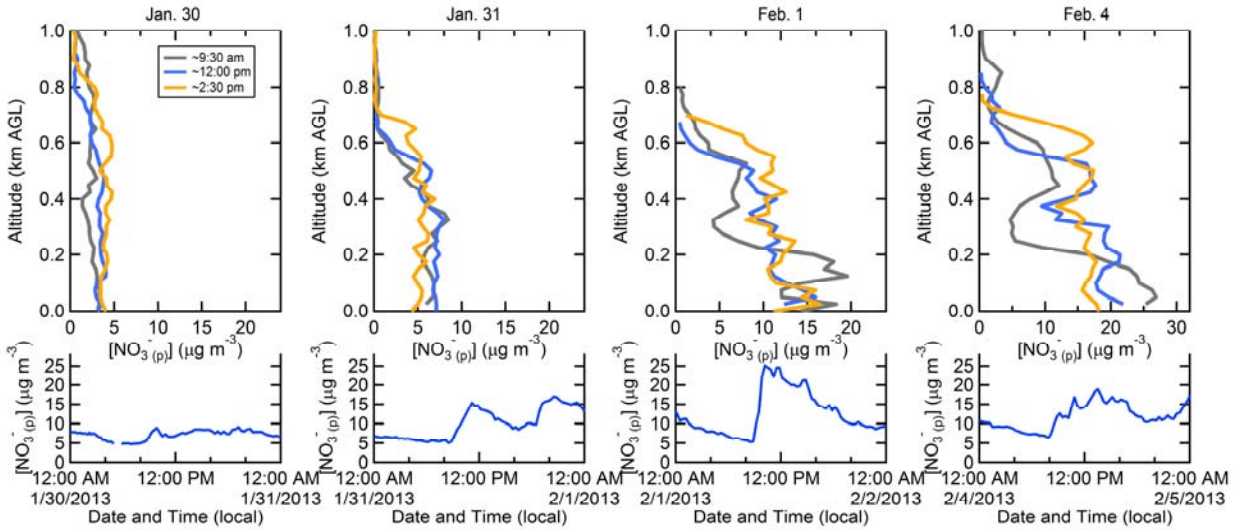

Figure 2-24: (top row) Vertical profiles of estimated $NO_3^-(p)$ concentrations during the flight days in the second episode. The different curves are for individual flight legs. (bottom row) The individual day diurnal variability in the surface $NO_3^-(p)$ concentrations for each flight day.

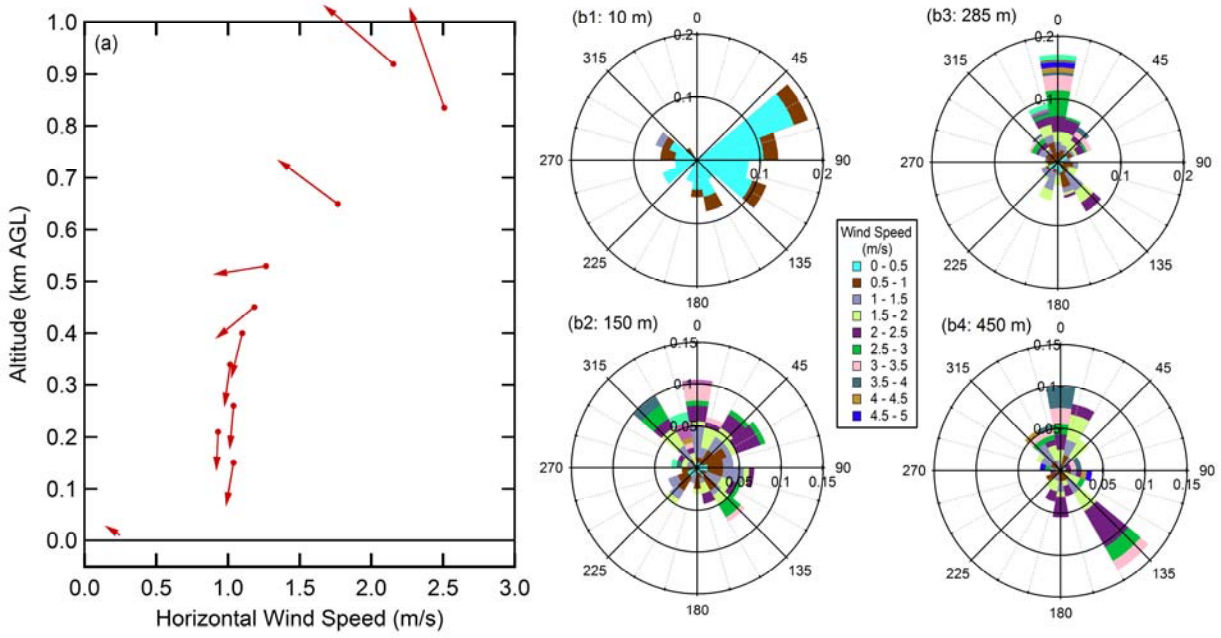

Figure 2-25: (a) Vertical profile of the average night time (19:00-07:00) horizontal winds over Visalia, CA (65 km SE of Fresno) and the surface (10 m) wind in Fresno during Episode 2 (Jan. 29-Feb. 4). The length of the arrows corresponds to the wind speed and the direction to the average wind direction. (b) Corresponding wind roses for (b1) the surface, (b2) 125-175 m, (b3) 225-345 m, and (b4) 400-500 m. The length of each arc corresponds to the normalized probability and the colors indicate the wind speed (m/s; see legend). Data are from the National Oceanic and Atmospheric Administration, Earth System Research Laboratory, Physical Sciences Division Data and Image Archive (https://www.esrl.noaa.gov/psd/data/obs/datadisplay/, accessed 3 June 2017).

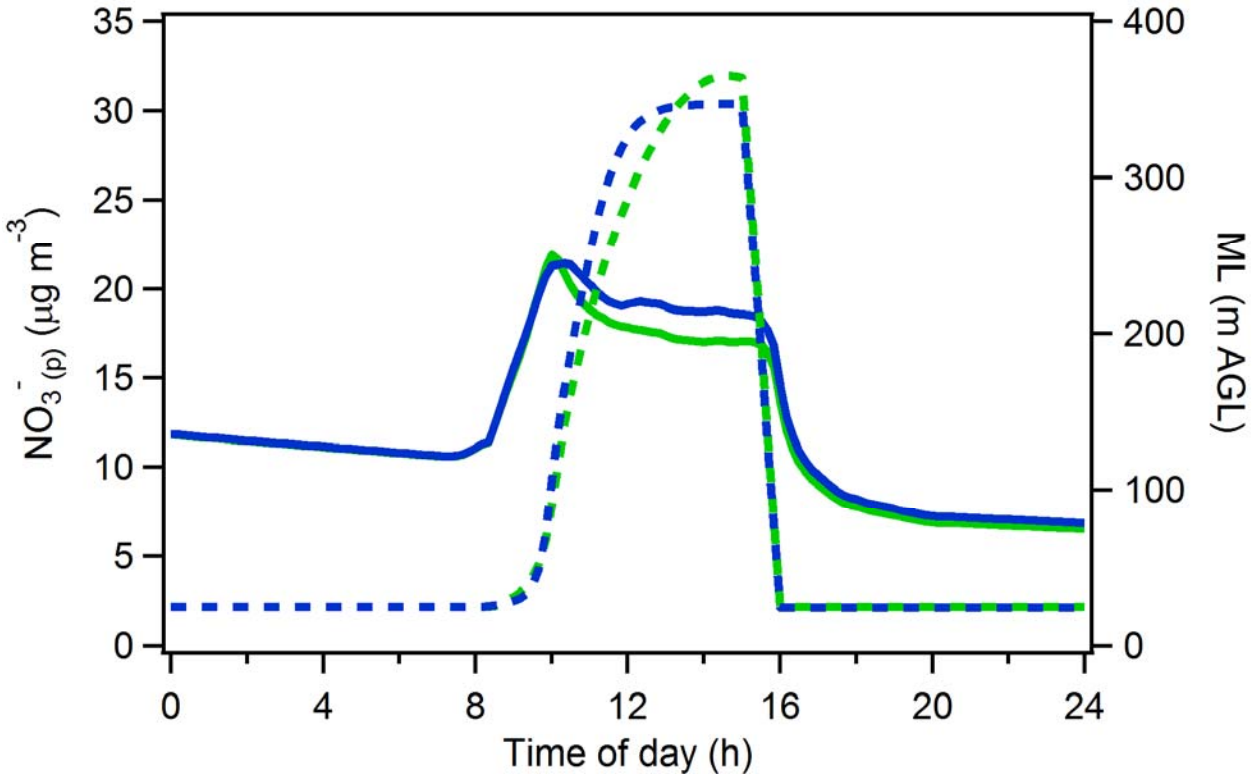

Figure 2-26: Average modelled surface $NO_3^-{}_{(p)}$ (solid lines) using the CLASS model output (green) and a sigmoid fit to the observed ML heights (blue). The ML heights used in the model are shown in dashed lines.

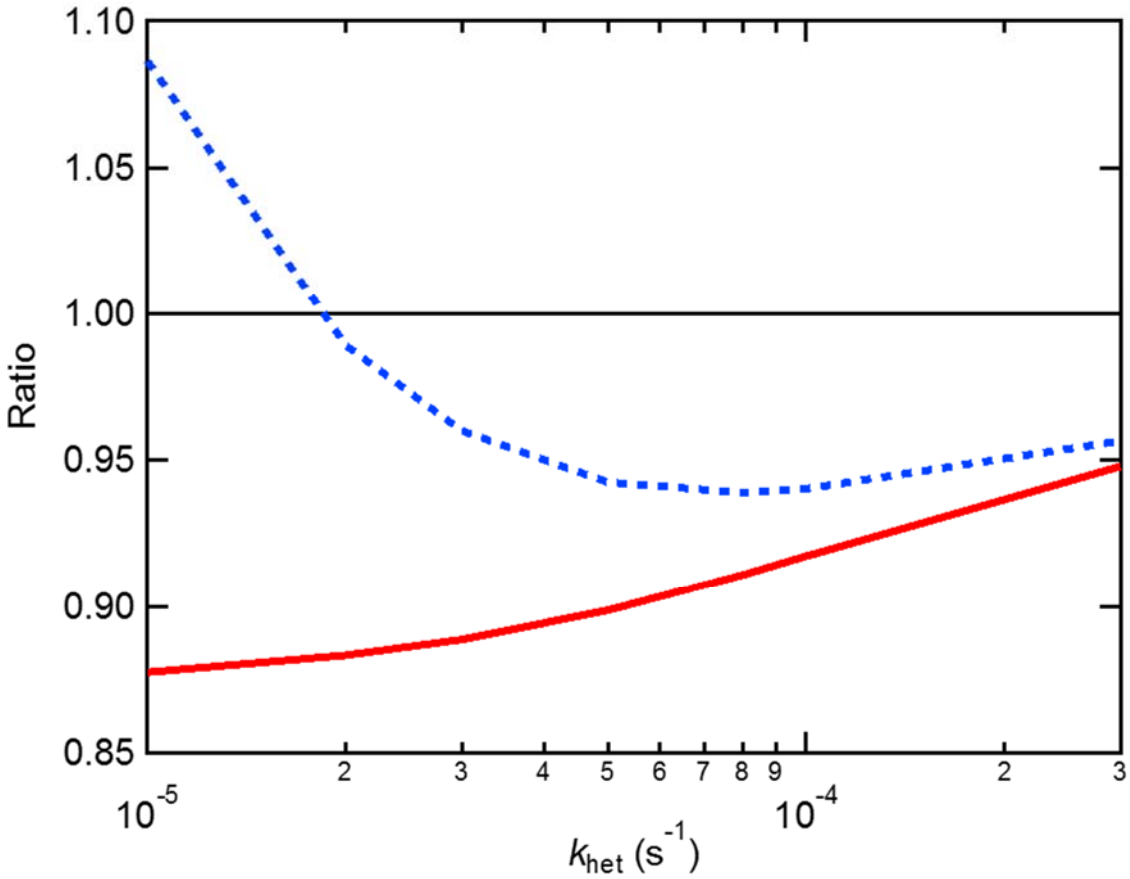

Figure 2-27: Model results showing the influence of including NO_3 + VOC reactions on HNO_3 production via the heterogeneous hydrolysis of N_2O_5, as a function of the heterogeneous oxidation rate. The red line shows the ratio between the HNO_3 produced via N_2O_5 hydrolysis when reactions with VOCs are considered and when they are not. Reaction of NO_3 with VOCs reduces the HNO_3 formed via hydrolysis. The blue line shows the ratio between the total HNO_3 produced from either N_2O_5 hydrolysis or NO_3 + VOC reactions when reactions with VOCs are considered and when they are not.

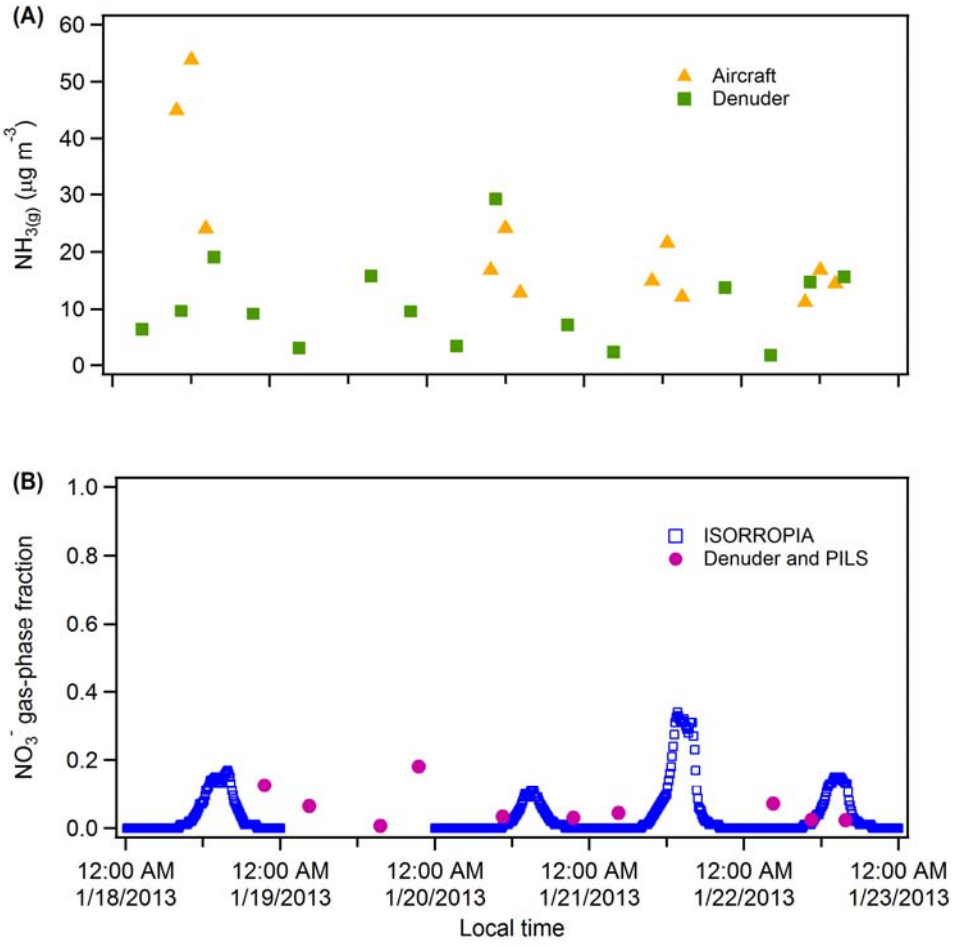

Figure 2-28: (A) Time series of $NH_{3(g)}$ (µg m^{-3}) measured with the denuder at the surface (green squares) and at the lowest altitudes by CIMS onboard P3-B aircraft (yellow triangles). (B) The nitrate gas-phase fraction estimated by ISORROPIA (blue squares) and the observed fraction determined from the denuder $HNO_{3(g)}$ and PILS $NO_3^-{}_{(p)}$ measurements (pink circles) (Parworth et al., 2017).

2.10 Tables

Table 2-1. Summary of instruments deployed and measurements on ground and on aircraft made during the DISCOVER-AQ campaign.

Platform	Measurement	Instrument	Uncertainty	Response time
NASA P3-B aircraft + Ground	Total and submicron scattering at 450, 550 and 700 nm	Integrating Nephelometer (TSI 3563)	5%	1 s
NASA P3-B Aircraft	Nitrate (gas+particle)	Thermal Dissociation - Laser Induced Fluorescence (TD-LIF)	15%	1 s
NASA P3-B Aircraft	Carbon monoxide (CO), Methane (CH_4)	Differential Absorption CO Measurement (DACOM)	< 2%	1 s
NASA P3-B Aircraft	Nitrogen monoxide (NO), Nitrogen dioxide (NO_2), and Ozone (O_3)	4-channel Chemiluminiscence	10% for NO, 15% for NO_2, and 5% for O_3	1 to 3 s
NASA P3-B Aircraft	Ammonia (NH_3)	Picarro G2103	35%	10 s
NASA P3-B Aircraft	Aerosol size distribution (0.06 – 1 μm)	Ultra-High Sensitivity Aerosol Spectrometer (UHSAS)	20%	1 s
NASA P3-B Aircraft	Meteorological and navigational measurements onboard	P3-B Project Data System (PDS)	-	1 s
Ground	$PM_{2.5}$ mass concentration	Beta-Attenuation Mass (BAM) Monitor	16%	1 h
Ground	NO, NO_2	Chemiluminiscence	20%	1 h
Ground	O_3	NIST Standard Reference Photometer (SRP)	2%	1 h
Ground	Speciated non-refractory $PM_{1.0}$	High Resolution Time-of-Flight Aerosol Mass Spectrometer (HR-ToF-AMS)	25%	5 min
Ground	Water-soluble components of $PM_{2.5}$	Particle-Into-Liquid Sampler (PILS) coupled with two Ion chromatography systems	10 - 20%	20 min
Ground	Aerosol Particle Size	Scanning Mobility Particle Sizer (SMPS)	10%	1 min
Ground	Aerosol Particle Size	Aerodynamic Particle Sizer (APS)	20%	1 s
Ground	Refractive black carbon mass concentration	DMT Single Particle Soot Photometer (SP2)	30%	5 min
Ground	Relative humidity and temperature		Temperature: ± 0.1 K RH: ± 2%	1 h

Table 2-2. Summary of initial conditions measured at the surface-level (3 pm) used for calculation of k_{N2O5} and γ_{N2O5} for flight days during Episode 1.

Dates	NO (ppbv)	NO_2 (ppbv)	O_3 (ppbv)	T (K)	RH (%)	$NO_3^-{}_{(p)}$ (µg m^{-3})	$SO_4^{-2}{}_{(p)}$ (µg m^{-3})	$Cl^-{}_{(p)}$ (µg m^{-3})	$PNO_3^-{}_{(p)}$ (µg m^{-3} nt^{-1})^	S_a (µm^2 cm^{-3})	k_{N2O5} 1E-5 (s^{-1})	γ_{N2O5} 1E-4
17th – 18th Jan	6.3	23.8	23.7	290	31.8	8.5	0.70	0.12*	14.9	525.6	1.6	4.76
19th – 20th Jan	3.7	21.3	31.5	290	36.4	14.3	0.93	0.35	14.4	826.5	1.3	2.46
20th – 21st Jan	2.8	15.4	31.3	290	37.9	11.5	0.90	0.12	10.7	515.5	1.3	3.94
21st -22nd Jan	1.5	13.3	41.7	292	30.0	9.9	1.0	0.01	25.3	295.1	5.1	2.70

***** Equal to 1.24 x AMS Cl

^ Overnight particulate nitrate production rate estimated from the difference in the maximum $[NO_3^-{}_{(p)}]$ in the early-morning vertical profile at ~9:30 am and the ground-level $[NO_3^-{}_{(p)}]$ the previous day at 3 pm. The notation nt^{-1} indicates per night.

Table 2-3. VOC concentrations and reactivity with the NO_3 radical.

VOC	Daytime concentration[a] (ppb)	k_{rxn}[b] (cm^3 $molecules^{-1}$ s^{-1})	Reactivity (s^{-1})
α-Pinene	0.06	6.20E-12	9.34E-03
β-Pinene	0.02	2.60E-12	1.21E-03
i-Butene	0.11	3.50E-13	9.78E-04
Isoprene	0.05	7.00E-13	8.64E-04
DMS[c]	0.01	1.10E-12	2.86E-04
trans-2-Butene	0.03	3.50E-13	3.00E-04
cis-2-Butene	0.03	3.50E-13	2.89E-04
Ethanol[c]	2.45	2.00E-15	1.22E-04
Acetaldehyde[c]	5.14	2.60E-15	3.34E-04
1-3-Butadiene[c]	0.03	1.10E-13	9.17E-05
Propene	0.40	9.40E-15	9.29E-05
Methanol[c]	8.52	1.30E-16	2.77E-05
1-Butene	0.08	1.30E-14	2.54E-05
m-Xylene	0.28	2.30E-15	1.64E-05
o-Xylene	0.20	3.90E-15	1.90E-05
1-Pentene	0.03	1.50E-14	1.04E-05
Propane[c]	4.55	7.00E-17	7.97E-06
Ethene	1.73	2.00E-16	8.65E-06
1-2-4-Trimethylbenzene	0.09	1.72E-15	3.81E-06
Ethyne	1.81	1.00E-16	4.53E-06
Others[c]	0.29	2.1E-17	1.52E-07

[a]From canister samples, averaged for the afternoon period

[b]From Calvert et al., *The Mechanisms of Reactions Influencing Atmospheric Ozone*, Oxford University Press, 2015, pp. 130-160.

[c]These VOCs are assumed to react with NO_3 radicals to form HNO_3.

3 INFLUENCES OF EMISSION SOURCES AND METEOROLOGY ON AEROSOL CHEMISTRY IN A POLLUTED URBAN ENVIRONMENT: RESULTS FROM DISCOVER-AQ CALIFORNIA

3.1 Introduction

Ambient aerosols have long been recognized as having adverse effects on human health (Pope and Dockery, 2006) although it is unclear which aerosol property, or properties, are responsible for such effects (Harrison and Yin, 2000). Atmospheric particles can also significantly impact the Earth's climate (Pöschl, 2005) and represent one of largest sources of uncertainty in predicting future climate change (IPCC, 2013), primarily due to the complex nature of the particles. This is in part due to many different components contributing to particulate matter (PM), which have a range of chemical compositions and originate from a large range of sources and processes (Seinfeld and Pandis, 2006a). This is especially true in the case of organic aerosols (OA), which often represent the largest component of the total fine PM mass, contributing up to 90% depending on location (Kanakidou et al., 2005;Zhang et al., 2007a). However, the sources, atmospheric aging, properties, and impacts of OA are not well understood despite being the focus of numerous studies (e.g. Gelencsér et al., 2007;Jimenez et al., 2009;Ng et al., 2010;Ervens et al., 2011).

In addition to effects on human health and climate, aerosols are also known to influence air quality, and elevated PM concentrations are common issues in urban areas due to anthropogenic emissions and meteorological conditions (Watson, 2002). The importance of different emissions and conditions varies with season; increased primary emissions coupled with stagnant conditions in winter result in pollution events, whereas increased photochemical activity during the summer leads to photochemical haze or smog (Goldstein et al., 2009;Martin et al., 2011). The San Joaquin Valley (SJV) in California experiences persistent air quality problems and remains one of the most polluted regions in the US despite many years of regulatory control efforts (e.g. Chow et al., 2006a). Located in central California with mountainous topography, the geographic features of the SJV trap pollutants and subsequently lead to deterioration of air quality, particularly during winter. Consequently, the SJV often exceeds the National Ambient Air Quality Standards (NAAQS) for $PM_{2.5}$ and PM_{10} (particles with aerodynamic diameters less than 2.5 μm and 10 μm, respectively) (Gorin et al., 2006;Lurmann et al., 2006;Ngo et al., 2010). In addition, residents of the SJV suffer the highest rates of cardio-respiratory diseases in the country (Hall et al., 2008;Association, 2015).

Previous studies have shown that the composition of ambient aerosols in Fresno, one of the most populated cities in the SJV, is complex, with organic species representing an important component of PM, often contributing up to two-thirds of the total mass(Chu et al., 2004;Chow et al., 2006a;Turkiewicz et al., 2006;Ge et al., 2012a). Intense urban and agricultural emissions have been found to contribute to both local and regional PM pollution problems in Fresno (Chow et al., 1993;Watson et al., 2000;Sorooshian et al., 2008;Ge et al., 2012a). PM pollution is particularly severe in winter due to a combination of factors including elevated emissions from residential

wood combustion for heating and lower boundary layer height and stagnant conditions that favor the accumulation of PM and secondary aerosol precursors (Brown et al., 2006b). In addition, the typical cold and high humidity weather in the winter promotes gas-to-particle partitioning of semi-volatile species. Regional fog events that enhance aqueous phase formation of sulfate and secondary organic aerosol (SOA) also frequently occur in the area (Collett et al., 1999;Ge et al., 2012a;Herckes et al., 2007;Ge et al., 2012b). The interactions between these factors affect the composition, size, hygroscopicity, and optical properties of wintertime aerosols within the SJV in a complicated and dynamic manner (Ge et al., 2012a;Ge et al., 2012b). Unraveling the various sources and processes affecting the physico-chemical properties of aerosols as well as how these change both temporally and spatially is important to better inform and further develop pollution abatement strategies and to improve parameterizations in air quality models. In particular, detailed information obtained from in situ measurements can facilitate fundamental understanding of processes that influence formation, properties, and transport of atmospheric aerosols and can lead to improvements in our ability to predict how changes in atmospheric composition influence air quality.

As part of the NASA DISCOVER-AQ (Deriving Information on Surface conditions from COlumn and VERtically resolved observations relevant to Air Quality) campaign many aerosol, gas-phase, and meteorological measurements were made during winter 2013 at the ground supersite in Fresno at the Fresno-Garland California Air Resources Board (CARB) monitoring station. The aim of this study was to obtain a comprehensive and detailed understanding of the chemical, microphysical, and optical properties of wintertime aerosols within the SJV and the processes that drive the observed temporal and diurnal variations and vertical distribution of particles over this region. Here we report the results from an Aerodyne High Resolution Time-of-Flight Aerosol Mass Spectrometer (HR-ToF-AMS) which was deployed for the 4-week intensive measurement campaign to characterize size-resolved chemical composition of non-refractory submicron particulates (NR-PM_1) with high time resolution (Canagaratna et al., 2007). In addition to the high-resolution mass spectra and elemental ratios determined by the HR-ToF-AMS (Canagaratna et al., 2015;Aiken et al., 2008), factor analysis of aerosol mass spectra can provide insight into the sources, evolution, and temporal trends of OA (Zhang et al., 2011). In this paper we will discuss the chemical composition of the aerosols at Fresno, particularly the results from analysis of the OA fraction using Positive Matrix Factorization (PMF, Ulbrich et al., 2009) including the detailed chemical composition of the resolved components and their temporal variations to investigate emission sources. Volatile organic compound (VOC) measurements from the Proton Transfer Reaction Time-of-Flight Mass Spectrometer (PTR-TOF-MS) are used to help interpret AMS data and to support the aerosol sources identified from factor analysis. In addition we will also compare results with those obtained from a similar study performed in 2010 to gain insight into the role of meteorology in influencing aerosol chemical composition.

3.2 Materials and Methods

3.2.1 DISCOVER-AQ project

DISCOVER-AQ is a coordinated effort mission combining surface and aircraft based measurements to characterize and understand how aerosols and trace gases evolve throughout the day and across urban areas. The overarching aim of the DISCOVER-AQ project (http://discover-aq.larc.nasa.gov/) is to relate concurrent observations of column abundances to surface concentrations of key gaseous pollutants and aerosols to improve the interpretation of satellite observations and diagnoses of near-surface air quality (http://discover-aq.larc.nasa.gov/pdf/DISCOVER-AQ_science.pdf). One of the objectives is to characterize the differences in diurnal variation of surface and column observations for key trace gases and aerosols. To achieve this goal, gas and particle-phase measurements were made throughout the day from two aircraft and a network of US ground sites that experience diverse meteorological and surface conditions. The factors that contribute to local air quality problems (e.g., emissions, transport, and chemistry) also vary between the sites. Of the two aircraft, the NASA P-3B made daytime measurements close to the ground, at constant altitudes of ~2500 m or ~400 m, or flew in tight spirals to measure vertical profiles throughout the SJV. The vertical profile measurements were made over seven select ground locations, including the Fresno supersite where detailed ground measurements were made to allow for quantitative connections to be made between the surface aerosol concentrations and properties and those observed aloft **(e.g. Pusede et al., 2016)**. Data from the DISCOVER-AQ project is available to the public at: http://www-air.larc.nasa.gov/missions/discover-aq/discover-aq.html.Fresno supersite and instrumentation

Situated approximately 320 km north of Los Angeles, 260 km east of the Pacific Ocean, and 275 km south of Sacramento, Fresno is an ideal location to study the influence of different sources on PM. Therefore, there was a particular focus on aerosol properties and processes in the winter 2013 DISCOVER-AQ campaign which took place from January 13 to February 10. During this time, the weather was cold (average temperature of 7.9 °C) and relatively dry (average RH of 69 %) with frequent sunshine. Comprehensive, real-time measurements of particle composition, size distribution, optical and radiative properties, hygroscopicity, and volatility along with a broad suite of *in-situ* gas-phase and aerosol column measurements were made at the ground supersite at the Fresno-Garland monitoring station of the California Air Resource Board (CARB) (36.7854°, -119.7732°, 97 m a.s.l., **Figure 3-1**a). A wide range of meteorological and air-quality data were also collected routinely by CARB from this site. The Yosemite FWY-41 highway is located approximately 1 km to the west of the sampling site, residential areas surround the site to the north and a commercial area is to the south (**Figure 3-1**b).

Highly time-resolved *in situ* PM measurements at the Fresno supersite provide the data necessary to elucidate aerosol sources and processes and to interpret the comprehensive airborne datasets and remote sensing observations. The setup of the real-time particle instruments deployed at the

Fresno supersite is shown in **Figure 3-1**c. NR-PM_1 chemical composition and speciated size distributions were measured by an Aerodyne HR-ToF-AMS at a time resolution of 2.5 min and measurements of $PM_{2.5}$ water-soluble composition of both inorganic and organic ions, including sulfate, nitrate, nitrite, ammonium, sodium, potassium, formate, and glycolate, were obtained using the Particle Into Liquid Sampler (PILS; Metrohm) coupled with two Ion Chromatography systems (IC) (Parworth et al., In preparation). Black carbon mass concentration and size distribution (between ~100-400 nm volume equivalent diameter) were measured with the single particle soot photometer (SP2; DMT) (Schwarz et al., 2006a), which measures the per-particle mass of refractory BC in individual particles by illuminating particles with high intensity 1064 nm radiation. Further information on the operation and analysis of the SP2 can be found in Zhang et al. (2016a). For VOC analysis an Ionicon high resolution PTR-TOF-MS 8000 (Ionicon Analytik, Austria) was used (Graus et al., 2010;Müller et al., 2013). Particle size distributions were measured with a Scanning Mobility Particle Sizer (SMPS) over the mobility diameter range 8-858 nm (Setyan et al., 2012). The hourly ambient temperature and relative humidity (RH) data as well as trace gas (e.g., CO and NO_2) concentrations were acquired from the CARB website (http://www.arb.ca.gov/html/ds.htm). Solar radiation measurements were obtained from the nearby Clovis site (36.8193°, -119.7164°, 113 m a.s.l.) maintained by the San Joaquin Air Pollution Control District. The solar radiation sensor is a Met One instrument, Model 095, with a broadband spectral response between 285 and 2800 nm. The data reported in this paper are in local time, which is Pacific Standard Time (PST) and 8 h earlier than Coordinated Universal Time (UTC).

The focus of this study is on the measurements from the HR-ToF-AMS (DeCarlo et al., 2006), which was operated in the standard configuration and sampled mass spectra (MS) and particle time of flight (PToF) data downstream of a $PM_{2.5}$ cyclone (URG) (**Figure 3-1**c). Further, the HR-ToF-AMS was operated under 'V' and 'W' ion optical modes, where higher sensitivity but lower mass resolution is achieved in 'V' mode, and lower sensitivity but higher mass resolution is achieved with 'W' mode. Ionization efficiency (IE) and particle sizing calibrations were performed following standard protocols (Canagaratna et al., 2007) on January 13, January 19, and February 8.

3.2.2 Data analysis

3.2.2.1 Basic HR-ToF-AMS data analysis and intercomparisons with collocated measurements

HR-ToF-AMS data were processed and analyzed within Igor Pro (Wavemetrics) using the standard ToF-AMS analysis toolkit software package, SQUIRREL (SeQUential Igor data RetRiEval) v1.56D, and the PIKA module v1.15D (available for download at http://cires.colorado.edu/jimenez-group/ToFAMSResources/ToFSoftware/index.html). The standard fragmentation table described by Allan et al. (2004) was used with some small modifications to process the raw mass spectra. The modifications were based on data from three

filtered air periods during the campaign, which enable the contribution of background gas-phase signal to be estimated and removed from the particle-phase signals. Adjustments made included those to the measured CO_2^+ (*m/z* = 44) signal in order to remove contributions from gas phase CO_2 as well as the $^{15}N^+$ to $^{14}N^+$ ratio for air signals at *m/z* = 29. For improved oxygen-to-carbon (O/C) estimations, there is a need to perform a time-dependent CO_2^+ subtraction (Collier and Zhang, 2013), however, due to high organic aerosol loading during this study, gas-phase contribution represented a minor fraction of the total CO_2^+ signal and using a constant background CO_2^+ subtraction had little influence on the determination of org-CO_2^+ signals. Relative ionization efficiencies (RIE) of 1.05, 1.256, and 3.65 were used for nitrate, sulfate, and ammonium, respectively, and were determined based on calibrations using pure NH_4NO_3 and $(NH_4)_2SO_4$ particles. Although applying a collection efficiency (CE) of 0.5 (default) to whole datasets has been deemed valid for measurements from most ambient environments, several factors, including the relative humidity of the sampling line, ammonium nitrate content, and acidity/neutralization of the sulfate content, have been found to influence the particle phase in the AMS. Consequently, a time- and composition-dependent CE was applied to the data based on the algorithm by Middlebrook et al. (2012). Although nitrate was often observed to be an important component of PM_1 during this study, the campaign average ($\pm 1\sigma$) CE was 0.5 ± 0.04. Quantification of NR-PM_1 species was validated through comparisons between the total PM_1 mass concentration (NR-PM_1 plus BC) and the apparent particle volume concentration from the SMPS (**Figure 3-2**). The AMS total mass-based size distribution compares well with the volume size distribution of the SMPS throughout the day (**Figure 3-3**). Extensive comparisons were also made between the AMS and PILS-IC measurements, where strong correlations were found for nitrate (NO_3^-), sulfate (SO_4^{2-}), ammonium (NH_4^+), and chloride (Cl^-) (Pearson's r of 0.96, 0.94, 0.97, and 0.90, respectively) with orthogonal distance regression fit slopes of 1.26, 1.27, 1.34, and 1.25, respectively (Parworth et al., In preparation). The difference between PILS-IC and AMS measurements is likely because the PILS-IC measures $PM_{2.5}$ and the AMS measures NR-PM_1. Elemental ratios between oxygen (O), carbon (C), hydrogen (H), and nitrogen (N) as well as the organic mass-to-carbon ratio (OM/OC) of OA were determined from analysis of the W mode high resolution mass spectra (HRMS) data following the method reported recently in Canagaratna et al. (2015). This method is an update to the Aiken-Ambient method (Aiken et al., 2008) and is referred to as the Improved-Ambient method. The elemental ratios calculated using both the Aiken-Ambient and Improved-Ambient methods are detailed in **Table 3-1**. The elemental ratios calculated using the Aiken-Ambient method are compared to those calculated using the Improved-Ambient method (**Figure 3-4**) and show high correlation; the slope and r^2 for O/C are 0.76 and 0.995, for H/C are 0.91 and 0.980, and for OM/OC are 0.92 and 0.988. These comparisons are consistent with the average differences for the ratios between the two methods reported in Canagaratna et al. (2015), with increases of 27, 11, and 9 % for O/C, H/C, and OM/OC ratios, respectively. Unless otherwise indicated, the O/C, H/C, and OM/OC ratios stated in this paper from other studies have been calculated using the updated elemental analysis method and are detailed in the Supplement of Canagaratna et al. (2015) (**Table 3-1** and **Table 3-2**). This updated method reproduces ratios that are within 28% for O/C

and 13% for H/C of the known molecular values of individual oxidized standards. The precision of these measurements, however, is much higher, with good mass spectral precision between different AMS instruments. Further, AMS mass spectra of structurally stable compounds are highly comparable to those in the NIST database.

3.2.2.2 Positive Matrix Factorization (PMF) of HR-ToF-AMS Organic Spectra

PMF analysis was performed using the PMF2 algorithm in robust mode (Paatero and Tapper, 1994) and conducted using the PMF Evaluation Toolkit (PET) v2.05 (Ulbrich et al., 2009) downloaded from http://cires1.colorado.edu/jimenez-group/wiki/index.php/PMF-AMS_Analysis_Guide#PMF_Evaluation_Tool_Software. The data and error matrices were prepared according to the protocol as described by Ulbrich et al. (2009) and outlined in Zhang et al. (2011). In brief, a minimum error value was added to the error matrix and ions were assessed and treated according to their signal-to-noise ratio (SNR); ions with a SNR less than 0.2 were removed and those with a SNR between 0.2 and 2 were downweighted by increasing their errors by a factor of 2. Further, ions related to *m/z* 44 (CO_2^+) were also downweighted so as to not overestimate the contribution of CO_2^+. Finally, isotopes were not included in the matrices as their signals are scaled to their parent ions rather than being measured directly. The resulting matrix therefore consisted of ions between *m/z*'s 12 and 120.

PMF was applied to the data and the number of factors (*p*) in the solution was explored from 1 up to 9. However, as the number of factors in the real dataset is unknown and the PMF algorithm is able to provide a number of mathematically sound solutions which could be deemed physically meaningful, several criteria are used to carefully evaluate and select the appropriate number of factors from the model. As this is one of the most critical aspects of PMF analysis, the recommendations outlined in Zhang et al. (2011), including investigation of the key diagnostic plots, mass spectral signatures, diurnal profiles, and correlations with external tracers, were followed to assess the quality and suitability of a solution set.

Within the PMF analysis toolkit, there are several diagnostics that can be used to aid the choosing of the best modeled number of factors including Q and f_{Peak}. Q is the quality of fit parameter and the ratio of the expected Q (Q/Q_{exp}) indicates how well the model fit the data; as the number of factors in a solution increase, the degrees of freedom increase and Q/Q_{exp} decreases close to 1 as more data are able to be fit. The f_{Peak} parameter is used to demonstrate the variation of the solutions and can indicate the rotational stability of the solution sets. Negative f_{Peak} values result in variations in the time series and positive values result in variations in the mass spectra of the solutions. However, the solution set is most likely to be physically meaningful when f_{Peak} is zero (Paatero et al., 2002). In this study, the rotational stability of each of the solution sets were explored through the f_{Peak} parameter from -1 to 1, with an increment of 0.1. The 6-factor solution with f_{Peak} 0 (Q/Q_{exp} = 2.85) was chosen for further analyses as the solution was deemed robust and representative as it satisfied the above criteria including good separation of the temporal and mass spectral variations of the six factors. A summary of the key diagnostics is presented in **Figure 3-5** and a comparison

of the factor mass spectra with reference mass spectra, including those determined from a campaign in Fresno in winter 2010, are listed in **Table 3-2**. The 6-factor solution was found to be very stable as the mass fraction of each of the factors remained relatively constant between f_{Peaks} -0.4 and +1, inclusive (**Figure 3-5**c). Figure S5 shows the mass spectra and time series of the 5- and 7-factor solutions. Factors 5 and 2 in the 5-factor solution set could be identified as hydrocarbon-like OA (HOA) and cooking OA (COA), respectively, but are more oxidized than similar factors from previous studies, possibly due to mixing of factors with an oxygenated OA (OOA) factor, thus implying the factors could be further separated. In contrast, the temporal variations of several factors are similar in the 7-factor solution set, indicative of factor splitting. In addition, three potential oxygenated OA (OOA) factors are identified in the 7-factor solution (Factors 1, 2, and 4), but the mass spectrum of Factor 2 appears to be a combination of the other two factors. Further, Factor 4 is predominantly composed of *m/z* 43, which is unlikely to be physically real. Consequently, the 6-factor solution, including two biomass burning OA (BBOA) and two OOA factors, was deemed the best solution to represent the organic aerosols in this study.

3.2.2.3 Estimation of the OA factor size distributions

Size distributions can provide some insight into the nature of the aerosol such as whether they are primary or secondary in nature and if they have likely undergone aqueous-phase processing. The size distributions of each of the OA factors from PMF analysis were therefore determined using a multivariate linear regression algorithm defined as:

$$ms_{t,i} = \sum_{p=1}^{n} ms_p \times c_{p,t,i} \qquad \text{(Eq. 1)}$$

where $ms_{t,i}$ is the measured mass spectrum of organics in unit mass resolution (UMR) for time period t and size bin i, ms_p is the UMR mass spectrum of the factor p from PMF analysis of the OA HRMS, and $c_{p,t,i}$ is the corresponding fitting parameter. This algorithm decomposes the mass spectra of OA corresponding to individual size-bins into the linear combination of the unit mass resolution mass spectra of the n number of factors determined from PMF analysis of the HRMS, assuming the spectral profile of each factor in different size bins is constant.

In this study, all mass spectra consist of *m/z*'s 12 to 120 amu. The measured organic mass spectral matrix is size-resolved for the whole measurement period over the size range 40-1200 nm and to improve the signal to noise ratio the matrix was averaged into 23 size bins. This input data vector, $ms_{t,i}$, was also normalized to the average OA mass spectrum from high resolution analysis prior to being linearly decomposed. For this analysis only 4 main OA factors were used (HOA, COA, BBOA, and OOA), as a more robust result was obtained compared to when all six individual factors were used. The mass spectra of the two BBOA factors were summed according to the contribution of each of the two factors to total BBOA mass and the time series were summed prior to linear decomposition. The semi-volatile OOA (SV-OOA) and low volatility OOA (LV-OOA) factors were treated in the same way to produce a total average OOA mass spectrum and time series. A summary of the key diagnostics from the fitting is presented in **Figure 3-7**, where it can

be seen that for each size bin there is good agreement between the reconstructed OA and the measured OA (r = 0.9993, **Figure 3-7**a). Furthermore, the mass-weighted size distributions of the four OA factors, which are normalized to their corresponding mass concentrations, compare well with that of the total organics (**Figure 3-7**d).

3.2.2.4 Calculation of the ammonium nitrate gas-to-particle partitioning equilibrium constant

The oxidation of nitrogen dioxide (NO_2) in the atmosphere forms nitric acid (HNO_3), which tends to remain in the gas phase when there is limited availability of ammonia (NH_3). However, when sufficient NH_3 is available (e.g. Lurmann et al., 2006), as is the case in the SJV, HNO_3 reacts with NH_3 to form particulate NH_4NO_3 (Eq. 2).

$$NH_3(g) + HNO_3(g) \leftrightarrow NH_4NO_3(s) \qquad \text{(Eq. 2)}$$

The partitioning between the gas and particle phases depends strongly on the ambient temperature and the equilibrium constant K_{AN} of Eq. 2 can be calculated as:

$$K_{AN} = K_{AN}(298)exp\left\{a\left(\frac{298}{T} - 1\right) + b\left[1 + \ln\left(\frac{298}{T}\right) - \frac{298}{T}\right]\right\} \qquad \text{(Eq. 3)}$$

where T is the ambient temperature in Kelvin, $K_{AN}(298) = 3.36 \times 10^{16}$ (atm^{-2}), $a = 75.11$, and $b = -13.5$ (Seinfeld and Pandis, 2006a).

3.2.2.5 Derivation of the HNO3 production rate

Overnight, NO_2 and O_3 react to form N_2O_5, which can react heterogeneously to form HNO_3. The equations governing the nighttime formation of N_2O_5, nitrate radical (NO_3), and HNO_3 are:

$$NO_2 + O_3 \rightarrow NO_3 + O_2 \qquad \text{(Eq. 4)}$$

$$NO_3 + NO_2 \rightarrow N_2O_5 \qquad \text{(Eq. 5a)}$$

$$N_2O_5 \rightarrow NO_2 + NO_3 \qquad \text{(Eq. 5b)}$$

$$N_2O_5 + H_2O\ (het) \rightarrow 2HNO_3 \qquad \text{(Eq. 6)}$$

From Equations 4 – 6, the formation rates of NO_3, N_2O_5, and HNO_3 can be derived as follows:

$$\frac{d[NO_3]}{dt} = -k_{5a}[NO_2][NO_3] + k_{5b}[N_2O_5] + k_4[NO_2][O_3] \qquad \text{(Eq. 7)}$$

$$\frac{d[N_2O_5]}{dt} = -k_6[N_2O_5] - k_{5b}[N_2O_5] + k_{5a}[NO_2][NO_3] \qquad \text{(Eq. 8)}$$

$$\frac{d[HNO_3]}{dt} = k_6[N_2O_5] \qquad \text{(Eq. 9)}$$

If one assumes that N_2O_5 and NO_3 are both in steady state (Brown et al., 2006e), the net production rates for both species should be zero thus their steady-state concentrations are:

$$[NO_3]_{SS} = \frac{k_{5b}[N_2O_5]+k_4[NO_2][O_3]}{k_{5a}[NO_2]} \qquad \text{(Eq. 10)}$$

$$[N_2O_5]_{SS} = \frac{k_{5a}[NO_2][NO_3]}{k_6+k_{5b}} \qquad \text{(Eq. 11)}$$

By combining Equations 9 – 11, we found that both the steady-state concentration of N_2O_5 and the nighttime production rate of HNO_3 are proportional to the product of the concentrations of NO_2 and O_3:

$$[N_2O_5]_{SS} = \frac{k_4}{k_6}[NO_2][O_3] \qquad \text{(Eq. 12)}$$

$$\frac{d[HNO_3]}{dt} = k_4[NO_2][O_3] \qquad \text{(Eq. 13)}$$

3.3 Results and discussion

3.3.1 Temporal and diurnal variations of PM_1 composition and size distribution

Frequent PM pollution events were observed at Fresno during DISCOVER-AQ; PM_1 concentrations exceeded the 24-hour NAAQS for $PM_{2.5}$ (35 μg m^{-3}) on 50% of the days (**Figure 3-8**). $PM_{2.5}$ concentrations are estimated to be approximately 25% greater than PM_1 (Parworth et al., In preparation) thus it is likely that $PM_{2.5}$ concentrations violated these standards for two-thirds of the campaign. Between January 13 and February 11, 2013 the average PM_1 concentration was 31.0 μg m^{-3}, with a maximum concentration of 130 μg m^{-3} measured on 14 January (**Figure 3-8** and **Table 3-3**). OA contributed, on average, 55% to the total PM_1 mass, representing the largest component, followed by NO_3^- (27%), with smaller contributions from NH_4^+ (9%), BC (5%), SO_4^{2-} (3%), and Cl^- (1%) (**Figure 3-9**a and **Table 3-3**). In addition, the molar equivalent ratios of total inorganic anions to ammonium (= (SO_4^{2-}/48 + NO_3^-/62 + Cl^-/35.5) / (NH_4^+/18)) were close to 1, indicating the presence of neutralized inorganic aerosols in the form of ammonium salts during the campaign (Zhang et al., 2007b).

Diurnal patterns and particle size distributions can offer insight into aerosol sources, formation processes, and behavior. During this study, high OA and BC concentrations occurred overnight, with maximum concentrations usually observed at 22:00 PST (**Figure 3-10**a and b), associated with a shallow boundary layer (BL) coupled with enhanced emissions from activities such biomass burning for residential space heating. In addition, a smaller morning peak (~7:00-8:00 PST) is observed in the diurnal profiles of BC and can be associated with morning traffic rush hour. Conversely, daily variations in inorganic species concentrations were similar, with a sharp increase between 08:00-10:00 PST and peaking around midday (**Figure 3-10**c-f), suggesting they have

similar sources. This daytime peak in concentrations is consistent with previous observations (Brown et al., 2006b;Lurmann et al., 2006) and has been attributed to the mixing down of secondary aerosols formed at night in a residual layer aloft associated with BL dynamics (Watson and Chow, 2002a, b;Chow et al., 2006a;Pusede et al., 2016). During this study, BL heights were estimated to range between 300-700 m (Pusede et al., 2016).

In terms of mass-based size distributions, OA exhibited a broad size distribution, peaking between 350-450 nm in vacuum aerodynamic diameter (D_{va}) (**Figure 3-9**b). The mode of OA size distribution varied as a function of time of day (**Figure 3-10**g and **Figure 3-11**a); a narrower size distribution peaking at ~ 400 nm is observed during the day with a broadening and shifting to smaller sizes from the evening and into the morning. Nitrate, sulfate, and ammonium all peaked in size close to D_{va} of 500 nm (**Figure 3-9**b) and the peak size varied little across the day (**Figure 3-10**h-j and **Figure 3-11**b-d). Differences in size distribution patterns between the organic and inorganic species suggest that the formation of secondary inorganic species were influenced by aqueous-phase processes, consistent with findings from a previous study in Fresno (Ge et al., 2012b). Both primary and secondary aerosols contribute to the broad size distribution of organics, with anthropogenic primary emissions predominantly from fossil fuel and biomass combustion emissions influencing the distribution in the morning and evening and secondary formation influencing the daytime size distributions.

3.3.2 Organic aerosol characteristics and source apportionment

3.3.2.1 Bulk composition and elemental ratios of organic aerosol

Organic aerosols are a complex mixture of hundreds of carbon-containing compounds that are emitted from different sources and have undergone different atmospheric processes. OA exhibit a range of properties and subsequently will have a number of impacts on air quality, human health, and climate. Understanding the elemental composition of OA and separating the organic fraction into its various components are important in order to gain insight into the sources and atmospheric processing of particulate organics as well as the behavior and characteristics of the aerosols.

In winter 2013 at Fresno the OA fraction was found to be composed of approximately 68% carbon, 23% oxygen, 8% hydrogen and 1% nitrogen (**Figure 3-12**a). The average carbon-normalized molecular formula of OA was $C_1H_{1.7}O_{0.42}N_{0.017}S_{0.0004}$, yielding an average OM/OC of 1.71. The O/C and H/C atomic ratios (**Table 3-1**) are similar to revised values observed at other urban locations (Canagaratna et al., 2015 and references within). The influence of anthropogenic emissions is evident in the diurnal profile of the H/C ratio (**Figure 3-12**b), which exhibits peaks at 08:00 and 20:00 PST, likely reflecting the morning and evening rush hours as well as evening meal times and residential heating. However, compared to nighttime, higher O/C and lower H/C ratios were observed during a large part of the day suggesting that production of secondary organic aerosol (SOA) was prevalent during the day and outweighed emissions of primary organic aerosol (POA), with the converse true in the evening. The diurnal profile of the nitrogen-to-carbon (N/C)

ratio is relatively similar to that of the O/C ratio suggesting that although nitrogen-containing organic ions are scarce, the majority of the N in OA is likely associated with SOA in this study.

The largest component of the OA mass spectral signal was found to be the $C_xH_y^+$ ion family (47%, **Figure 3-12**a), followed by the $C_xH_yO_1^+$ (31%) and $C_xH_yO_2^+$ (15%) ion families and smaller contributions from the $C_xH_yN_p^+$ (3%), $C_xH_yN_pO_z^+$ (2%), and $H_yO_1^+$ (2%) ion families. The largest peak in the average OA spectrum is at *m/z* 43 (**Figure 3-12**c), accounting for 8% of the total OA signal with a composition of 71% $C_2H_3O^+$, 27% $C_3H_7^+$, 1% $CHON^+$, and 1% $C_2H_5N^+$. The second largest peak in the average OA spectrum is *m/z* 44, which is dominated by the CO_2^+ ion (84%). The peak at *m/z* 60 is composed almost entirely of $C_2H_4O_2^+$ (98%) and 88% of the peak at *m/z* 73 is composed of $C_3H_5O_2^+$. The strong signals at *m/z*'s 60 and 73 are of particular interest as they are known fragment ions in the electron impact mass spectrum (EI-MS) of levoglucosan and anhydrous sugars, which are all tracers of biomass burning aerosol (Alfarra et al., 2007;Aiken et al., 2008). *m/z* 57, which is used as a tracer for HOA for urban datasets (Zhang et al., 2005a) and noted as a main fragment ion of levoglucosan (Schneider et al., 2006), is composed predominantly of $C_4H_9^+$ (50%) and $C_3H_5O^+$ (48%) in this study.

Separation of the organic fraction into its components can be achieved through the application of multivariate models such as PMF (Lanz et al., 2007;Ulbrich et al., 2009;Zhang et al., 2011). In this study, six OA factors were identified from PMF analysis of the high resolution organic mass spectra consisting of four POA factors (HOA, COA, BBOA1, and BBOA2) and two SOA factors (LV-OOA and SV-OOA). An overview of the chemical composition and temporal variations of the six factors is shown in **Figure 3-13**. LV-OOA (24%) represents the largest fraction of OA mass and the smallest faction of OA is accounted for by HOA (9%). COA, BBOA1, BBOA2, and SV-OOA, on average, account for 18, 13, 20, and 16% of the total OA mass, respectively. On average, the primary components together account for ~60% of the total OA mass in Fresno during winter 2013 (**Figure 3-13**s) and LV-OOA accounts for ~60% of the total SOA mass. The chemical composition, size distribution, and temporal variations of each factor are discussed in detail in sections 3.3.2.2-3.3.2.5.

3.3.2.2 Hydrocarbon-like OA (HOA)

The O/C ratio of the HOA in this study is low (0.09) whereas the H/C ratio is very high (2.10) indicating that chemically reduced hydrocarbon species dominate the composition. This is confirmed by the HOA mass spectrum which is dominated by the $C_xH_y^+$ ion family (85%, **Figure 3-13**a), with major peaks at *m/z*'s 41, 43, 55, and 57 that comprise signals from the $C_3H_5^+$, $C_3H_7^+$, $C_4H_7^+$, and $C_4H_9^+$ ions, respectively. These major peaks and the overall picket fence fragmentation pattern resulting from the $C_nH_{2n+1}^+$ ions are typical in HOA mass spectra from other studies due to the association of these aerosols with fossil fuel combustion activities (e.g. Zhang et al., 2005a;Lanz et al., 2008;Sun et al., 2011;Ge et al., 2012a). In this study, the HOA mass spectrum agrees well with those from vehicle emission studies (e.g. r = 0.92-0.98 for the correlations with spectra from Collier et al., 2015) (**Figure 3-14**). HOA exhibits a relatively broad size distribution

and peaks at the smallest size of all the OA factors at around 190 nm (**Figure 3-13**u). The largest contribution of HOA to total OA is in the ultrafine mode (< 100 nm; **Figure 3-13**v), which is the size associated with aerosols from combustion activities (Zhang et al., 2005a;Drewnick et al., 2004;Alfarra et al., 2004).

Strong correlations are observed between the time series of HOA and the $C_nH_{2n\pm1}^+$ ions, e.g., $C_3H_7^+$ (r = 0.92), $C_4H_7^+$ (r = 0.90), $C_4H_9^+$ (r = 0.95) and $C_5H_{11}^+$ (r = 0.96) (**Table 3-4**). The time series of HOA correlates well with tracers for vehicular emissions, particularly aromatic species such as benzene and toluene (r = 0.83 and 0.75, respectively; **Figure 3-13**g and **Table 3-4**). Polar plots showing the concentration of a pollutant as a function of wind speed and direction also suggest similar local sources for HOA, benzene, and toluene as they have similar spatial distributions with the highest concentrations at low wind speeds (**Figure 3-15**). The association of HOA and traffic is further supported by the diurnal profile of HOA, as shown in **Figure 3-13**m, where concentrations peak at times corresponding to rush hour traffic. However, the morning peak at 07:00 PST is slightly earlier than that from a similar campaign performed in a nearby location in winter 2010 (Ge et al., 2012a), where the morning peak was observed between 08:00-10:00 PST. The evening peak is also relatively broad in the current study (18:00-00:00 PST) with a maximum at 22:00 PST, which is later than expected for a peak in rush hour traffic so may indicate that lower BL heights result in enhanced HOA concentrations at night.

3.3.2.3 Cooking OA (COA)

The COA in this study has an O/C ratio of 0.19, which is lower than the revised O/C ratio for COA in Barcelona (0.27) and New York City (0.23)(0.23, Sun et al., 2011) but is higher than the COA identified in Fresno in 2010 (0.14) (**Table 3-6**). The OM/OC ratio is 1.42 and the H/C ratio is 1.90. The mass-based size distribution of COA peaks in the accumulation mode at approximately 400 nm (**Figure 3-13**u), greater than that of HOA and consistent with previous observations of COA size distributions (e.g. Canagaratna et al., 2004;Ge et al., 2012a) although a wide range of sizes of particles emitted from cooking activities can be observed due to the different methods of cooking, ingredients used, and distances from the cooking source. Compared to the other OA factors, the fractional contribution of COA to total OA does not vary as dramatically with size (**Figure 3-13**v).

COA has been observed to be an important component of ambient aerosols in many urban locations (Allan et al., 2010;Sun et al., 2011;Mohr et al., 2012;Crippa et al., 2013) where *m/z*'s 55, 57, 41, and 43 have been used as key *m/z*'s to identify the presence of aerosols from cooking related activities. In addition, Sun et al. (2011) suggested that $C_5H_8O^+$, $C_6H_{10}O^+$, and $C_7H_{12}O^+$ are likely good tracer ions for COA. As the main peaks in the COA spectrum are also important in HOA, Mohr et al. (2012) developed a method for estimating COA in ambient datasets to a first order based on fractions of the organic signals at *m/z*'s 55 and 57. When HRMS data are available the $C_3H_3O^+$ and $C_3H_5O^+$ ions at *m/z*'s 55 and 57 may be used; $C_3H_3O^+$ is typically observed to dominate the signal at *m/z* 55 compared to $C_4H_7^+$ in COA with the converse true for HOA. However, BBOA and OOA can also contribute to the signal at *m/z* 55 and in this study the total

BBOA contributes 34% to the $C_3H_3O^+$ ion (BBOA1 = 13%, BBOA2 = 21%), whereas COA only contributes 29% (**Figure 3-16**) thus the method to distinguish between HOA and COA developed by Mohr et al. (2012) may therefore not be particularly useful here due to the influence from BBOA. However, COA contains a greater proportion of oxygen-containing ions such as $C_xH_yO_1^+$ and $C_xH_yO_2^+$ than HOA which contribute a total of 29.5% to COA and only 10.5% to HOA (**Figure 3-17**).

The diurnal pattern of COA exhibits a large evening peak, with a maximum concentration at 19:00 PST which gradually decreases during the night (**Figure 3-13**n). The evening peak is likely associated with dinnertime cooking activities, although this could be enhanced due to influences from residential wood combustion activities. As the COA from a campaign in Fresno during winter 2010 (Ge et al., 2012a) appears to be less influenced by BBOA, the COA mass spectrum from Ge et al. (2012a) is used to estimate the contribution of BBOA to COA in 2013. The resulting mass spectrum exhibits characteristics of BBOA (**Figure 3-18**a) and contributes approximately 20% to COA in 2013. The diurnal profile of COA with the estimated BBOA influence removed is compared to that of the COA retrieved from PMF analysis (**Figure 3-18**b); the concentrations during the night are reduced in the profile without the BBOA influence but a lunchtime peak is still not evident in 2013. Nevertheless, the time series of COA correlates well with the $C_3H_3O^+$ (r = 0.88) and $C_7H_{12}O^+$ (r = 0.94) ions (**Figure 3-13**h and **Table 3-4**) as well as with $C_6H_{10}O^+$ (r = 0.92) and $C_5H_8O^+$ (r =0.94). COA also contributes 56%, 69%, and 64% to the $C_5H_8O^+$, $C_6H_{10}O^+$, and $C_7H_{12}O^+$ ions, respectively (**Figure 3-16**). These observations thus support the identification of this factor as COA.

3.3.2.4 Biomass burning OA (BBOA1 and BBOA2)

Residential space heating is recognized as an important source of aerosols in many locations, especially in urban locations where BBOA and solid fuel OA (SFOA) factors have been identified in source apportionment studies (Aiken et al., 2009;Mohr et al., 2012;Young et al., 2015a;Young et al., 2015b;Allan et al., 2010;Ge et al., 2012a;Lanz et al., 2007;Xu et al., 2015). BBOA is typically associated with wood combustion and is prevalent during the winter in the SJV (Chow et al., 2006a;Chen et al., 2007;Ge et al., 2012a). The importance of biomass burning emissions in this area is further highlighted as two BBOA factors were derived from PMF analysis of OA, together contributing 33% to the total OA. According to the polar plots showing potential source influences, high concentrations of both BBOA1 and BBOA2 occur at low wind speeds (**Figure 3-15**) indicating emissions likely arise from similar local activities rather than being transported to the site. This is further indicated by the mass-based size distribution of total BBOA, which is more similar to that of HOA than the OOAs. The total BBOA size distribution peaks in the accumulation mode, at 220 nm (**Figure 3-13**u). In addition, BBOA dominates the mass fraction of OA at small sizes, particularly at $100 < D_{va} < 200$ nm (**Figure 3-13**v), supporting the association of these aerosols with combustion activities.

As the chemical composition of ambient BBOA is found to be highly variable (DeCarlo et al., 2010;Parworth et al., 2015), multiple BBOA factors identified from factorization analyses could represent differences in the degree of atmospheric processing (e.g. Brito et al., 2014), combustion conditions (e.g. Young et al., 2015b), and fuel types. Both BBOA mass spectra contain enhanced biomass burning tracer peaks at *m/z* = 60 (mostly $C_2H_4O_2^+$) and 73 (mostly $C_3H_5O_2^+$) (**Figure 3-13**c and d) but *m/z* = 60 and 73 contribute less to the total BBOA1 signal (1.6% and 0.95%, respectively) than to the total BBOA2 signal (5.8% and 2.5%, respectively). This difference is particularly evident when the two factors are plotted in the triangular space used to investigate the BBOA evolution proposed by Cubison et al. (2011) (**Figure 3-19**a). BBOA2 also has a higher O/C ratio than BBOA1 (0.60 vs. 0.33; **Figure 3-13**c and d), whereas the $C_xH_y^+$ ion family contributes more to BBOA1 than BBOA2 (57.6% vs 34.3%; **Figure 3-17**). The difference in oxidation (indicated by the O/C ratio) and f_{60} between the factors could therefore suggest different burning behaviors or fuel type. Indeed, a wide range of O/C ratios for primary organic emissions from biomass burning has been observed in various studies (0.15-0.60 e.g. Heringa et al., 2011;Ortega et al., 2013) due to differences in burner type, combustion phases, and fuel types.

The time series of BBOA1 and BBOA2 are compared with those of wood burning relevant species frequently used in the literature (Simoneit et al., 1999;Jordan et al., 2006;Otto et al., 2006;Aiken et al., 2009). Tracers such as acetonitrile are external measurements and are independent of the BBOA identification from PMF analysis whereas org60 is measured by the AMS and is used to identify BBOA factors. However, some biomass burning tracers measured by the AMS, such as polycyclic aromatic hydrocarbons (PAHs), are independent of the BBOA identification; PAHs are at *m/z*'s greater than 200 and PMF in this study was only performed on *m/z*'s up to 120. BBOA1 correlates well with nitrogen-containing ions (**Table 3-4**), particularly $C_3H_7N^+$ (r = 0.74) and CHN^+ (r = 0.69) (**Figure 3-13**i), consistent with emissions of nitriles from biomass burning and combustion activities (Simoneit et al., 2003), although BBOA2 correlates more strongly with acetonitrile than BBOA1 (r = 0.61 vs. r = 0.43), with similar polar plots of both factors and acetonitrile (**Figure 3-15**). BBOA2 also has stronger correlations than BBOA1 with other biomass burning tracer species, including potassium (r = 0.86) and BC (r = 0.79). Often used as tracers for biomass burning activities, PAHs are byproducts of incomplete combustion, many of which are mutagenic and carcinogens (Hannigan et al., 1998;Marr et al., 2006;Dzepina et al., 2007). Using the method described in Dzepina et al. (2007), total PAHs were estimated from the AMS; a stronger correlation is observed between BBOA2 and PAHs than BBOA1 (r = 0.87 compared to r = 0.61). Consequently, adverse health effects associated with biomass burning emissions should be of great concern, especially during wintertime.

Both BBOA1 and BBOA2 have similar diurnal trends, with concentrations increasing overnight and low concentrations during the day. This diurnal behavior provides strong confidence that BBOA is associated with residential wood combustion for space heating. However, BBOA2 has a more distinct diurnal profile (**Figure 3-13**o), with an especially large difference between daytime and nighttime concentrations, whereas the difference in BBOA1 concentrations between the day

and night is not as large (**Figure 3-13**p). Further, the greatest BBOA1 concentration occurs at the beginning of the campaign (Figs. 6i and j), which coincides with particularly low ambient temperatures (**Figure 3-8**a). To investigate the influence of meteorology (in particular, temperature), the campaign is split into two periods: Period 1 covers the beginning of the campaign up until 20 January and Period 2 covers the remainder of the campaign. The first period was found to be colder than the rest of the campaign with an average temperature of 5.5 °C and a minimum of -4.1 °C compared to an average of 8.7 °C and a minimum of -0.3 °C for Period 2. During this first period, BBOA1 contributes up to 60% to the total OA mass and averages 25% whereas BBOA2 only contributes an average of 15% to OA mass (**Figure 3-8**g). BBOA is observed to dominate the composition of PM_1 at low temperatures during the campaign (**Figure 3-20**a); BBOA1 contributes 22% and BBOA2 contributes 14% at the very coldest temperatures, which occur over night and peak in the early morning (**Figure 3-20**b). As this first period was particularly cold there may have been an increase in residential wood burning. Given these observations of differences in the temporal trends and the associated meteorological differences, it is likely that the two factors are associated with different burning behaviors, although we are unable to fully explain the differences between the two BBOA factors in terms of their sources.

3.3.2.5 Low volatility and semi-volatile oxygenated OA (LV-OOA and SV-OOA)

Two oxygenated OA (OOA) factors were identified in this study, together accounting for 40% of the total OA mass (**Figure 3-13**s). The mass spectra of both factors contain two major peaks at CO_2^+ ($m/z = 44$) and $C_2H_3O^+$ ($m/z = 43$) (**Figure 3-13**e and f). Following analysis of thermodenuder data (not reported here), the more oxidized OOA (O/C = 0.90; H/C = 1.57) is labeled as low volatility OOA (LV-OOA) and the less oxygenated factor (O/C = 0.63; H/C = 1.70) is labeled as semi-volatile OOA (SV-OOA). The O/C ratio of SV-OOA is higher than HOA and COA and the O/C ratio of LV-OOA is significantly higher than those of the POA factors, consistent with observations that ambient primary OA tend to be less oxidized than secondary OA.

The secondary nature of OOA is further supported by the mass-based size distribution of the total OOA (**Figure 3-13**u), which is similar to that of the secondary inorganics (**Figure 3-9**b). The total OOA size distribution is the narrowest of all the OA factors and peaks at the largest D_{va} in the accumulation mode (~460 nm), similar to that of OOA from 2010 (Ge et al., 2012a). The mass fraction of OOA increases with increasing particle size (**Figure 3-13**v), contributing more than 50% to the total OA mass at sizes greater than approximately 500 nm.

The f_{44} vs. f_{43} space (Ng et al., 2010) is frequently used to describe and explain OA evolution in the atmosphere. In this study, LV-OOA falls within the region previously identified by Morgan et al. (2010) as corresponding to LV-OOA (**Figure 3-19**b) and, although located outside of the triangle, SV-OOA still falls within its respective region. All four POA factors identified in this study are located at the bottom left of the triangle thus are far from the two SOA factors, highlighting the differences in sources and precursors (as suggested by the f_{43} values) and degree of oxygenation (as inferred from the f_{44} values) between POA and SOA. Methanesulfonic acid

(MSA) has been shown to be secondary in previous studies and is mostly the product of dimethyl sulfide (DMS) oxidation (von Glasow and Crutzen, 2004). The AMS has successfully measured MSA in several studies, both over the ocean as well as in urban areas (Ge et al., 2012b;e.g. Phinney et al., 2006;Zorn et al., 2008). Consequently, the secondary nature of SV-OOA and LV-OOA is further supported by strong correlations observed with the AMS spectral ions for MSA (**Table 3-4**): $CH_2SO_2^+$ (r = 0.80 and 0.47 for SV-OOA and LV-OOA, respectively), $CH_3SO_2^+$ (r = 0.81 and 0.45), and $CH_4SO_2^+$ (r = 0.77 and 0.44).

The regional versus local nature of SOA is often inferred from correlations with various tracers. As detailed in **Table 3-4**, SV-OOA and LV-OOA correlate relatively strongly with nitrate (r = 0.88 and 0.59, respectively) and sulfate (r = 0.74 and 0.64, respectively). Sulfate is typically observed to be regional and nitrate is often formed more locally due to the emission patterns of their respective precursor gases thus SV-OOA is likely more local whereas LV-OOA is likely to be more regional. Compared to the POA factors, which have local sources, the highest SOA concentrations are found at a larger range of wind speeds and directions (**Figure 3-23**), however SV-OOA appears to be influenced more by local emissions or events as high concentrations are associated with a smaller range of wind speeds and directions than LV-OOA. The diurnal profiles of SV-OOA and LV-OOA are similar with a mid-morning peak in concentration (10:00-11:00 PST, **Figure 3-13**q and r) yet the trend is more distinct for SV-OOA as LV-OOA concentrations are more constant throughout the day. These observations indicate the fresher, more localized nature of SV-OOA and the more aged and regional nature of LV-OOA.

The fractional contribution of SOA to total OA mass is greatest during the day whereas POA dominates in the evening until mid-morning (**Figure 3-13**t), indicating the influence of boundary layer dynamics, local anthropogenic emissions, and photochemical activity. Furthermore, the contribution of LV-OOA to total OA mass also increases during two distinct periods of the campaign (24-28 January 2013 and 5-9 February 2013) (**Figure 3-8**g) although the total organic aerosol concentration is relatively low. These periods are characterized by an average RH of 80%. Furthermore the RH is greater than 90% for 15% of this time compared to a frequency of only 0.4% for the other times suggesting that aqueous-phase processing may have influenced the production of secondary aerosol species (Dall'Osto et al., 2009;Ge et al., 2012b), leading to increased LV-OOA concentrations during humid periods.

3.3.3 Comparison of weekday and weekend diurnal profiles and insights into PM sources

Diurnal profiles can provide insight into aerosol sources as well as atmospheric processes and dynamics. As many aerosol sources can be anthropogenic, comparing the diurnal profiles between the weekdays and weekends can help to separate the influence of different sources and processes on the temporal variations in the aerosol concentrations. Weekdays can be considered to be Monday to Friday, inclusive, with Saturday and Sunday being weekends. However, as the

concentrations of some species, particularly secondary species like nitrate, may be controlled by emissions from the previous day (e.g. NO_x), an alternative classification where Tuesday to Friday, inclusive, were considered weekdays and only Sunday as a weekend (**Figure 3-21**a and b) was also used for examining the diurnal profiles. Since little difference in the trends is observed in the diurnal profiles between the two classifications, the Monday-Friday and Saturday-Sunday definitions are used for the following analyses.

The weekday and weekend diurnal profiles for PM_1 species, the six OA factors from PMF analysis, several VOC species as well as various gas phase species and meteorological parameters are shown in **Figure 3-22** (also see **Figure 3-23**). As expected, the diurnal variations in meteorology do not change significantly from the weekdays to the weekends. The diurnal pattern of COA only varies slightly between weekdays and weekends; weekend concentrations are slightly higher than those during the week, which could be due to people continuing their cooking activities longer into the evenings. Similarly, BBOA2 differs a little between the weekdays and weekends, with slightly higher concentrations in the evenings at weekends. Acetonitrile exhibits similar diurnal variations to that of BBOA2. In contrast, the concentration of BBOA1 is greater during the week than during the weekend, with concentrations approximately a factor of 2 greater, particularly during the morning. However, these results are likely skewed by the first week of particularly cold temperatures, which is evident when the diurnal profiles for the weekdays and weekend days for the first week are compared with those from the remaining three weeks (**Figure 3-24**). Such temperatures likely lead to an increase in burning activities. Biomass burning likely influences chloride concentrations, as is evident from the similarity of the diurnal profiles as well as the strong correlations between chloride and total BBOA ($r = 0.58$, **Table 3-4**) and biomass burning tracers potassium and acetonitrile ($r = 0.67$ and 0.51, respectively. Not shown here).

Differences in weekday and weekend diurnal variations can also be attributed to changes in anthropogenic behavior. For example, it is clear that HOA is associated with traffic as the morning rush-hour peak is only evident in the weekday diurnal and the evening peak in concentration is slightly reduced at the weekends (**Figure 3-22** and **Figure 3-23**). This is also the case for NO_x, CO, and BC, which are all fossil fuel combustion tracers. In addition, the diurnal profiles of VOCs associated with vehicle emissions such as benzene and toluene on weekdays and weekends are similar to that of HOA. The diurnal profiles of isoprene are also similar to HOA indicating that isoprene may be associated with vehicle emissions. Previous studies report the predominance of anthropogenic sources of isoprene in urban areas during winter (Borbon et al., 2001;Seco et al., 2013), however, other hydrocarbons (e.g. cycloalkanes) could also be contributing to the PTR-MS signal at the *m/z* assigned to isoprene (e.g. Yuan et al., 2014). Odd oxygen ($O_x = O_3 + NO_2$) is used here to examine the differences between weekdays and weekends rather than O_3 due to the influence of NO_x on O_3 concentrations (Herndon et al., 2008); O_3 is observed to be lower during the weekdays due to titration by NO whereas NO_x is lower at the weekends thus O_3 concentrations are higher. The diurnal profile of O_x is therefore comparable between weekday and weekends. SO_2 also exhibits a similar trend with a prominent morning peak only on weekdays, indicating that

traffic is a main source of SO_2 in Fresno. Indeed, the SO_2 diurnal profiles between weekdays and weekends with those associated with traffic combustion (e.g., NO_x, HOA, and BC) are similar and strong correlations between SO_2 and NO_x are observed (r = 0.877, **Figure 3-25**a). However, SO_4^{2-} exhibits a late morning peak during the day on both the weekdays and at weekends. A similar trend is seen for the other secondary inorganics as well as the secondary organics, although the morning increase is less distinct for LV-OOA.

3.3.4 Insights into meteorological influences

3.3.4.1 Pollution events in Fresno during winter 2013

Two main pollution events occurred during the campaign (14 January-23 January and 29 January-5 February), characterized by persistent exceedances of the NAAQS (**Figure 3-8**e). The average PM_1 concentration was higher during the first event than the second event (44 μg m^{-3} compared to 36 μg m^{-3}) (**Figure 3-8**h and j) and the average compositions of PM_1 are also fairly different. POA accounted for a greater proportion of the PM_1 mass during the first event than the second event (37% vs. 29%) (**Figure 3-8**i and k), mainly due to the larger contribution of BBOA during the first event. The mass concentration of BBOA1, in particular, differs by a factor of five between the two events. Lower temperatures were experienced during the first event (6.2 °C vs. 9.5 °C), which likely lead to an increase in biomass burning activities. On the other hand, both the RH and temperature were, on average, higher during the second event (63.8 % vs. 68.9 %), as well as the average concentration of ozone (6.2 ppb vs. 9.5 ppb), which may have influenced the formation of secondary species through aqueous-phase processing and photochemistry. However, the difference in mass concentrations of SV-OOA and LV-OOA between the first and second events is not as large as that for BBOA1 suggesting that temperature has the largest influence on BBOA and thus the chemical composition during these two pollution events. Nevertheless, it is evident that meteorology influences both primary emissions and the production of secondary species during the campaign; although high PM_1 concentrations are predominantly driven by primary species, the contributions from secondary species are still important (**Figure 3-26**).

3.3.4.2 Comparison with winter 2010

In January 2010, similar measurements were made in Fresno at a site approximately 2.75 km from the one in this study (Ge et al., 2012a;Ge et al., 2012b). Despite both campaigns taking place during wintertime and the close proximity of the two sites, there are notable differences between observed aerosol characteristics (**Table 3-5**). For example, the PM_1 mass loading was much greater and approximately 2.5 times larger in 2013 than in 2010 (31.0 μg m^{-3} vs. 12.7 μg m^{-3}, Fig 10a). The average O/C ratio of organics was also higher in 2013 (0.42 vs. 0.35 in 2010) and the H/C was lower (1.70 vs. 1.75). One of the most noticeable differences between the two campaigns arises from the number and type of OA factors identified from PMF analysis of the organic aerosol fraction. In 2010, four OA factors were identified: HOA, COA, BBOA, and OOA, whereas in 2013 six factors were identified including two BBOA and two OOA factors yet the type of emission sources are not expected to have significantly changed within three years.

Meteorological conditions were noticeably different during the two measurement periods; on average, winter 2010, due to the influence of El Niño, had 16% higher RH and was 1.8°C warmer than winter 2013 (**Figure 3-28**), with nearly 6°C difference in the coldest temperatures (4.0°C in 2013 vs. 9.7°C in 2010 for the 25th percentile). The average wind speed was much lower in 2013 (1.0 m s^{-1} compared to 5.7 m s^{-1} in 2010), and solar radiation was greater in 2013 and 2010 (average of 273 W m^{-2} and 146 W m^{-2}, respectively, for daylight hours, 6:00-17:00 PST). The higher total mass concentration in 2013 (**Figure 3-27**a) can thus be attributed to the particularly stagnant conditions, which favor the accumulation of primary pollutants, from a more severe winter inversion with lower wind speeds and colder temperatures than those in 2010. In terms of fractional contributions of the species to the total mass, HOA and OOA are greater in 2010 than 2013 whereas nitrate and BBOA are greater in 2013 (**Figure 3-27**b). In addition to winter 2013 being colder on average than winter 2010, especially low ambient temperatures during the first week (average of 5.5 °C) likely led to an increase in biomass burning in an effort to increase temperatures within the home during this period as discussed in Section 3.3.2.4. In comparison, it is likely that winter biomass burning activities are represented by only a single BBOA factor in 2010 due to the milder conditions and less dramatic temperature changes. In addition, since stagnant meteorological conditions tend to promote longer residence time of air pollutants and stronger solar radiation generally causes more intense photochemical processing of air pollutants, aerosol particles were likely overall more aged in 2013 than in 2010. The estimated size distributions of the OA factors, as well as nitrate and sulfate, were compared between 2013 and 2010 (Ge et al., 2012b); the particle sizes are observed to be narrower and larger in 2013 than in 2010 (**Figure 3-30**). These differences appear to be consistent with overall more aged aerosol in 2013.

Ammonium nitrate is semi-volatile with a strong dependency on temperature and humidity. Thus, for the following analyses all dense fog and precipitation events have been removed from the 2010 data, and the cold period and precipitation events have been removed from the 2013 data with the resulting mass concentrations and fractional contributions of PM_1 species shown in **Figure 3-27**c and d. There are several different nitrate production mechanisms including gas-to-particle partitioning, photochemical production of HNO_3, as well as the mixing down of a nocturnal residual layer. In 2010, the diurnal cycle of nitrate (**Figure 3-29**a) was attributed to enhanced gas-to-particle partitioning and near-surface aqueous-phase processing from nighttime fogs (Ge et al., 2012a), where the nighttime fogs were not necessarily dense fogs. The diurnal profile of nitrate in 2013, however, is very different, with the highest average concentrations occurring during the late morning, suggesting that temporal variability in gas-to-particle partitioning due to surface-level fogs or instantaneous surface-level temperature is not a major pathway for nitrate production during winter 2013. This is further supported by the calculated diurnal profile of the ammonium nitrate equilibrium constant (see Sect. 3.2.2.4 for equations) (Seinfeld and Pandis, 2006a) (Seinfeld and Pandis, 2006a) (Seinfeld and Pandis, 2006a) [*Seinfeld and Pandis*, 2006a] (Seinfeld and Pandis, 2006), which peaks in the early morning, approximately 4-5 hours before the peak in nitrate concentrations (**Figure 3-29**b). It is estimated that on average, ~90% of the total nitrate (the sum of particle-phase nitrate and the HNO_3 for gas-phase nitrate) is in the particle phase indicating that

most HNO_3 that formed has likely partitioned to the particle-phase (Parworth et al., In preparation). However, the measurements of HNO_3 concentrations in 2013 are only approximately seven-hourly averages. Therefore, a proxy for the daytime photochemical HNO_3 production rate, [NO_2] times solar radiation (e.g. Zhang et al., 2005b), is used here to better characterize any rapid changes in concentrations and thus likely daytime formation of nitrate. The proxy exhibits a similar peak in the diurnal pattern to that of nitrate suggesting photochemical production plays some role in the production of nitrate. However, the change in morning nitrate concentrations in 2013 is greater than 2010 and is larger than would be expected from the difference in the peak in the proxy between the two years. Consequently, photochemical production of nitrate likely only plays a small role in 2013.

In a study conducted at Fresno between 2000 and 2005 (Chow et al., 2008b) a peak in daily nitrate concentrations at 11:00-12:00 PST during winter was observed and attributed to the mixing down of a residual layer where particulate nitrate was formed aloft during the night and brought to the surface after sunrise following the break-up of the boundary layer (Watson and Chow, 2002a, b;Brown et al., 2006b;Chow et al., 2006a). To investigate the influence of a residual layer in enhancing nitrate concentrations at the surface in 2010 and 2013 the diurnal variations in CO, to represent changes in boundary layer dynamics, and in O_3*NO_2, a proxy for nighttime HNO_3 production rate (see Sect. 3.2.2.5), are examined (**Figure 3-29**). The CO profile is very similar in the evenings during the weekdays and weekend (**Figure 3-22**) indicating that boundary layer dynamics are more important in influencing CO concentrations than rush hour emissions in the evening. Thus at around 17:00 PST the sun sets, the boundary layer starts to collapse, and pollutants that mixed aloft during the day would be decoupled from the surface (Pusede et al., 2016). Consequently, the concentration of nitrate that could have formed during the night would depend on the initial concentrations of the pollutants such as NO_2 and O_3 in the residual layer. Overnight, NO_2 and O_3 react to form N_2O_5, which can react heterogeneously to form HNO_3. As demonstrated in Sect. 3.2.2.5, under the assumption that N_2O_5 and NO_3 are both in steady state (Brown et al., 2006e), the nighttime HNO_3 production rate is proportional to $k_1[NO_2][O_3]$. Thus, the product of the NO_2 and O_3 concentrations at the point where the residual layer is formed (i.e. when the aloft atmosphere decouples from the surface) provides an approximation of HNO_3 production in the nocturnal boundary layer. The concentration of NO_2 at 17:00 PST was similar in 2010 as in 2013 (26 ppb vs. 20 ppb, on average) while the O_3 concentration in 2010 at 17:00 PST was smaller than in 2013 (5.5 ppb vs. 21 ppb). This indicates that HNO_3 production from the N_2O_5 pathway was likely greater on average in 2013 than in 2010, which suggests the influence of the residual layer on daytime nitrate concentrations was more important in 2013. The influence of the residual layer in 2013 is evident on several days (**Figure 3-21**c). In addition, it could be that the daytime losses of nitrate also differed between the two years. For example, the higher temperatures in 2010 may have resulted in a slightly greater fraction of HNO_3 remaining in the gas phase.

The formation of other secondary species in 2010 was primarily attributed to in-fog processing and overall high humidity with enhanced gas-to-particle partitioning also playing an important

role. However, in 2013 it is the nocturnal residual layer that appears to have the greatest influence on the diurnal variations of the secondary species; the diurnal profiles of the secondary inorganics, SV-OOA, and to some extent LV-OOA, are similar to that of nitrate, exhibiting the late morning peak in concentrations (**Figure 3-10** and **Figure 3-13**). The influence of the residual layer is particularly clear when comparing the weekday and weekend diurnal profiles of sulfate and its precursor gas, SO_2 ; the profiles are similar between weekdays and weekends for sulfate, but not for SO_2 (**Figure 3-22**). In addition, a strong correlation is observed between SO_2 and CO ($r = 0.871$, **Figure 3-25**b). Although the nocturnal residual layer has previously been observed in Fresno (e.g. Watson and Chow, 2002a;Chow et al., 2006a), its presence and subsequent influence on aerosol concentrations at the surface has typically been considered only in the context of nitrate. To our knowledge, this is the first time that the influence of the residual layer on other secondary species, such as sulfate, has been reported.

In contrast to 2010, two OOA subtypes, SV-OOA and LV-OOA, were identified in 2013, which is surprising since more than one OOA factor is typically only observed at the same time during summer periods when the range in photochemical conditions and ambient temperature is larger (Jimenez et al., 2009). However, the solar radiation and the range of temperatures were larger in 2013 than 2010 (**Figure 3-28** and **Table 3-5**). Thus, it is possible that the contrast in meteorological conditions that influenced secondary aerosol formation in 2013 enabled OOA to be separated into the two subcomponents whereas the conditions were not as significantly different during the 2010 winter study. However, the fractional contribution of OOA to the total secondary aerosol mass is greater in 2010 than 2013 (**Figure 3-27**b), which could be in part due to the large contribution from nitrate in 2013 but also due to aqueous-phase processing in fogs in 2010 (Ge et al., 2012b). The contribution of total OOA is similar between the two years when the dense fogs, precipitation events and cold periods are removed from the respective datasets (27% vs. 25%), suggesting that aqueous-phase processing was more important for production of OOA in 2010 as the RH was higher on average throughout the 2010 campaign, whereas the greater solar radiation in 2013 led to more photochemical production of more oxidized OOA.

3.4 Conclusions

Particulate matter was characterized during winter 2013 at Fresno, one of the most populated cities in the SJV in California, using an HR-ToF-AMS as part of the NASA DISCOVER-AQ campaign. The average PM_1 concentration was 31.0 $\mu g\ m^{-3}$ and the total mass was dominated by organic aerosols (55%), which had an average concentration of 17.1 $\mu g\ m^{-3}$. OA had an average O/C ratio of 0.42 and an H/C ratio of 1.70 using the Improved-Ambient elemental analysis method recently reported in Canagaratna et al. (2015).

To gain insight into the sources and processes influencing the aerosols in Fresno, PMF was applied to the OA fraction where six factors were identified: HOA associated with local traffic, COA associated with food cooking activities, two BBOAs (BBOA1 and BBOA2) associated with

residential space heating from wood combustion, SV-OOA and LV-OOA formed via chemical reactions in the atmosphere. During winter 2013, the four POA factors (HOA, COA, BBOA1, and BBOA2) accounted for 60% of the total OA mass with the other 40% accounted for by the two secondary OA factors. LV-OOA represents the largest OA component (24%) and accounts for 60% of the total SOA mass.

The two BBOAs differed temporally and chemically, where BBOA1 was markedly present during the first few days of the campaign and had a less distinct diurnal profile compared to BBOA2. BBOA2 was observed to be more oxygenated than BBOA1 and correlated better with most biomass burning tracers other than the nitrogen-containing species with which BBOA1 had a stronger relationship. Differences in the two factors were likely due predominantly to burning behaviors and variations in meteorology whereby temperatures during the first week of the campaign were below freezing, leading to an increase in residential wood combustion for space heating.

Similar measurements were performed at a nearby location during winter in 2010 yet the resulting aerosol chemistry is considerably different to that of 2013, where the average NR-PM_1 concentration in 2013 was more than a factor of two greater than 2010 (29.6 μg m^{-3} compared to 11.7 μg m^{-3}). In 2013 the contribution of nitrate to the total PM_1 (NR-PM_1 plus BC) was greater than in 2010 and another BBOA and OOA factor were identified in addition to the HOA, COA, BBOA, and OOA factors derived from the 2010 OA dataset. As the types of aerosol sources are unlikely to have changed significantly between the two years, observed differences are predominantly due to meteorological influences, with colder and drier conditions in 2013 than 2010. Coupled with low wind speeds, the stagnant conditions in 2013 favored the accumulation of pollution. In addition, the first week of the 2013 campaign was characterized by a period of particularly low temperatures, likely resulting in an increase in biomass burning activities and thus the identification of two BBOA factors in 2013. However, gas-to-particle partitioning due to lower temperatures could not fully explain the observed increase in nitrate concentrations from 2010 to 2013. The excess nitrate mass was attributed to photochemical formation during the day as well as the addition of nitrate in the late morning which had formed in a residual layer aloft during the night. The nocturnal residual layer is also observed to influence the diurnal variation in concentrations of other secondary inorganic and organic aerosols. The greater solar radiation and larger range in temperature likely lead to both SV-OOA and LV-OOA being observed in 2013 whereas the meteorological conditions were not as contrasting in 2010 and OOA production was influenced more by aqueous-phase processes, particularly in fogs.

3.5 Figures

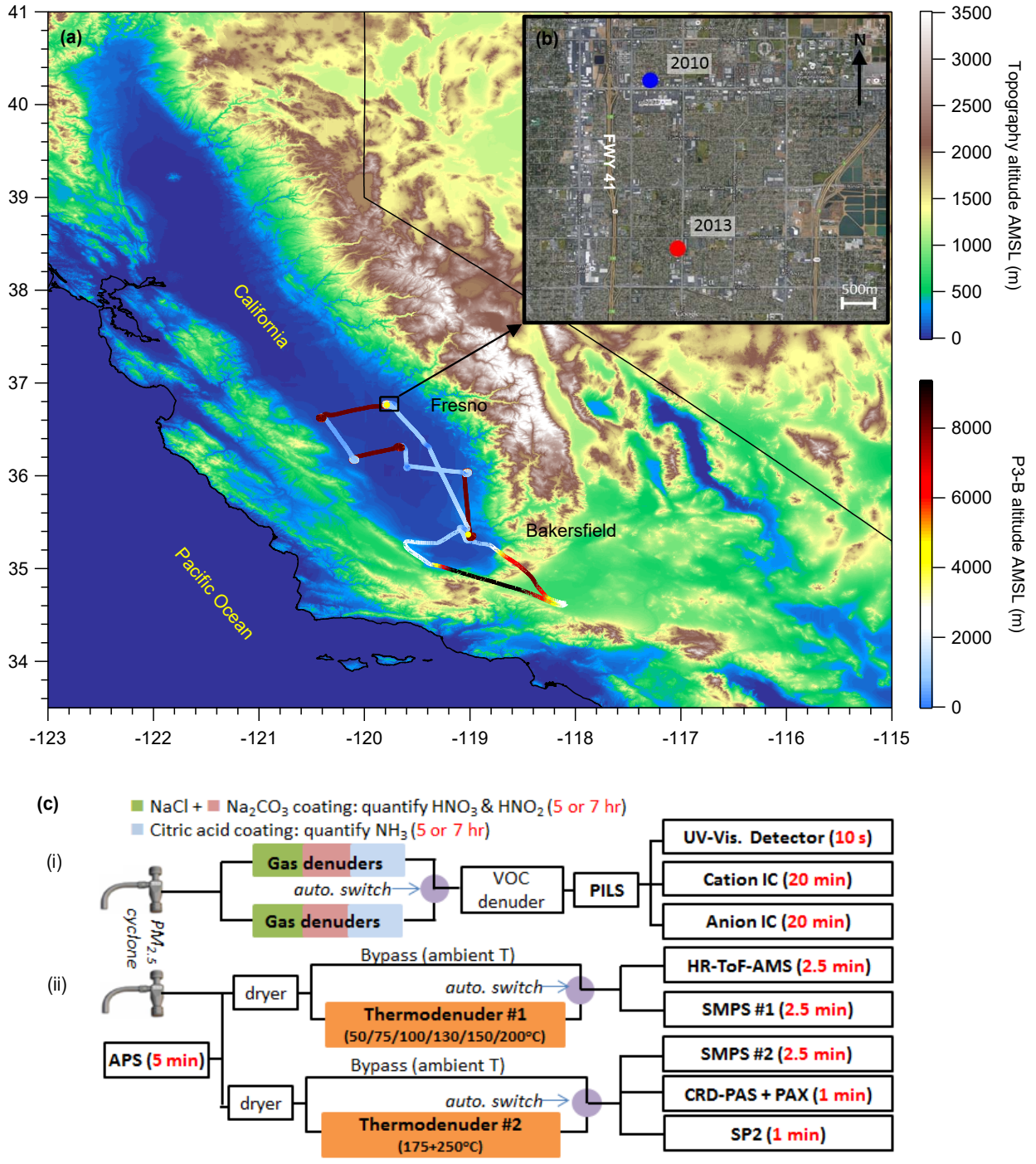

Figure 3-1: (a) Topographical map of the San Joaquin Valley (SJV) of California and NASA P-3B flight tracks during the winter 2013 DISCOVER-AQ campaign; **(b)** the inset shows the location of the supersite in Fresno from winter 2013 (denoted by the red circle) and the location of a similar campaign that took place in winter 2010 (Ge et al., 2012b;Ge et al., 2012a) (denoted by the blue

circle); **(c)** setup of the real-time instruments deployed at the Fresno supersite. (i) A particle-into-liquid sampler (PILS) was coupled with two ion chromatographs (IC) and a UV-Vis detector. The PILS sampled after a fresh set of three annular denuders every 5 or 7 hours; (ii) After a $PM_{2.5}$ inlet, the flow was split into three paths: the first path included the high-resolution time-of-flight aerosol mass spectrometer (HR-ToF-AMS) and a scanning mobility particle sizer (SMPS) which sampled alternatively through a bypass line and a thermodenuder (TD). The second path included a SMPS, a cavitiy ring-down photoacoustic spectrometer (CRD-PAS) and particle extinctometer (PEX) and a single particle soot photometer (SP2). A TD was used to volatilize aerosol at 175 °C then 250 °C. The third path led to an aerodynamic particle sizer (APS).

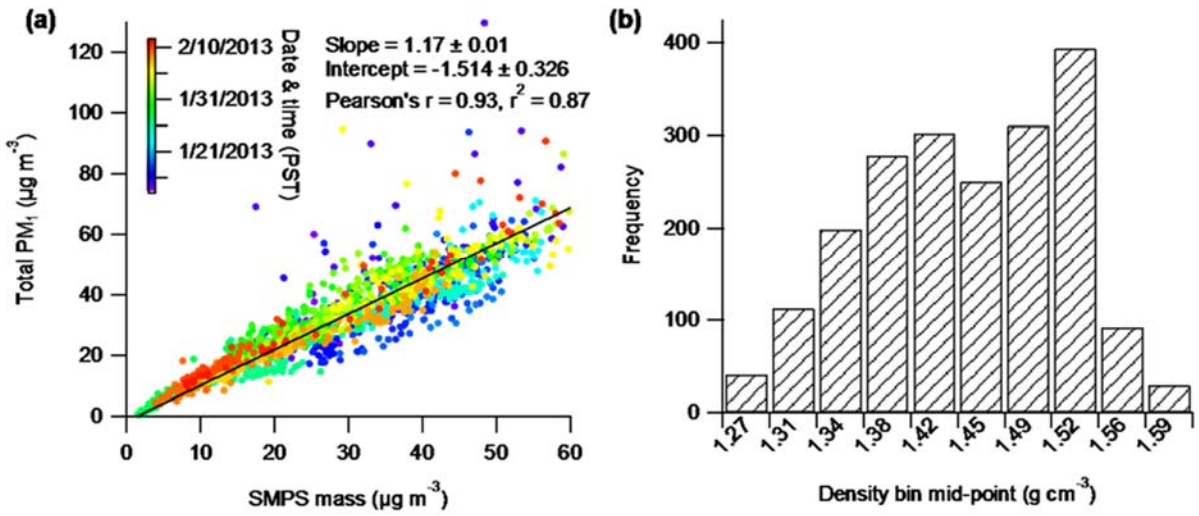

Figure 3-2: (a) Scatter plot of the total PM_1 mass (NR-PM_1 plus BC) versus SMPS mass, where the NR-PM_1 has been corrected using a time- and composition-dependent collection efficiency (Middlebrook et al., 2012). The SMPS mass was calculated using a time-varying composition dependent density from the AMS. The density was calculated based on PM_1 composition, which consists of ~34% ammonium nitrate (density = 1.72 g cm^{-3}), ~4.3% ammonium sulfate (density = 1.77 g cm^{-3}), ~1.6% ammonium chloride (density = 1.52 g cm^{-3}), ~55% OA (density = 1.18 g cm^{-3}), and ~4.8% BC (density = 1.77 g cm^{-3}), averaging 1.44 g cm^{-3}. The densities for ammonium nitrate and ammonium sulfate are from Cross et al. (2007), for ammonium chloride the value is from Haynes (2014), the OA density was calculated using the method reported in Kuwata et al. (2012) based on the O/C and H/C ratios for bulk OA, and the BC density is from Cross et al. (2007) and Zhang et al. (2015); **(b)** histogram of particle density calculated based on PM_1 composition.

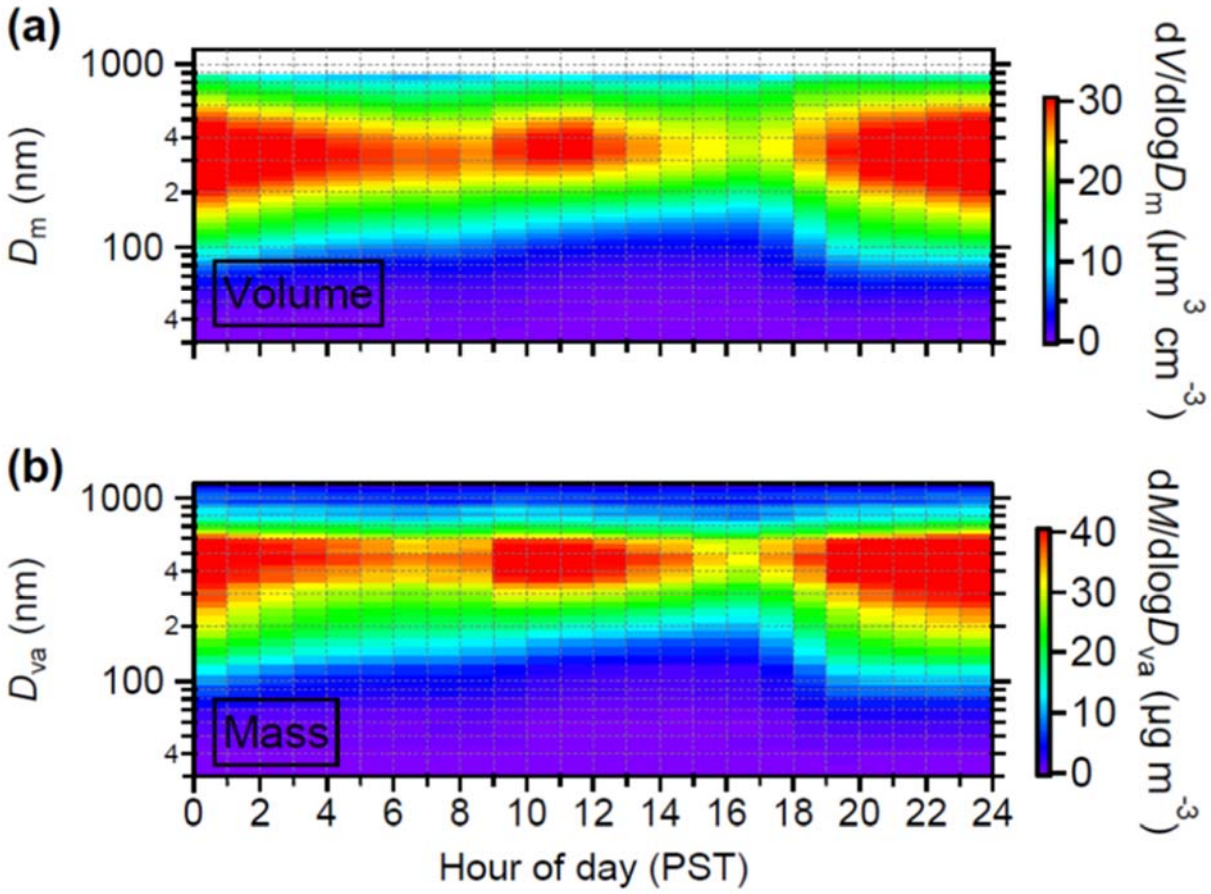

Figure 3-3: Diurnal variations of the size distribution of **(a)** volume from the SMPS (in mobility diameter, D_m); **(b)** NR-PM_1 mass from the AMS (in vacuum aerodynamic diameter, D_{va}).

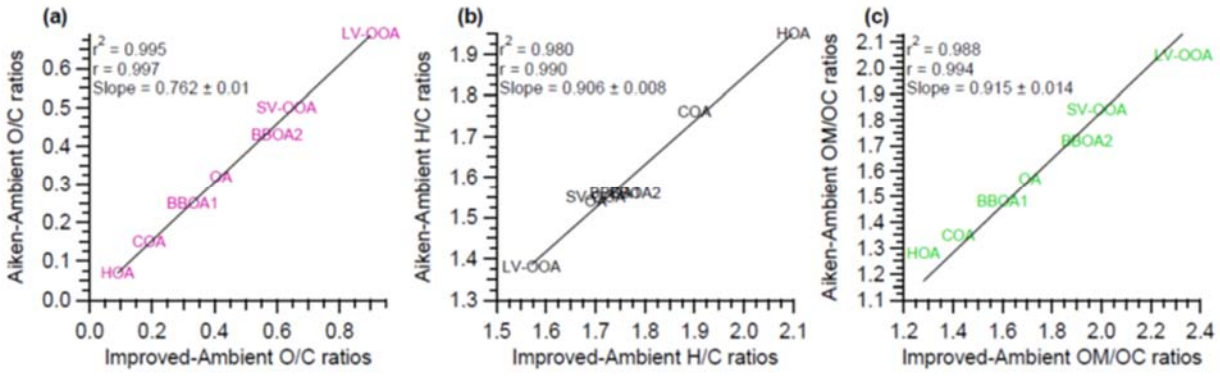

Figure 3-4: Comparison of the **(a)** O/C, **(b)** H/C, and **(c)** OM/OC ratios for bulk OA and the six OA factors identified from PMF analysis calculated using the Aiken-Ambient method (Aiken et al., 2008) and the Improved-Ambient method (Canagaratna et al., 2015).

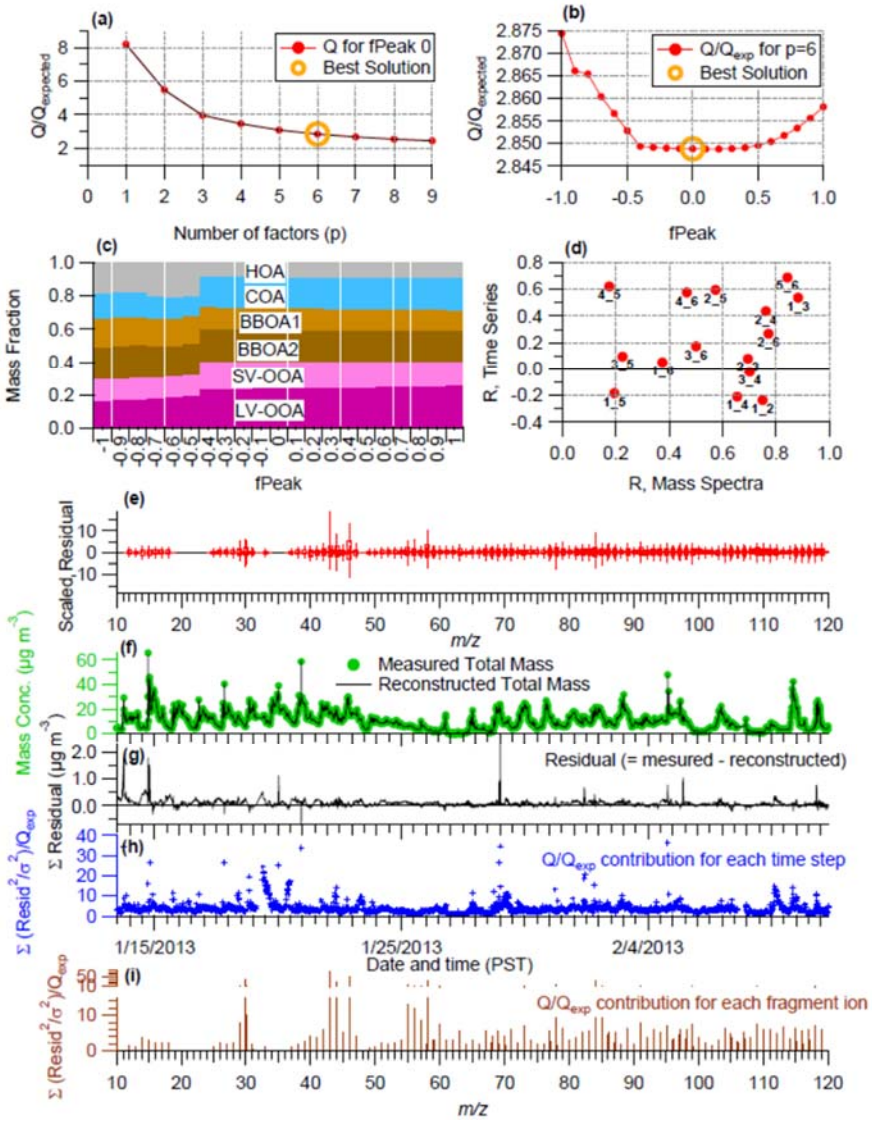

Figure 3-5: Summary of the key diagnostic plots of the chosen 6-factor solution from PMF analysis of the organic aerosol fraction: (a) Q/Q_{exp} as a function of the number of factors (p) explored in PMF analysis, with the best solution denoted by the open orange circle. Plots b-i are for the chosen solution set, containing 6 factors: (b) Q/Q_{exp} as a function of fPeak; (c) mass fractional contribution to the total OA mass of each of the PMF factors, including the residual (in black), as a function of fPeak; (d) Pearson's r correlation coefficient values for correlations among the time series and mass spectra of the PMF factors. Here, 1 = LV-OOA, 2 = BBOA1, 3 = SV-OOA, 4 = BBOA2, 5 = HOA, and 6 = COA; (e) box and whiskers plot showing the distributions of scaled residuals for each *m/z*; (f) time series of the measured organic mass and the reconstructed organic mass from the sum of the six OA factors; (g) time series of the variations in the residual (= measured – reconstructed) of the fit; (h) the Q/Q_{exp} for each point in time; (i) the Q/Q_{exp} values for each fragment ion.

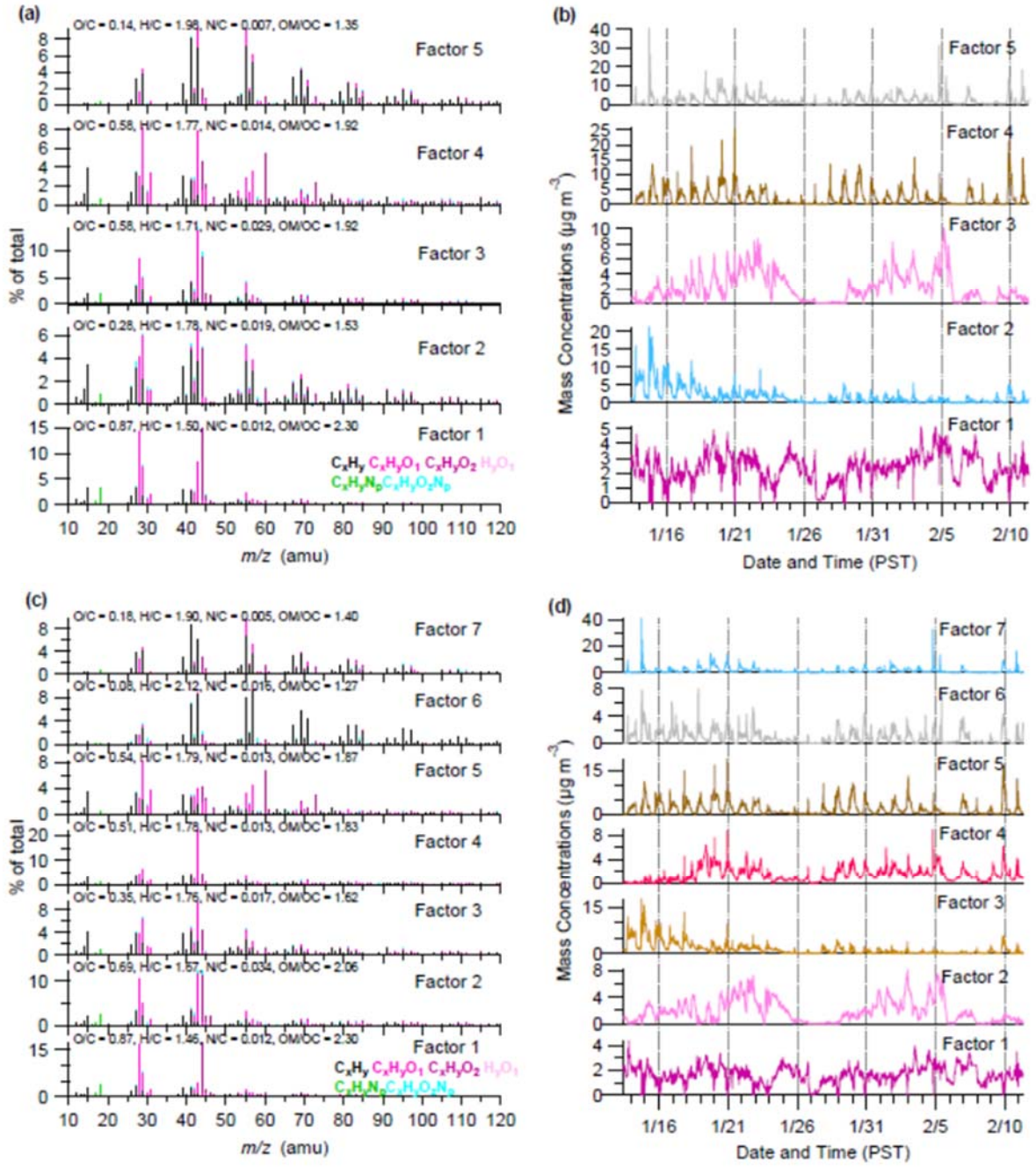

Figure 3-6: Overview of two other solution sets from PMF analysis: **(a)(b)** High resolution mass spectra and time series of the different OA factors from the 5-factor solution; **(c)(d)** High resolution mass spectra and time series of the different OA factors from the 7-factor solution. The mass spectra are colored by different ion families and the time series are colored by possible factor sources (grey = HOA, blue = COA, brown = BBOA, pink = OOA). See Sect. 3.2.2.2 in the main manuscript for a discussion on these solution sets.

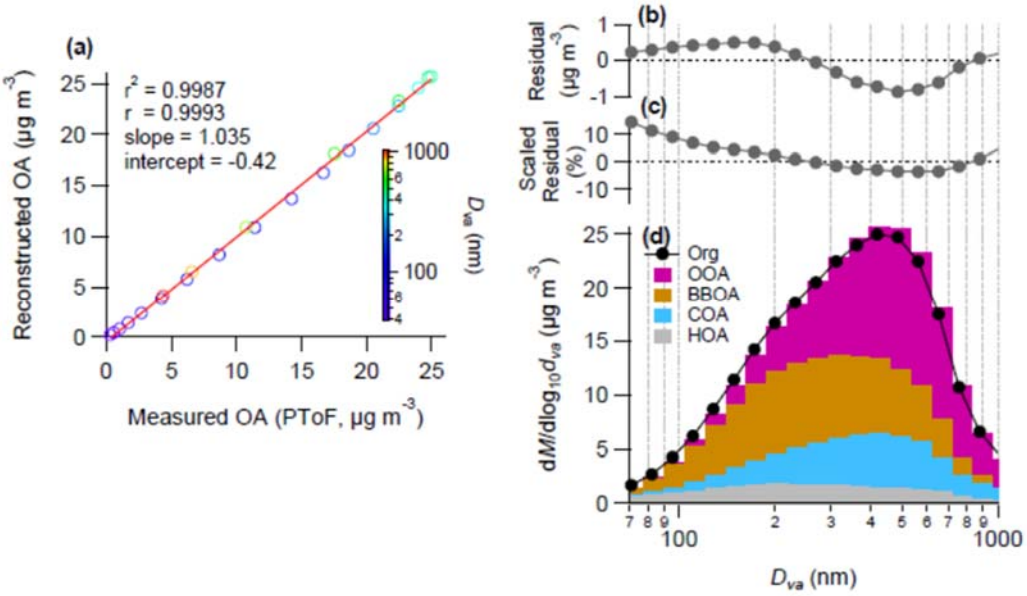

Figure 3-7: Summary of key diagnostics from the fitting of the derived size distributions of the four main OA factors from the whole measurement campaign: **(a)** scatter plot of the reconstructed vs. measured OA mass concentration for each size bin (40-1200 nm); **(b)** absolute residual of the reconstructed compared to the measured OA mass concentration for each size bin; **(c)** scaled residual of the reconstructed compared to the measured OA mass concentration for each size bin; and **(d)** stacked size distributions of the OA factors and the total measured organic aerosol size distribution.

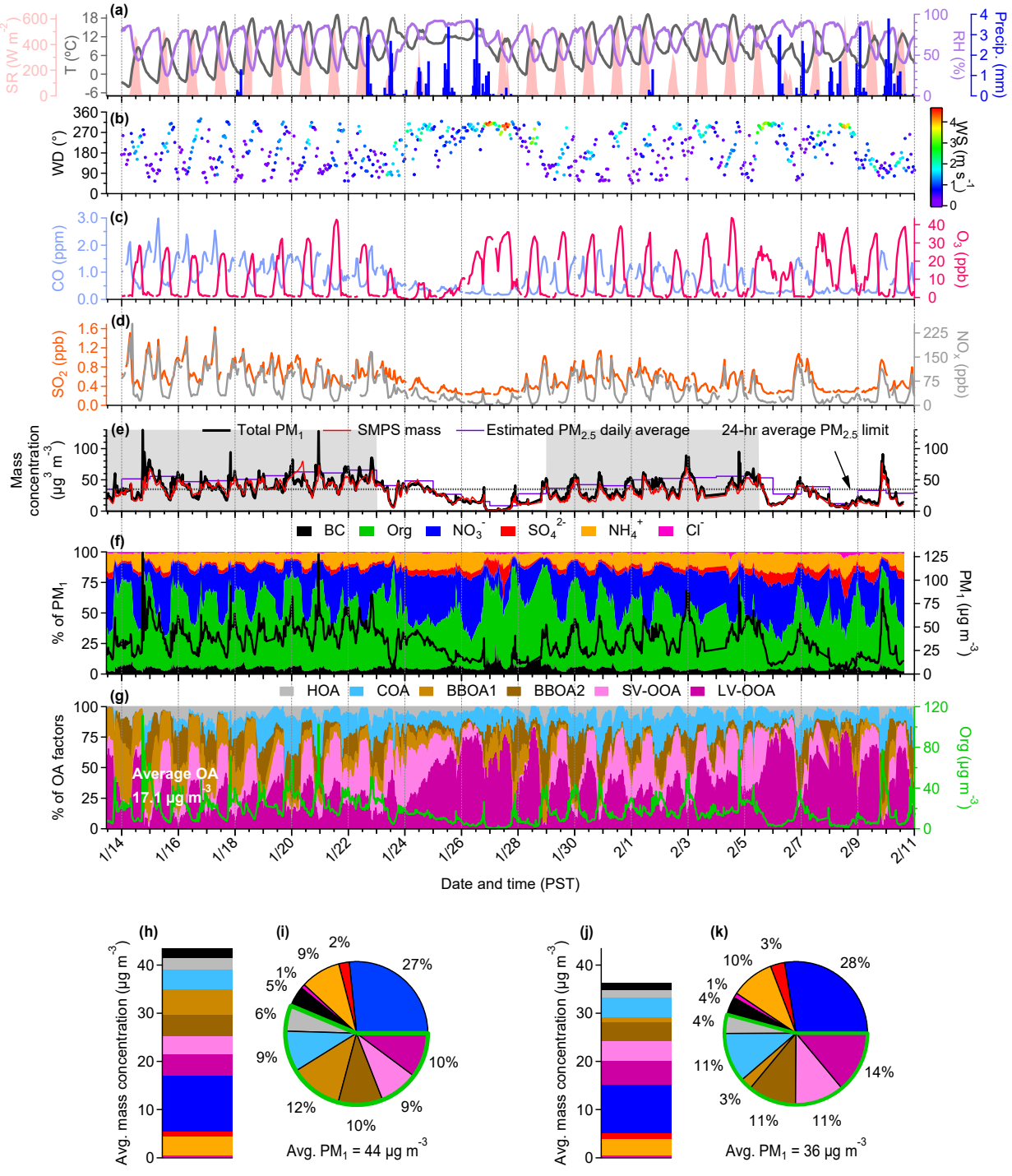

Figure 3-8: Overview of the chemical composition and temporal trends of submicron aerosols at Fresno in the San Joaquin Valley in January and February 2013 including **(a)** time series of ambient

air temperature (T), relative humidity (RH), solar radiation (SR), and precipitation (Precip.); **(b)** time series of wind direction (WD) colored by wind speed (WS); **(c)** time series of gas phase pollutants (CO and O_3); **(d)** time series of gas phase pollutants (SO_2 and NO_x); **(e)** time series of total PM_1 and SMPS mass concentrations where SMPS mass was calculated using a time-varying density based on measured particle composition (see **Figure 3-2**b). Also shown are the 24-hour average National Ambient Air Quality Standard for $PM_{2.5}$ (35 μg m^{-3}) and the calculated average daily $PM_{2.5}$ concentrations for comparison. Persistent exceedances of this standard characterize the two pollution periods highlighted by the gray shading (14-23 January and 29 January–5 February); **(f)** time series of the mass fractional contribution of organic aerosols (Org.), nitrate (NO_3^-), sulfate (SO_4^{2-}), ammonium (NH_4^+), chloride (Cl^-) and BC to total PM_1 and time series of the total PM_1 concentration on the right axis; and **(g)** time series of the mass fractional contribution to total organic aerosol (OA) of the six factors derived from positive matrix factorization (PMF) analysis (see Sect. 3.2.2.2) and the time series of the organic aerosols. **(h)** average mass concentration of the PM_1 species during the first polluted period. The organic aerosol fraction has been split into its components as derived from PMF analysis; **(i)** compositional pie chart of the PM_1 species from the first polluted period; **(j)** average mass concentration of the PM_1 species during the second polluted period. The organic aerosol fraction has been split into its components as derived from PMF analysis; **(k)** compositional pie chart of the PM_1 species from the second polluted period.

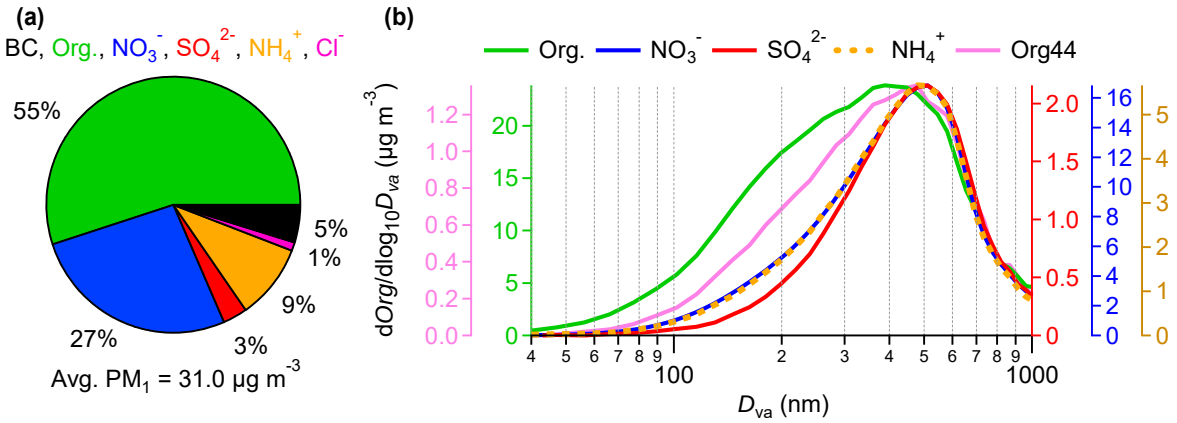

Figure 3-9: (a) Average compositional pie chart of PM_1 species (non-refractory-PM_1 plus BC) for the whole campaign; **(b)** Campaign-averaged size distributions for individual NR-PM_1 species where Org44 is used to represent secondary organic aerosols. The organic aerosol distribution has been smoothed using the binomial smooth algorithm within Igor.

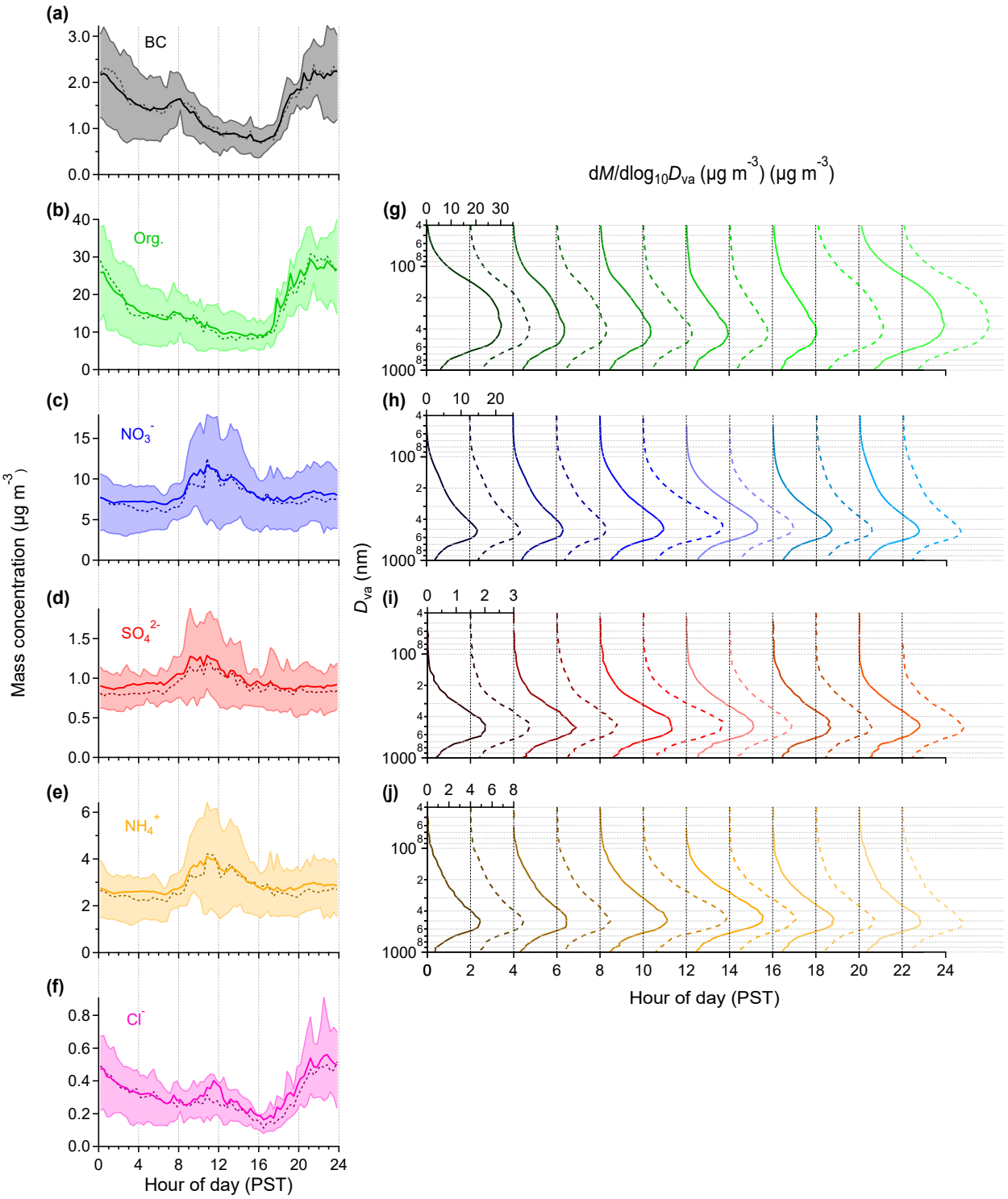

Figure 3-10: (a-f) Average diurnal profiles of each of the PM_1 species where BC measurements are from the SP2 (the 75th and 25th percentiles are denoted by the top and bottom of the shaded region, the median values are denoted by the broken, dark colored lines, and the mean values are denoted by the solid, light-colored lines); **(g-j)** Two-hour average diurnal size distributions for

each of the NR-PM_1 species. The size distribution of chloride is not included here due to its low signal-to-noise. The vertical gridlines indicate the zero line for each of the two-hour averaged mass-based size distributions and the starting hour of the averaging period (e.g. the zero line for the average size distribution for 06:00-08:00 PST is the vertical line at the 6 hour tick). Each size distribution is scaled to the maximum mass range for that species, as indicated by the top axis for the 00:00-02:00 PST distribution. The organic aerosol distribution has been smoothed using the binomial smoothing algorithm within Igor. Mass-based diurnal size distributions between 30 and 1400 nm, of NR-PM_1 species, Org44, used to represent secondary organic aerosols, and Org41, used to represent hydrocarbon containing aerosols, are shown in **Figure 3-11**.

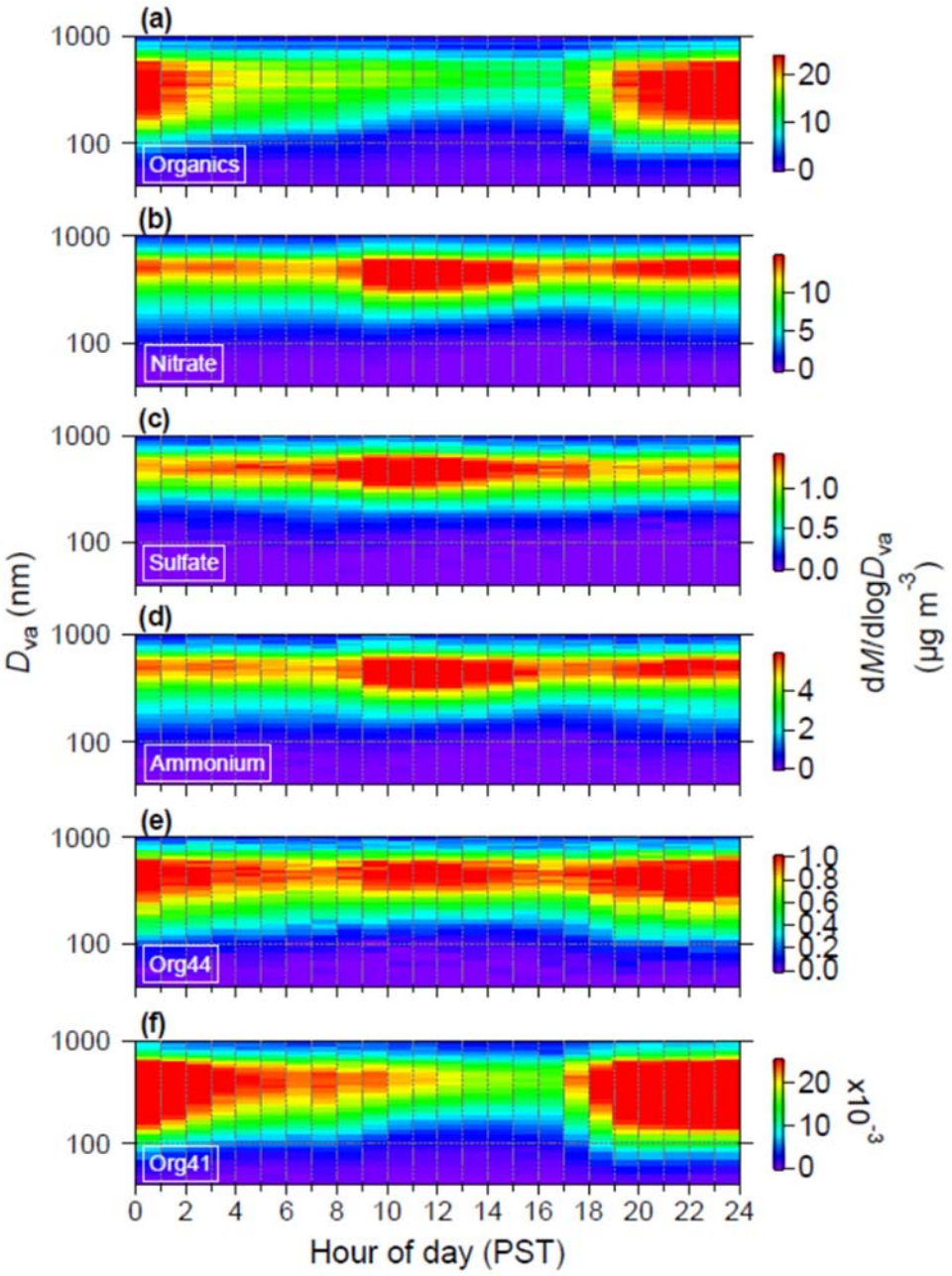

Figure 3-11: Diurnal variations of mass-based size distributions of **(a)** organics; **(b)** nitrate; **(c)** sulfate; **(d)** ammonium; **(e)** Org44 as a tracer for secondary organic aerosols; and **(f)** Org41 as a tracer for hydrocarbon containing aerosols.

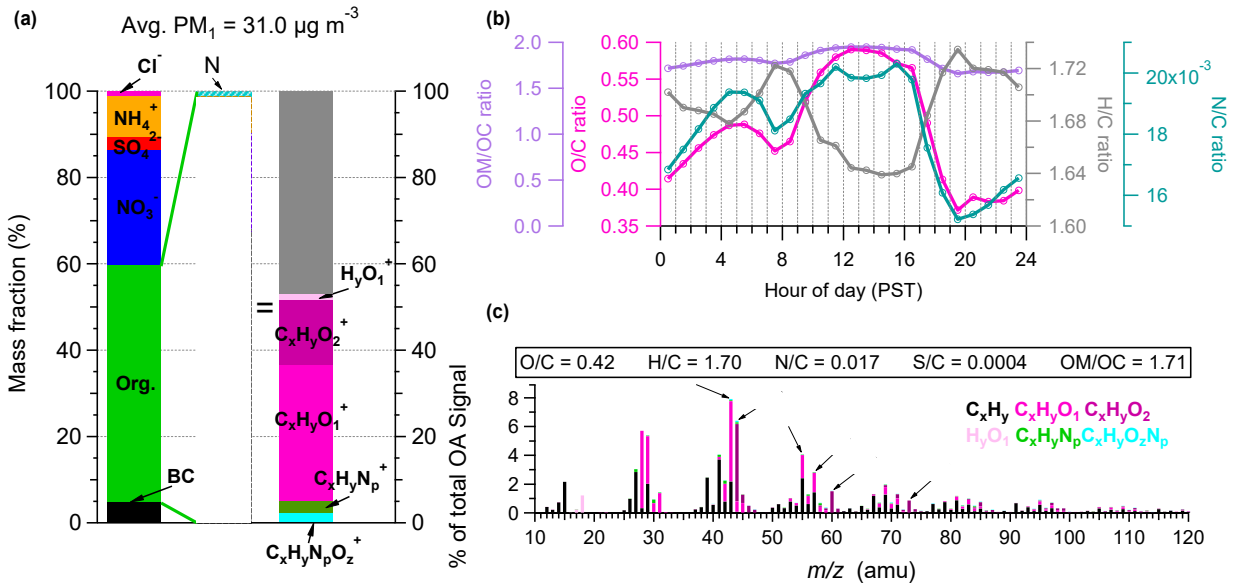

Figure 3-12: (a) Overview of the average PM_1 and OA compositions in Fresno 2013; **(b)** Average diurnal profiles of the oxygen-to-carbon (O/C), hydrogen-to-carbon (H/C), nitrogen-to-carbon (N/C), and organic matter-to-organic carbon (OM/OC) ratios of OA, where the O/C, H/C and OM/OC elemental ratios were determined using the Canagaratna-Ambient method (Canagaratna et al., 2015); and **(c)** Average high-resolution mass spectrum of OA colored by ion families. The average elemental ratios for the organic aerosol fraction are detailed in the box.

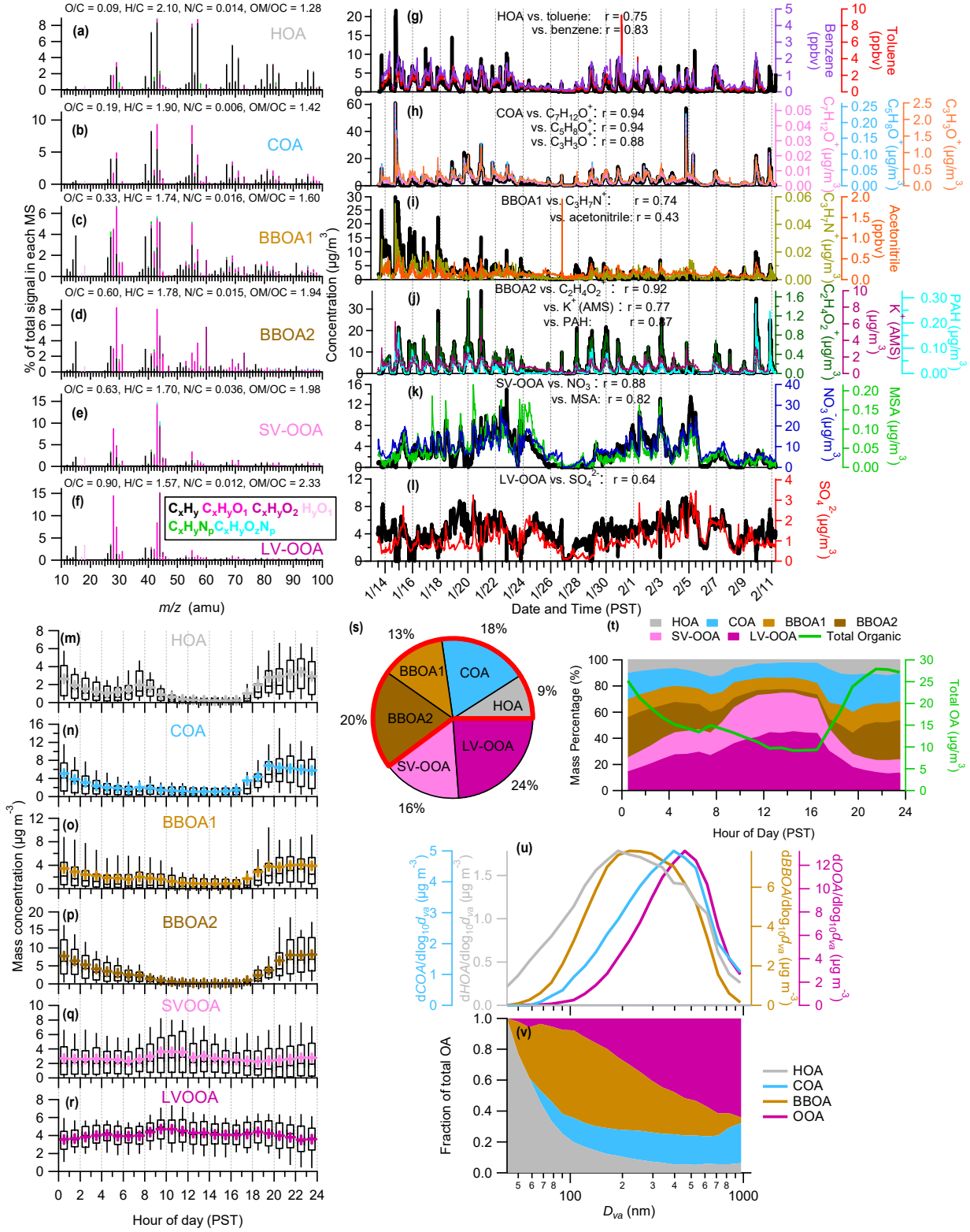
O/C = 0.09, H/C = 2.10, N/C = 0.014, OM/OC = 1.28
(a)
HOA
O/C = 0.19, H/C = 1.90, N/C = 0.006, OM/OC = 1.42
(b)
COA
O/C = 0.33, H/C = 1.74, N/C = 0.016, OM/OC = 1.60
(c)
BBOA1
O/C = 0.60, H/C = 1.78, N/C = 0.015, OM/OC = 1.94
(d)
BBOA2
O/C = 0.63, H/C = 1.70, N/C = 0.036, OM/OC = 1.98
(e)
SV-OOA
O/C = 0.90, H/C = 1.57, N/C = 0.012, OM/OC = 2.33
(f)
LV-OOA
% of total signal in each MS
m/z (amu)
(g)
HOA vs. toluene: r = 0.75
vs. benzene: r = 0.83
Benzene (ppbv)
Toluene (ppbv)
(h)
COA vs. C7H12O+: r = 0.94
vs. C5H8O+: r = 0.94
vs. C3H3O+: r = 0.88
(i)
BBOA1 vs. C3H7N+: r = 0.74
vs. acetonitrile: r = 0.43
Acetonitrile (ppbv)
(j)
BBOA2 vs. C2H4O2+: r = 0.92
vs. K+ (AMS): r = 0.77
vs. PAH: r = 0.87
K+ (AMS)
PAH (μg/m3)
(k)
SV-OOA vs. NO3-: r = 0.88
vs. MSA: r = 0.82
MSA (μg/m3)
(l)
LV-OOA vs. SO42-: r = 0.64
Concentration (μg/m3)
Date and Time (PST)
(m)
HOA
(n)
COA
(o)
BBOA1
(p)
BBOA2
(q)
SVOOA
(r)
LVOOA
Mass concentration (μg m-3)
Hour of day (PST)
(s)
13%
18%
9%
20%
24%
16%
(t)
HOA
COA
BBOA1
BBOA2
SV-OOA
LV-OOA
Total Organic
Mass Percentage (%)
Total OA (μg/m3)
Hour of Day (PST)
(u)
dCOA/dlog10dva (μg m-3)
dHOA/dlog10dva (μg m-3)
dBBOA/dlog10dva (μg m-3)
dOOA/dlog10dva (μg m-3)
(v)
Fraction of total OA
HOA
COA
BBOA
OOA
Dva (nm)

Figure 3-13: Overview of the results from positive matrix factorization (PMF) analysis including high-resolution mass spectra of the **(a)** hydrocarbon-like OA (HOA), **(b)** cooking OA (COA), **(c)** biomass burning OA 1 (BBOA1), **(d)** biomass burning OA 2 (BBOA2), **(e)** semi volatile oxygenated OA (SV-OOA), and **(f)** low volatility oxygenated OA (LV-OOA) colored by different ion families; **(g-l)** time series of each of the OA factors and various tracer species; **(m-r)** average diurnal profiles of each of the OA factors (the 90^{th} and 10^{th} percentiles are denoted by the whiskers above and below the boxes, the 75^{th} and 25^{th} percentiles are denoted by the top and bottom of the boxes, the median values are denoted by the horizontal line within the box, and the mean values are denoted by the colored markers); **(s)** compositional pie chart of the average fractional contribution of each of the OA factors to the total OA for the campaign; **(t)** average diurnal mass fractional contribution of each of the OA factors to the total OA diurnal and the total OA mass loading; and **(u)** average size distributions of the OA factors where BBOA1 and BBOA2 were summed together to BBOA before performing the analysis. Similarly, SV-OOA and LV-OOA were also summed to OOA before performing the analysis. **(v)** average mass fractional contributions of the OA components to the total OA mass as a function of size.

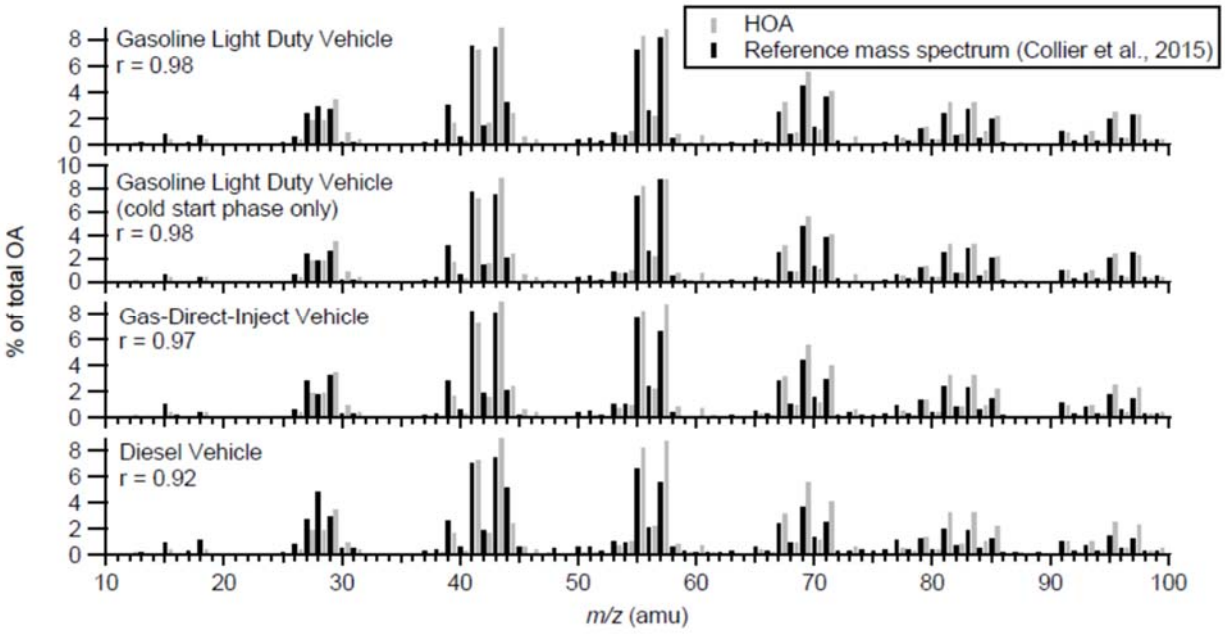

Figure 3-14: Comparison of the HOA mass spectrum from the current study and mass spectra of different types of vehicles from a vehicle emissions study (Collier et al., 2015).

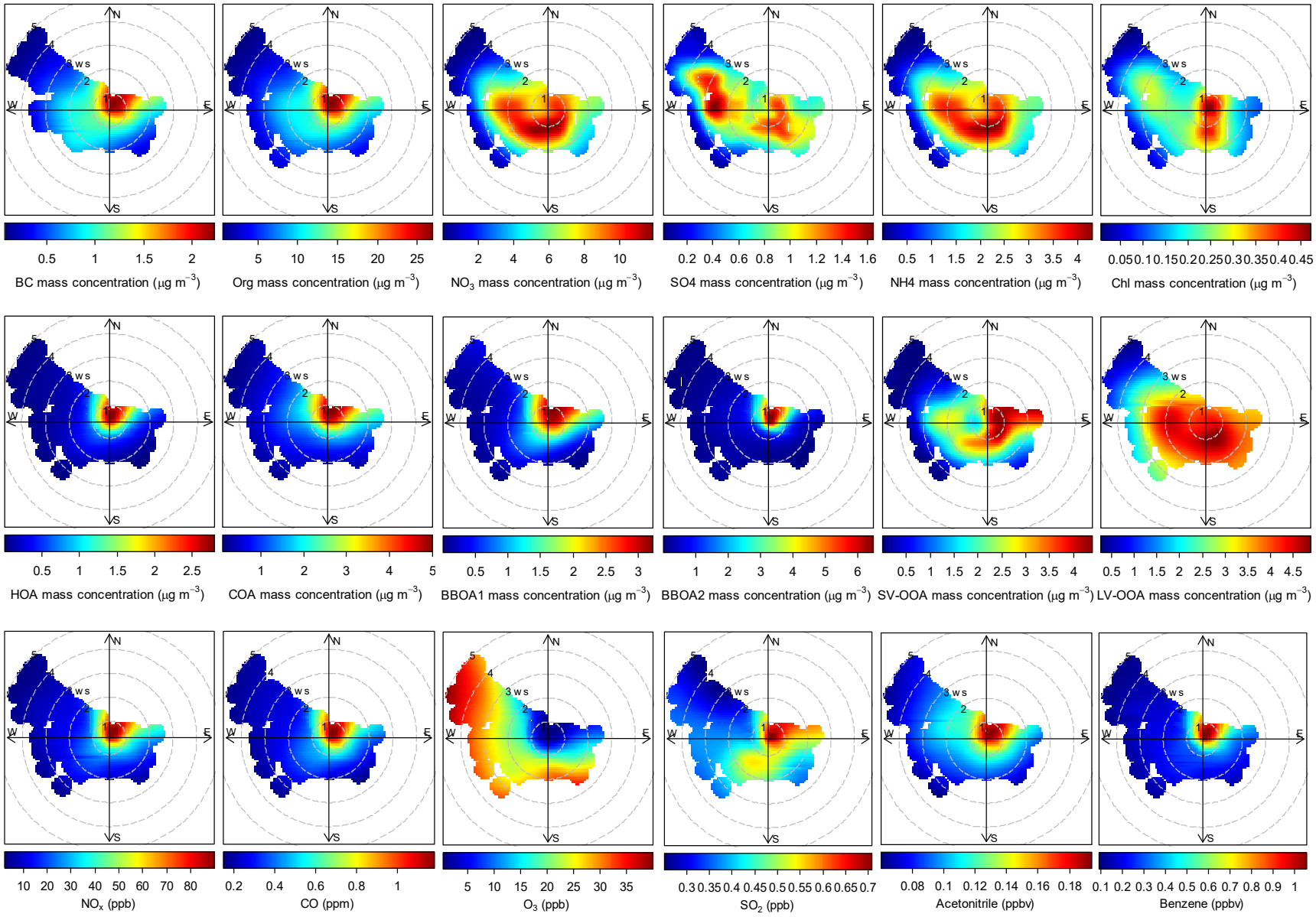
N
E
S
W
3 ws
0.5 1 1.5 2
BC mass concentration (μg m−3)
5 10 15 20 25
Org mass concentration (μg m−3)
2 4 6 8 10
NO3 mass concentration (μg m−3)
0.2 0.4 0.6 0.8 1 1.2 1.4 1.6
SO4 mass concentration (μg m−3)
0.5 1 1.5 2 2.5 3 3.5 4
NH4 mass concentration (μg m−3)
0.05 0.1 0.15 0.2 0.25 0.3 0.35 0.4 0.45
Chl mass concentration (μg m−3)
0.5 1 1.5 2 2.5
HOA mass concentration (μg m−3)
1 2 3 4 5
COA mass concentration (μg m−3)
0.5 1 1.5 2 2.5 3
BBOA1 mass concentration (μg m−3)
1 2 3 4 5 6
BBOA2 mass concentration (μg m−3)
0.5 1 1.5 2 2.5 3 3.5 4
SV-OOA mass concentration (μg m−3)
0.5 1 1.5 2 2.5 3 3.5 4 4.5
LV-OOA mass concentration (μg m−3)
10 20 30 40 50 60 70 80
NOx (ppb)
0.2 0.4 0.6 0.8 1
CO (ppm)
5 10 15 20 25 30 35
O3 (ppb)
0.3 0.35 0.4 0.45 0.5 0.55 0.6 0.65 0.7
SO2 (ppb)
0.08 0.1 0.12 0.14 0.16 0.18
Acetonitrile (ppbv)
0.1 0.2 0.3 0.4 0.5 0.6 0.7 0.8 0.9 1
Benzene (ppbv)

Figure 3-15: Polar plots of hourly averaged PM_1 species concentrations (top row), mass concentrations of the six OA factors identified from PMF analysis (middle row), and mixing ratios of various gas phase species from the CARB monitoring station as well as acetonitrile and benzene VOCs measured by the PTR-TOF-MS (bottom row) as a function of wind speed and direction. These polar plots were plotted in R using the openair package (Carslaw and Ropkins, 2012;Carslaw, 2015), a data analysis tool for investigating air pollution.

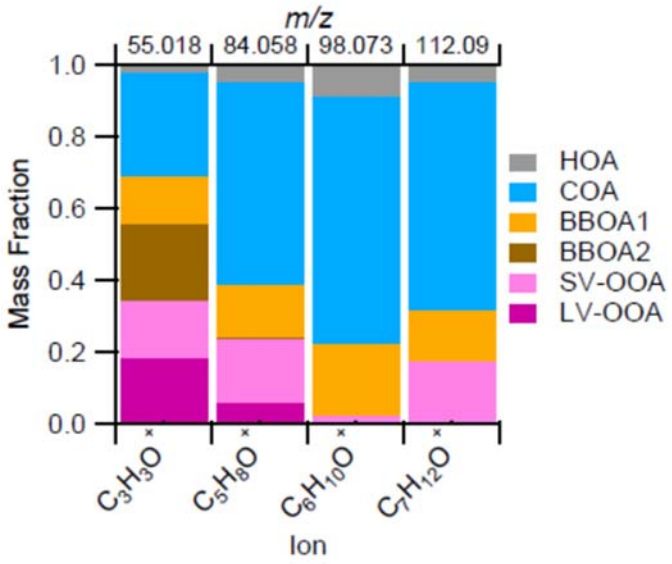

Figure 3-16: Mass fractional contribution of the six OA factors from PMF analysis to various ions.

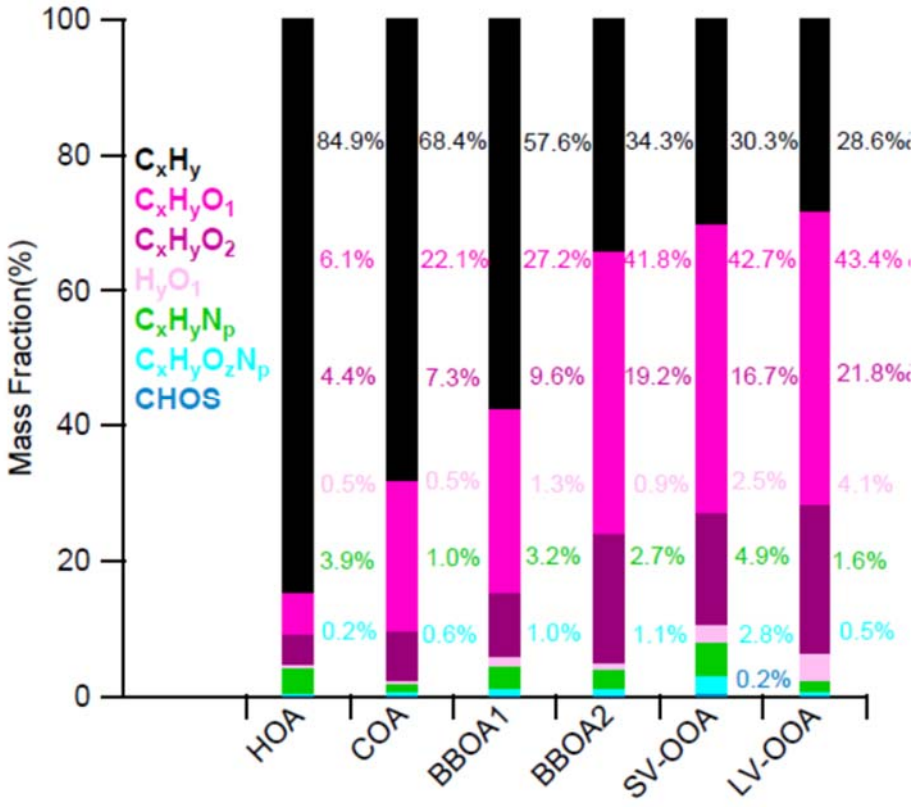

Figure 3-17: Average mass fractional contributions of seven ion families to each of the OA factors.

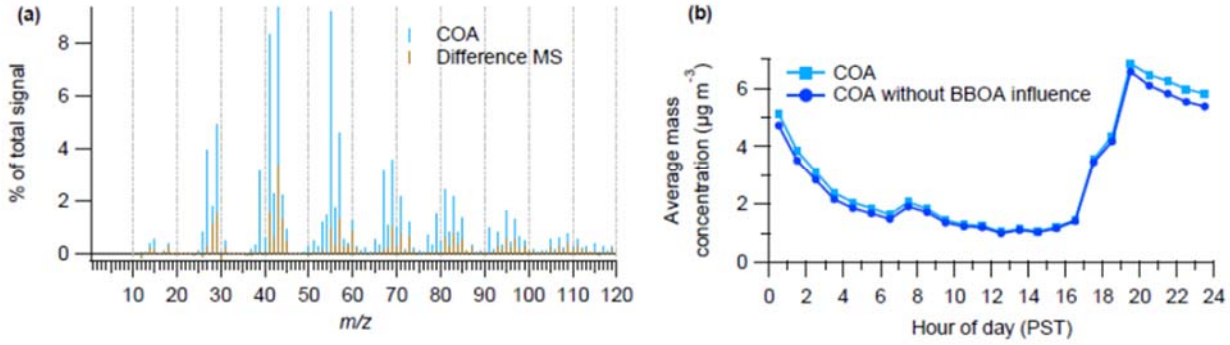

Figure 3-18: (a) Mass spectra of COA and the difference of between COA from 2013 and 2010 (after scaling the 2013 COA mass spectrum (MS) based on the ratio between $C_3H_3O^+$ in 2010 and 2013) and **(b)** Average diurnal profiles of the COA derived from PMF analysis and COA with the influence of BBOA removed (see Sect. 3.2.2.2 for more details)

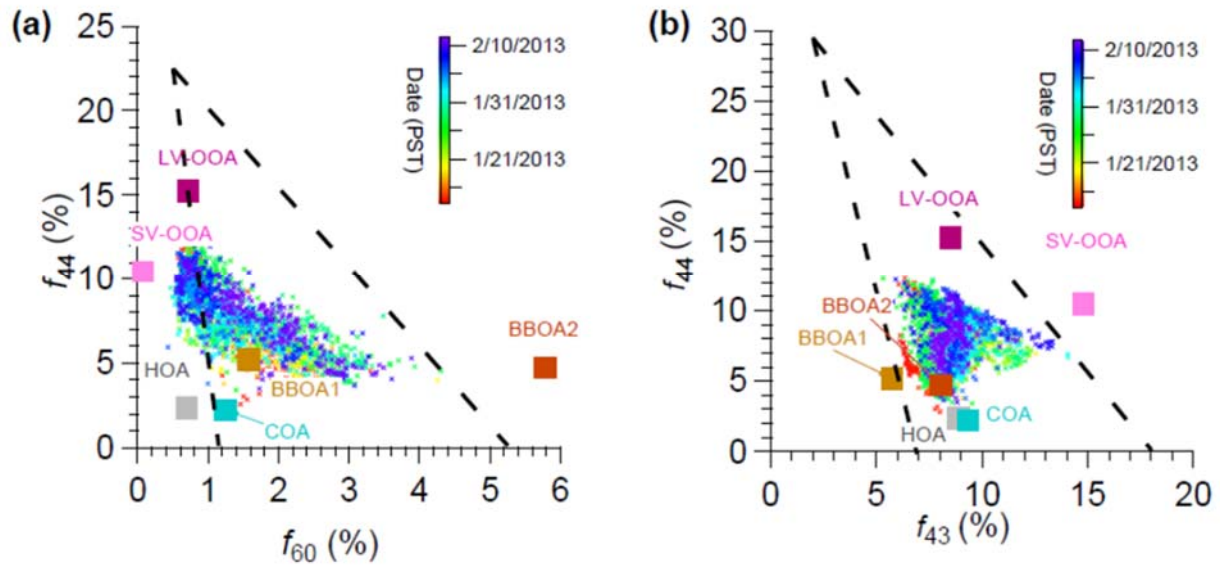

Figure 3-19: Triangle plots of **(a)** f_{44} vs. f_{60} and **(b)** f_{44} vs. f_{43} for the six OA factors and all measured OA data (dots), colored by date. f_{44}, f_{60}, and f_{43} are the ratios of the organic signal at m/z = 44, 60, and 43 to the total organic signal in the component mass spectrum, respectively. The triangular space in (a) is used to investigate the evolution of BBOA and was proposed by Cubison et al. (2011). In this study BBOA1 locates at the lower left corner whereas BBOA2 locates outside of the triangle on the right due to its high m/z 60 signal. The triangular space in (b) is used to investigate the evolution of OA, particularly OOA. OOA is typically observed to fall into a well-defined triangular region within which SV-OOA and LV-OOA tend to occupy discrete regions, thus it is suggested that SV-OOA represents fresh SOA with low f_{44} and LV-OOA represents aged and highly oxidized OA, with high f_{44}. It has been observed that fresh SOA becomes increasingly oxidized and less volatile through additional processing in the atmosphere resulting in LV-OOA, thus the evolution of SOA is regarded as a continuum of oxidation.

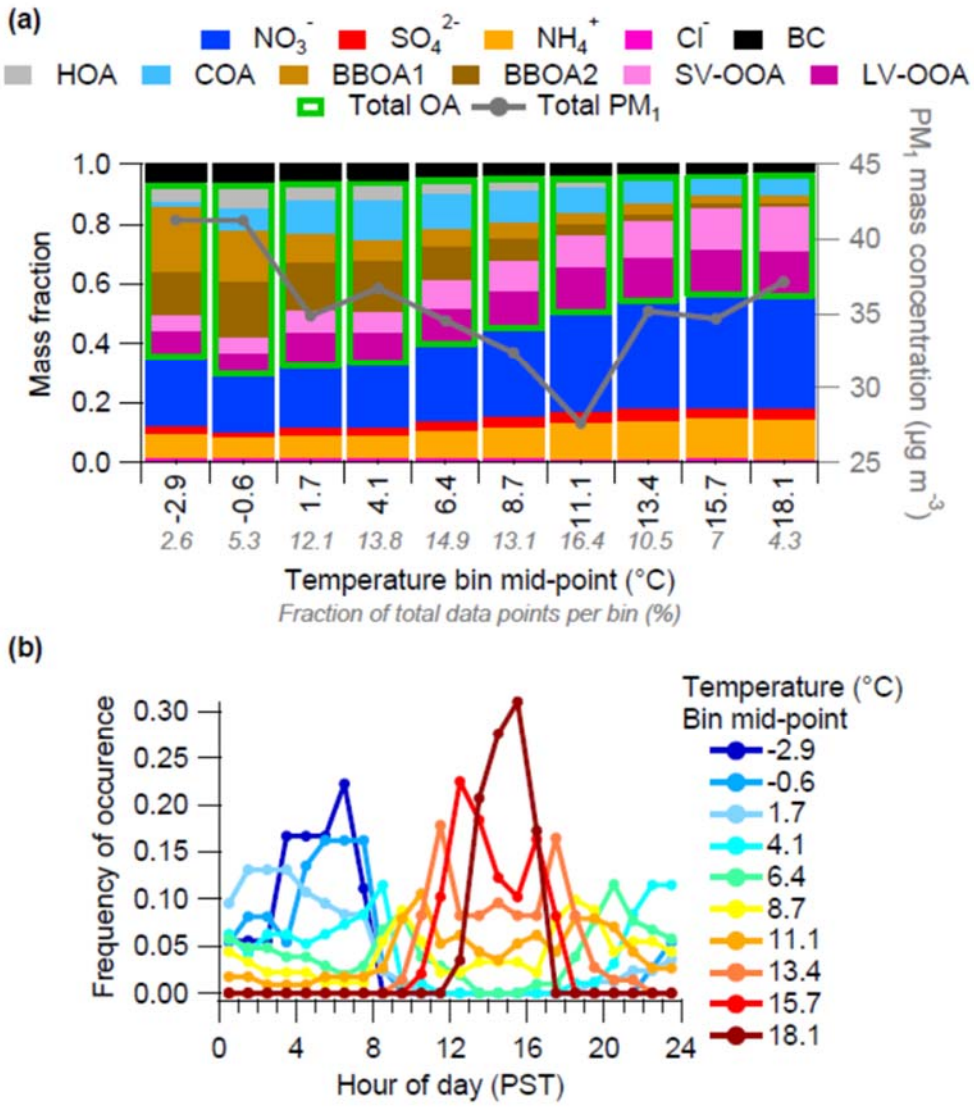

Figure 3-20: (a) Mass fractional contribution to total PM_1 of the non-refractory secondary inorganic species (nitrate (NO_3^-), sulfate (SO_4^{2-}), ammonium (NH_4^+), chloride (Cl^-)), black carbon (BC), and the six OA factors (hydrocarbon-like OA (HOA), cooking OA (COA), biomass burning OA 1 (BBOA1), biomass burning OA 2 (BBOA2), semi-volatile oxygenated OA (SV- OOA), low volatility oxygenated OA (LV-OOA)) as a function of temperature during the whole campaign and average total PM_1 as a function of temperature; **(b)** frequency of occurrence of the temperature bins in plot (a) as a function of hour of the day.

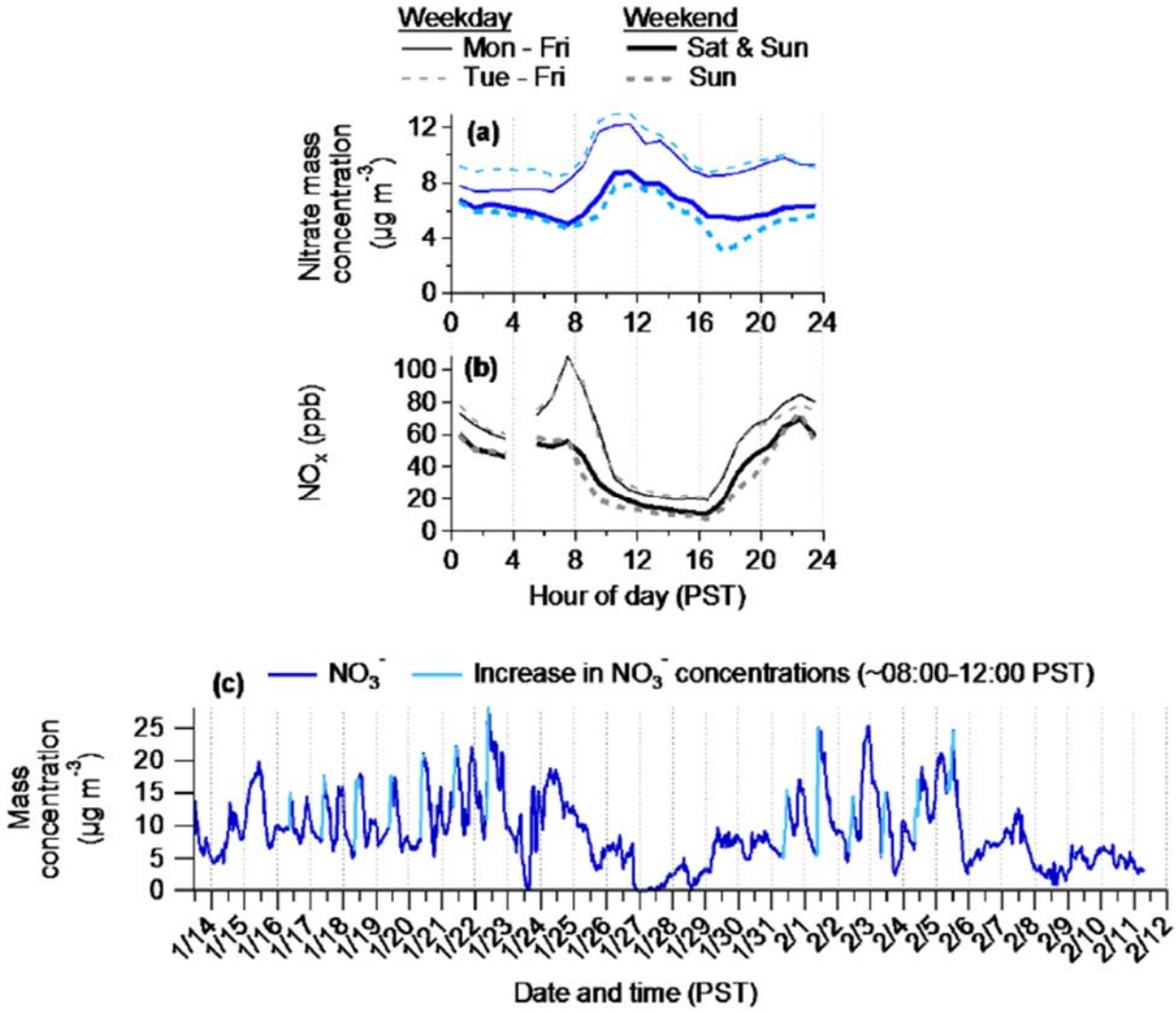

Figure 3-21: Average diurnal mass concentrations when different definitions of weekdays and weekends are used for **(a)** nitrate and **(b)** NO_x, a gaseous precursor of particulate nitrate. **(c)** Time series of nitrate highlighted with the occasions when a rapid increase in concentration during the morning (between approximately 08:00 and 12:00 PST) is observed.

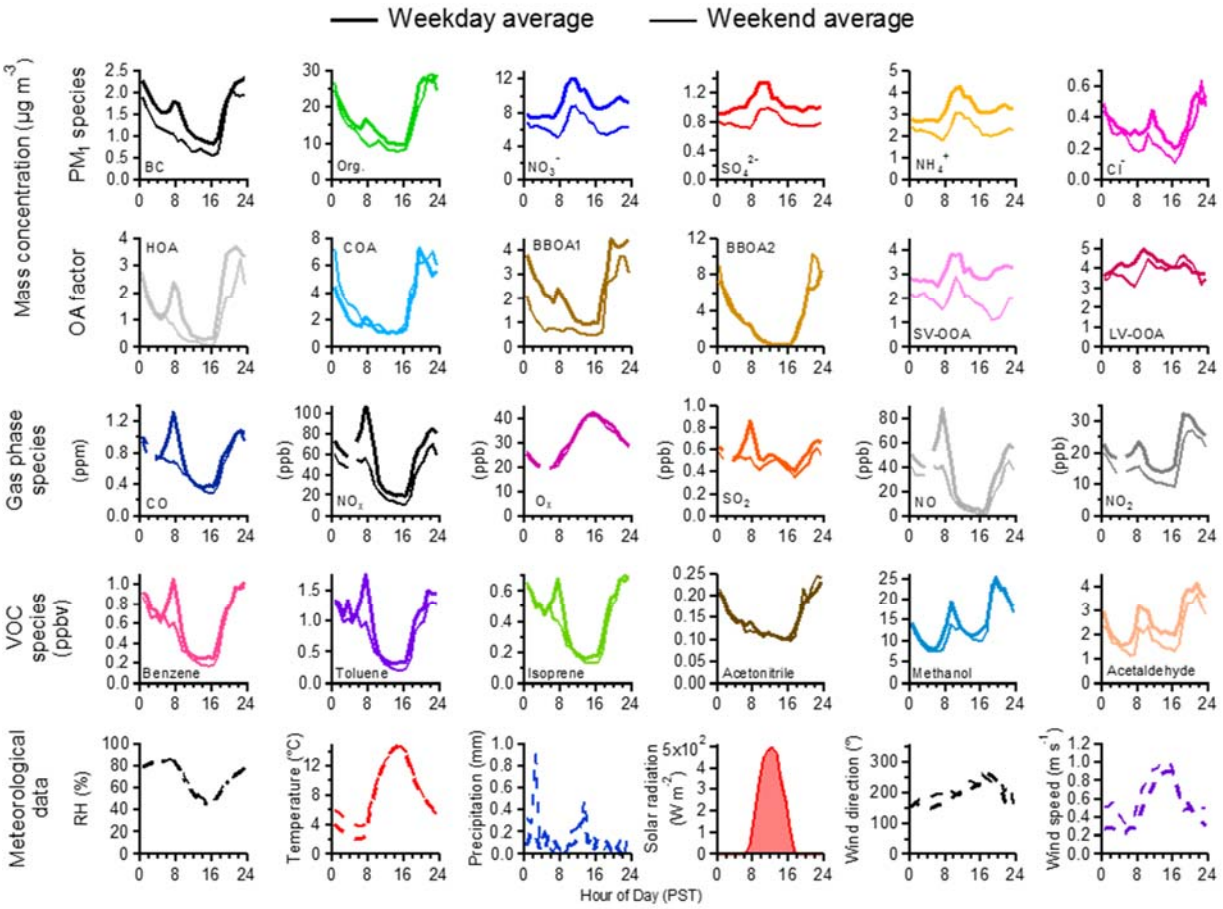

Figure 3-22: Average diurnal profiles for weekdays (Monday to Friday inclusive) and weekends (Saturday and Sunday) for the PM_1 species measured by the AMS and SP2 (top row), the six OA factors identified from PMF analysis (second row from the top), various gas phase species from the CARB monitoring station (middle row), several VOCs measured by the PTR-MS (second row from the bottom) and various meteorological parameters (bottom row). The average diurnal profiles along with the standard deviations for all species for weekdays and weekends are shown in S15.

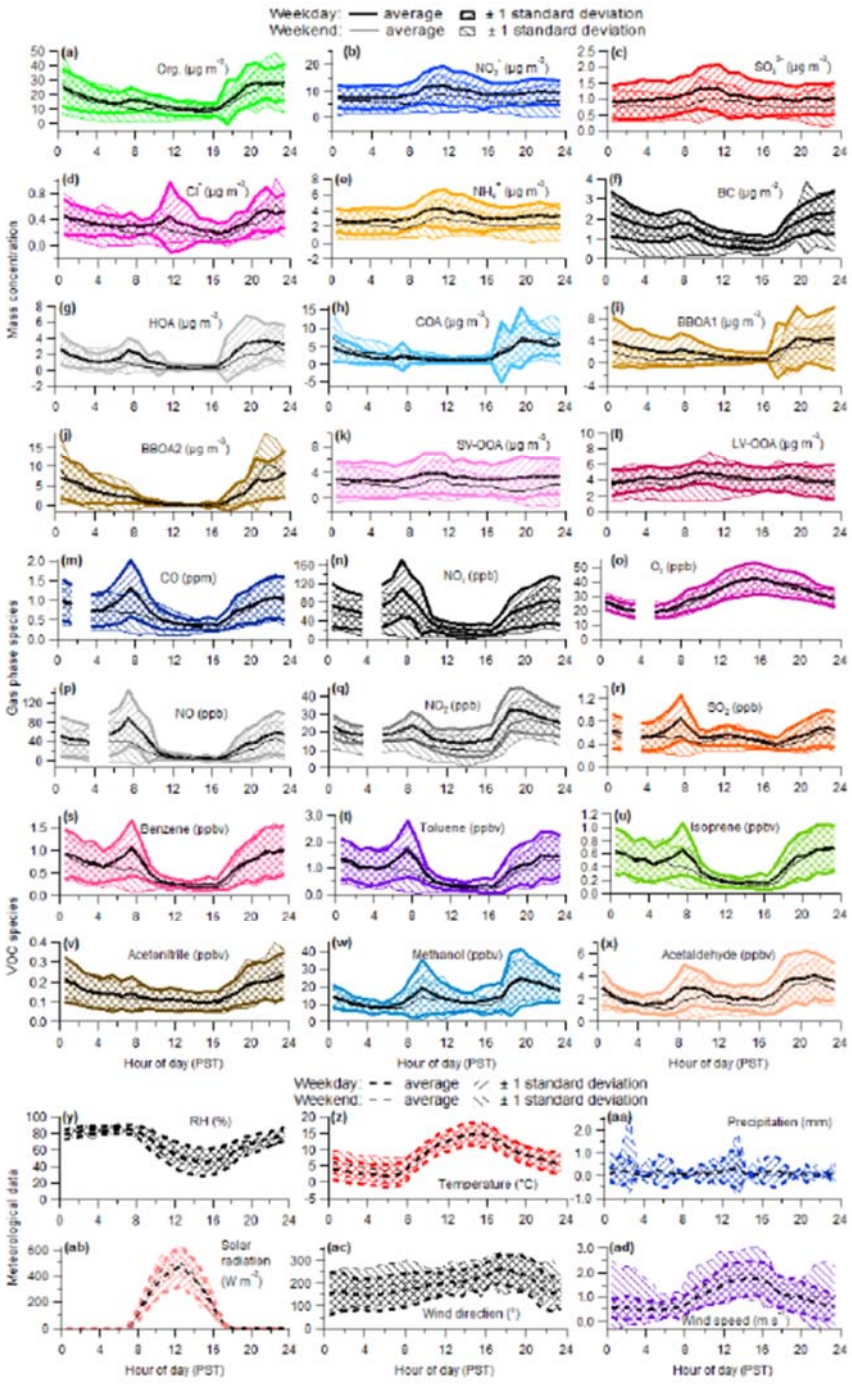

Figure 3-23: Diurnal profiles of **(a-f)** PM_1 species, **(g-l)** OA factors from PMF analysis, **(m-r)** various gas-phase species from the CARB monitoring station, **(s-x)** several VOCs measured by the PTR-TOF-MS, and **(v-ad)** various meteorological parameters. In all plots, thick lines relate to weekday diurnal variables and thin lines relate to weekend diurnal variables. Weekdays are defined as Monday-Friday, inclusive, and weekends are defined as Saturday and Sunday. Black lines represent the average diurnal profile with the hatched pattern denotes the ± one standard deviation

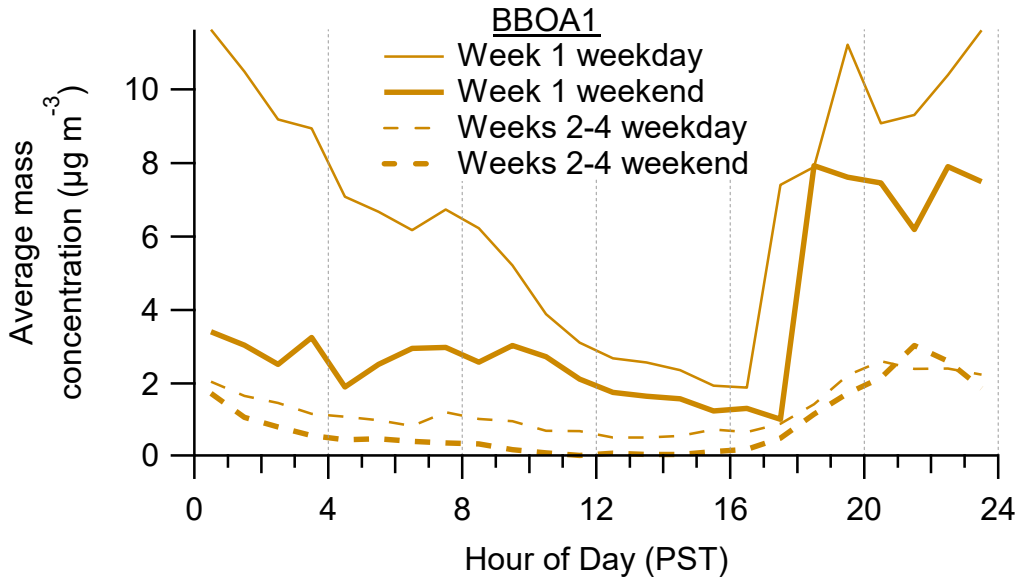

Figure 3-24: Average mass concentration diurnals for BBOA1 for the weekday and weekends for the first week of the campaign and weeks 2-4.

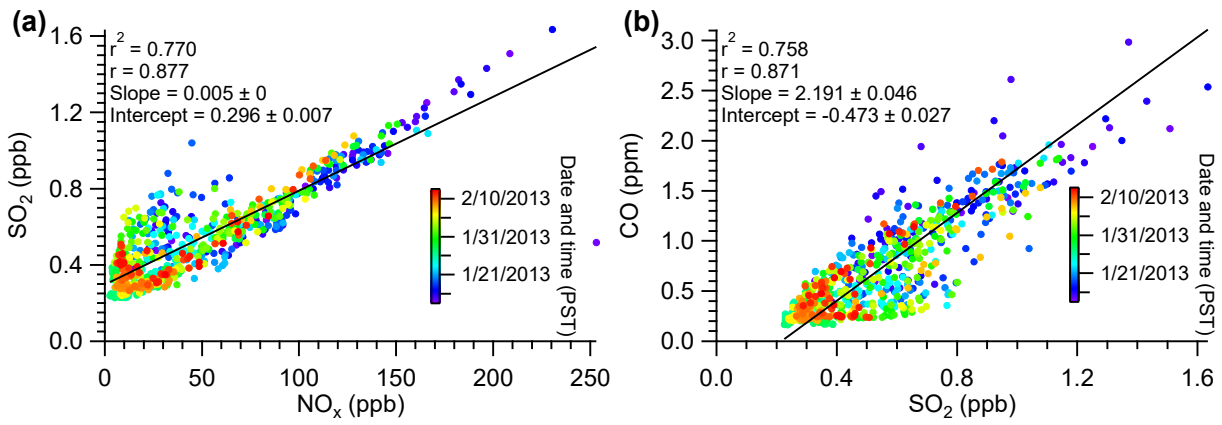

Figure 3-25: Scatter plots between various gas-phase species: **(a)** SO_2 vs. NO_x, which are gaseous precursors to particulate sulfate and nitrate, respectively; and **(b)** CO vs. SO_2, where CO is used as an indicator for boundary layer dynamics.

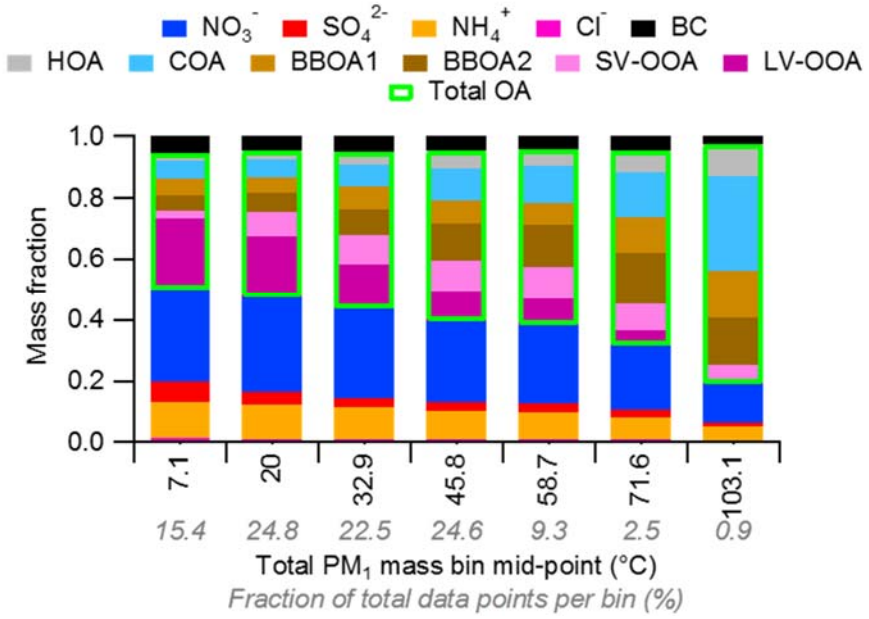

Figure 3-26: Mass fractional contribution to total PM_1 of the non-refractory secondary inorganic species (nitrate (NO_3^-), sulfate (SO_4^{2-}), ammonium (NH_4^+), chloride (Cl^-)), black carbon (BC), and the six OA factors (hydrocarbon-like OA (HOA), cooking OA (COA), biomass burning OA 1 (BBOA1), biomass burning OA 2 (BBOA2), semi-volatile oxygenated OA (SV-OOA), low volatility oxygenated OA (LV-OOA)) as a function of total PM_1 mass during the whole campaign. The green outline indicates to the fraction of total OA. Note that the final bin comprises the top four mass bins in order to improve the statistics for these high loading bins.

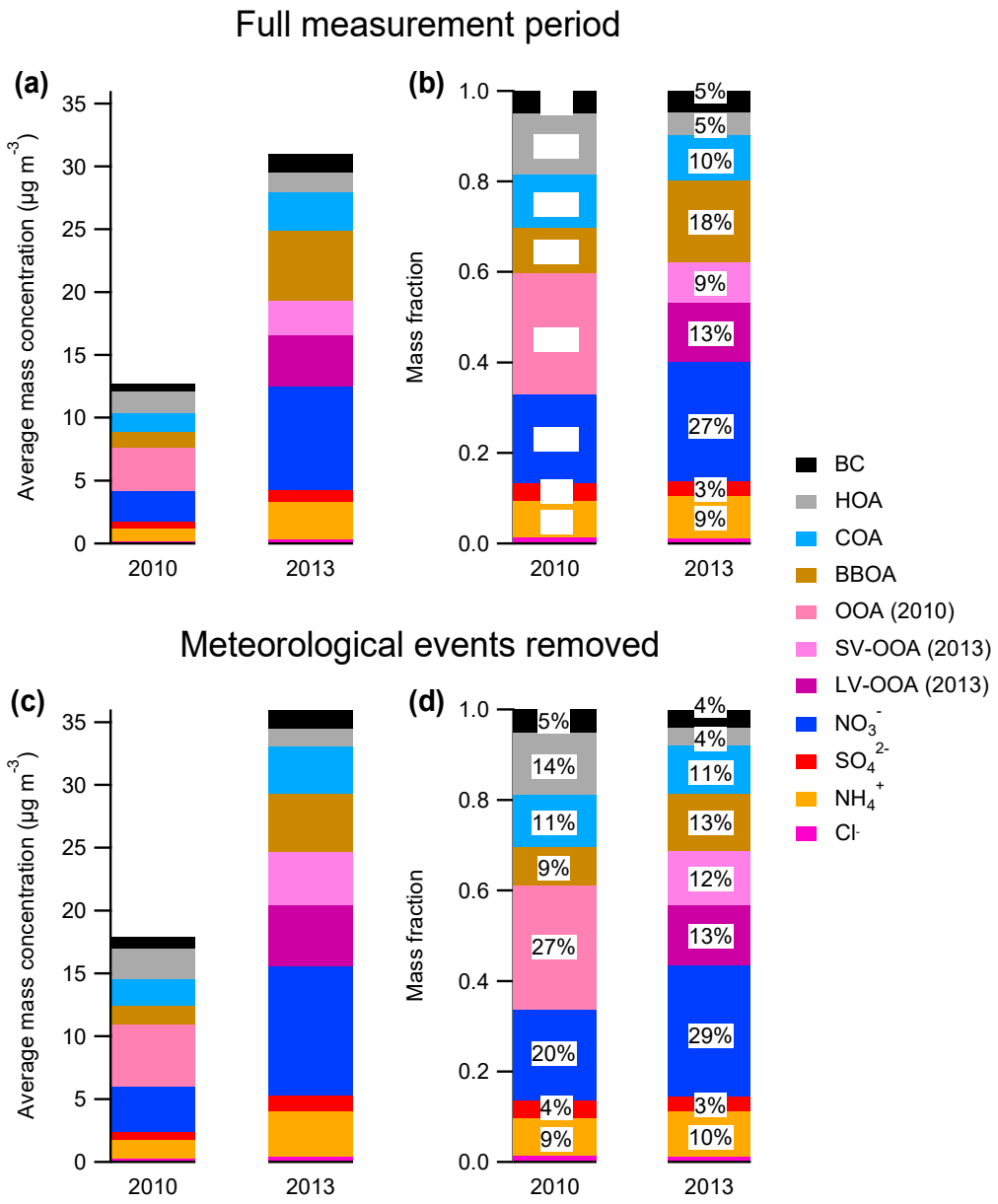

Figure 3-27: Comparison of aerosol composition between 2010 and 2013: **(a)** Mass concentrations of all PM_1 species for the full measurement period; **(b)** Fractional contributions of PM_1 species to the total PM_1 mass for the full measurement period; **(c)** and **(d)** are the same as (a) and (b) except for the fog events and precipitation events are removed from the 2010 dataset and the cold period and precipitation events are removed from the 2013 dataset. In all cases, the organic fraction has been separated into its respective components determined from PMF analysis. BBOA1 and BBOA2 from 2013 have been summed to give the total BBOA mass and fractional contributions. BC in 2010 was estimated assuming the contribution to total PM_1 mass was similar to 2013 (~5%). The contribution of chloride to total mass is 1% in all cases.

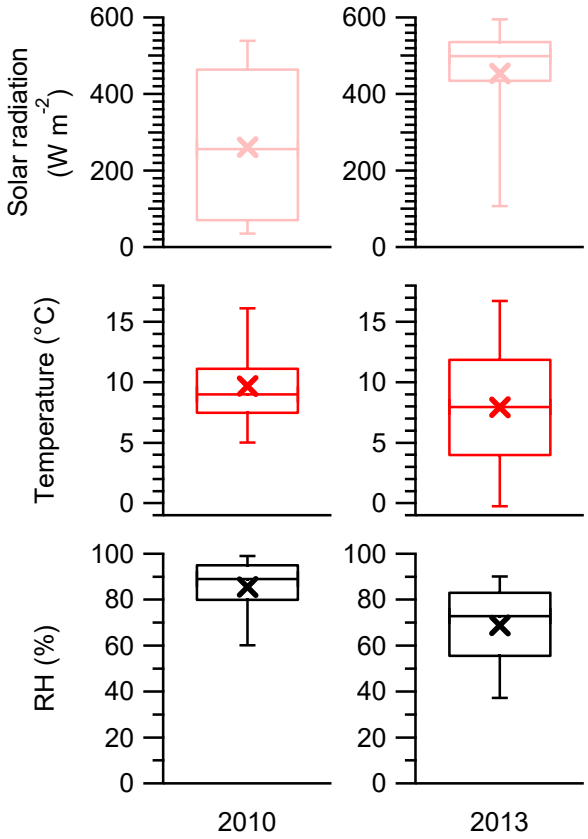

Figure 3-28: Box and whisker plots of solar radiation, temperature and RH for the winter 2010 and 2013 campaigns. Solar radiation data plotted here are for the daytime peak between 12:00 and 13:00 for both years. The 95th and 5th percentiles are denoted by the whiskers above and below the boxes, the 75th and 25th percentiles are denoted by the top and bottom of the boxes, the median values are denoted by the horizontal line within the box, and the mean values are denoted by the cross markers.

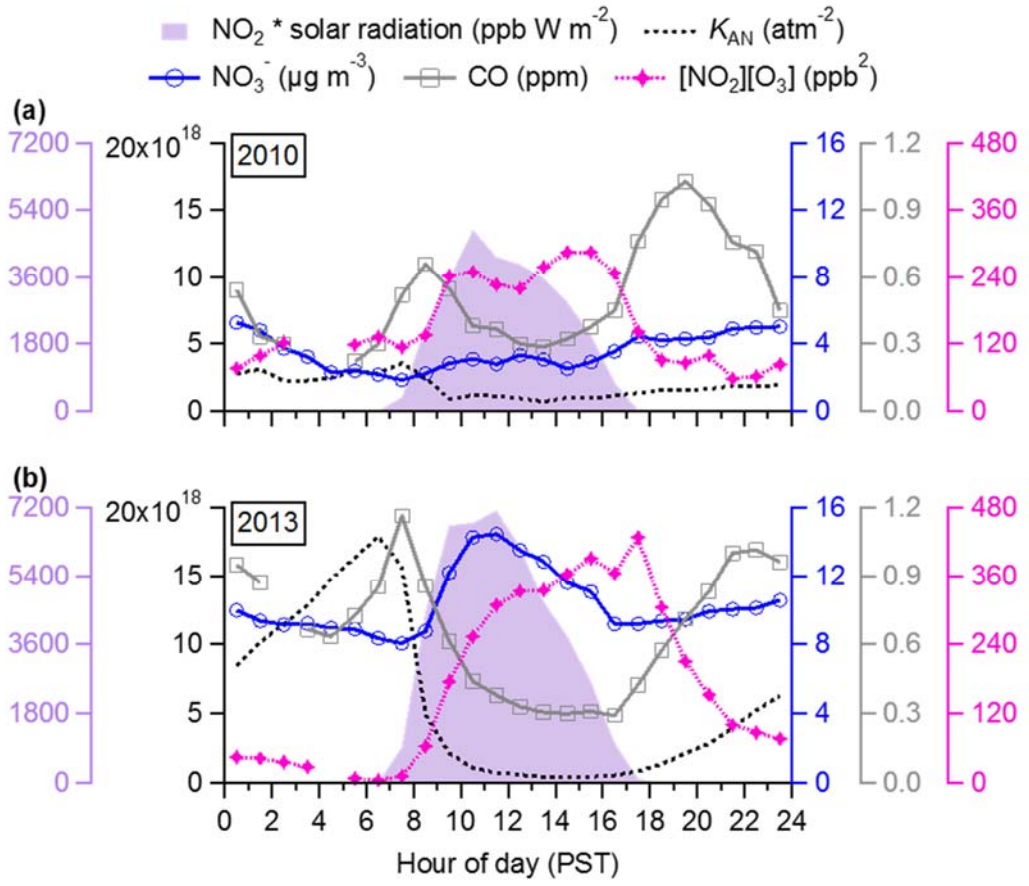

Figure 3-29: Diurnal profiles for nitrate and various parameters and proxies for formation pathways in 2010 **(a)** and 2013 **(b)**. Parameters shown include temperature, CO for boundary layer dynamics, $NO_2 \times O_3$ as a proxy for nighttime formation of HNO_3 and subsequently particulate nitrate, $NO_2 \times$solar radiation as a proxy for daytime HNO_3 formation, K_{AN} is the equilibrium constant for gas-to-particle partitioning for ammonium nitrate. As ammonium nitrate formation is dependent on temperature and humidity, fog events, cold periods, and precipitation events have been removed from the respective datasets prior to the analysis.

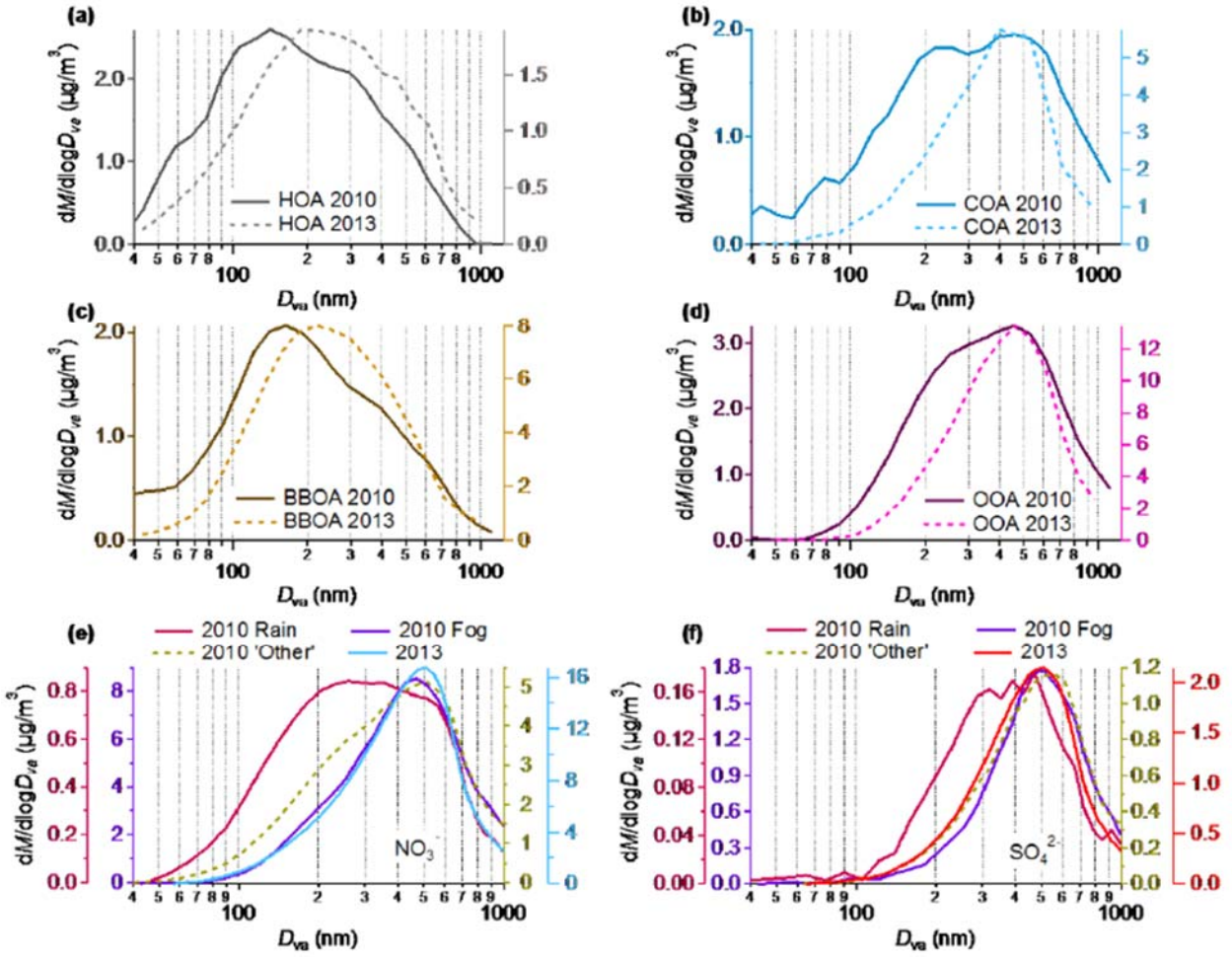

Figure 3-30: Comparisons of the average size distributions between 2013 and 2010 (Ge et al., 2012b) for the estimated size distributions of the OA factors **(a)** HOA, **(b)** COA, **(c)** BBOA, and **(d)** OOA. **(e)** and **(f)** show the average size distribution of nitrate and sulfate, respectively, from 2013 compared with the average size distribution of the same species from 2010 during different meteorological conditions, defined as rain, fog, and 'other' (see Ge et al. (2012b) for further details).

3.6 Tables

Table 3-1. Comparison of the O/C, H/C, and OM/OC ratios of total OA and the six OA factors identified from PMF analysis calculated using the Aiken-Ambient method (Aiken et al., 2008) and the Canagaratna Improved-Ambient method (Canagaratna et al., 2015).

Species	Ratio	Aiken-Ambient	Improved-Ambient
OA	O/C	0.32	0.42
	H/C	1.54	1.70
	OM/OC	1.57	1.71
HOA	O/C	0.07	0.09
	H/C	1.95	2.10
	OM/OC	1.28	1.28
COA	O/C	0.15	0.19
	H/C	1.76	1.90
	OM/OC	1.35	1.42
BBOA1	O/C	0.25	0.33
	H/C	1.56	1.74
	OM/OC	1.48	1.60
BBOA2	O/C	0.43	0.60
	H/C	1.56	1.78
	OM/OC	1.72	1.94
SV-OOA	O/C	0.50	0.63
	H/C	1.55	1.70
	OM/OC	1.84	1.98
LV-OOA	O/C	0.69	0.90
	H/C	1.38	1.57
	OM/OC	2.05	2.33

Table 3-2. Correlation coefficient (Pearson's r) for comparisons between the mass spectra of the OA factors derived in this study with reference mass spectra from Ng et al. (2010) and those determined from the winter 2010 campaign (Ge et al., 2012a).

	Reference mass spectrum	Pearson's r	2010 campaign mass spectrum	Pearson's r
HOA	HOA	0.98	HOA	0.98
COA	COA*	0.95	COA	0.99
BBOA1	BBOA	0.94	BBOA	0.91
BBOA2	BBOA	0.90	BBOA	0.97
SV-OOA	SV-OOA	0.90	OOA	0.96
LV-OOA	LV-OOA	0.84	OOA	0.95

*COA mass spectrum from Allan et al. (2010).

Table 3-3. Average (± one standard deviation), minimum and maximum concentrations of the PM_1 species and the total PM_1 mass over the whole campaign and the average contribution of each of the PM_1 species to the total PM_1 mass.

	Average concentration ± one standard deviation ($\mu g\ m^{-3}$)	Minimum concentration ($\mu g\ m^{-3}$)	Maximum concentration ($\mu g\ m^{-3}$)	Fraction of total PM_1 ± one standard deviation (%)
Organics	17.1 ± 12.2	0.38	111	55 ± 39
Nitrate	8.23 ± 5.38	0.08	28.0	27 ± 17
Sulfate	0.97 ± 0.57	0.10	3.47	3 ± 2
Ammonium	2.94 ± 1.82	0.03	9.08	9 ± 6
Chloride	0.34 ± 0.26	0.001	3.29	1 ± 1
Black carbon	1.48 ± 0.93	0.07	8.32	5 ± 3
Total PM_1	31.0 ± 17.6	0.70	130	-

Table 3-4. Correlation coefficient (Pearson's r) for linear regressions between OA factors (including the sum of both BBOA factors as well as the sum of the OOA factors) and various particle- and gas-phase species and ions.

r	HOA	COA	BBOA1	BBOA2	BBOA1 + BBOA2	SV-OOA	LV-OOA	SV-OOA + LV-OOA
Nitrate	0.14	0.15	0.16	0.00	0.08	0.88	0.59	0.88
Sulfate	0.04	0.08	-0.05	-0.08	-0.08	0.74	0.64	0.80
Ammonium	0.13	0.14	0.14	-0.01	0.06	0.87	0.62	0.89
Chloride	0.53	0.43	0.42	0.56	0.58	0.40	0.25	0.39
Org60	0.73	0.67	0.54	0.93	0.89	0.09	-0.02	0.05
CO_2^+ (AMS)	0.48	0.54	0.39	0.43	0.48	0.77	0.64	0.83
K (AMS)	0.76	0.73	0.60	0.77	0.81	0.43	0.22	0.40
PAH	0.72	0.60	0.61	0.87	0.89	-0.05	-0.18	-0.12
BC	0.76	0.58	0.60	0.79	0.83	0.24	0.06	0.19
CO	0.81	0.48	0.64	0.69	0.76	0.19	-0.03	0.12
NO_x	0.81	0.45	0.61	0.64	0.71	0.16	-0.07	0.08
Acetonitrile	0.62	0.51	0.43	0.61	0.61	0.15	0.05	0.12
Benzene	0.83	0.58	0.59	0.77	0.79	0.14	-0.02	0.09
Toluene	0.75	0.53	0.43	0.64	0.63	0.22	0.05	0.18
Acetaldehyde	0.64	0.50	0.51	0.43	0.53	0.47	0.15	0.39
Acetic acid	0.41	0.36	0.49	0.28	0.42	0.29	0.03	0.22
Acetone	0.33	0.35	0.19	0.23	0.24	0.31	0.19	0.30
Methanol	0.46	0.42	0.36	0.30	0.37	0.36	0.13	0.30
Acetone/propanal	0.29	0.33	0.12	0.20	0.19	0.29	0.20	0.29
C_8 alkylbenzenes	0.76	0.54	0.44	0.61	0.62	0.23	0.05	0.18
C_9 alkylbenzenes	0.75	0.54	0.35	0.60	0.57	0.24	0.05	0.19
Isoprene	0.83	0.61	0.51	0.72	0.72	0.24	-0.03	0.15
MVK/MACR*	0.77	0.58	0.40	0.64	0.62	0.26	0.05	0.21
Monoterpenes	0.73	0.52	0.53	0.71	0.73	0.19	-0.01	0.12
$C_2H_5N^+$	0.65	0.43	0.72	0.40	0.61	0.55	0.12	0.43
$C_3H_3O^+$	0.79	0.88	0.58	0.77	0.81	0.40	0.21	0.38
$C_3H_7^+$	0.92	0.90	0.63	0.69	0.77	0.22	0.03	0.17
$C_3H_7N^+$	0.52	0.24	0.74	0.27	0.54	0.36	0.03	0.27
$C_4H_7^+$	0.90	0.92	0.60	0.66	0.74	0.29	0.08	0.24
$C_4H_9^+$	0.95	0.87	0.62	0.68	0.76	0.18	-0.01	0.12
$C_5H_{11}^+$	0.96	0.85	0.62	0.68	0.76	0.18	-0.01	0.12
$C_5H_8O^+$	0.78	0.94	0.51	0.58	0.64	0.38	0.18	0.35
$C_6H_{10}O^+$	0.80	0.92	0.55	0.53	0.63	0.19	0.04	0.15
$C_7H_{12}O^+$	0.77	0.94	0.48	0.57	0.62	0.36	0.15	0.32
$C_9H_7^+$	0.82	0.74	0.72	0.90	0.96	0.18	-0.05	0.10
CHN^+	0.49	0.37	0.69	0.35	0.56	0.58	0.36	0.57

Table 3-4 Continued

r	HOA	COA	BBOA1	BBOA2	BBOA1 + BBOA2	SV-OOA	LV-OOA	SV-OOA + LV-OOA
CN^+	0.42	0.29	0.56	0.25	0.44	0.52	0.30	0.49
$CH_2SO_2^+$	0.01	0.07	0.00	-0.11	-0.08	0.80	0.47	0.77
$CH_3SO_2^+$	0.06	0.07	0.10	-0.06	0.00	0.81	0.45	0.76
$CH_4SO_2^+$	-0.01	0.02	0.05	-0.10	-0.05	0.77	0.44	0.73

*MVK stands for methylvinylketone and MACR stands for methacrolein.

Table 3-5. Comparison of aerosol properties and meteorological parameters between the campaign in Fresno in winter 2010 and winter 2013.

	Jan. 9 – Jan. 23, 2010	Jan. 13 – Feb. 11, 2013
Average NR-PM_1 mass concentration ± one standard deviation ($\mu g\ m^{-3}$)	11.7 ± 10.8	29.6 ± 16.9
O/C (H/C) ratio*	0.35 ± 0.07 (1.75 ± 0.08)	0.42 ± 0.10 (1.70 ± 0.05)
OA factors from PMF	HOA, COA, BBOA, OOA	HOA, COA, BBOA1, BBOA2, SV-OOA, LV-OOA
Temperature (°C) (Average ± 1σ)	9.7 ± 3.1	7.9 ± 5.2
RH (%) (Average ± 1σ)	85 ± 12	69 ± 17

*calculated using the improved Canagaratna-ambient method (Canagaratna et al., 2015).

Table 3-6. Comparison of the O/C ratios for COA from various locations calculated using the Improved-Ambient and the Aiken-Ambient methods and the associated references for where the values are reported.

Location	Improved-Ambient O/C ratio*	Reference	Aiken-Ambient O/C ratio	Reference
Barcelona	0.27	Canagaratna et al. (2015)	0.21	Mohr et al. (2012)
New York City	0.23	Canagaratna et al. (2015)	0.18	Sun et al. (2011)
Fresno	0.14	Canagaratna et al. (2015)	0.11	Ge et al. (2012a)

*Calculated and reported in the Supplement of Canagaratna et al. (2015).

4 SUMMARY AND CONCLUSIONS

Despite years of efforts, wintertime particulate matter (PM) air pollution in the San Joaquin Valley (SJV) of California remains the worst in the state, often exceeding the US Environmental Protection Agency (EPA) 24-hour standard for PM with aerodynamic diameters less than 2.5 micrometers ($PM_{2.5}$) of 35 μg m^{-3} (**Figure 4-1**). To address this problem, it is necessary that the sources and atmospheric processes that contribute to the high PM levels be understood in detail. In this study, a combination of aircraft and ground measurements made within the SJV in January and February, 2013 have been used to test, refine, and update the conceptual model of $PM_{2.5}$ in the SJV during winter. This project has served to develop clearer understanding of the sources that contribute to high-$PM_{2.5}$ episodes and the atmospheric processes—including emissions—that lead to the build-up/dissipation of the episodes.

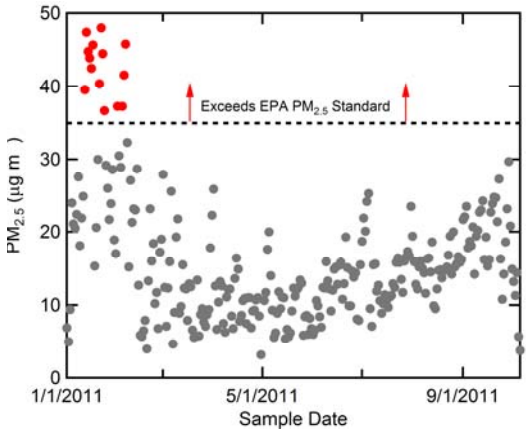

Figure 4-1. Daily average $PM_{2.5}$ concentrations at the Fresno-Drummond site during 2011. Days that exceed the EPA $PM_{2.5}$ standard are shown in red. Notice that these occur entirely during winter months.

The data used in this study were obtained during the NASA Deriving Information on Surface Conditions from COlumn and VERtically Resolved Observations Relevant to Air Quality (DISCOVER-AQ). The study took place in the SJV during January and February, 2013. The overall project aim was to assess and improve the ability of satellites to diagnose surface air quality with respect to O_3 and PM. However, the measurements made during DISCOVER-AQ were ideally suited for assessment and updating of the conceptual model of $PM_{2.5}$ formation in the SJV during winter and have been exploited in our study.

DISCOVER-AQ was a broad collaborative study with participants from three NASA centers, four universities (UC Davis, UC Berkeley, University of Maryland-Baltimore County, Innsbruck University) and research partners from agencies at federal, state and local levels including the National Center for Atmospheric Research (NCAR) and the National Oceanic and Atmospheric Administration (NOAA). Measurements of particle and gas composition and concentrations were made at (i) the Fresno-Garland ground site and (ii) onboard the NASA P-3B aircraft. A complete list of instruments used in the analysis here is provided in **Table 2-1**. Aerosol backscattering profiles were also measured from the NASA B200 aircraft. These measurements allowed for assessment of compositionally resolved diurnal profiles and temporal variability across the campaign at the Fresno-Garland ground site, and of vertical profiles of aerosols and gases above Fresno and other SJV locations three times daily (on flight day): in the morning, early afternoon and late afternoon.

Analysis of the observations at the Fresno-Garland site confirms that submicron PM is primarily composed of organic aerosol (OA) and ammonium nitrate (AN), with small contributions from ammonium sulfate. The observed large NH_3 concentrations in the region makes it such that a very large fraction of the total nitrate (the sum of gas-phase HNO_3 and particulate NH_4NO_3) is in the particulate phase under the wintertime conditions experienced. While the overall particle composition is primarily OA and AN, these exhibit distinctly different diurnal profiles (**Figure 4-2**).

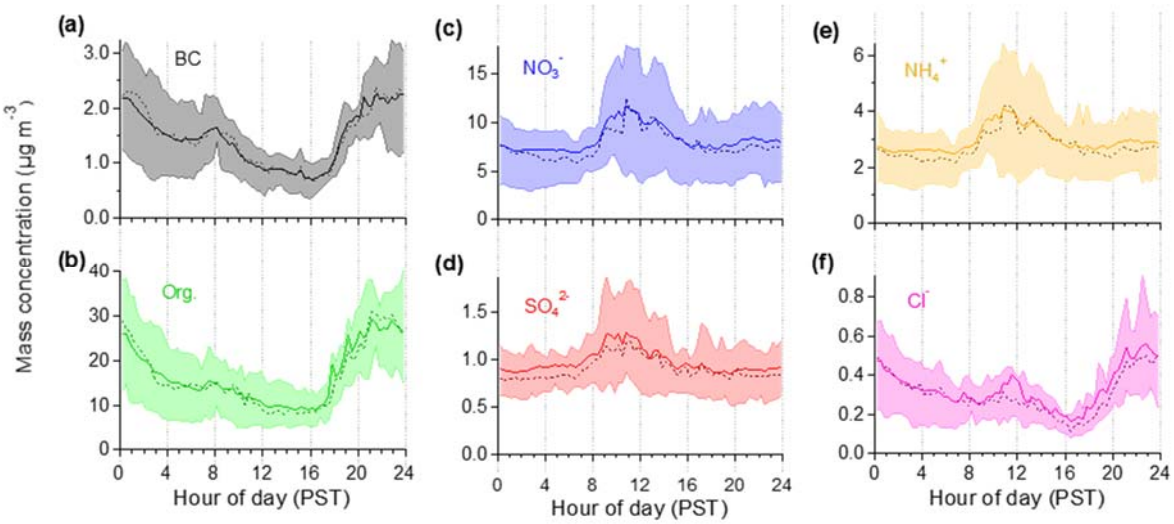

Figure 4-2. Diurnal profiles of (a) black carbon, (b) particulate organic aerosol, (c) particulate nitrate, (d) particulate sulfate, (e) particulate ammonium, and (f) particulate chloride, observed during the DISCOVER-AQ study. Adapted from **Figure 3-10**.

4.1 Organic Aerosol

In general, the ground-level OA concentrations are largest at night (**Figure 4-2**). On average, the OA is approximately 60% from primary and 40% from secondary sources. The high OA concentrations at night result from a combination of (i) a very shallow nocturnal boundary layer and (ii) substantial emissions of primary vehicle, cooking and biomass-combustion related particles. Concentrations of these primary OA types are much reduced during the daytime due to dilution resulting from entrainment of air from aloft that has low POA concentrations. The secondary OA contributes largely to a persistent, elevated background, but there is also an increase in secondary OA often observed during early morning after daybreak. Most likely, this increase reflects entrainment of air from aloft into the surface mixed layer along with some small amount of daytime production. The much reduced diurnal variability of the secondary OA compared to the primary OA likely indicates a comparably more regional source for the secondary OA.

The OA measurements were analyzed using positive matrix factorization (PMF). Six distinct sources of OA (PMF factors) were identified. Four of these were characterized as primary OA: (i)

hydrocarbon-like OA, HOA, associated with local traffic; (ii) cooking OA, COA, associated with food cooking activities; and (iii-iv) two types of biomass burning OA, BBOA, likely associated with residential wood combustion. Two factors were characterized as secondary OA: (i) a semivolatile oxygenated OA, SV-OOA, and (ii) a low-volatility oxygenated OA, LV-OOA.

On average, all of the primary OA factor concentrations exhibited a clear increase after sunset, peaking in concentration around midnight and then decreasing into the morning (**Figure 4-3**). This behavior results from a combination of there being a very shallow nocturnal boundary layer and greater emissions from some sources at night. The HOA (vehicle related) factor also showed slightly enhanced concentrations around sunrise, most likely a reflection of rush hour traffic. The two BBOA factors shared similarities in terms of their temporal variability, but also had distinct differences. One of the BBOA factors appeared to be more associated with colder temperatures, potentially reflecting different burning behavior. Also, the diurnal variability for one of the BBOA factors was more pronounced, suggesting that one might represent fresher emissions and that other a combination of fresh emissions with some regional background. However, at this point it is not entirely possible to explain the differences in behavior of the two factors in terms of their sources.

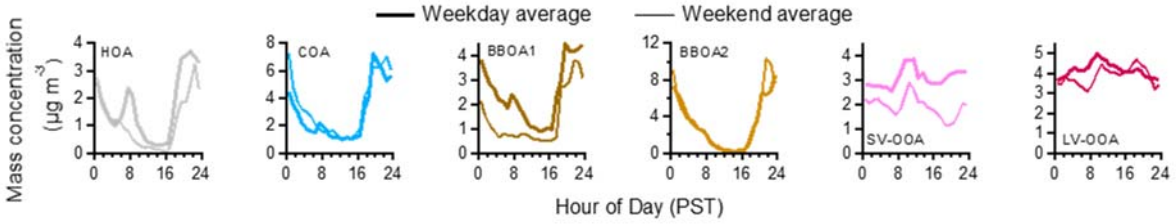

Figure 4-3. Average diurnal profiles of the six OA factors, separated by weekday (thick lines) and weekend (thin lines). Adapted from **Figure 3-22**.

On average, the two secondary OA factors exhibited relatively small diurnal variability, certainly in comparison with the primary OA factors (**Figure 4-3**). However, the SV-OOA diurnal profile did exhibit a clear increase starting around sunrise, with a peak in concentration around 11 am. This is similar to the behavior of particulate nitrate (**Figure 4-2**) and suggestive of a nocturnal source for SV-OOA that is relatively local in nature. The LV-OOA factor diurnal profile was also exhibited a small increase around sunrise, but overall the profile was relatively flat (limited dependence on time of day). This suggests that the LV-OOA is more regional in nature compared to the SV-OOA. There is some indication in the data that aqueous-phase processing plays a role in LV-OOA formation, although this requires further investigation. Also, the SV-OOA factor concentrations were lower, on average, on weekends than weekdays, similar to particulate nitrate. This is in contrast to LV-OOA, which shows minimal weekend/weekday differences. This could indicate that SV-OOA is a result of nitrate radical-driven oxidation of organic precursor gases, although further work will be necessary to establish the production mechanisms and sources for secondary OA in this region. While it is clear that secondary OA contributes substantially to the total OA burden, the identities of the precursor gases most responsible for this secondary OA remain elusive.

Because the primary OA and secondary OA exhibit distinctly different diurnal dependencies, the overall OA burden at night is dominated by the primary OA factors while during the day the secondary OA factors dominate. However, this behavior is largely driven by the very strong diurnal variability in the primary OA factors and the much weaker variability in the secondary OA factors. Thus, the diurnal variability of the total OA concentration is strong and visually most similar to the primary factors, but with an offset from zero that is determined by the secondary OA.

4.2 Ammonium Nitrate

The diurnal behavior of AN is somewhat more variable. During the two distinct pollution events observed during DISCOVER-AQ the AN concentration exhibited a sharp increase starting at daybreak (**Figure 4-2**). This increase persisted through the late morning, peaking around 10-11 am, before declining through the afternoon. Overnight the AN concentration was relatively constant. Most of the individual days during the first of the two events exhibited similar behavior to the event-average. During the second event, the AN exhibited a similar diurnal profile as the first event in the average. However, the day-to-day variability was substantial, with a number of days where the AN concentration was constant throughout the day. Complementary measurements of the average AN diurnal profile made in winter 2010 yielded an overall flat profile (i.e. limited variability). The AN concentration was also lower during 2010 than 2013 (at least for the time periods characterized). This difference in behavior of AN (in terms of concentration and diurnal variability) seems most related to differences in (i) wind speed, (ii) temperature and (iii) O_3 concentrations.

Combining the surface measurements of AN with vertical profiles of AN and other gas-phase species and meterological variables allowed for assessment of formation pathways. The observations demonstrate that nighttime formation of AN in layers above the surface have a controlling influence on daytime concentrations at the surface for these wintertime conditions.

We developed a 2D box model of particulate nitrate formation and of vertical mixing to understand and quantify the relative contributions of nighttime formation in atmospheric layers above the surface and of daytime photochemical production, and of loss processes. The model accounted for chemical formation of nitrate, temperature and RH-dependent gas-particle partitioning of ammonium nitrate, dry deposition of HNO_3 and particles, time-varying gas-precursor concentrations and time-varying entrainment of air into the surface mixed layer. The box model was constrained by the time-varying surface observations and by the vertical profiles of AN and other key species.

The observationally constrained model demonstrates that nighttime AN formation in layers above the surface (that is, in the nocturnal residual layer, NRL) is substantial. The extent of AN production in the NRL is determined largely by the initial O_3 and NO_2 concentrations, which are in turn determined by the concentrations in the well-mixed boundary layer just prior to sunset. In

the hour or so just prior to sunset the rapid decr.ease in solar heating of the surface engenders a rapid decline in the vertical (turbulent) mixing. The result is that the air that was above the surface in the mixed boundary layer at this time (~4 pm) decouples from the surface layer (**Figure 4-4**). Thus, the O_3 and NO_2 concentrations near sunset on one day can have a strong influence on the AN concentration the following day when air from the NBL is entrained to the surface (**Figure 4-5**).

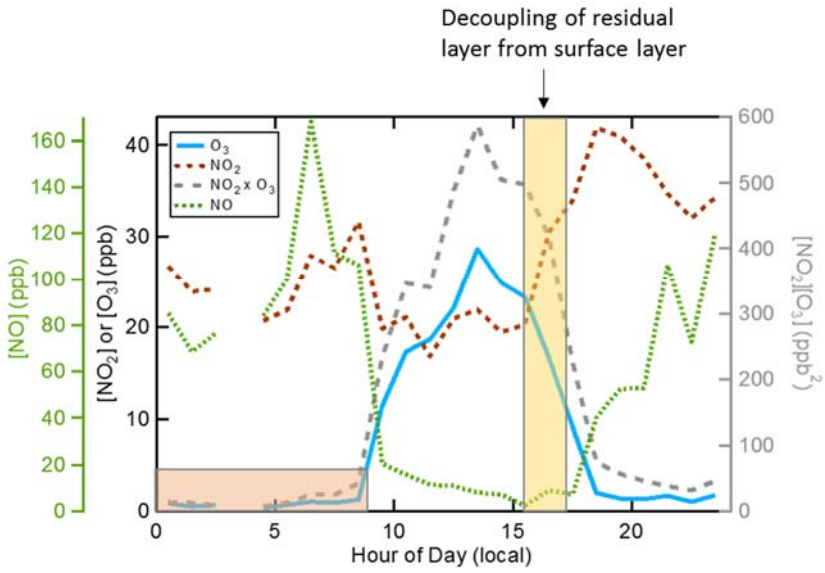

Figure 4-4. Average diurnal profile of the AN precursor gases NO, NO_2 and O_3, and the product $[NO_2][O_3]$. The yellow shaded region indicates the key time period for establishing the concentration of O_3 and NO_2 in the residual layer, and thus of AN production rates in the residual layer. The orange shaded region indicates the very low nighttime O_3 concentrations at the surface, which substantially limits AN formation at the surface overnight. Based on **Figure 2-16**.

The extent to which reaction between O_3 and NO_2 leads to AN production in the NBL is limited in two key ways: (i) by the rate of conversion of N_2O_5 into HNO_3 and (ii) by horizontal advection. NO_2 and O_3 undergo a series of reactions that form N_2O_5, with the NO_3 radical as a key intermediate. While NO_3 radicals can react with volatile organic compounds, which reduces N_2O_5 formation, we find that the concentration of VOCs that react efficiently with NO_3 is sufficiently low in the winter that this is not an important sink. The N_2O_5 is converted to HNO_3 via hydrolysis on particles. The conversion efficiency depends on particle composition, including water, and the total particle surface area for reaction. Thermodynamic calculations of the particle water content, constrained by measurements of temperature and RH, in the NRL leads to the conclusion that the conversion efficiency is relatively low. However, because the N_2O_5 has the entire night to react the net conversion into HNO_3 can still be substantial. Consideration of the vertical profiles of the gas-phase precursors, RH and T indicates that there is likely to be only small variability in the chemical production rate of AN with altitude within the NRL, absent advection.

Advection impacts local formation of AN by bringing in generally cleaner (with respect to NO_2, O_3 and AN) air from outside of city centers such as Fresno. Related, advection exports pollution from cities to the greater SJV and contributes more broadly to the regional background. The nocturnal AN production rate scales approximately as the product of [NO_2] and [O_3]. There is a strong gradient in [NO_2] from population centers, and a weaker gradient in [O_3]. Thus, dilution via advection limits the extent of AN formation over cities, largely through a decrease in the NO_2. However, AN formation likely occurs in the NRL throughout the SJV, just faster and to a greater extent near population centers. Advection also serves to reduce the concentration in the NRL locally above population centers such as Fresno. This has consequences for the AN pollution that is experienced at the surface when air from the NRL is entrained to the surface following sunrise. We show, using the day-to-day evolution of AN vertical profiles, that advection within the NRL varies with altitude, leading to a reshaping of the vertical profile overnight and affecting both the timing and magnitude of the late-morning peak in AN at the surface (**Figure 4-5**).

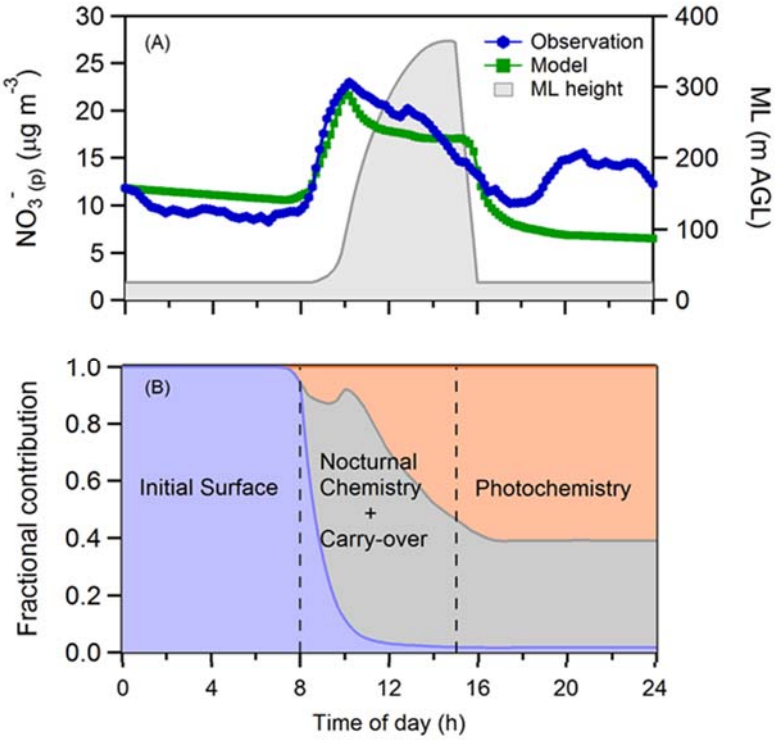

Figure 4-5. (a) The observed average diurnal variability in particulate nitrate (blue) for the first pollution episode and the result from the observationally constrained box-model calculations (green). The temporal variation in the mixed layer height (gray) is shown for reference. **(b)** The average fractional contribution to the surface-level AN concentration over the course of a day, with contributions from what was initially at the surface (blue), what was formed in the residual layer overnight and mixed down to the surface (gray), and what was photochemically produced (orange). Based on **Figure 2-20**.

The wintertime daytime mixed layer height and, especially, the nocturnal boundary layer height are very shallow. We find that the NBL height may only be a few tens of meters during strong pollution episodes when wind speeds are low. The NBL height may be only ~5% of the daytime mixed layer height. Consequently, chemical production of AN and other PM components (e.g. SOA) in the NRL can have a substantial impact on daytime surface concentrations, especially in the mid-to-late morning. Nighttime production of AN at the surface is found to be negligible. Primary NO_x emissions are primarily in the form of NO, and the very shallow NBL means that NO concentrations can build up to be quite large, many times larger than O_3. This can lead to nearly complete titration of O_3 in the NBL (unlike in the NRL), which substantially suppresses AN formation at the surface.

Daytime AN production is slow, but non-negligible (**Figure 4-5**). Ammonium nitrate in the daytime is formed from reaction of NO_2 with OH to form HNO_3, and subsequent condensation of HNO_3 onto particles to form AN. While wintertime OH concentrations are lower than those in summer, they are nonetheless sufficiently high for substantial conversion of NO_2 to HNO_3 to occur.

Besides advection, there are two additional important mechanisms for AN loss. The first is the dry deposition of HNO_3 gas. Dry deposition velocities of sticky gases such as HNO_3 are much larger than for particles. Dry deposition of HNO_3 represents a sink for AN because the AN will evaporate in response to a change in the gas-particle equilibrium. We find, however, that loss via this evaporation-deposition mechanism is limited in importance. The SJV has a large excess of ammonia. Consequently, most HNO_3 is condensed onto particles in the form of AN. This strongly limits loss. Additionally, the gas-particle partitioning is temperature dependent. While there is a somewhat larger (although still small) fraction of gas-phase nitrate during the day due to warmer temperatures and lower RH, the mixed layer during the day is highest. This limits deposition because the deposition loss rate scales as the inverse of the mixed layer height. At night, when the mixed layer is very shallow and deposition could theoretically proceed faster, the lower temperatures and higher RH lead to nearly all nitrate being in the particulate phase. Thus, dry deposition at night is negligible. However, right near sunset, when temperatures are declining yet still relatively high and the mixed layer height is shallow, HNO_3 deposition and AN evaporation can be temporarily enhanced, leading to a temporary decline

The second important loss mechanism is daytime entrainment and dilution. This differs from advection in that, once the daytime mixed layer is fully grown, air is exchanged with the (typically) much cleaner free troposphere. Estimated entrainment rates indicate that this can substantially reduce AN concentrations (as well as the concentrations of other pollutant species) within the mixed layer during the daytime. This entrainment offsets or even overwhelms much of the daytime photochemical production. Entrainment of cleaner free tropospheric air serves as a net pollution sink for the entire SJV, both within and outside of pollution centers. This is in contrast to horizontal

advection, which can reduce peak concentrations within pollution centers (i.e. cities), but does not actually remove pollution from the SJV as a whole, only spreads it out.

Overall, our observations and box-modeling lead to the following conceptual model of ammonium nitrate dynamics over population centers within the SJV, and in the SJV as a whole.

- Nocturnal formation of AN within the nocturnal residual layer is a key production mechanism. The extent of formation in the NRL depends largely on the NO_2 and O_3 concentrations that exist just prior to sunset, as these feed the NRL.
- When wind speeds are low, nocturnal AN production in the NRL can be substantial over pollution centers. Entrainment of the NRL air to the surface can lead to substantial increases and very large concentrations of AN at the surface in the mid-to-late morning, after sunrise. The AN concentrations in the morning after sunrise are controlled almost entirely by processes that occurred overnight in the NRL, given the very shallow nocturnal boundary layer.
- When wind speeds are higher, export of NO_2 from pollution centers via horizontal advection limits local AN formation but contributes to a regional background of AN. There will be less of a contrast between the AN concentration within the NBL and the NRL over cities, and thus there will be a much smaller change in the AN concentration at the surface in the morning.
- Variability in nocturnal advection with altitude has a strong influence on the shape of the AN vertical profile in the early morning, and consequently on the timing and peak concentration of AN at the surface in the mid-to-late morning as air from the NRL is entrained to the surface mixed layer.
- Nocturnal formation of AN at the surface is substantially limited within pollution centers by titration of O_3 by NO as a consequence of the very shallow nocturnal boundary layer.
- Daytime formation of AN via NO_2 photooxidation is an important production mechanism within pollution centers where daytime NO_2 is somewhat elevated.
- Entrainment of typically cleaner free tropospheric air is maximum during the daytime and a substantial sink for AN and other pollutants. The rate of free troposphere entrainment (and associated dilution) is similar to the photochemical production rate and with similar timing, such that these can be largely offsetting. Entrainment of free troposphere air is the key AN sink during pollution episodes.
- Dry deposition of HNO_3 as a sink for AN is strongly limited by the excess of NH_3 and low nighttime temperatures. The $[NH_3]:([HNO_3]+[\text{particulate } NO_3])$ ratio is sufficiently large that reductions in this ratio through ammonia control are unlikely to have a substantial impact on AN concentrations.
- Strong AN-driven pollution episodes occur when production of AN exceeds loss day after day. This is largely controlled by processes that occur in the nocturnal residual layer, but modulated through feedbacks that occur through advection of NO_2 from cities to surroundings and through daytime production and loss.

5 RECOMMENDATIONS

This project demonstrates that 24-h average $PM_{2.5}$ concentrations during pollution events result from high concentrations of both OA and AN. The sources and processes that determine the ambient OA and AN concentrations differ and impact the temporal variability. OA concentrations are highest at night, and AN concentrations highest during the day, in general. Because these are out of phase (with respect to time of day), the combination of the two serves to keep total $PM_{2.5}$ concentrations elevated throughout the day, impacting the 24-h average.

Currently, high surface concentrations of OA during pollution events are particularly related to strong surface emissions at night from vehicles, cooking and biomass burning (most likely from residential wood combustion), with the latter being most important. That emissions from these sources give rise to especially high OA concentrations is strongly linked to the very shallow nocturnal boundary layer heights that can occur in wintertime in the SJV. Reduction in emissions from these primary sources should directly lead to reductions in OA concentrations at night. However, OA from secondary production is found to also make up a substantial fraction of the total OA burden, contributing to elevated concentrations during both daytime and nighttime. The major sources of the precursor gases and the pathways that control the formation of this secondary OA remain ill-understood. Thus, future efforts to understand the sources of the secondary OA are necessary. It may be that the same sources of primary OA (vehicles, cooking, biomass burning) are also the sources of the secondary OA precursors, but this is unknown. It is also unclear whether this secondary OA is derived primarily through daytime photochemical production, nocturnal chemical production, or through fog-water chemistry. Understanding the major formation pathways and sources for secondary OA would allow for development of targeted control strategies.

Ammonium nitrate concentrations tend to be elevated during the daytime. However, the formation of AN results from both nighttime and daytime chemical processes. Much of the nighttime production currently occurs in atmospheric layers in the few 100's of meters above the surface; production in these above-surface layers does not directly impact surface concentrations at night, but does impact surface concentrations during the daytime when the air from aloft is mixed to the surface. The AN production rate at night in these layers aloft is directly dependent on the daytime NO_2 and O_3. Thus, reductions in either NO_x or daytime O_3 will lead to reductions in nocturnal production in the layers aloft, so long as the other does not increase. Efforts to understand the effectiveness of AN control targeting this nighttime pathway via reduction in NO_x must account for potential feedbacks on daytime production of O_3. Nonetheless, reduction of NO_x is likely to have a direct impact on AN production and concentrations via this nighttime pathway.

The daytime AN production results from photochemical reaction between NO_2 and OH. Reductions in NO_2 may lead to reductions in AN, but negative feedbacks between NO_2 reductions and OH production can substantially offset AN reductions; it may be that substantial reductions in

daytime AN formation will only be observed when NO_x is reduced to a very large extent. Full understanding of the extent of NO_x reductions necessary to decrease daytime AN formation requires fuller knowledge of the major processes that control OH concentrations in the wintertime SJV, which depend non-linearly on the concentrations of OH precursors, NO_x and VOC concentrations. Monitoring of formaldehyde (CH_2O), nitrous acid (HONO) and OH reactivity and VOC concentrations may prove useful.

There is limited direct nocturnal surface production currently as a result of the nearly complete titration of O_3 that occurs due to high surface NO concentrations in the nocturnal boundary layer, which is a result of the very shallow boundary layer height during pollution events coupled with nighttime NO sources. In the future, it will be important to pay attention to changes in the nighttime surface O_3 concentrations and how these respond to changes in NO_x; if surface nocturnal O_3 increases it may be that nocturnal surface AN production will become important. An investigation into the long-term, diurnal behavior of surface O_3 concentrations, both during and outside of strong pollution episodes, using historical data may provide further guidance.

Ammonium nitrate results from reaction between nitric acid (HNO_3)) and ammonia (NH_3) gas; AN is in equilibrium with HNO_3 and NH_3, with the equilibrium dependent on ambient temperature and particle water content via the relative humidity. Currently, ammonia is in great excess over HNO_3, so most nitrate is in the form of ammonium nitrate, that is contributes to the $PM_{2.5}$ burden. Theoretically, reductions in NH_3 could lead to reduction of AN via evaporation into HNO_3 and NH_3. However, the extent to which NH_3 concentrations would have to be reduced to have any meaningful impact on AN concentrations are sufficiently large to be infeasible, and would have to occur in the absence of any decrease in nitrate. Thus, control of NH_3 is not recommended at this point in time as an effective control strategy for AN pollution.

6 REFERENCES

Aiken, A. C., Decarlo, P. F., Kroll, J. H., Worsnop, D. R., Huffman, J. A., Docherty, K. S., Ulbrich, I. M., Mohr, C., Kimmel, J. R., Sueper, D., Sun, Y., Zhang, Q., Trimborn, A., Northway, M., Ziemann, P. J., Canagaratna, M. R., Onasch, T. B., Alfarra, M. R., Prévôt, A. S. H., Dommen, J., Duplissy, J., Metzger, A., Baltensperger, U., and Jimenez, J. L.: O/C and OM/OC ratios of primary, secondary, and ambient organic aerosols with high-resolution time-of-flight aerosol mass spectrometry, Environ. Sci. Technol., 42, 4478-4485, 10.1021/Es703009q, 2008.

Aiken, A. C., Salcedo, D., Cubison, M. J., Huffman, J. A., DeCarlo, P. F., Ulbrich, I. M., Docherty, K. S., Sueper, D., Kimmel, J. R., Worsnop, D. R., Trimborn, A., Northway, M., Stone, E. A., Schauer, J. J., Volkamer, R. M., Fortner, E., de Foy, B., Wang, J., Laskin, A., Shutthanandan, V., Zheng, J., Zhang, R., Gaffney, J., Marley, N. A., Paredes-Miranda, G., Arnott, W. P., Molina, L. T., Sosa, G., and Jimenez, J. L.: Mexico City aerosol analysis during MILAGRO using high resolution aerosol mass spectrometry at the urban supersite (T0) – Part 1: Fine particle composition and organic source apportionment, Atmos. Chem. Phys., 9, 6633-6653, 10.5194/acp-9-6633-2009, 2009.

Akira, K., Akikazu, K., Kiyoshi, I., Yoshio, I., Masahiko, S., Lal, S. M., and Balkrishan, S.: Investigation of air pollution concentration in Kalthmandu valley during winter season, Journal of Environmental Sciences, 17, 1008-1013, 1001-0742(2005)06-1008-06, 2005.

Alfarra, M. R., Coe, H., Allan, J. D., Bower, K. N., Boudries, H., Canagaratna, M. R., Jimenez, J. L., Jayne, J. T., Garforth, A. A., Li, S.-M., and Worsnop, D. R.: Characterization of urban and rural organic particulate in the Lower Fraser Valley using two Aerodyne Aerosol Mass Spectrometers, Atmos. Environ., 38, 5745-5758, 10.1016/j.atmosenv.2004.01.054, 2004.

Alfarra, M. R., Prevot, A. S. H., Szidat, S., Sandradewi, J., Weimer, S., Lanz, V. A., Schreiber, D., Mohr, M., and Baltensperger, U.: Identification of the Mass Spectral Signature of Organic Aerosols from Wood Burning Emissions, Environ. Sci. Technol., 41, 5770-5777, 10.1021/es062289b, 2007.

Allan, J. D., Delia, A. E., Coe, H., Bower, K. N., Alfarra, M. R., Jimenez, J. L., Middlebrook, A. M., Drewnick, F., Onasch, T. B., Canagaratna, M. R., Jayne, J. T., and Worsnop, D. R.: A generalised method for the extraction of chemically resolved mass spectra from aerodyne aerosol mass spectrometer data, J Aerosol Sci, 35, 909-922, 10.1016/j.jaerosci.2004.02.007, 2004.

Allan, J. D., Williams, P. I., Morgan, W. T., Martin, C. L., Flynn, M. J., Lee, J., Nemitz, E., Phillips, G. J., Gallagher, M. W., and Coe, H.: Contributions from transport, solid fuel burning and cooking to primary organic aerosols in two UK cities, Atmos. Chem. Phys., 10, 647-668, 10.5194/acp-10-647-2010, 2010.

State of the air: 2014 report: http://www.stateoftheair.org/2014/assets/ALA-SOTA-2014-Full.pdf, access: 3 April 2017, 2014.

Association, A. L.: State of the Air: 2015 Report, http://www.lung.org/local-content/california/our-initiatives/state-of-the-air/2015/state-of-the-air-2015.html, 2015.

Baasandorj, M., Hoch, S. W., Bares, R., Lin, J. C., Brown, S. S., Millet, D. B., Martin, R., Kelly, K., Zarzana, K. J., Whiteman, C. D., Dube, W. P., Tonnesen, G., Jaramillo, I. C., and Sohl, J.:

Coupling between Chemical and Meteorological Processes under Persistent Cold-Air Pool Conditions: Evolution of Wintertime PM2.5 Pollution Events and N2O5 Observations in Utah's Salt Lake Valley, Environ. Sci. Technol., 10.1021/acs.est.6b06603, 2017.

Bao, J.-W., Michelson, S. A., Persson, P. O. G., Djalalova, I. V., and Wilczak, J. M.: Observed and WRF-Simulated Low-Level Winds in a High-Ozone Episode during the Central California Ozone Study, J. Appl. Meteor. Clim., 47, 2372-2394, doi:10.1175/2008JAMC1822.1, 2008.

Bertram, T. H., Thornton, J. A., Riedel, T. P., Middlebrook, A. M., Bahreini, R., Bates, T. S., Quinn, P. K., and Coffman, D. J.: Direct observations of N2O5 reactivity on ambient aerosol particles, Geophys. Res. Lett., 36, L19803, 10.1029/2009gl040248, 2009.

Beyersdorf, A. J., Ziemba, L. D., Chen, G., Corr, C. A., Crawford, J. H., Diskin, G. S., Moore, R. H., Thornhill, K. L., Winstead, E. L., and Anderson, B. E.: The impacts of aerosol loading, composition, and water uptake on aerosol extinction variability in the Baltimore–Washington, D.C. region, Atmos. Chem. Phys., 16, 1003-1015, 10.5194/acp-16-1003-2016, 2016.

Bianco, L., Djalalova, I. V., King, C. W., and Wilczak, J. M.: Diurnal Evolution and Annual Variability of Boundary-Layer Height and Its Correlation to Other Meteorological Variables in California's Central Valley, Boundary Layer Meteor., 140, 491-511, 10.1007/s10546-011-9622-4, 2011.

Bigi, A., Ghermandi, G., and Harrison, R. M.: Analysis of the air pollution climate at a background site in the Po valley, J. Environ. Monitoring, 14, 552-563, 10.1039/C1EM10728C, 2012.

Borbon, A., Fontaine, H., Veillerot, M., Locoge, N., Galloo, J. C., and Guillermo, R.: An investigation into the traffic-related fraction of isoprene at an urban location, Atmos. Environ., 35, 3749-3760, http://dx.doi.org/10.1016/S1352-2310(01)00170-4, 2001.

Brent, L. C., Thorn, W. J., Gupta, M., Leen, B., Stehr, J. W., He, H., Arkinson, H. L., Weinheimer, A., Garland, C., Pusede, S. E., Wooldridge, P. J., Cohen, R. C., and Dickerson, R. R.: Evaluation of the use of a commercially available cavity ringdown absorption spectrometer for measuring NO2 in flight, and observations over the Mid-Atlantic States, during DISCOVER-AQ, J. Atmos. Chem., 72, 503-521, 10.1007/s10874-013-9265-6, 2015.

Brito, J., Rizzo, L. V., Morgan, W. T., Coe, H., Johnson, B., Haywood, J., Longo, K., Freitas, S., Andreae, M. O., and Artaxo, P.: Ground-based aerosol characterization during the South American Biomass Burning Analysis (SAMBBA) field experiment, Atmos. Chem. Phys., 14, 12069-12083, 10.5194/acp-14-12069-2014, 2014.

Brown, S. G., Hyslop, N. P., Roberts, P. T., McCarthy, M. C., and Lurmann, F. W.: Wintertime Vertical Variations in Particulate Matter (PM) and Precursor Concentrations in the San Joaquin Valley during the California Regional Coarse PM/Fine PM Air Quality Study, J. Air & Waste Manage. Assoc., 56, 1267-1277, 10.1080/10473289.2006.10464583, 2006a.

Brown, S. G., Roberts, P. T., McCarthy, M. C., Lurmann, F. W., and Hyslop, N. P.: Wintertime vertical variations in particulate matter (PM) and precursor concentrations in the San Joaquin Valley during the California Regional coarse PM/fine PM Air Quality Study, J. Air & Waste Manage. Assoc., 56, 1267-1277, 2006b.

Brown, S. S., Neuman, J. A., Ryerson, T. B., Trainer, M., Dubé, W. P., Holloway, J. S., Warneke, C., de Gouw, J. A., Donnelly, S. G., Atlas, E., Matthew, B., Middlebrook, A. M., Peltier, R., Weber, R. J., Stohl, A., Meagher, J. F., Fehsenfeld, F. C., and Ravishankara, A. R.: Nocturnal odd-

oxygen budget and its implications for ozone loss in the lower troposphere, Geophys. Res. Lett., 33, L08801, 10.1029/2006GL025900, 2006c.

Brown, S. S., Ryerson, T. B., Wollny, A. G., Brock, C. A., Peltier, R., Sullivan, A. P., Weber, R. J., Dube, W. P., Trainer, M., Meagher, J. F., Fehsenfeld, F. C., and Ravishankara, A. R.: Variability in nocturnal nitrogen oxide processing and its role in regional air quality, Science, 311, 67-70, 10.1126/science.1120120, 2006d.

Brown, S. S., Ryerson, T. B., Wollny, A. G., Brock, C. A., Peltier, R., Sullivan, A. P., Weber, R. J., Dubé, W. P., Trainer, M., Meagher, J. F., Fehsenfeld, F. C., and Ravishankara, A. R.: Variability in Nocturnal Nitrogen Oxide Processing and Its Role in Regional Air Quality, Science, 311, 67-70, 10.1126/science.1120120, 2006e.

Burkholder, J. B., Sander, S. P., Abbatt, J., Barker, J. R., Huie, R. E., Kolb, C. E., Kurylo, M. J., Orkin, V. L., Wilmouth, D. M., and Wine, P. H.: Chemical Kinetics and Photochemical Data for Use in Atmospheric Studies, Evaluation No. 18, 11/2/2016, Jet Propulsion Laboratory, Pasadena, 2015, http://jpldataeval.jpl.nasa.gov.

Cabañas, B., Salgado, S., Martín, P., Baeza, M. T., and Martínez, E.: Night-time Atmospheric Loss Process for Unsaturated Aldehydes: Reaction with NO3 Radicals, J. Phys. Chem. A, 105, 4440-4445, 10.1021/jp0029459, 2001.

Canagaratna, M. R., Jayne, J. T., Ghertner, D. A., Herndon, S., Shi, Q., Jimenez, J. L., Silva, P. J., Williams, P., Lanni, T., Drewnick, F., Demerjian, K. L., Kolb, C. E., and Worsnop, D. R.: Chase studies of particulate emissions from in-use New York City vehicles, Aerosol Sci. Technol., 38, 555-573, 10.1080/02786820490465504, 2004.

Canagaratna, M. R., Jayne, J. T., Jimenez, J. L., Allan, J. D., Alfarra, M. R., Zhang, Q., Onasch, T. B., Drewnick, F., Coe, H., Middlebrook, A., Delia, A., Williams, L. R., Trimborn, A. M., Northway, M. J., DeCarlo, P. F., Kolb, C. E., Davidovits, P., and Worsnop, D. R.: Chemical and microphysical characterization of ambient aerosols with the aerodyne aerosol mass spectrometer, Mass Spectrom Rev, 26, 185-222, 10.1002/Mas.20115, 2007.

Canagaratna, M. R., Jimenez, J. L., Kroll, J. H., Chen, Q., Kessler, S. H., Massoli, P., Hildebrandt Ruiz, L., Fortner, E., Williams, L. R., Wilson, K. R., Surratt, J. D., Donahue, N. M., Jayne, J. T., and Worsnop, D. R.: Elemental ratio measurements of organic compounds using aerosol mass spectrometry: characterization, improved calibration, and implications, Atmos. Chem. Phys., 15, 253-272, 10.5194/acp-15-253-2015, 2015.

Cappa, C. D., Onasch, T. B., Massoli, P., Worsnop, D. R., Bates, T. S., Cross, E. S., Davidovits, P., Hakala, J., Hayden, K. L., Jobson, B. T., Kolesar, K. R., Lack, D. A., Lerner, B. M., Li, S.-M., Mellon, D., Nuaaman, I., Olfert, J. S., Petäjä, T., Quinn, P. K., Song, C., Subramanian, R., Williams, E. J., and Zaveri, R. A.: Radiative Absorption Enhancements Due to the Mixing State of Atmospheric Black Carbon, Science, 337, 1078-1081, 10.1126/science.1223447, 2012.

Carslaw, D.: The openair manual — open-source tools for analysing air pollution data., Manual for version 1.1-4, King's College London., 2015.

Carslaw, D. C., and Ropkins, K.: openair — An R package for air quality data analysis, Environmental Modelling & Software, 27-28, 52-61, 10.1016/j.envsoft.2011.09.008, 2012.

Chen, L. W. A., Watson, J. G., Chow, J. C., and Magliano, K. L.: Quantifying PM2.5 source contributions for the San Joaquin Valley with multivariate receptor models, Environ. Sci. Technol., 41, 2818-2826, 10.1021/Es0225105, 2007.

Chow, J. C., Watson, J. G., Lowenthal, D. H., Solomon, P. A., Magliano, K. L., Ziman, S. D., and Richards, L. W.: Pm(10) and Pm(2.5) Compositions in California San Joaquin Valley, Aerosol Sci. Technol., 18, 105-128, 1993.

Chow, J. C., Watson, J. G., Lowenthal, D. H., Hackney, R., Magliano, K., Lehrman, D., and Smith, T.: Temporal variations of PM2. 5, PM10, and gaseous precursors during the 1995 integrated monitoring study in central California, J. Air & Waste Manage. Assoc., 49, 16-24, 1999.

Chow, J. C., Chen, L. W. A., Watson, J. G., Lowenthal, D. H., Magliano, K. A., Turkiewicz, K., and Lehrman, D. E.: PM2.5 chemical composition and spatiotemporal variability during the California Regional PM10/PM2.5 Air Quality Study (CRPAQS), J Geophys Res-Atmos, 111, D10S04, 10.1029/2005JD006457, 2006a.

Chow, J. C., Chen, L. W. A., Watson, J. G., Lowenthal, D. H., Magliano, K. A., Turkiewicz, K., and Lehrman, D. E.: PM2. 5 chemical composition and spatiotemporal variability during the California Regional PM10/PM2. 5 Air Quality Study (CRPAQS), J. Geophys. Res.-Atmos, 111, D10S04, 10.1029/2005JD006457, 2006b.

Chow, J. C., Watson, J. G., Lowenthal, D. H., and Magliano, K. L.: Size-resolved aerosol chemical concentrations at rural and urban sites in Central California, USA, Atmos. Res., 90, 243-252, 10.1016/j.atmosres.2008.03.017, 2008a.

Chow, J. C., Watson, J. G., Lowenthal, D. H., Park, K., Doraiswamy, P., Bowers, K., and Bode, R.: Continuous and filter-based measurements of PM2.5 nitrate and sulfate at the Fresno Supersite, Environ Monit Assess, 144, 179-189, DOI 10.1007/s10661-007-9987-5, 2008b.

Chu, S. H., Paisie, J. W., and Jang, B. W. L.: PM data analysis - a comparison of two urban areas: Fresno and Atlanta, Atmos. Environ., 38, 3155-3164, 10.1016/j.atmosenv.2004.03.018, 2004.

Collett, J. L., Hoag, K. J., Sherman, D. E., Bator, A., and Richards, L. W.: Spatial and temporal variations in San Joaquin Valley fog chemistry, Atmos. Environ., 33, 129-140, 10.1016/S1352-2310(98)00136-8, 1999.

Collier, S., and Zhang, Q.: Gas-Phase CO2 Subtraction for Improved Measurements of the Organic Aerosol Mass Concentration and Oxidation Degree by an Aerosol Mass Spectrometer, Environ. Sci. Technol., 47, 14324-14331, 10.1021/es404024h, 2013.

Collier, S., Zhou, S., Kuwayama, T., Forestieri, S., Brady, J., Zhang, M., Kleeman, M., Cappa, C., Bertram, T., and Zhang, Q.: Organic PM Emissions from Vehicles: Composition, O/C Ratio, and Dependence on PM Concentration, Aerosol Sci. Technol., 49, 86-97, 10.1080/02786826.2014.1003364, 2015.

Crawford, J. H., and Pickering, K. E.: DISCOVER-AQ: Advancing strategies for air quality observations in the next decade. In: EM, Air and Waste Management Association, 2014.

Crippa, M., DeCarlo, P. F., Slowik, J. G., Mohr, C., Heringa, M. F., Chirico, R., Poulain, L., Freutel, F., Sciare, J., Cozic, J., Di Marco, C. F., Elsasser, M., Nicolas, J. B., Marchand, N., Abidi, E., Wiedensohler, A., Drewnick, F., Schneider, J., Borrmann, S., Nemitz, E., Zimmermann, R., Jaffrezo, J. L., Prévôt, A. S. H., and Baltensperger, U.: Wintertime aerosol chemical composition and source apportionment of the organic fraction in the metropolitan area of Paris, Atmos. Chem. Phys., 13, 961-981, 10.5194/acp-13-961-2013, 2013.

Cubison, M. J., Ortega, A. M., Hayes, P. L., Farmer, D. K., Day, D., Lechner, M. J., Brune, W. H., Apel, E., Diskin, G. S., Fisher, J. A., Fuelberg, H. E., Hecobian, A., Knapp, D. J., Mikoviny, T.,

Riemer, D., Sachse, G. W., Sessions, W., Weber, R. J., Weinheimer, A. J., Wisthaler, A., and Jimenez, J. L.: Effects of aging on organic aerosol from open biomass burning smoke in aircraft and laboratory studies, Atmos. Chem. Phys., 11, 12049-12064, 10.5194/acp-11-12049-2011, 2011.

Curci, G., Ferrero, L., Tuccella, P., Barnaba, F., Angelini, F., Bolzacchini, E., Carbone, C., Denier van der Gon, H. A. C., Facchini, M. C., Gobbi, G. P., Kuenen, J. P. P., Landi, T. C., Perrino, C., Perrone, M. G., Sangiorgi, G., and Stocchi, P.: How much is particulate matter near the ground influenced by upper-level processes within and above the PBL? A summertime case study in Milan (Italy) evidences the distinctive role of nitrate, Atmos. Chem. Phys., 15, 2629-2649, 10.5194/acp-15-2629-2015, 2015.

Dall'Osto, M., Harrison, R. M., Coe, H., and Williams, P.: Real-time secondary aerosol formation during a fog event in London, Atmos. Chem. Phys., 9, 2459-2469, 10.5194/acp-9-2459-2009, 2009.

Day, D. A., Wooldridge, P. J., Dillon, M. B., Thornton, J. A., and Cohen, R. C.: A thermal dissociation laser-induced fluorescence instrument for in situ detection of NO2, peroxy nitrates, alkyl nitrates, and HNO3, J. Geophys. Res.-Atmos, 107, D64046, 10.1029/2001JD000779, 2002.

De Andrade, J. B., De Aragão, N. M., and Araújo, F. R. J.: Nitric Acid-Air Diffusion Coefficient: Experimental Determination Using a Diffusion Cell, Int. J. Environ. Anal. Chem., 49, 103-109, 10.1080/03067319208028130, 1992.

DeCarlo, P. F., Kimmel, J. R., Trimborn, A., Northway, M. J., Jayne, J. T., Aiken, A. C., Gonin, M., Fuhrer, K., Horvath, T., Docherty, K. S., Worsnop, D. R., and Jimenez, J. L.: Field-Deployable, High-Resolution, Time-of-Flight Aerosol Mass Spectrometer, Analytical Chemistry, 78, 8281-8289, 10.1021/ac061249n, 2006.

DeCarlo, P. F., Ulbrich, I. M., Crounse, J., de Foy, B., Dunlea, E. J., Aiken, A. C., Knapp, D., Weinheimer, A. J., Campos, T., Wennberg, P. O., and Jimenez, J. L.: Investigation of the sources and processing of organic aerosol over the Central Mexican Plateau from aircraft measurements during MILAGRO, Atmos. Chem. Phys., 10, 5257-5280, 10.5194/acp-10-5257-2010, 2010.

Dentener, F. J., and Crutzen, P. J.: Reaction of N2O5 on tropospheric aerosols - Impact on the global distributions of NOX, O3, and OH, J. Geophys. Res.-Atmos., 98, 7149-7163, 10.1029/92jd02979, 1993.

Drewnick, F., Jayne, J. T., Canagaratna, M., Worsnop, D. R., and Demerjian, K. L.: Measurement of Ambient Aerosol Composition During the PMTACS-NY 2001 Using an Aerosol Mass Spectrometer. Part II: Chemically Speciated Mass Distributions Special Issue of Aerosol Science and Technology on Findings from the Fine Particulate Matter Supersites Program, Aerosol Sci. Technol., 38, 104-117, 10.1080/02786820390229534, 2004.

Dzepina, K., Arey, J., Marr, L. C., Worsnop, D. R., Salcedo, D., Zhang, Q., Onasch, T. B., Molina, L. T., Molina, M. J., and Jimenez, J. L.: Detection of particle-phase polycyclic aromatic hydrocarbons in Mexico City using an aerosol mass spectrometer, International Journal of Mass Spectrometry, 263, 152-170, 10.1016/j.ijms.2007.01.010, 2007.

Ervens, B., Turpin, B. J., and Weber, R. J.: Secondary organic aerosol formation in cloud droplets and aqueous particles (aqSOA): a review of laboratory, field and model studies, Atmos. Chem. Phys., 11, 11069-11102, 10.5194/acp-11-11069-2011, 2011.

Farmer, D. K., Chen, Q., Kimmel, J. R., Docherty, K. S., Nemitz, E., Artaxo, P. A., Cappa, C. D., Martin, S. T., and Jimenez, J. L.: Chemically Resolved Particle Fluxes Over Tropical and Temperate Forests, Aerosol Sci. Technol., 47, 818-830, 10.1080/02786826.2013.791022, 2013.

Fountoukis, C., and Nenes, A.: ISORROPIA II: a computationally efficient thermodynamic equilibrium model for K^+, $Ca2^+$, $Mg2^+$,$NH4^+$, Na^+, SO_4^{2-}, NO_3^-, Cl^-, H_2O aerosols, Atmos. Chem. Phys., 7, 4639-4659, 10.5194/acp-7-4639-2007, 2007.

Ge, X., Setyan, A., Sun, Y., and Zhang, Q.: Primary and secondary organic aerosols in Fresno, California during wintertime: Results from high resolution aerosol mass spectrometry, J. Geophys. Res.-Atmos, 117, n/a-n/a, 10.1029/2012jd018026, 2012a.

Ge, X., Zhang, Q., Sun, Y., Ruehl, C. R., and Setyan, A.: Effect of aqueous-phase processing on aerosol chemistry and size distributions in Fresno, California, during wintertime, Environ. Chem., 9, 221-235, 10.1071/EN11168, 2012b.

Ge, X., Setyan, A., Sun, Y., and Zhang, Q.: Primary and secondary organic aerosols in Fresno, California during wintertime: Results from high resolution aerosol mass spectrometry, J. Geophys. Res.-Atmos., 10.1029/2012JD018026, 2012.

Gelencsér, A., May, B., Simpson, D., Sánchez-Ochoa, A., Kasper-Giebl, A., Puxbaum, H., Caseiro, A., Pio, C., and Legrand, M.: Source apportionment of PM2.5 organic aerosol over Europe: Primary/secondary, natural/anthropogenic, and fossil/biogenic origin, - 112, 2007.

Goldstein, A. H., Koven, C. D., Heald, C. L., and Fung, I. Y.: Biogenic carbon and anthropogenic pollutants combine to form a cooling haze over the southeastern United States, Proceedings of the National Academy of Sciences, 106, 8835-8840, 10.1073/pnas.0904128106, 2009.

Gorin, C. A., Collett, J. L., and Herckes, P.: Wood Smoke Contribution to Winter Aerosol in Fresno, CA, J. Air & Waste Manage. Assoc., 56, 1584-1590, 10.1080/10473289.2006.10464558, 2006.

Graus, M., Müller, M., and Hansel, A.: High Resolution PTR-TOF: Quantification and Formula Confirmation of VOC in Real Time, Journal of the American Society for Mass Spectrometry, 21, 1037-1044, 10.1016/j.jasms.2010.02.006, 2010.

Hall, J. V., Braker, V., and Lurmann, F. W.: The Benefits of Meeting Federal Clean Air Standards in the South Coast and San Jjoaquin Valley Air Basins, 2008.

Hannigan, M. P., Cass, G. R., Penman, B. W., Crespi, C. L., Lafleur, A. L., Busby, W. F., Thilly, W. G., and Simoneit, B. R. T.: Bioassay-Directed Chemical Analysis of Los Angeles Airborne Particulate Matter Using a Human Cell Mutagenicity Assay, Environ Sci Technol, 32, 3502-3514, 10.1021/es9706561, 1998.

Harrison, R. M., and Yin, J.: Particulate matter in the atmosphere: which particle properties are important for its effects on health?, Science of the Total Environment, 249, 85-101, 10.1016/S0048-9697(99)00513-6, 2000.

Herckes, P., Leenheer, J. A., and Collett, J. L.: Comprehensive Characterization of Atmospheric Organic Matter in Fresno, California Fog Water, Environ. Sci. Technol., 41, 393-399, 10.1021/es0607988, 2007.

Heringa, M. F., DeCarlo, P. F., Chirico, R., Tritscher, T., Dommen, J., Weingartner, E., Richter, R., Wehrle, G., Prévôt, A. S. H., and Baltensperger, U.: Investigations of primary and secondary particulate matter of different wood combustion appliances with a high-resolution time-of-flight

aerosol mass spectrometer, Atmos. Chem. Phys., 11, 5945-5957, 10.5194/acp-11-5945-2011, 2011.

Herndon, S. C., Onasch, T. B., Wood, E. C., Kroll, J. H., Canagaratna, M. R., Jayne, J. T., Zavala, M. A., Knighton, W. B., Mazzoleni, C., Dubey, M. K., Ulbrich, I. M., Jimenez, J. L., Seila, R., de Gouw, J. A., de Foy, B., Fast, J., Molina, L. T., Kolb, C. E., and Worsnop, D. R.: Correlation of secondary organic aerosol with odd oxygen in Mexico City, Geophys. Res. Lett., 35, 10.1029/2008GL034058, 2008.

Horii, C. V., Munger, J. W., Wofsy, S. C., Zahniser, M., Nelson, D., and McManus, J. B.: Atmospheric reactive nitrogen concentration and flux budgets at a Northeastern US forest site, Ag. Forest Meteor., 133, 210-225, 10.1016/j.agrformet.2004.08.009, 2005.

IPCC: Summary for policymakers, in: Climate Change 2013: The Physical Science Basis. Contribution of Working Group 1 to the Fifth Assessment Report of the Intergovernmental Panel on Climate Change, edited by: Stocker, T. F., Qin, D., Plattner, G.-K., Tignor, M., Allen, S. K., Boschung, J., Nauels, A., Xia, Y., Bex, V., and Midgley, P. M., Cambridge University Press, Cambridge, UK, New York, NY, USA, 3-29, 2013.

Janssen, R. H. H., Vilà-Guerau de Arellano, J., Ganzeveld, L. N., Kabat, P., Jimenez, J. L., Farmer, D. K., van Heerwaarden, C. C., and Mammarella, I.: Combined effects of surface conditions, boundary layer dynamics and chemistry on diurnal SOA evolution, Atmos. Chem. Phys., 12, 6827-6843, 10.5194/acp-12-6827-2012, 2012.

Janssen, R. H. H., Vilà-Guerau de Arellano, J., Jimenez, J. L., Ganzeveld, L. N., Robinson, N. H., Allan, J. D., Coe, H., and Pugh, T. A. M.: Influence of boundary layer dynamics and isoprene chemistry on the organic aerosol budget in a tropical forest, J. Geophys. Res.-Atmos, 118, 9351-9366, 10.1002/jgrd.50672, 2013.

Jimenez, J. L., Canagaratna, M. R., Donahue, N. M., Prevot, A. S. H., Zhang, Q., Kroll, J. H., DeCarlo, P. F., Allan, J. D., Coe, H., Ng, N. L., Aiken, A. C., Docherty, K. S., Ulbrich, I. M., Grieshop, A. P., Robinson, A. L., Duplissy, J., Smith, J. D., Wilson, K. R., Lanz, V. A., Hueglin, C., Sun, Y. L., Tian, J., Laaksonen, A., Raatikainen, T., Rautiainen, J., Vaattovaara, P., Ehn, M., Kulmala, M., Tomlinson, J. M., Collins, D. R., Cubison, M. J., E., Dunlea, J., Huffman, J. A., Onasch, T. B., Alfarra, M. R., Williams, P. I., Bower, K., Kondo, Y., Schneider, J., Drewnick, F., Borrmann, S., Weimer, S., Demerjian, K., Salcedo, D., Cottrell, L., Griffin, R., Takami, A., Miyoshi, T., Hatakeyama, S., Shimono, A., Sun, J. Y., Zhang, Y. M., Dzepina, K., Kimmel, J. R., Sueper, D., Jayne, J. T., Herndon, S. C., Trimborn, A. M., Williams, L. R., Wood, E. C., Middlebrook, A. M., Kolb, C. E., Baltensperger, U., and Worsnop, D. R.: Evolution of Organic Aerosols in the Atmosphere, Science, 326, 1525-1529, 10.1126/science.1180353, 2009.

Jordan, T. B., Seen, A. J., and Jacobsen, G. E.: Levoglucosan as an atmospheric tracer for woodsmoke, Atmos. Environ., 40, 5316-5321, 10.1016/j.atmosenv.2006.03.023, 2006.

Kanakidou, M., Seinfeld, J. H., Pandis, S. N., Barnes, I., Dentener, F. J., Facchini, M. C., Van Dingenen, R., Ervens, B., Nenes, A., Nielsen, C. J., Swietlicki, E., Putaud, J. P., Balkanski, Y., Fuzzi, S., Horth, J., Moortgat, G. K., Winterhalter, R., Myhre, C. E. L., Tsigaridis, K., Vignati, E., Stephanou, E. G., and Wilson, J.: Organic aerosol and global climate modelling: a review, Atmos. Chem. Phys., 5, 1053-1123, 10.5194/acp-5-1053-2005, 2005.

Kiendler-Scharr, A., Mensah, A. A., Friese, E., Topping, D., Nemitz, E., Prevot, A. S. H., Äijälä, M., Allan, J., Canonaco, F., Canagaratna, M., Carbone, S., Crippa, M., Dall Osto, M., Day, D. A.,

De Carlo, P., Di Marco, C. F., Elbern, H., Eriksson, A., Freney, E., Hao, L., Herrmann, H., Hildebrandt, L., Hillamo, R., Jimenez, J. L., Laaksonen, A., McFiggans, G., Mohr, C., O'Dowd, C., Otjes, R., Ovadnevaite, J., Pandis, S. N., Poulain, L., Schlag, P., Sellegri, K., Swietlicki, E., Tiitta, P., Vermeulen, A., Wahner, A., Worsnop, D., and Wu, H. C.: Organic nitrates from night-time chemistry are ubiquitous in the European submicron aerosol, Geophys. Res. Lett., 43, 7735-7744, 10.1002/2016GL069239, 2016.

Kim, H., Zhang, Q., Bae, G. N., Kim, J. Y., and Lee, S. B.: Sources and atmospheric processing of winter aerosols in Seoul, Korea: insights from real-time measurements using a high-resolution aerosol mass spectrometer, Atmos. Chem. Phys., 17, 2009-2033, 10.5194/acp-17-2009-2017, 2017.

Kim, Y. J., Spak, S. N., Carmichael, G. R., Riemer, N., and Stanier, C. O.: Modeled aerosol nitrate formation pathways during wintertime in the Great Lakes region of North America, J. Geophys. Res.-Atmos., 119, 12420-12445, 10.1002/2014jd022320, 2014.

Kleeman, M. J., Ying, Q., and Kaduwela, A.: Control strategies for the reduction of airborne particulate nitrate in California's San Joaquin Valley, Atmos. Environ., 39, 5325-5341, 10.1016/j.atmosenv.2005.05.044, 2005.

Kuprov, R., Eatough, D. J., Cruickshank, T., Olson, N., Cropper, P. M., and Hansen, J. C.: Composition and secondary formation of fine particulate matter in the Salt Lake Valley: Winter 2009, J. Air & Waste Manage. Assoc., 64, 957-969, 10.1080/10962247.2014.903878, 2014.

Lack, D. A., Richardson, M. S., Law, D., Langridge, J. M., Cappa, C. D., McLaughlin, R. J., and Murphy, D. M.: Aircraft instrument for comprehensive characterization of aerosol optical properties, Part 2: black and brown carbon absorption and absorption enhancement measured with photo acoustic spectroscopy, Aerosol Sci. Technol., 46, 555-568, 10.1080/02786826.2011.645955, 2012.

Lanz, V. A., Alfarra, M. R., Baltensperger, U., Buchmann, B., Hueglin, C., and Prévôt, A. S. H.: Source apportionment of submicron organic aerosols at an urban site by factor analytical modelling of aerosol mass spectra, Atmos. Chem. Phys., 7, 1503-1522, 10.5194/acp-7-1503-2007, 2007.

Lanz, V. A., Alfarra, M. R., Baltensperger, U., Buchmann, B., Hueglin, C., Szidat, S., Wehrli, M. N., Wacker, L., Weimer, S., Caseiro, A., Puxbaum, H., and Prevot, A. S. H.: Source Attribution of Submicron Organic Aerosols during Wintertime Inversions by Advanced Factor Analysis of Aerosol Mass Spectra, Environ. Sci. Technol., 42, 214-220, 10.1021/es0707207, 2008.

Lowe, D., Archer-Nicholls, S., Morgan, W., Allan, J., Utembe, S., Ouyang, B., Aruffo, E., Le Breton, M., Zaveri, R. A., and Di Carlo, P.: WRF-Chem model predictions of the regional impacts of N2O5 heterogeneous processes on night-time chemistry over north-western Europe, Atmos. Chem. Phys., 15, 1385-1409, 10.5194/acp-15-1385-2015, 2015.

Lurmann, F. W., Brown, S. G., McCarthy, M. C., and Roberts, P. T.: Processes Influencing Secondary Aerosol Formation in the San Joaquin Valley during Winter, J. Air & Waste Manage. Assoc., 56, 1679-1693, 10.1080/10473289.2006.10464573, 2006.

Ma, J., and Daggupaty, S. M.: Effective Dry Deposition Velocities for Gases and Particles over Heterogeneous Terrain, J. Appl. Meteor., 39, 1379-1390, 10.1175/1520-0450(2000)039<1379:eddvfg>2.0.co;2, 2000.

Marr, L. C., Dzepina, K., Jimenez, J. L., Reisen, F., Bethel, H. L., Arey, J., Gaffney, J. S., Marley, N. A., Molina, L. T., and Molina, M. J.: Sources and transformations of particle-bound polycyclic

aromatic hydrocarbons in Mexico City, Atmos. Chem. Phys., 6, 1733-1745, 10.5194/acp-6-1733-2006, 2006.

Martin, C. L., Allan, J. D., Crosier, J., Choularton, T. W., Coe, H., and Gallagher, M. W.: Seasonal variation of fine particulate composition in the centre of a UK city, Atmos. Environ., 45, 4379-4389, 10.1016/j.atmosenv.2011.05.050, 2011.

Massoli, P., Bates, T. S., Quinn, P. K., Lack, D. A., Baynard, T., Lerner, B. M., Tucker, S. C., Brioude, J., Stohl, A., and Williams, E. J.: Aerosol optical and hygroscopic properties during TexAQS-GoMACCS 2006 and their impact on aerosol direct radiative forcing, J. Geophys. Res.-Atmos, 114, D00F07, 10.1029/2008JD011604, 2009.

Meyers, T., Huebert, B., and Hicks, B.: HNO_3 deposition to a deciduous forest, Boundary Layer Meteor., 49, 395-410, 10.1007/BF00123651, 1989.

Middlebrook, A. M., Bahreini, R., Jimenez, J. L., and Canagaratna, M. R.: Evaluation of Composition-Dependent Collection Efficiencies for the Aerodyne Aerosol Mass Spectrometer using Field Data, Aerosol Sci. Technol., 46, 258-271, 10.1080/02786826.2011.620041, 2012.

Mohr, C., DeCarlo, P. F., Heringa, M. F., Chirico, R., Slowik, J. G., Richter, R., Reche, C., Alastuey, A., Querol, X., Seco, R., Peñuelas, J., Jiménez, J. L., Crippa, M., Zimmermann, R., Baltensperger, U., and Prévôt, A. S. H.: Identification and quantification of organic aerosol from cooking and other sources in Barcelona using aerosol mass spectrometer data, Atmos. Chem. Phys., 12, 1649-1665, 10.5194/acp-12-1649-2012, 2012.

Morgan, W. T., Allan, J. D., Bower, K. N., Highwood, E. J., Liu, D., McMeeking, G. R., Northway, M. J., Williams, P. I., Krejci, R., and Coe, H.: Airborne measurements of the spatial distribution of aerosol chemical composition across Europe and evolution of the organic fraction, Atmos. Chem. Phys., 10, 4065-4083, 10.5194/acp-10-4065-2010, 2010.

Müller, M., Mikoviny, T., Jud, W., D'Anna, B., and Wisthaler, A.: A new software tool for the analysis of high resolution PTR-TOF mass spectra, Chemometrics and Intelligent Laboratory Systems, 127, 158-165, j.chemolab.2013.06.011, 2013.

DISCOVER-AQ data and information, access: 01/26/2017.

Ng, N. L., Canagaratna, M. R., Zhang, Q., Jimenez, J. L., Tian, J., Ulbrich, I. M., Kroll, J. H., Docherty, K. S., Chhabra, P. S., Bahreini, R., Murphy, S. M., Seinfeld, J. H., Hildebrandt, L., Donahue, N. M., DeCarlo, P. F., Lanz, V. A., Prévôt, A. S. H., Dinar, E., Rudich, Y., and Worsnop, D. R.: Organic aerosol components observed in Northern Hemispheric datasets from Aerosol Mass Spectrometry, Atmos. Chem. Phys., 10, 4625-4641, 10.5194/acp-10-4625-2010, 2010.

Ng, N. L., Brown, S. S., Archibald, A. T., Atlas, E., Cohen, R. C., Crowley, J. N., Day, D. A., Donahue, N. M., Fry, J. L., Fuchs, H., Griffin, R. J., Guzman, M. I., Herrmann, H., Hodzic, A., Iinuma, Y., Jimenez, J. L., Kiendler-Scharr, A., Lee, B. H., Luecken, D. J., Mao, J., McLaren, R., Mutzel, A., Osthoff, H. D., Ouyang, B., Picquet-Varrault, B., Platt, U., Pye, H. O. T., Rudich, Y., Schwantes, R. H., Shiraiwa, M., Stutz, J., Thornton, J. A., Tilgner, A., Williams, B. J., and Zaveri, R. A.: Nitrate radicals and biogenic volatile organic compounds: oxidation, mechanisms, and organic aerosol, Atmos. Chem. Phys., 17, 2103-2162, 10.5194/acp-17-2103-2017, 2017.

Ngo, M. A., Pinkerton, K. E., Freeland, S., Geller, M., Ham, W., Cliff, S., Hopkins, L. E., Kleeman, M. J., Kodavanti, U. P., Meharg, E., Plummer, L., Recendez, J. J., Schenker, M. B., Sioutas, C., Smiley-Jewell, S., Haas, C., Gutstein, J., and Wexler, A. S.: Airborne particles in the San Joaquin Valley may affect human health, California Agriculture, 64, 12-16, 2010.

Nowak, J. B., Neuman, J. A., Bahreini, R., Brock, C. A., Middlebrook, A. M., Wollny, A. G., Holloway, J. S., Peischl, J., Ryerson, T. B., and Fehsenfeld, F. C.: Airborne observations of ammonia and ammonium nitrate formation over Houston, Texas, J. Geophys. Res.-Atmos, 115, D22304, 10.1029/2010JD014195, 2010.

Ortega, A. M., Day, D. A., Cubison, M. J., Brune, W. H., Bon, D., de Gouw, J. A., and Jimenez, J. L.: Secondary organic aerosol formation and primary organic aerosol oxidation from biomass-burning smoke in a flow reactor during FLAME-3, Atmos. Chem. Phys., 13, 11551-11571, 10.5194/acp-13-11551-2013, 2013.

Otto, A., Gondokusumo, R., and Simpson, M. J.: Characterization and quantification of biomarkers from biomass burning at a recent wildfire site in Northern Alberta, Canada, Applied Geochemistry, 21, 166-183, 10.1016/j.apgeochem.2005.09.007, 2006.

Ouwersloot, H. G., and Vilà-Guerau de Arellano, J.: Analytical Solution for the Convectively-Mixed Atmospheric Boundary Layer, Boundary Layer Meteor., 148, 557-583, 10.1007/s10546-013-9816-z, 2013.

Paatero, P., and Tapper, U.: Positive matrix factorization: A non-negative factor model with optimal utilization of error estimates of data values, Environmetrics, 5, 111-126, 10.1002/env.3170050203, 1994.

Paatero, P., Hopke, P. K., Song, X.-H., and Ramadan, Z.: Understanding and controlling rotations in factor analytic models, Chemometrics and Intelligent Laboratory Systems, 60, 253-264, 10.1016/S0169-7439(01)00200-3, 2002.

Parworth, C., Fast, J., Mei, F., Shippert, T., Sivaraman, C., Tilp, A., Watson, T., and Zhang, Q.: Long-term measurements of submicrometer aerosol chemistry at the Southern Great Plains (SGP) using an Aerosol Chemical Speciation Monitor (ACSM), Atmos. Environ., 106, 43-55, 10.1016/j.atmosenv.2015.01.060, 2015.

Parworth, C., Young, D., Kim, H., Zhou, S., Collier, S., Zhang, X., Cappa, C., and Zhang, Q.: Water-soluble inorganic and organic ions in Fresno, CA during winter 2013 NASA DISCOVER-AQ campaign, in preparation, In preparation.

Parworth, C. L., Young, D. E., Kim, H., Zhang, X., Cappa, C. D., Collier, S., and Zhang, Q.: Wintertime water-soluble aerosol composition and particle water content in Fresno, California: Results from DISCOVER-AQ 2013, J. Geophys. Res.-Atmos, 122, 3155-3170, 10.1002/2016JD026173, 2017.

Petters, M. D., and Kreidenweis, S. M.: A single parameter representation of hygroscopic growth and cloud condensation nucleus activity, Atmos. Chem. Phys., 7, 1961-1971, 10.5194/acp-7-1961-2007, 2007.

Phinney, L., Richard Leaitch, W., Lohmann, U., Boudries, H., Worsnop, D. R., Jayne, J. T., Toom-Sauntry, D., Wadleigh, M., Sharma, S., and Shantz, N.: Characterization of the aerosol over the sub-arctic north east Pacific Ocean, Deep Sea Research Part II: Topical Studies in Oceanography, 53, 2410-2433, 10.1016/j.dsr2.2006.05.044, 2006.

Pope, C. A., and Dockery, D. W.: Health Effects of Fine Particulate Air Pollution: Lines that Connect, J. Air & Waste Manage. Assoc., 56, 709-742, 10.1080/10473289.2006.10464485, 2006.

Pöschl, U.: Atmospheric Aerosols: Composition, Transformation, Climate and Health Effects, Angew. Chem. Int. Ed. , 44, 7520-7540, 10.1002/anie.200501122, 2005.

Pusede, S. E., Gentner, D. R., Wooldridge, P. J., Browne, E. C., Rollins, A. W., Min, K. E., Russell, A. R., Thomas, J., Zhang, L., Brune, W. H., Henry, S. B., DiGangi, J. P., Keutsch, F. N., Harrold, S. A., Thornton, J. A., Beaver, M. R., St. Clair, J. M., Wennberg, P. O., Sanders, J., Ren, X., VandenBoer, T. C., Markovic, M. Z., Guha, A., Weber, R., Goldstein, A. H., and Cohen, R. C.: On the temperature dependence of organic reactivity, nitrogen oxides, ozone production, and the impact of emission controls in San Joaquin Valley, California, Atmos. Chem. Phys., 14, 3373-3395, 10.5194/acp-14-3373-2014, 2014.

Pusede, S. E., Duffey, K. C., Shusterman, A. A., Saleh, A., Laughner, J. L., Wooldridge, P. J., Zhang, Q., Parworth, C. L., Kim, H., Capps, S. L., Valin, L. C., Cappa, C. D., Fried, A., Walega, J., Nowak, J. B., Weinheimer, A. J., Hoff, R. M., Berkoff, T. A., Beyersdorf, A. J., Olson, J., Crawford, J. H., and Cohen, R. C.: On the effectiveness of nitrogen oxide reductions as a control over ammonium nitrate aerosol, Atmos. Chem. Phys., 16, 2575-2596, 10.5194/acp-16-2575-2016, 2016.

Riemer, N., Vogel, H., Vogel, B., Schell, B., Ackermann, I., Kessler, C., and Hass, H.: Impact of the heterogeneous hydrolysis of N2O5 on chemistry and nitrate aerosol formation in the lower troposphere under photosmog conditions, J. Geophys. Res.-Atmos., 108, D44144, 10.1029/2002jd002436, 2003.

Rollins, A. W., Browne, E. C., Min, K.-E., Pusede, S. E., Wooldridge, P. J., Gentner, D. R., Goldstein, A. H., Liu, S., Day, D. A., Russell, L. M., and Cohen, R. C.: Evidence for NOx Control over Nighttime SOA Formation, Science, 337, 1210-1212, 10.1126/science.1221520, 2012.

Sachse, G. W., Hill, G. F., Wade, L. O., and Perry, M. G.: Fast-response, high-precision carbon monoxide sensor using a tunable diode laser absorption technique, J. Geophys. Res.-Atmos, 92, 2071-2081, 10.1029/JD092iD02p02071, 1987.

San Joaquin Airshed 2003 PM10 Plan https://www.valleyair.org/Air_Quality_Plans/docs/2003%20PM10%20Plan/PDF%202003%20PM10%20Plan%20adpt%20chapters/Ch%202-Final.pdf, access: 6/20/2016, 2003.

Schiferl, L. D., Heald, C. L., Nowak, J. B., Holloway, J. S., Neuman, J. A., Bahreini, R., Pollack, I. B., Ryerson, T. B., Wiedinmyer, C., and Murphy, J. G.: An investigation of ammonia and inorganic particulate matter in California during the CalNex campaign, J. Geophys. Res.-Atmos, 119, 1883-1902, 10.1002/2013JD020765, 2014.

Schneider, J., Weimer, S., Drewnick, F., Borrmann, S., Helas, G., Gwaze, P., Schmid, O., Andreae, M. O., and Kirchner, U.: Mass spectrometric analysis and aerodynamic properties of various types of combustion-related aerosol particles, International Journal of Mass Spectrometry, 258, 37-49, 10.1016/j.ijms.2006.07.008, 2006.

Schwarz, J. P., Gao, R. S., Fahey, D. W., Thomson, D. S., Watts, L. A., Wilson, J. C., Reeves, J. M., Darbeheshti, M., Baumgardner, D. G., Kok, G. L., Chung, S. H., Schulz, M., Hendricks, J., Lauer, A., Kärcher, B., Slowik, J. G., Rosenlof, K. H., Thompson, T. L., Langford, A. O., Loewenstein, M., and Aikin, K. C.: Single-particle measurements of midlatitude black carbon and light-scattering aerosols from the boundary layer to the lower stratosphere, Journal of Geophysical Research: Atmospheres, 111, n/a-n/a, 10.1029/2006JD007076, 2006a.

Schwarz, J. P., Gao, R. S., Fahey, D. W., Thomson, D. S., Watts, L. A., Wilson, J. C., Reeves, J. M., Darbeheshti, M., Baumgardner, D. G., Kok, G. L., Chung, S. H., Schulz, M., Hendricks, J., Lauer, A., Kärcher, B., Slowik, J. G., Rosenlof, K. H., Thompson, T. L., Langford, A. O.,

Loewenstein, M., and Aikin, K. C.: Single-particle measurements of midlatitude black carbon and light-scattering aerosols from the boundary layer to the lower stratosphere, J. Geophys. Res.-Atmos, 111, 10.1029/2006JD007076, 2006b.

Seco, R., Peñuelas, J., Filella, I., Llusia, J., Schallhart, S., Metzger, A., Müller, M., and Hansel, A.: Volatile organic compounds in the western Mediterranean basin: urban and rural winter measurements during the DAURE campaign, Atmos. Chem. Phys., 13, 4291-4306, 10.5194/acp-13-4291-2013, 2013.

Seinfeld, J. H., and Pandis, S. N.: Atmospheric Chemistry and Physics: From Air Pollution to Climate Change, 2nd ed., John Wiley & Sons, New York, 1232 pp., 2006a.

Seinfeld, J. H., and Pandis, S. N.: Atmospheric Chemistry and Physics: From Air Pollution to Climate Change, Second ed., John Wiley and sons, 2006b.

Setyan, A., Zhang, Q., Merkel, M., Knighton, W. B., Sun, Y., Song, C., Shilling, J. E., Onasch, T. B., Herndon, S. C., Worsnop, D. R., Fast, J. D., Zaveri, R. A., Berg, L. K., Wiedensohler, A., Flowers, B. A., Dubey, M. K., and Subramanian, R.: Characterization of submicron particles influenced by mixed biogenic and anthropogenic emissions using high-resolution aerosol mass spectrometry: results from CARES, Atmos. Chem. Phys., 12, 8131-8156, 10.5194/acp-12-8131-2012, 2012.

Simoneit, B. R. T., Schauer, J. J., Nolte, C. G., Oros, D. R., Elias, V. O., Fraser, M. P., Rogge, W. F., and Cass, G. R.: Levoglucosan, a tracer for cellulose in biomass burning and atmospheric particles, Atmos. Environ., 33, 173-182, 10.1016/s1352-2310(98)00145-9, 1999.

Simoneit, B. R. T., Rushdi, A. I., bin Abas, M. R., and Didyk, B. M.: Alkyl Amides and Nitriles as Novel Tracers for Biomass Burning, Environ. Sci. Technol., 37, 16-21, 10.1021/es020811y, 2003.

Sorooshian, A., Murphy, S. M., Hersey, S., Gates, H., Padro, L. T., Nenes, A., Brechtel, F. J., Jonsson, H., Flagan, R. C., and Seinfeld, J. H.: Comprehensive airborne characterization of aerosol from a major bovine source, Atmos. Chem. Phys., 8, 5489-5520, 10.5194/acp-8-5489-2008, 2008.

Stelson, A., and Seinfeld, J. H.: Relative humidity and temperature dependence of the ammonium nitrate dissociation constant, Atmos. Environ., 16, 983-992, 10.1016/0004-6981(82)90184-6, 1982.

Sun, Y. L., Zhang, Q., Schwab, J. J., Demerjian, K. L., Chen, W. N., Bae, M. S., Hung, H. M., Hogrefe, O., Frank, B., Rattigan, O. V., and Lin, Y. C.: Characterization of the sources and processes of organic and inorganic aerosols in New York city with a high-resolution time-of-flight aerosol mass apectrometer, Atmos. Chem. Phys., 11, 1581-1602, 10.5194/acp-11-1581-2011, 2011.

Terrenoire, E., Bessagnet, B., Rouïl, L., Tognet, F., Pirovano, G., Létinois, L., Beauchamp, M., Colette, A., Thunis, P., Amann, M., and Menut, L.: High-resolution air quality simulation over Europe with the chemistry transport model CHIMERE, Geosci. Model Dev., 8, 21-42, 10.5194/gmd-8-21-2015, 2015.

Thornton, J. A., Kercher, J. P., Riedel, T. P., Wagner, N. L., Cozic, J., Holloway, J. S., Dubé, W. P., Wolfe, G. M., Quinn, P. K., Middlebrook, A. M., Alexander, B., and Brown, S. S.: A large atomic chlorine source inferred from mid-continental reactive nitrogen chemistry, Nature, 464, 271-274, 10.1038/nature08905, 2010.

Turkiewicz, K., Magliano, K., and Najita, T.: Comparison of Two Winter Air Quality Episodes during the California Regional Particulate Air Quality Study, J. Air & Waste Manage. Assoc., 56, 467-473, 10.1080/10473289.2006.10464525, 2006.

Ulbrich, I. M., Canagaratna, M. R., Zhang, Q., Worsnop, D. R., and Jimenez, J. L.: Interpretation of organic components from Positive Matrix Factorization of aerosol mass spectrometric data, Atmos. Chem. Phys., 9, 2891-2918, 2009.

Vilà-Guerau De Arellano, J., Heerwaarden, C.C. van, Stratum, B.J.H. van & Dries, K. van den: Atmospheric Boundary Layer, Integrating Air Chemistry and Land Interactions, Cambridge University Press, New York, 2015.

von Bobrutzki, K., Braban, C. F., Famulari, D., Jones, S. K., Blackall, T., Smith, T. E. L., Blom, M., Coe, H., Gallagher, M., Ghalaieny, M., McGillen, M. R., Percival, C. J., Whitehead, J. D., Ellis, R., Murphy, J., Mohacsi, A., Pogany, A., Junninen, H., Rantanen, S., Sutton, M. A., and Nemitz, E.: Field inter-comparison of eleven atmospheric ammonia measurement techniques, Atmos. Meas. Tech., 3, 91-112, 10.5194/amt-3-91-2010, 2010.

von Glasow, R., and Crutzen, P. J.: Model study of multiphase DMS oxidation with a focus on halogens, Atmos. Chem. Phys., 4, 589-608, 2004.

Wagner, N. L., Riedel, T. P., Young, C. J., Bahreini, R., Brock, C. A., Dubé, W. P., Kim, S., Middlebrook, A. M., Öztürk, F., Roberts, J. M., Russo, R., Sive, B., Swarthout, R., Thornton, J. A., VandenBoer, T. C., Zhou, Y., and Brown, S. S.: N2O5 uptake coefficients and nocturnal NO2 removal rates determined from ambient wintertime measurements, J. Geophys. Res.-Atmos, 118, 9331-9350, 10.1002/jgrd.50653, 2013.

Walker, J. M., Philip, S., Martin, R. V., and Seinfeld, J. H.: Simulation of nitrate, sulfate, and ammonium aerosols over the United States, Atmos. Chem. Phys., 12, 11213-11227, 10.5194/acp-12-11213-2012, 2012.

Wang, X., Zhang, Y., Chen, H., Yang, X., Chen, J., and Geng, F.: Particulate Nitrate Formation in a Highly Polluted Urban Area: A Case Study by Single-Particle Mass Spectrometry in Shanghai, Environ. Sci. Technol., 43, 3061-3066, 10.1021/es8020155, 2009.

Watson, J. G., Chow, J. C., Bowen, J. L., Lowenthal, D. H., Hering, S., Ouchida, P., and Oslund, W.: Air quality measurements from the Fresno Supersite, J. Air & Waste Manage. Assoc., 50, 1321-1334, 2000.

Watson, J. G.: Visibility: Science and Regulation, J. Air & Waste Manage. Assoc., 52, 628-713, 10.1080/10473289.2002.10470813, 2002.

Watson, J. G., and Chow, J. C.: A wintertime PM2.5 episode at the fresno, CA, supersite, Atmospheric Environment, 36, 465-475, 10.1016/s1352-2310(01)00309-0, 2002a.

Watson, J. G., and Chow, J. C.: Comparison and evaluation of in situ and filter carbon measurements at the Fresno Supersite, J. Geophys. Res.-Atmos., 107, D218341, 10.1029/2001jd000573, 2002b.

Watson, J. G., and Chow, J. C.: A wintertime PM 2.5 episode at the Fresno, CA, supersite, Atmos. Environ., 36, 465-475, 10.1016/S1352-2310(01)00309-0, 2002c.

Whiteman, C. D., Hoch, S. W., Horel, J. D., and Charland, A.: Relationship between particulate air pollution and meteorological variables in Utah's Salt Lake Valley, Atmos. Environ., 94, 742-753, 10.1016/j.atmosenv.2014.06.012, 2014.

Wild, R. J., Edwards, P. M., Bates, T. S., Cohen, R. C., de Gouw, J. A., Dubé, W. P., Gilman, J. B., Holloway, J., Kercher, J., Koss, A. R., Lee, L., Lerner, B. M., McLaren, R., Quinn, P. K., Roberts, J. M., Stutz, J., Thornton, J. A., Veres, P. R., Warneke, C., Williams, E., Young, C. J., Yuan, B., Zarzana, K. J., and Brown, S. S.: Reactive nitrogen partitioning and its relationship to winter ozone events in Utah, Atmos. Chem. Phys., 16, 573-583, 10.5194/acp-16-573-2016, 2016.

Xu, L., Guo, H., Boyd, C. M., Klein, M., Bougiatioti, A., Cerully, K. M., Hite, J. R., Isaacman-VanWertz, G., Kreisberg, N. M., Knote, C., Olson, K., Koss, A., Goldstein, A. H., Hering, S. V., de Gouw, J., Baumann, K., Lee, S. H., Nenes, A., Weber, R. J., and Ng, N. L.: Effects of anthropogenic emissions on aerosol formation from isoprene and monoterpenes in the southeastern United States, Proceedings of the National Academy of Sciences of the United States of America, 112, 37-42, 10.1073/pnas.1417609112, 2015.

Young, D. E., Allan, J. D., Williams, P. I., Green, D. C., Flynn, M. J., Harrison, R. M., Yin, J., Gallagher, M. W., and Coe, H.: Investigating the annual behaviour of submicron secondary inorganic and organic aerosols in London, Atmos. Chem. Phys., 15, 6351-6366, 10.5194/acp-15-6351-2015, 2015a.

Young, D. E., Allan, J. D., Williams, P. I., Green, D. C., Harrison, R. M., Yin, J., Flynn, M. J., Gallagher, M. W., and Coe, H.: Investigating a two-component model of solid fuel organic aerosol in London: processes, PM_1 contributions, and seasonality, Atmos. Chem. Phys., 15, 2429-2443, 10.5194/acp-15-2429-2015, 2015b.

Young, D. E., Kim, H., Parworth, C., Zhou, S., Zhang, X., Cappa, C. D., Seco, R., Kim, S., and Zhang, Q.: Influences of emission sources and meteorology on aerosol chemistry in a polluted urban environment: results from DISCOVER-AQ California, Atmos. Chem. Phys., 16, 5427-5451, 10.5194/acp-16-5427-2016, 2016.

Yuan, B., Warneke, C., Shao, M., and de Gouw, J. A.: Interpretation of volatile organic compound measurements by proton-transfer-reaction mass spectrometry over the deepwater horizon oil spill, International Journal of Mass Spectrometry, 358, 43-48, 10.1016/j.ijms.2013.11.006, 2014.

Zhang, Q., Alfarra, M. R., Worsnop, D. R., Allan, J. D., Coe, H., Canagaratna, M. R., and Jimenez, J. L.: Deconvolution and Quantification of Hydrocarbon-like and Oxygenated Organic Aerosols Based on Aerosol Mass Spectrometry, Environ Sci Technol, 39, 4938-4952, 10.1021/es048568l, 2005a.

Zhang, Q., Canagaratna, M. R., Jayne, J. T., Worsnop, D. R., and Jimenez, J. L.: Time- and size-resolved chemical composition of submicron particles in Pittsburgh: Implications for aerosol sources and processes, J. Geophys. Res.-Atmos., 110, D07S09, 10.1029/2004jd004649, 2005b.

Zhang, Q., Jimenez, J. L., Canagaratna, M. R., Allan, J. D., Coe, H., Ulbrich, I., Alfarra, M. R., Takami, A., Middlebrook, A. M., Sun, Y. L., Dzepina, K., Dunlea, E., Docherty, K., DeCarlo, P. F., Salcedo, D., Onasch, T., Jayne, J. T., Miyoshi, T., Shimono, A., Hatakeyama, S., Takegawa, N., Kondo, Y., Schneider, J., Drewnick, F., Borrmann, S., Weimer, S., Demerjian, K., Williams, P., Bower, K., Bahreini, R., Cottrell, L., Griffin, R. J., Rautiainen, J., Sun, J. Y., Zhang, Y. M., and Worsnop, D. R.: Ubiquity and dominance of oxygenated species in organic aerosols in anthropogenically-influenced Northern Hemisphere midlatitudes, Geophys. Res. Lett., 34, n/a-n/a, 10.1029/2007gl029979, 2007a.

Zhang, Q., Jimenez, J. L., Worsnop, D. R., and Canagaratna, M.: A case study of urban particle acidity and its influence on secondary organic aerosol, Environ. Sci. Technol., 41, 3213-3219, 10.1021/Es061812j, 2007b.

Zhang, Q., Jimenez, J. L., Canagaratna, M. R., Ulbrich, I. M., Ng, N. L., Worsnop, D. R., and Sun, Y.: Understanding atmospheric organic aerosols via factor analysis of aerosol mass spectrometry: a review, Anal Bioanal Chem, 401, 3045-3067, 10.1007/s00216-011-5355-y, 2011.

Zhang, X., Massoli, P., Quinn, P. K., Bates, T. S., and Cappa, C. D.: Hygroscopic growth of submicron and supermicron aerosols in the marine boundary layer, J. Geophys. Res.-Atmos, 119, 8384-8399, 10.1002/2013JD021213, 2014.

Zhang, X., Kim, H., Parworth, C., Young, D., Zhang, Q., Metcalf, A. R., and Cappa, C. D.: Optical Properties of Wintertime Aerosols from Residential Wood Burning in Fresno, CA: Results from DISCOVER-AQ 2013 Study, Environ. Sci. Technol., 50, 1681-1690, 10.1021/acs.est.5b04134, 2016a.

Zhang, X., Kim, H., Parworth, C. L., Young, D. E., Zhang, Q., Metcalf, A. R., and Cappa, C. D.: Optical Properties of Wintertime Aerosols from Residential Wood Burning in Fresno, CA: Results from DISCOVER-AQ 2013, Environ. Sci. Technol., 50, 1681-1690, 10.1021/acs.est.5b04134, 2016b.

Zorn, S. R., Drewnick, F., Schott, M., Hoffmann, T., and Borrmann, S.: Characterization of the South Atlantic marine boundary layer aerosol using an aerodyne aerosol mass spectrometer, Atmos. Chem. Phys., 8, 4711-4728, 2008.

7 LIST OF PUBLICATIONS PRODUCED

Prabhakar, G., Parworth, C., Zhang, X., Kim, H., Young, D. E., Beyersdorf, A. J., Ziemba, L. D., Nowak, J. B., Bertram, T. H., Faloona, I. C., Zhang, Q., and Cappa, C. D.: Observational assessment of the role of nocturnal residual-layer chemistry in determining daytime surface particulate nitrate concentrations, Atmos. Chem. Phys., 17, 14,747-714,770, 10.5194/acp-17-14747-2017, 2017.

Pusede, S. E., Duffey, K. C., Shusterman, A. A., Saleh, A., Laughner, J. L., Wooldridge, P. J., Zhang, Q., Parworth, C. L., Kim, H., Capps, S. L., Valin, L. C., Cappa, C. D., Fried, A., Walega, J., Nowak, J. B., Weinheimer, A. J., Hoff, R. M., Berkoff, T. A., Beyersdorf, A. J., Olson, J., Crawford, J. H., and Cohen, R. C.: On the effectiveness of nitrogen oxide reductions as a control over ammonium nitrate aerosol, Atmos. Chem. Phys., 16, 2575-2596, 10.5194/acp-16-2575-2016, 2016.

Young, D. E., Kim, H., Parworth, C., Zhou, S., Zhang, X., Cappa, C. D., Seco, R., Kim, S., and Zhang, Q.: Influences of emission sources and meteorology on aerosol chemistry in a polluted urban environment: results from DISCOVER-AQ California, Atmos. Chem. Phys., 16, 5427-5451, 10.5194/acp-16-5427-2016, 2016.

8 SUMMARY OF TERMS AND ABBREVIATIONS

AMS – Aerosol Mass Spectrometer
AN – ammonium nitrate
BBOA – Biomass-burning derived organic aerosol
BL – boundary layer
CARB - California Air Resources Board
DISCOVER-AQ –Deriving Information on Surface Conditions from COlumn and VERtically Resolved Observations Relevant to Air Quality
HNO_3 – gas-phase nitric acid
HOA – Hydrocarbon-like Organic Aerosol
ICs - initial conditions
IR – Incremental Reactivity
ML – mixed layer
NBL – nocturnal boundary layer
NH_4^+ / N(-III) - ammonium
$NO_{3(p)}^-$ – particulate nitrate
NO_3 – nitrate radical
NOx - oxides of nitrogen
NRL – nocturnal residual layer
O_3 - ozone
OC - organic carbon

OM – Organic Matter
OH - hydroxyl radical
OOA – Oxygenated Organic Aerosol
PILS – particle into liquid sampler
PM_{10} - Airborne particle mass with aerodynamic diameter less than 10.0 μm.
$PM_{2.5}$ - Airborne particle mass with aerodynamic diameter less than 2.5 μm.
PM_{1} - Airborne particle mass with aerodynamic diameter less than 1 μm.
PM - Airborne particulate matter
PMF – positive matrix factorization
POA – primary organic aerosol
RL – residual layer
SJV - San Joaquin Valley Air Basin
SOA – secondary organic aerosol
SO_4^{2-} / S(VI) – sulfate
TD-LIF – thermal desorption laser induced fluorescence
UCD - University of California at Davis
VOC - volatile organic compounds